Dissertation zur Erlangung des Doktorgrades
der Fakultät für Chemie und Pharmazie
der Ludwig-Maximilians-Universität München

Applying cryo-EM techniques to investigate disease-related protein interactions and regulations

Christopher Cyrus Kuhn
aus
München, Deutschland

2023

Erklärung

Diese Dissertation wurde im Sinne von § 7 der Promotionsordnung vom 28. November 2011 von Frau Hon.-Prof. Dr. Elena Conti betreut.

Eidesstattliche Versicherung

Diese Dissertation wurde eigenständig und ohne unerlaubte Hilfe erarbeitet.

München, 1.6.2023

Christopher Cyrus Kuhn

Dissertation eingereicht am:	16.3.2023
1. Gutachterin:	Prof. Dr. Elena Conti
2. Gutachter:	Prof. Dr. Karl-Peter Hopfner
Mündliche Prüfung am:	10.5.2023

Table of Contents

List of Figures

Summary

Within the last years, cryo-electron microscopy (cryo-EM) evolved to a powerful technique that is able to unveil the architecture of biological specimen in detail. On the molecular level, single particle cryo-EM and the following analysis provide high-resolution information of macromolecules and the mechanisms behind their biochemical properties. On the contrary, *in situ* cryo-electron tomography (cryo-ET) provides structural insights at the cellular level, and thus to observe the interactions of different protagonists at a molecular level. This thesis presents two independent research projects focused on the structural investigation of biological processes. By applying modern cryo-EM single particle analysis (SPA) and *in situ* cryo-ET approaches, biological questions are addressed at different scales.

The first project addresses coagulopathic events of platelets in context of the infection with novel coronavirus severe acute respiratory syndrome coronavirus 2 (SARS-CoV-2). The SARS-CoV-2 spike protein (S protein), mainly interacting with the angiotensin-converting enzyme 2 (ACE2) host cell receptor, causes its high pathogenicity of the virus. Whether platelet expressing ACE2 is unclear, however, their hyperactive behavior in the presence of SARS-CoV-2 or its spike protein was observed. In this study, biochemical, cell biology-based and structural experiments were used to investigate the behavior of human platelets in the presence of the SARS-CoV-2 S protein. After addition of S protein, live-cell imaging reveals the deformation and increased activation of isolated platelets. Additional densities on filopodial platelet which resembles the S protein were observed by cellular cryo-ET. Interestingly, the S protein has an RGD-motif in its receptor binding domain (RBD), a short stretch recognized by integrins. Further biochemical experiments confirmed that the S protein is able to interact, albeit with low affinity, to the integrin $\alpha_v\beta_3$ on platelets.
Taken together, these observations imply the direct interaction between the SARS-CoV-2 spike protein and platelets, probably mediated by integrin $\alpha_v\beta_3$. The binding of the S protein to the platelet surface can induce their deformation and activation, which can contribute to the coagulopathic events of COVID-19.

In the second project, the resolution of Holliday junctions (HJ), an DNA intermediate occurring during homologous recombination (HR), was investigated. In particular, the study focused on the eukaryotic Holliday junction resolvase GEN1, which dimerically assembles on HJs and subsequently cleaves the DNA four-way junction. Previous structural studies on GEN1 revealed the domain architecture of the nuclease core, but the dimer formation on its HJ substrate and the

mechanisms underlying the nick counter-nick cleavage are still elusive. In this study, biochemical and structural approaches were applied to characterize the binding of GEN1 to its DNA substrates. A single-particle cryo-EM structure of GEN1 from *Chaetomium thermophilum* (*Ct*GEN1) dimerized on Holliday junction was resolved to 3.5 Å. The structure shows that a unique loop from one subunit extends to the other and thereby stabilizing the asymmetric dimer on HJ. In addition, cleavage activity of 5' flap structures was observed. This activity was poorly investigated in *Ct*GEN1. The cryo-EM structure of a monomeric GEN1 bound to a 5' flap DNA indicates the structural rearrangement while interacting with different DNA substrates.

The results presented in the second chapter reveal the substrate recognition of GEN1 and provide structural insight into its asymmetric assembly on HJ. Furthermore, structural and biochemical evidence show that *Ct*GEN1 can also process 5' flap DNA structures. The mechanisms of GEN1 recognizing different substrates will be discussed.

Chapter 1 – Methodological Introduction

1.1 A brief history of cryo-electron microscopy

In the past decades, cryo-electron microscopy (cryo-EM) advanced as methodology to obtain structural information of biological samples and reveal details of biochemical and cellular processes.

In the 1980s, the advance of cryo-EM was initialized by the development of a simple vitrification method by Dubochet and colleagues (Dubochet et al., 1982). In the following years, several significant achievements demonstrated the scientific possibilities of cryo-EM, including Henderson and colleagues' first near-atomic structure by deploying electron crystallography of 2D crystals in 1990 and the 70S ribosome translation model proposed from a 25 Å structure based on the single-particle reconstruction method in 1995 by Frank et al., (Frank et al., 1995; Henderson et al., 1990). Further innovations in hardware components, comprising the introduction of direct detection detectors (DDDs) with an increased readout frequency and more coherent electron sources in form of field emission guns (FEG), led to remarkable technical advancements of transmission electron microscopes (TEM) and allowed novel computational approaches (Nogales and Scheres, 2015). For example, the collection of multi-frame movies on DDDs allows the correction for beam-induced movements as well as electron dose-dependent fractioning, enhancing the extraction of high-resolution information from raw micrographs (Zheng et al., 2017). As a result, an exponential increase of high-resolution Coulomb maps were published, starting a new era of the cryo-EM field, the so-called the 'Resolution Revolution'(Kuhlbrandt, 2014). Eventually, the contributions of Jacques Dubochet, Joachim Frank and Richard Henderson were highlighted by the Noble Price in Chemistry in 2017 *"for developing cryo-electron microscopy for the high-resolution structure determination of biomolecules in solution"* (<https://www.nobelprize.org/prizes/chemistry/2017/summary/>).

1.2 Protein structure determination by single particle analysis

1.2.1 From the tube to the grid

The continuous advances in the field established cryo-EM as a powerful method to map protein structures (Chua et al., 2022). Compared to X-ray crystallography, cryo-EM single particle analysis (SPA) has the advantage that only relatively small protein amounts are required, opening the opportunity to analyze scarcely isolatable protein complexes. Additionally, SPA offers the potential

to obtain structural information from large and flexible protein complexes, which are often difficult to crystallize.(Nogales and Scheres, 2015).

First, an aqueous sample is applied on cryo-EM grids and then, after removal of excess solution, the grid is rapidly immersed in liquid ethane. The abrupt temperature drop to below -140°C, at the speed of 10^4 K/s, leads to the vitrification of the biological sample. In this state, the frozen water has an amorphous character, preserving sample integrity (Figure 1.1) (Adrian et al., 1984; Dubochet *et al.*, 1982).

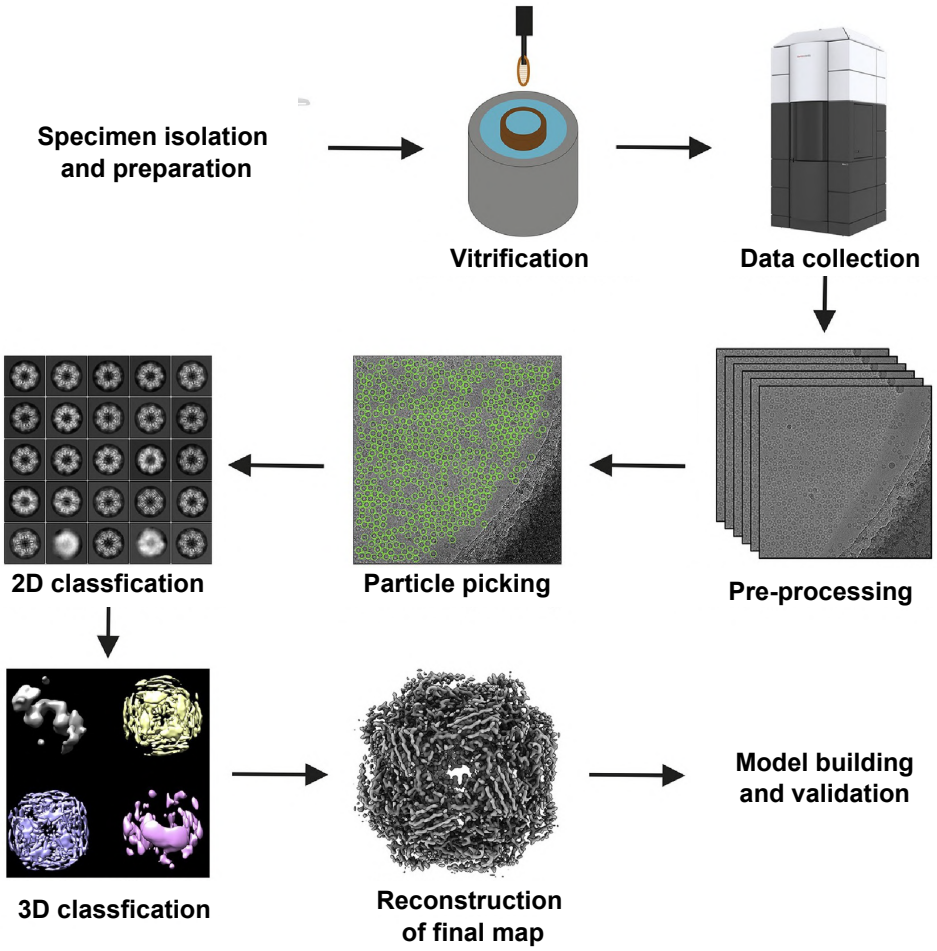

Figure 1.1. Single particle workflow.

After isolation and preparation of the specimen, the sample is plunge frozen in liquid ethane. Movies are collected during the data acquisition. During pre-processing, beam-induced motion is corrected and the CTF determined, which is essential for restoring high-resolution information. Particles, which represent the biological sample, are picked and further classified in 2D and 3D to obtain a homogonous set of particles. These particles are used to reconstruct a refined structure of the specimen, which can be used for model fitting, building and validation. Adapted from (Johnson et al., 2019).

This grid preparation process has several drawbacks, including rough temperature and humidity control, comparatively long preparation time and the creation of an extensive water-air

interface (AWI), all of which may result in grid variability and sample damage. The AWI is a serious problem for most protein complexes, since it can cause protein denaturation, aggregation, preferred orientation and complex dissociation (D'Imprima et al., 2019; Noble et al., 2018). To avoid the interaction between the biological specimen and the AWI, the addition of detergents during sample preparation is a widely used approach. It is based on the idea that the amphiphilic compounds align at the water surface, thereby shielding the proteinaceous particles from direct contact with air. However, detergents are harsh chemicals and can impact the stability of biological specimen (Glaeser and Han, 2017; Weissenberger et al., 2021). As a consequence, several developments addressed the sample preparation process in the last years. For example, various types of grid-covering support films with different geometries can influence the particle orientation and additionally reduce particle motion during data collection (Naydenova et al., 2020; Russo and Passmore, 2016a). Also, alternative methods of sample application to the grid, with drastically reduced preparation times, have been developed . Recently, new plunge freezing devices were designed that focus on a minimal time span between sample application and vitrification, aiming to reduce the amount of AWI events (Dandey et al., 2018; Ravelli et al., 2020; Razinkov et al., 2016).

1.2.2 Image formation in cryo-transmission electron microscopy

Subsequent to grid preparation, the samples are inserted into the cryo-TEM under cryogenic temperatures and high vacuum. Electrons, emitted from an electron gun on a high voltage, are accelerated in a coherent electron beam (see Figure 1.2) (Wu and Lander, 2020). Electrons are transmitted through the column and the beam is directed by a set of condenser lenses, which are composed of water-cooled electromagnetic coils. Once the beam reaches the sample, the electrons pass through and different scattering events occur (Franken et al., 2020). Inelastically scattered electrons transmit part of their energy to the specimen, thereby causing radiation damage of the sample. The inelastically scattered electrons can be removed by an energy filter, thereby enhancing the amplitude contrast of the obtained image. However, the image is primarily formed by phase contrast. Here, the information is obtained by elastically scattered electrons. These electrons experienced a 'zero energy-loss' deflection throughout the sample which results in a phase-shift of the electron wave. The interference of the elastically scattered electron wave with the unscattered electrons generates the phase contrast, important for the restoration of high-resolution information (Bhella, 2019; Murata and Wolf, 2018). The initial image is further magnified by a system of projector lenses and passed forward towards the detector chip. The final image becomes visible to the human eye and is recorded by the detector at the bottom of the electron microscope.

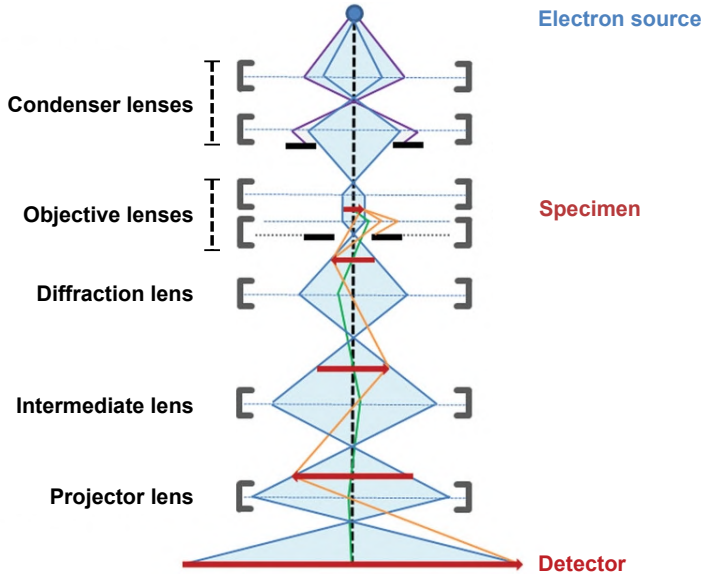

Figure 1.2. A simplified scheme of an transmission electron microscope.
The path of the electron beam emitted from the electron source is depicted in blue. The red arrow represents the specimen, which is magnified through the electron microscope before it is recorded by the detector. In green and orange, the path of differently scattered electrons is shown. The different lenses are depicted in grey, while the apertures are labelled black. Adapted from (Franken *et al.*, 2020).

1.2.3 SPA processing: from particles to structures

Images, recorded with DDDs, are short multi-frame videos, which can be corrected for beam-induced motion and filtered according to their accumulated electron exposure, thereby restoring and emphasizing high-resolution information in the collected micrographs (Zheng *et al.*, 2017). Next, the oscillation of the contrast transfer function (CTF) has to be estimated and corrected for values beyond the first zero, making this information available during later analysis steps (Rohou and Grigorieff, 2015).

In the subsequent step the particles of interest have to be identified on the micrographs, which can be done manually or automatically by template-free or template-based approaches (Figure 1.1) (Cheng et al., 2015; Zhang, 2016). Lately, convolutional neuronal network-based particle pickers like crYOLO and TOPAZ have been shown to pick reliably on different samples. Applying a pre-trained model or training a model based on a small set of manually identified particles potentially improves the recognition of particles in rarely represented orientations and avoids the selection of undesigned particles. The following processing steps can benefit from more precise particle selection. (Bepler et al., 2019; Wagner et al., 2019). Software packages such as RELION and cryoSPARC provide computational approaches to sort the particles in a set of

two-dimensional (2D) classes by rotationally aligning and grouping them by similarity. The implementation of external software packages, such as image pre-processing and particle picking further increased their popularity as SPA processing platforms. (Kimanius et al., 2021; Punjani et al., 2017). During the 2D classification steps, low-resolution classes and "junk" particles can be removed after manual inspection (Scheres, 2012). For further three-dimensional (3D) processing, either a low resolution map from available structures or an ab-initio model created from a subset of selected particles is required. Next, the low-resolution 3D model is used as reference to classify the subset of particles selected from 2D classification. The angular assignments for each particle are determined and then classified in 3D. Different particle composition, conformations and their spatial motion can be addressed during the 3D image analysis steps, eventually resulting in different states of the same protein complex (Nakane et al., 2018; Punjani and Fleet, 2021). For the final set of particles, higher-order aberrations and per particle CTF information can be estimated to further improve the resolution (Zivanov et al., 2018; Zivanov et al., 2020).

As a result of the continuous progress in cryo-TEM and the associated computational data analysis, the first SPA structures at atomic resolution were presented in 2020, obtained with the use of innovative hardware like the cold field emission gun and UltraFoil gold grids (Kato, 2019; Nakane et al., 2020; Yip et al., 2020; Zhang et al., 2020b). These results indicate an exciting promise to more detailed insights in the mechanics of biochemical processes. Furthermore, these recent developments also influenced major breakthroughs in the field of cryo-electron tomography (cryo-ET) and its affiliated analysis approaches.

1.3 Cellular cryo-electron tomography

Molecular architecture in their cellular environment can be visualized by *in situ* cryo-ET studies. Instead of extracting biomolecular complexes from their host, they are imaged directly in their native environment. During the data collection process, the area of interest is incrementally tilted, resulting in a stack of projections from different angular perspectives. The obtained stack of images is computationally reconstructed into a 3D volume, revealing the ultrastructural composition behind biological processes (Beck and Baumeister, 2016; Turk and Baumeister, 2020).

1.3.1 From the dish to the grid

Prior to the insertion into the transmission electron microscope, the biological samples have to be fixed on the grid. Similar to SPA approaches, the introduction of robust vitrification processes allows the subsequent extraction of highly resolved biological features from their direct native environment (Dubochet *et al.*, 1982). Initially, cells have to be grown on EM grids. Usually, the

holey carbon film on the gold mesh of the grid surface is additionally coated with a biological matrix to facilitate the adherence of cells and potentially trigger biological processes (Toro-Nahuelpan et al., 2020). Next, the samples can be plunge-frozen, commonly by gently blotting excess solution form the back-side of the grid to avoid rupture of the plasma membrane (Figure 1.3A) (Dobro et al., 2010). However, if the sample exceeds a thickness of 5 μm, the plunge-freezing process will lead to the formation of crystalline ice (Dubochet et al., 1988). Therefore, the method of high-pressure freezing is applied on thicker samples, ensuring the liquid-amorphous phase transition necessary for generation of vitreous ice (Ladinsky, 2010). Generally, cellular protrusions and cell periphery with less than 1000 nm in thickness can be visualized without further processing. Other cellular regions need further preparation steps prior to imaging to improve their electron transparency and reduce the background signal by inelastically scattered electrons during data collection (Lucic et al., 2013).

Cryo-focused ion beam (cryo-FIB) milling has been established as an effective method for thinning samples up to 100-250 nm. A gallium ion beam is utilized to mill through the cellular sample, leaving a thin slice of the specimen for subsequent tomogram acquisition (Marko et al., 2007; Rigort et al., 2012). Furthermore, the development of cryo-FIB lift-out opened the opportunity to use samples of several hundred micrometer thickness, by removing a segment of the bulk specimen and FIB-mill a thin lamella suitable for cryo-ET (Schaffer et al., 2019). In case particular subcellular compartments are studied, cryo-correlative light electron microscopy(cryo-CLEM) can assist in the localization of specific regions by tracing fluorescently labeled markers in the vitrified sample, thus allowing precise cryo-FIB thinning (Sartori et al., 2007; Schwartz et al., 2007).

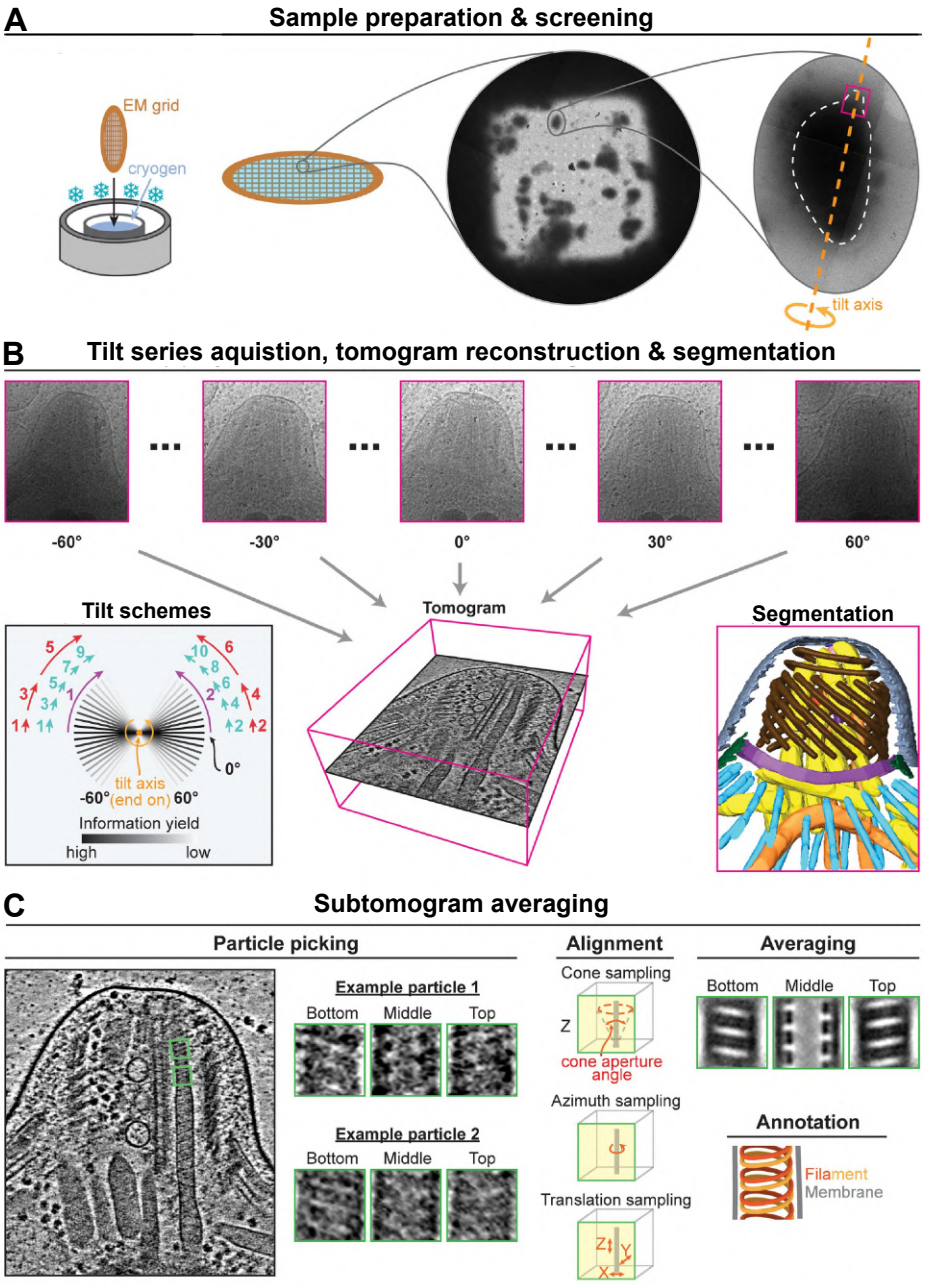

Figure 1.3. Cellular cryo-ET workflow.

(A) Cellular samples prepared for cryo-electron tomography have to be vitrified. Subsequently, areas of interest have to be identified during the screening process of the cryo-EM grid. (B) At suitable areas, which are selected during the screening process, tilt series are acquired. Different tilt schemes can be therefore applied, ideally with dose-symmetric electron exposure. Individual acquisitions from each tilt are reconstructed into a 3D volume. Cellular compartments can be visualized for further analysis by segmentation approaches. (C) During subtomogram averaging, abundant particles within tomograms are picked, aligned and averaged to restore high-resolution information. Based on the obtained structure, further analysis can be conducted. Adapted from (Theveny et al., 2022).

1.3.2 Tilt series collection

At the selected regions of interest, a series of images can be collected by tilting the specimen within a ±60° range and acquiring micrographs at each tilt. Usually, this acquisition of a tilt series is conducted in a dose-symmetric manner, starting at 0° tilt and alternating the tilting direction while proceeding to the maximum angle, therefore collecting positive and negative tilts of the same angle right after each other. This has the advantage that high-resolution information is more conserved by collecting first collect on tilts with shorter electron paths through the specimen (Figure 1.3B) (Hagen et al., 2017; Turonova et al., 2020a). The necessity to distribute the electron dose over the whole tilt series results in a low signal-to-noise ratio (SNR) for the individual images, as each tilt is only exposed to 1.5-3$e^-/Å^2$ (Lucic et al., 2005).

1.3.3 Reconstruction of a 3D tomogram

The multi-frame images from each angle have to be corrected for electron beam-induced motion (Zheng *et al.*, 2017). Next, the individual tilts have to be aligned by either using fiducial markers, patch tracking or high contrast features, thus correcting for potential movements of the stage during the data collection. The alignment process results in tilt series with a unified coordination system, adjusted along the individual angles (Chen et al., 2019; Fernandez et al., 2018; Mastronarde and Held, 2017). Subsequently, the defocus of the individual tilts can be estimated and CTF-corrected (Rohou and Grigorieff, 2015).

To obtain a 3D volume from the aligned tilt series, the final tomogram can be reconstructed either in real or Fourier space. Most commonly, the real space-based weighted back-projection (WBP) algorithm is used for this purpose, where individual 2D projections are geometrically sorted in accordance to their acquisition angle. Before the images are transformed into a 3D volume, individual tilts are filtered in Fourier space (Figure 1.3B) (Radermacher, 1988; Turk and Baumeister, 2020). Nevertheless, tomograms reconstructed from the WBP suffer from the "missing wedge" problem. This phenomenon occurs due to lack of tilts above 60° during data collection, since samples thickness and the electron microscope stage limit image acquisition beyond this angle (Galaz-Montoya and Ludtke, 2017). The alignment of tilts, the creation of a tilt series as well as the following tomogram reconstruction are integrated in software packages such as IMOD, which facilitates cryo-ET analysis by semi-automatically generating multiple tomograms (Mastronarde and Held, 2017).

1.3.4 Analysis and interpretation of tomographic reconstructions

After reconstruction, different analytical approaches are available to interpret the tomographic section. Commonly, a 3D map is generated based on segmented organelles and traced cytoskeletal filaments, showing their arrangement in distinct moments of cellular processes (Figure 1.3B) (Collado and Fernandez-Busnadiego, 2017). For instance, a series of tomograms on neurons shed light on the sequential orchestration of cytoskeletal filaments and organelles during the axonal branching process (Nedozralova et al., 2022). The curvature of segmented membranes can be estimated, potentially showing the impact of external factors on cellular lipid-layers. Furthermore, traced filaments can be determined in their length and spatial orientation to derive information about their geometrical organization during cellular processes (Mageswaran et al., 2021; Salfer et al., 2020).

The abundant presence of large molecular machineries allows for the hunt for high-resolution structures by subtomogram-averaging (STA) (Figure 1.3C) (Wan and Briggs, 2016). First, these structures have to be located within the tomogram. Apart from manual selection, template-matching approaches can be applied to identify the macromolecules of interest (Bohm et al., 2000; Castano-Diez et al., 2012). The template is generated by low-pass filtering of a known structure of the complex. The generated map is then rotated along a predefined set of Euler angles, thus scanning for all possible orientations of the particle within the tomogram. A scoring system based on the similarity between template and determined locations in the tomogram is utilized to filter the final set of particles by their cross-correlation values (Frangakis et al., 2002; Lucic *et al.*, 2005). Subsequently, the particles are extracted as so-called subtomograms, small 3D volumes exclusively comprising the complex of interest. Next, an iterative alternation of classification and refinement steps follows, aiming for the highest resolution. Apart from solely sorting for best particles, 3D classification can separate diverse complex compositions and conformations within their cellular environment (Bharat and Scheres, 2016; Wan and Briggs, 2016).

Generally, maps obtained from STA display lower resolution than their SPA counterparts (Leigh et al., 2019). Challenges such as a smaller pool of particles, lower SNR and higher irradiation impede effective restoration of high-resolution information (Xue et al., 2022). Although the final set of particles can allow for an coverage of angular distributions, the missing wedge, the missing wedge in Fourier space substantially influences the achievable resolution (Galaz-Montoya and Ludtke, 2017). Nonetheless, STA provides the unique possibility to obtain high-resolution structural information of molecular machineries in their native environment, thereby bridging cellular and molecular studies.

Chapter 2 – SARS-CoV-2 spike protein induces platelet deformation

Preface

The following chapter summarizes the current research on SARS-CoV-2, with particular interest on its binding to cellular receptors and its impact on coagulation disorders. This chapter presents the impact of SARS-CoV-2 S protein on human platelets using light-microcopy as well as cryo-electron tomography. In addition, the molecular interaction of the SARS-CoV-2 spike protein with platelets and the underlying morphological changes are shown. The research in this chapter resulted in following publication:

Kuhn C.C., Basnet N., Bodakuntla S., Alvarez-Brecht P., Nichols S., Martinez-Sanchez A., Agostini L., Soh YM., Takagi J., Biertümpfel C., Mizuno N. Direct cryo-ET observation of platelet deformation induced by SARS-CoV-2 spike protein. *Nature Communications* **14 (1)**. (2023)

PMID: 36739444

DOI: 10.1038/s41467-023-36279-5

Contribution

C.C.K., C.B. and N.M. conceived and supervised the project. C.C.K. isolated the platelets and prepared samples for the experiments. C.C.K. and N.B. collected the cryo-EM data. C.C.K., N.B., P.A.B., A.M.S. analyzed cryo-ET data with the help of L.A. C.C.K. and S.N., with the help of S.B., analyzed the light microscopy data. S.B., with the help of C.C.K., produced pseudo-typed viral particles and performed the immunoblots. C.C.K., Y.M.S., J.T. and C.B. performed and analyzed the ligand binding assays. S.B and C.C.K. performed the negative staining of lentiviral particles with the help of N.M. S.B. performed the flow cytometry analysis.

2.1 Introduction

2.1.1 The COVID-19 pandemic and research and other Coronaviruses

The emerge of the severe acute respiratory syndrome coronavirus 2 (SARS-CoV-2) and its uncontrollable global spread caused the coronavirus disease-19 (COVID-19) pandemic in the beginning of 2020. Its high infectivity and asymptomatic initial incubation period, complied ideal characteristics to spread hidden from the public health authorities (Coronaviridae Study Group of the International Committee on Taxonomy of, 2020; Wu et al., 2020; Zhu et al., 2020). As a consequence, various measures like hygiene concepts, locally restricted movement regulations and vaccination efforts were established, thereby safe-guarding the populations and relieve the public health systems. Still, the pandemic continues to have a disruptive impact on social and economic ties characteristic for our modern world.

Already in 2002, another pathogenic virus of the same family, the severe acute respiratory syndrome coronavirus (SARS-CoV), arose from a zoonotic jump and lead to infections around the world. (Cherry and Krogstad, 2004). The rapid global transmission alerted researchers and about four years later, Cheng et al. warned about further outbreaks originating from highly pathogenic *Coronaviridae* family (Cheng et al., 2007). In the following years, two more SARS-CoV-like viruses emerged from zoonotic origin, the Middle East respiratory syndrome coronavirus (MERS-CoV) in 2012 and eventually SARS-CoV-2 in 2019.

Continue researches within the past decades on coronaviruses, with landmarks achievements such as the decoding of full-length coronaviral genome, recombinant engineering of a coronavirus as well as electron microscopic and tomographic imaging of viral particles, allowing to gain insight in the biological principles of this virus family (Boursnell et al., 1987; Gosert et al., 2002; Knoops et al., 2008; Koetzner et al., 1992; van der Most et al., 1992). Nevertheless, to further understand their pathogenic impact on humans, it remains of importance to investigate SARS-CoV-2.

2.1.1.1 The severe acute respiratory syndrome coronavirus 2

SARS-CoV-2 is an enveloped, positive-sense single-stranded RNA *betacoronavirus* and member of the *Coronaviridae* family. Like the previous coronaviruses SARS-CoV and MERS-CoV, SARS-CoV-2 originates from zoonotic transmission (Corman et al., 2018; Coronaviridae Study Group of the International Committee on Taxonomy of, 2020). Genomic sequencing has shown a 79% homology to its predecessor SARS-CoV (Lu et al., 2020; Zhou et al., 2020). Though, the closest known family members are the BANAL-52, BANAL-103 and BANAL-236, with a sequence homology up to 96%. Interestingly, this group of *betacoronaviruses* exploits an ACE2-dependet entry mechanism which was also observed for SARS-CoV-2 in humans.

(Temmam et al., 2022; Yan et al., 2020). While mild and moderate infections with SARS-CoV-2 show symptoms similar to the 'common cold', a severe course of disease is often accompanied by dramatic complications including respiratory and organ failures as well as coagulopathic events, causing live threatening conditions and are eventually lethal (Al-Samkari et al., 2020; Chen et al., 2020; Guo et al., 2020; Huang et al., 2020a).

2.1.1.2 Architecture of SARS-CoV-2 viral particles

SARS-CoV-2 virions are roughly 100 nm in diameter and comprised of four structural proteins, the envelope (E) protein, the membrane (M) protein, the nucleocapsid (N) protein and the spike (S) glycoprotein (see Figure 2.1) (Arya et al., 2021; Ke et al., 2020; Laue et al., 2021).

The E protein administers the lysis and subsequent release of the SARS-CoV-2 genomic RNA during host cell invasion (Yang and Rao, 2021). Relatively small in size (8.5 kDa), the E protein assembles in homopentameric helical bundles and adopts the function of a cationic selective channels (Mandala et al., 2020).

The M protein is translocated into the viral lipid bilayer by a triple transmembrane domain. Here, it compiles as homodimer and can alternate between a compact and a long form, which influences the curvature formation of the viral membrane (Astuti and Ysrafil, 2020; Neuman et al., 2011; Wong and Saier, 2021). In addition, the membrane protein was shown to interfere with the generation of immune response against pathogens in the host cells (Fang et al., 2007; Wong and Saier, 2021).

The N protein encapsulates the viral RNA and further oligomerizes into the helical ribonucleocapsid (RNP) complex, assumed to be connected in a 'beads on string' manner (Bai et al., 2021; Klein et al., 2020). Structurally, the nucleocapsid protein is organized in two major domains, the N-terminal domain (N-NTD) and the C-terminal domain (N-CTD). While the N-CTD is important for the oligomerization during the genomic RNA packaging, the N-NTD recognizes and binds the genomic RNA (Chang et al., 2009; Ye et al., 2020).

The S-protein protrudes from the viral surface, capturing receptors on the host cell membrane (Satarker and Nampoothiri, 2020). Subsequent to the receptor binding on the cellular surface, a conformational rearrangement activates the viral membrane fusion machinery. This leads to the invasion to the host cell, the release of the viral genomic RNA and thereby initiates proliferation life-cycle of SARS-CoV-2 (See Figure 2.1) (Cai et al., 2020; Walls et al., 2020). Further details about the S protein and its role in the host cell invasion are described in chapter 'SARS-CoV-2 Spike Protein – the viral grappling hook'.

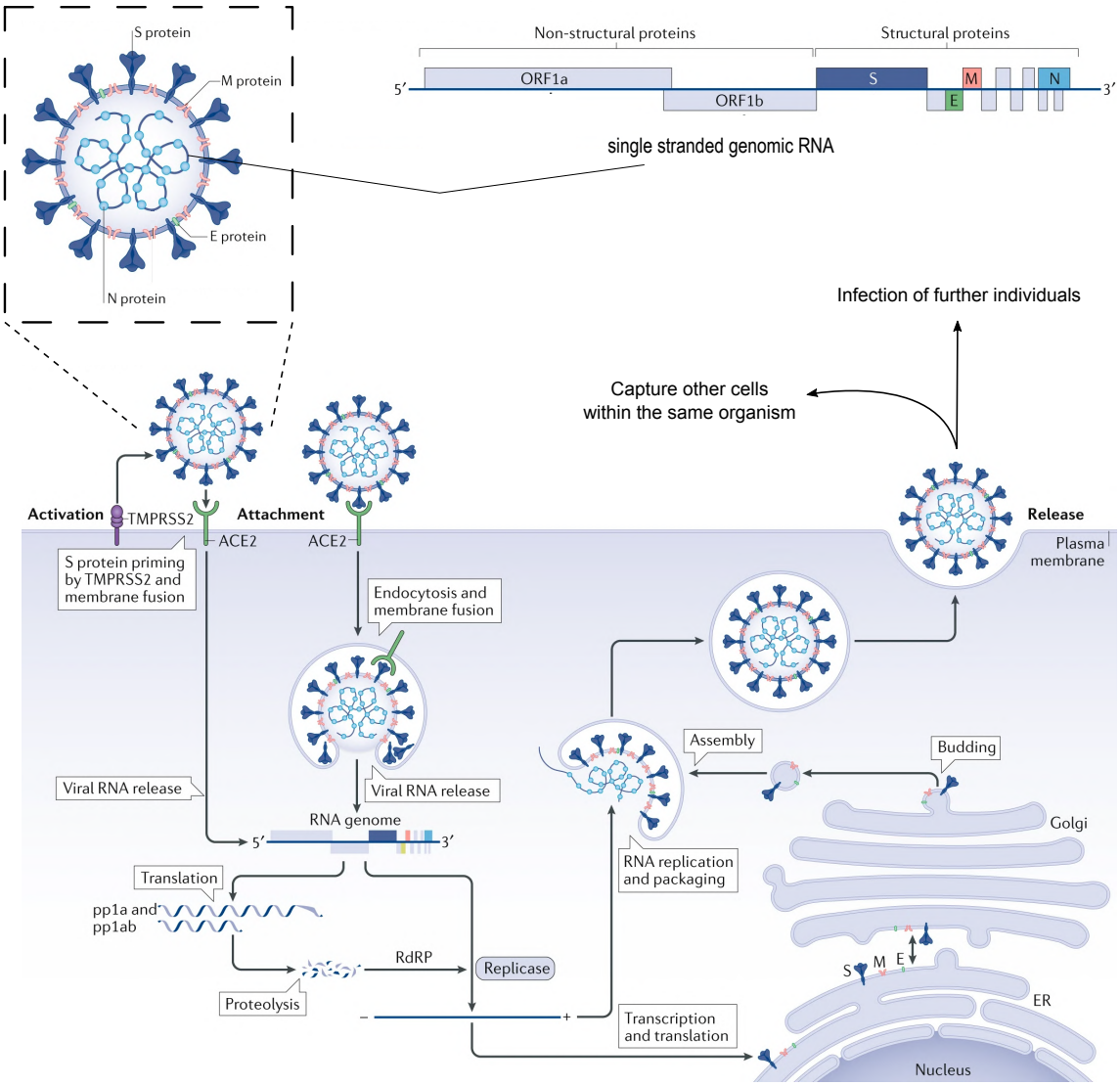

Figure 2.1. Architecture and Life-cycle of SARS-CoV-2.

The SARS-CoV-2 is organized by four structural proteins, the spike (S), the envelope (E), the membrane (M) and the RNA-bound nucleocapsid (N) protein. The genomic ssRNA encodes at the 5'-terminal end for the non-structural proteins, which are in charge of the replication process. At the 3'-terminus, the RNA holds the information for the structural proteins, important for proper viral assembly and infectivity. SARS-CoV-2 viral particle usually bind to ACE2 receptors via their S protein. After release of viral RNA, the viral genome is translated and further replicated. The maturation of the structural proteins occurs along the ERGIC, and eventually result in the assembly of viral particles, enclosed in vesicles such as for lysosomal trafficking . Once SARS-CoV-2 is released from the cell, it can infect further cells of the same or be transmitted to another organism. The illustration is adapted from (Nishiga et al., 2020).

2.1.2 Life-cycle of SARS-CoV-2 inside the cellular host

2.1.2.1 Replication of SARS-CoV-2 genomic RNA

The replication of SARS-CoV-2 genomic RNA requires the non-structural proteins (nsps). These proteins derived from two polyproteins that encoded by the open-reading frames (ORF) 1a and 1b at the 5' end of genomic RNA (Finkel et al., 2021). After translation, these polyproteins are proteolytically processed to 16 non-structural proteins, assigned with individual tasks in the replication process (Helmy et al., 2020). The enzymatic separation of the nsps is performed by two cysteine proteases, residing in sub-modules nsp3 and nsp5 (Arya *et al.*, 2021). While nsp1 interferes with the protein production of the host cell, the remaining 15 non-structural proteins, including nsp3 and nsp5, compose to the viral replication and transcription complex (RTC) (Malone et al., 2022; Schubert et al., 2020; Thoms et al., 2020). The RTC displays an ensemble of different enzymatic components, performing multiple tasks such as RNA-processing, their subsequent modification and proof reading functions, to maintain the genome integrity of SARS-CoV-2. (Romano et al., 2020). Viral RNA synthesis occurs in double-membrane vesicles (DMVs), potentially arising from impaired autolysosome formation. Their connection to the endoplasmic reticulum (ER) could facilitate the innate immune system evasion (Klein *et al.*, 2020; Qu et al., 2021; Snijder et al., 2020). During the first step of replication, full-length negative sense genomic copies are generated. These are used as templates to synthesize the positive-sense genomic RNA for subsequent production of further RTCs or packed into virions during the viral assembly process (V'Kovski et al., 2021).

Structural and accessory proteins, are transcribed as a nested set of subgenomic mRNAs at the 3' end of SARS-CoV-2 genome (see Figure 2.1) (Nishiga *et al.*, 2020). While the structural proteins determine the formation of SARS-CoV-2, the accessory proteins modulate the virus-host interactions, thereby allow to evade the host immune system (Flower et al., 2021; Gao et al., 2021; Hartenian et al., 2020).

2.1.2.2 Formation of SARS-CoV-2 virions

The assembling of virion requires multiple steps and orchestration of structural proteins. For the packaging of viral RNA, the N proteins in close proximity to the DMVs bind RNAs exiting double-membrane spanning pores and form ribonucleocapsid complexes (Masters, 2019; Wolff et al., 2020). Around 30-35 RNPs oligomerize and form the viral core, encapsulating the genomic RNA (Klein *et al.*, 2020). In the meantime, M proteins oligomerization on the ER-Golgi intermediate compartment (ERGIC) membrane provide a scaffold which embeds the structural proteins E and S (Kumar et al., 2021; Mariano et al., 2020) Finally, the hydrophobic tail of the M

protein recognizes the ribonucleic core complex and completes the formation SARS-CoV-2 particles with the support of E proteins.(Lu et al., 2021; Luo et al., 2006)

2.1.2.3 SARS-CoV-2 egression from the cellular host

After assembly at the ERGIC, virus-containing vesicles are transported to the plasma membrane. Recently it has been shown that *betacoronaviruses* are able to hijack lysosomal trafficking for egression from their cellular host. Therefore, the lysosome acidification is impaired, the lysosomal degradative enzymes are inactivated and the antigen presentation pathways are disrupted (Ghosh et al., 2020).

In addition to lysosomal trafficking, SARS-CoV-2 was also observed in other vesicle types, including double-membrane structures. These observations suggest alternative trafficking routes for virion release, such as the biosynthetic secretary pathway, used by other enveloped viruses (Mendonca et al., 2021; Miao et al., 2021; Pizzorno et al., 2020; Siu et al., 2008). Once SARS-CoV-2 reaches the extracellular region, the virions are primed to infect other individuals through airborne transmission or hijack further host cells utilizing their crown of spike proteins (see Figure 2.1).

2.1.3 SARS-CoV-2 Spike Protein

The SARS-CoV-2 spike protein is glycosylated and form homotrimer protruding from the viral surface. It is a class-I transmembrane (TM) protein, anchored into the viral membrane via its C-terminal TM domain (Bosch et al., 2003; Weissenhorn et al., 1999). Among SARS-CoV-2 and SARS-CoV, the spike proteins are well-conserved and show an overall similarity of 76% (Wan et al., 2020). Though, minor differences were identified such as a unique furin cleavage site (^{681}PRRAR^{685}) on the S protein of SARS-CoV-2, which results in an increased pathogenicity (Coutard et al., 2020; Johnson et al., 2021).

With a total length of 1273 amino acids and various glycosylation on the extracellular region, the molecular weight of a monomeric S protein is between 180-200 kDa. At the N-terminal end, the S protein contains a signal peptide (residues 1-13) which is important for proper insertion to its destination membrane, followed by the S1 subunit (residues 14-685) and the S2 subunit (residues 686-1273) (Figure 2.2A) (Xia, 2021). The S1 subunit can be subdivided into the functional N-terminal domain (residues 14-305) and the receptor-binding domain (RBD; residues 319-514). Subunit S2 consists of the fusion peptide (FP; residues 788-806), two heptapeptide repeat sequences (HR1; residues 912-984 and HR2; residues 1163-1213), the TM domain (residues 1213-1237) and the cytoplasm domain (residues 1237-1273) (Huang et al., 2020b).

While the S1 subunit recognizes host cell receptors, primarily angiotensin-converting enzyme 2 (ACE2), the S2 subunit executes the subsequent invasion by rearranging the S protein structure (Zhu et al., 2021). Prior efficient host cell infiltration, the subunits S1 and S2 have to be separated by the human transmembrane serine protease 2 (TMPRSS2), which cleaves the furin cleavage motif located between S1 and S2 (Hoffmann et al., 2020).

Interestingly, cryo-electron tomography studies of SARS-CoV-2 virions revealed the flexible motion of the S protein on the viral surface (Ke *et al.*, 2020). The spike protein motion is archived by three hinges; the hip, the knee and the ankle, providing a wide pivot range (Turonova et al., 2020b). These properties enable the adjustment of the S protein's RBD towards cellular receptors, thereby ensuring the efficient grappling of the host surface membrane.

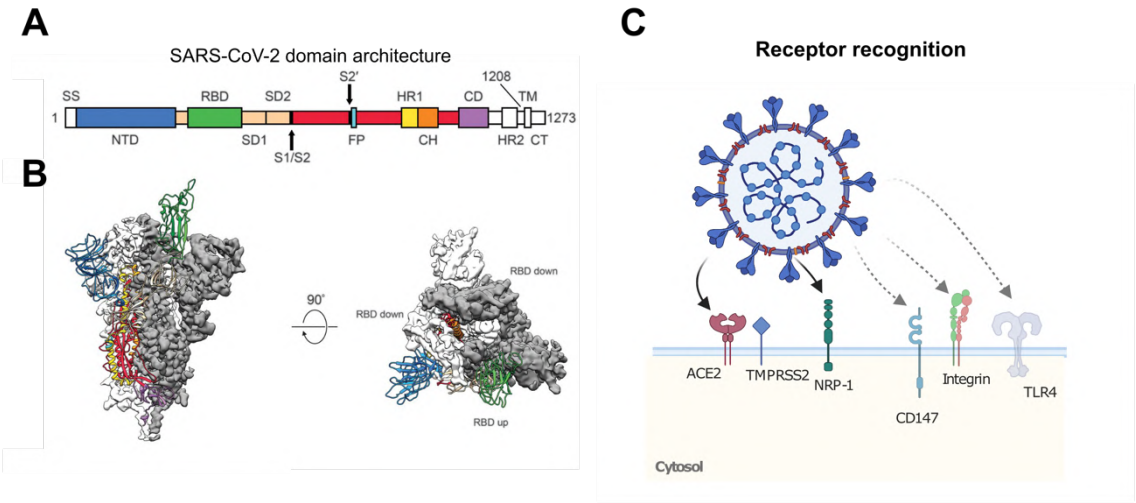

Figure 2.2. Structural and functional characteristics of the SARS-CoV-2 spike protein.

(A) Color-coded domain architecture of the S protein. (B) Side and top view of the trimeric spike glycoprotein with one RBD domain in the up position, essential for ACE2 binding. Two monomers are shown as density maps (dark grey & white), from the cryo-EM structure determination. The third monomer is shown as ribbon schematic with the domains coloured according to panel A. (C) Cellular receptor recognition by SARS-CoV-2 spike protein. ACE2 is the main receptor, priming of the S protein by TMPRSS2 is needed prior hijacking. Furthermore, NRP-1 can interact with the S-protein thereby increases the infectivity. Further cellular receptors, such as CD147, integrins and TLR4 indicate interactions with the S protein, though further information is needed to understand their role and impact during COVID-19. Created with Biorender.com

2.1.3.1 SARS-CoV-2 S1 subunit – the viral grappling hook

Studies have shown that S1-NTD plays a role in the initial host attachment by recognizing glycans on the cellular surface (Fantini et al., 2020; Lu et al., 2015). Especially the RBD is crucial for recognition and binding of the host cell. This region is similarly conserved between the SARS-CoV-2 and SARS-CoV as the entire S protein. Interestingly, only the receptor binding motif (RBM; 438-506 residues) which directly interacts with ACE2 shows lower conservation of roughly

50% (Wan *et al.*, 2020). Structural studies have shown that mutations in this region affect the affinity towards ACE2, such as SARS-CoV-2 S^{E484} enables an ionic interaction with $ACE2^{K31}$, or the SARS-CoV-2 S^{F486} mutation forms an aromatic-aromatic interaction with $ACE2^{Y83}$ (Lan et al., 2020; Wang et al., 2020b). Consequently, those results in a higher affinity of SARS-CoV-2 RBD to the host cell receptor ACE2. While SARS-CoV RBD has a K_D of 325.8 nM, SARS-CoV-2 RBD exhibits a 10 fold lower K_D of 34.6 nM, indicating a stronger binding of SARS-CoV-2 (Shang et al., 2020; Wrapp et al., 2020). Interestingly, pseudovirus entry assays detected a lower binding affinity of full-length SARS-CoV-2 spike protein compared to SARS-CoV spike protein (Shang *et al.*, 2020). The underlying cause of this observation can be explained with results from early cryo-electron microscopy (cryo-EM) studies. Cryo-EM maps of the S protein revealed an open and closed state of the trimer. The RBDs are buried in the closed conformation of the S protein, therefore being inaccessible for potential binding partners. In the open state, the RBD is facing up, thereby revealing the RBM and capturing ACE2 on the cellular surface (Figure 2.2B) (Walls *et al.*, 2020; Wrapp *et al.*, 2020). While SARS-CoV S protein mainly exposes its RBDs in the open conformation, SARS-CoV-2 S protein predominately exists in the closed state (Gui et al., 2017). The reduced RBM exposure of SARS-CoV-2 S protein could explain the lower binding affinity in the viral entry assays (Shang *et al.*, 2020).

2.1.3.2 SARS-CoV-2 S2 subunit – The Fusion Machinery

The fusion of the SARS-CoV-2 virions with the host cell membrane is mediated by the S2 subunit. Subsequent to receptor attachment, the FP domain triggers the rearrangement of the S protein from the pre- to post-fusion state (Tang et al., 2020b). Here, the mainly hydrophobic amino acids residing in the fusion peptide stretch contribute to its membrane piercing activity, which is crucial for the insertion to the host cell membrane (Millet and Whittaker, 2018). Furthermore, the engagement of the FP domain is facilitated by HR1 and HR2. Both HR domains exhibit heptapeptide repeats (HPPHCPC), where H locates the position of a hydrophobic, P of a polar and C of a charged residue (Chambers et al., 1990). During the fusion process, the interactions between the HR1 and HR2 domains in the spike protein trimer lead to the formation of a six-helix bundle, which can bridge the distance between viral and host membrane (Du et al., 2009; Xia et al., 2020).

2.1.3.3 Binding of alternative cellular receptors

The SARS-CoV-2 spike protein mainly binds to ACE2 on human cells (Yan *et al.*, 2020; Zhang et al., 2020a). Still, several studies identified further host receptors to interact with SARS-CoV-2 spike protein, enabling different cell entry routes (Figure 2.2C).

After the furin cleavage site is processed, the S1 proteins exposes an amino acid sequence (^{682}RRAR^{685}) at its C-terminus, the so-called 'C-end rule' (CendR) which is important for virus-host interaction(Teesalu et al., 2009). Transmembrane receptor neuopilin-1 (NRP-1), expressed on multiple cell types such as epithelial cells in blood vessels, is known to bind the CendR motif (Plein et al., 2014). In fact, cells expressing NRP-1 exhibit increased SARS-CoV-2 levels in cellular experiments as well as pathological samples. Furthermore, the interaction of NRP-1 and the S1 CendR motif was observed by X-ray crystallography and further supported by a series of biochemical studies. Ultimately, the mutation of the furin cleavage site in S1 subunit or depletion of NRP-1 expression in host cells significantly reduces the viral entry (Cantuti-Castelvetri et al., 2020; Daly et al., 2020).

In addition, the transmembrane protein cluster of differentiation 147 (CD147), can mediate bacteria and virus infection. For instance, viral entry of SARS-CoV is promoted by binding of CD147 via the S protein's RBD, therefore indicating a potential involvement in the SARS-CoV-2 infection (Chen et al., 2005). Indeed, *in cellulo* experiments have demonstrated that the facilitating role of CD147 during SARS-CoV-2 cell invasion, and additionally pinpointing the involvement of S protein based in negative staining TEM experiments (Wang et al., 2020a). However, the CD147 and SARS-CoV-2 S protein interaction was not observed in *in vitro* binding assays (Ragotte et al., 2021; Shilts et al., 2021). Nevertheless, these results highlight the importance of studying alternative viral entry routes, even though the potential interplay of SARS-CoV-2 S and CD147 is not fully understood (Behl et al., 2022).

Furthermore, the pathogen sensitive toll-like receptor 4 (TLR4) of the innate immune system is associated with targeting SARS-CoV-2 spike protein (Aboudounya and Heads, 2021; de Kleijn and Pasterkamp, 2003). Binding of S protein to TLR4 initiates an immune response similar to the one of bacterial lipopolysaccharides (Shirato and Kizaki, 2021; Zhao et al., 2021). Though, further studies are necessary to understand the immune cascade behind the elusive interaction of TLR4 and the spike protein.

Interestingly, unlike other pathogenic *betacoronaviruses,* the SARS-CoV-2 S protein presents an Arginine-Glycine-Aspartic acid (RGD) stretch in its RBD. Several members of the integrin family can recognize and bind the tripeptide sequence rising the question of a potential integrin contribution during SARS-CoV-2 infection (Sigrist et al., 2020). The role integrins during

SARS-CoV-2 infection is further described in chapter 'The S-protein and RGD-recognizing integrins'.

2.1.4 Coagulopathy in COVID-19

Coagulopathic events in context of COVID-19 are mainly observed in severe cases of infection. While generally low amounts of SARS-CoV-2 are detected in blood samples from COVID-19 patients, a significant increase in viral load is determined in correlation with the severity of disease (Brasen et al., 2021; Fajnzylber et al., 2020; Li et al., 2021). Especially in acute COVID-19 cases, a higher average load of 176 copies/ml was detected compared to an average of 82 copies/ml in milder cases (Chen et al., 2021). Usually, the dysregulated hemostasis induced by SARS-CoV-2 is associated with the development of disseminated intravascular coagulation, myocardial infarction, non-vessel thrombotic complications as well as the reduced count of platelets (thrombocytopenia) in the blood stream (Al-Samkari *et al.*, 2020; Lippi et al., 2020; Tang et al., 2020a). These abnormalities originate for instance from uncontrolled cytokine release by macrophages or antiphospholipid auto-antibodies, triggered by SARS-CoV-2. Though, also the direct interaction of activated immune cells with viral particles or other blood cells, for example the of neutrophil extracellular traps (NETs) during NETosis, can induce unregulated coagulation (Figure 2.3) (Koupenova et al., 2021; Lodigiani et al., 2020; Middleton et al., 2020; Zaid et al., 2020; Zhang et al., 2020c; Zuo et al., 2020). Hence, it is important to understand the effects of SARS-CoV-2 on the hemostatic system and the underlying causes of platelet hyperactivation for successful treatment of coagulopathy in connection with COVID-19.

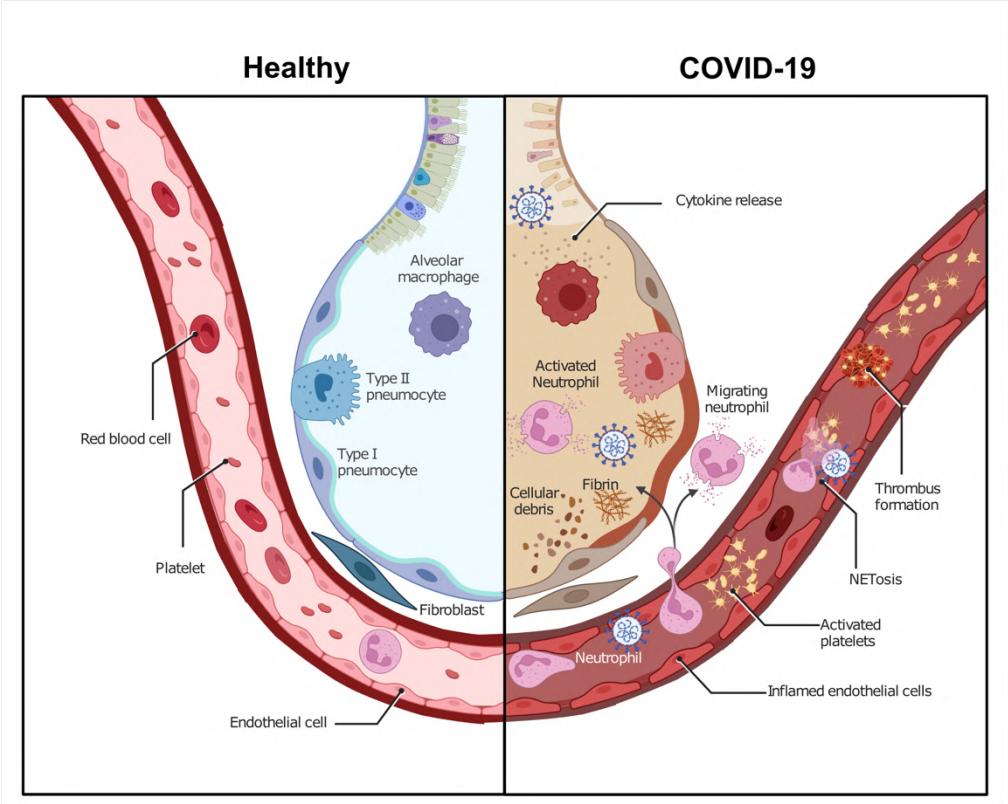

Figure 2.3. Coagulation as consequence of SARS-CoV-2 infection.

The left side of the panel shows the alveolus and blood vessel of an healthy person, the right panel the of a COVID-19 patient. After infection of the respiratory pathway, SARS-CoV-2 can enter the circulatory system. Several responses caused by the viral invasion such as the hyperactive engagement of immune cells or the inflammatory response can lead to the uncontrolled activation of platelets and resulting clot formation. Created with Biorender.com.

2.1.4.1 Platelets

Platelets are the crucial blood cells that play a crucial role in hemostasis. Anucleate and small in size, with a usual diameter of 2-3 µm, platelets circulate in high numbers through the vascular system. The iconic discoid appearance in the resting state is stabilized by the marginal band, a microtubule-based coil structure specific to platelets. Platelets are derived from the hematopoietic cells, megakaryocytes, in the bone marrow. Because of their relatively short lifespan of 5-9 days, megakaryocytes continuously release platelets into the circulatory system to maintain the approximate concentration of 1.5-4x10^9 platelets/liter (Ghoshal and Bhattacharyya, 2014).

During development of the megakaryocyte, platelet components are produced and accumulated, leading to an increase in megakaryocyte size. In their final stage, megakaryocytes form elongated pseudopodia-like protrusions (Becker and De Bruyn, 1976). The elongated protrusion can abscise and are defined as proplatelets, representing an immediate platelet precursor that contains the

cellular content of multiple platelets (Figure 2.4A) (Italiano et al., 1999). Platelet-sized swellings, connected by thin membrane bridges, decorate the elongated proplatelet, and it is hypothesized that additional fragmentation in the blood sinus lead to mature platelets (Deutsch and Tomer, 2006; Italiano, 2013). *In vivo* and *in vitro* observations of proplatelet formation followed by the release of platelets support this hypothesis (Choi et al., 1995; Junt et al., 2007). Additionally, the presence of preplatelets, a subpopulation of giant platelets that can remodel into barbell-shaped appearance and then undergo fission, provide further evidence of the intermediate proplatelet step during platelet maturation (Figure 2.4B) (Schwertz et al., 2010; Thon et al., 2012; Thon et al., 2010). Proplatelet-structures are formed in dependence of cytoskeletal forces, which mainly comprises the rearrangement of the marginal band. As a consequence, the destabilization of microtubules inhibits the proplatelet transition (Tablin et al., 1990; Thon *et al.*, 2010). On a physiological level, alterations in the proplatelet formation result in a reduced count of platelets and therefore are normally associated with bleeding disorders (Shivdasani et al., 1995).

Damages on the blood vessel wall trigger the activation of platelets, thereby initiating the controlled coagulation to prevent bleeding. Known as hemostasis, this process describes the primary role of platelets in the circulatory system. During activation, the platelet shape changes from a discoid to spread appearance, thus covering an increased surface area with plug-like properties (Figure 2.4C) (Ghoshal and Bhattacharyya, 2014; Thomas, 2019).

To ensure a sensitive response to vessel damages, the platelet surface is densely decorated with various receptors that interact with specific extracellular matrix (ECM) proteins (Rivera et al., 2009; Saboor et al., 2013; van der Meijden and Heemskerk, 2019). For example, the platelet-specific integrin $\alpha_{IIb}\beta_3$, highly concentrated on the platelet membrane, plays an important role in the coagulation process by binding to activated fibrinogen and von Willebrand factor (VWF)(Plow and Byzova, 1999). However, additional integrins on the platelet membrane can induce platelet activation by interaction with other exposed ECM proteins, like $\alpha_5\beta_1$ binding to fibronectin or vitronectin recognition by $\alpha_V\beta_3$ (Pytela et al., 1985; Saboor *et al.*, 2013; Schumacher et al., 2021). The interaction of integrin with ECM proteins activates the platelet focal adhesion machinery and pseudopodal protrusions emerge in an actin-dependent manner. The actin filaments are tethered to plasma membrane via talin in its extend form, which itself is bound to cytoplasmic tail of integrin (Dedden et al., 2019; Hartwig, 2006; Petrich et al., 2007; Tadokoro et al., 2003). Subsequent to the filopodia formation, microtubules reorganize and enter the cell periphery, completing the outside-in directed activation and hence the spreading process (Li et al., 2010). On the other hand, a cytoplasmic signal, for example initiated when GPIb-IX-V recognizes VWF, can trigger

inside-out activation and therefore increase the affinity of $\alpha_{IIb}\beta_3$ towards its ligands (Andrews et al., 1999; Huang et al., 2019; Mehrbod et al., 2013).

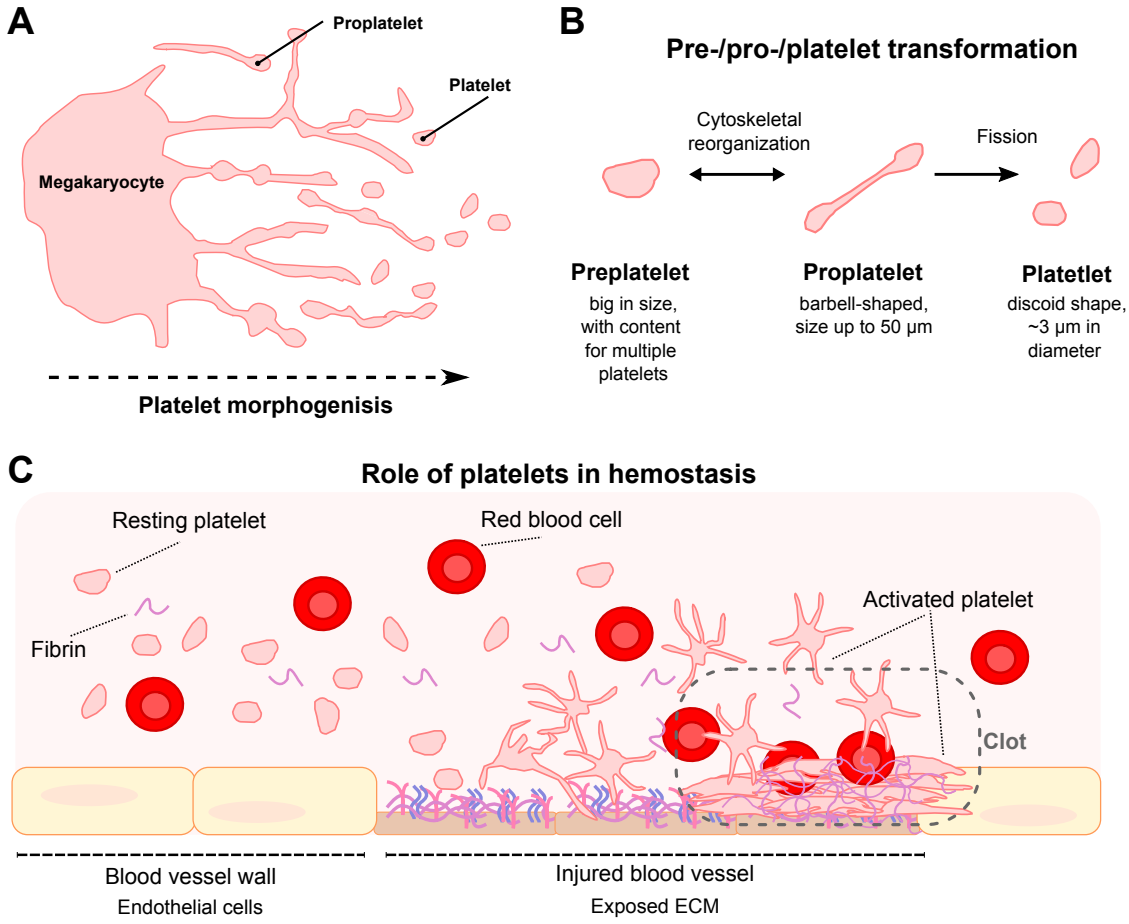

Figure 2.4. A short glance on platelets.

(A) Platelets originate from megakaryocytes, which form long protrusions. At the type of the protrusions, intermediate proplatelet are released and further divide into anucleate platelets. (B) A subpopulation of circulating platelets, bigger in size, are termed preplatelets. Preplatelets hold the content for multiple platelets, and by rearrangement of the cytoskeleton, they can reversibly transform in the barbell-shaped proplatelets. During a fission process, proplatelets can divide into multiple platelet in the blood stream. (C) An essential role of platelets in the blood circulation system is hemostasis. Here, surface receptors on platelets recognize exposed ECM, for example at injured blood vessel walls. Thereby, platelets are activated and coagulation cascade triggered, leading to the formation of a blood clot, plugging the injured region.

Apart from the ECM-receptors, numerous factors play crucial roles in the highly complex mechanism of hemostasis. After platelet activation, the release of different granules and other factors generate a procoagulant environment, thereby initiating an activation cascade and promote further platelet spreading events (Yun et al., 2016). A distinct feedback mechanism, composed of several protagonists, so called coagulation factors, regulates the coagulation process (Periayah et

al., 2017). Dysregulation of the underlying platelet activation and suspension of the coagulation factor cascade can lead to uncontrolled coagulation and the formation of blood clots as well as increased bleeding times (Nieswandt et al., 2011). Severe outcomes in this context, like thrombotic events, usually occur in medical conditions or as a direct response to pathogen invasion (Guo and Rondina, 2019; Portier and Campbell, 2021).

Owing to the high number of circulating platelets, an early platelet-pathogen encounter is likely. Interestingly, platelets exhibit a series of pattern recognition receptors (PRRs), such as Toll-like receptors (TLRs) and C-type lectin receptors, which can bind pathogens and biomolecules upregulated after infection, thus introducing platelets as part of the innate immune system (Middleton et al., 2016; Portier and Campbell, 2021). Engagement of these receptors lead to platelet activation and surface expression of leukocyte-specific receptors. Next, immune cells recognize the activated platelets and start pathogen clearance (Garraud et al., 2011; Guo and Rondina, 2019).

For example, the bloodborne dengue virus as well as Malaria interact with various receptors on the platelet plasma membrane. As a result, an increase in aggregation, caused by leukocyte infiltration and uncontrolled activation, is observed (Chao et al., 2019; Hottz et al., 2013; Simon et al., 2015; Srivastava et al., 2010). Furthermore, lipopolysaccharides on the bacterial membrane are recognized by TLR-4 and stimulate platelet activation(Clark et al., 2007; Stahl et al., 2006). In addition to PRRs, membrane proteins usually involved in hemostasis, can engage with pathogens. For instance, bacterial proteins, including *Staphylococcus epidermis* SdrG, can use their rouge RGD-motif to interact with integrins such as $\alpha_{IIb}\beta_3$ and causes platelet activation (Brennan et al., 2009).

The clinical picture of pathogen-platelet interaction usually has a similar appearance, mainly accompanied by dysfunction of hemostasis, thrombocytopenia and thromboinflammation (de Mast et al., 2007; Masri et al., 2019; O'Sullivan et al., 2016; Rondina et al., 2013).

2.1.4.2 Platelets and SARS-CoV-2

After infection with SARS-CoV-2, platelets exhibit hyperactive behavior resulting in increased spreading events, that can contribute to immunothrombosis. (Lodigiani *et al.*, 2020; Zaid *et al.*, 2020; Zuo *et al.*, 2020). (Manne et al., 2020). Previous studies have shown that the isolated platelets from healthy donors have faster thrombin-dependent clot retraction and upregulation of signaling factors in presence of SARS-CoV-2 or the SARS-CoV-2 S protein. Unexpectedly, the expression of ACE2 and TMPRSS2 was observed in these platelets, while other studies did not detect their

presence in platelets from healthy donors and COVID-19 patients. However, the transcriptional expression of N1 SARS-CoV-2 gene was observed in platelets from a few patients, suggesting an interaction independent of ACE2 (Manne *et al.*, 2020; Zaid *et al.*, 2020; Zhang *et al.*, 2020c).

In addition, several procoagulant players contribute to platelet hyperactivation during SARS-CoV-2 infection, such as tissue factor, neutrophil extracellular traps, elevated fibrinogen levels and dysregulated release of cytokines. These complex interactions and signaling pathways making it difficult to investigate the impact of actual SARS-CoV-2 platelet binding (Fajgenbaum and June, 2020; Hadid et al., 2021; Middleton *et al.*, 2020; Puhm et al., 2022). Therefore, the direct virus platelet interaction remains elusive. Thus, it is particular of interest to further understand the coagulopathic events after SARS-CoV-2 infection.

2.1.4.3 The S-protein and RGD-recognizing integrins

The unique RGD stretch in the RBD of SARS-CoV-2 S protein represents a distinct motif which is expected to interact with members of the integrin family which are also present on the platelet membrane (Figure 2.5) (Makowski et al., 2021; Sigrist *et al.*, 2020). Notably, initial studies indicate the involvement of integrin in the SARS-CoV-2 spike protein recognition (Beddingfield et al., 2021; Park et al., 2021). Furthermore, pull down and fluorescent-based protein interaction assays point at $\alpha_5\beta_1$ and $\alpha_V\beta_3$ as potential targets for SARS-CoV-2 binding (Liu et al., 2022; Nader et al., 2021). An immunochemistry study using labelled SARS-CoV-2 RBD on non-ACE2 cells(CHO-K1 cells) further indicate that $\alpha_5\beta_1$ as a potential alternative cell entry route for SARS-CoV-2 (Liu *et al.*, 2022). Moreover, the addition of Mn^{2+}, promoting integrin's transition from the bent to extended state, exhibits an increase in SARS-CoV-2 binding to cells, whereas the presence of the RGD-mimicking inhibitors like cilengitide and ATN-161 reduces the interaction with cells (Nader *et al.*, 2021; Simons et al., 2021).

Hence, it is of particular interest to understand the role of integrins in COVID-19, investigate their potential as SARS-CoV-2 spike protein receptor on platelets and further unravel coagulopathy after viral infection.

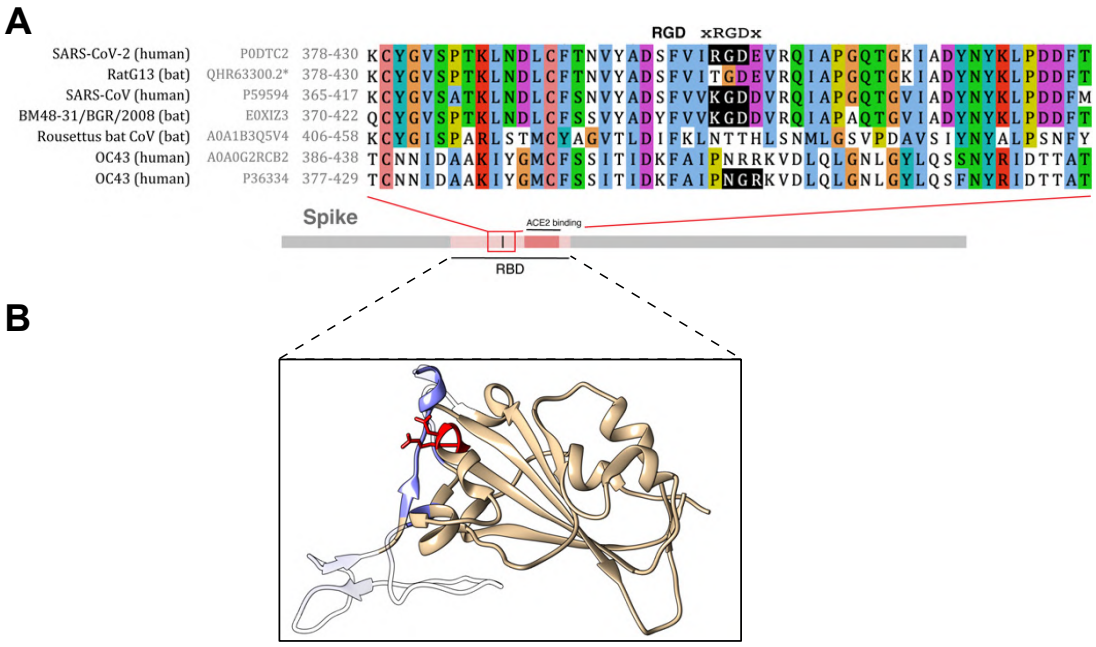

Figure 2.5. The RBD of the SARS-CoV-2 spike protein.

Sequence alignment of S protein RBD-domains from different coronaviruses. The RBD-domain of SARS-CoV-2 exposes an unique RGD-motif within the RBM. The RGD-motif is also well-known as binding motif of several integrins on platelets. Below the structure of SARS-CoV-2 S protein RBD. The ACE2 interaction surface is coloured in blue, the residues of the RGD-motif are highlighted in red.

2.1.5 Aim of the project

In late 2019, the highly infectious *betacoronavirus* SARS-CoV-2 emerged by zoonotic transmission. The rapidly spreading virus is the origin of COVID-19 and eventually led to a pandemic of global extent. COVID-19 is often associated with coagulopathy, which are in general conditions with impaired clotting behavior. Here, platelets play a central role and shown to be sensitive after viral invasion. Interestingly, SARS-CoV-2 S protein was shown to interact with platelets directly, though the molecular basis continues to be an open question. In comparison to its predecessors, the SARS-CoV-2 spike protein contains a RGD motif in the receptor binding domain, facilitating the interaction with various integrins found on the platelet surface. However, the S protein's potential to exploit this interaction or other recognition patterns on the cell surface is still under investigation. Nevertheless, the binding process on a molecular level and its impact on the ultrastructural platelet remodeling continues to be of high interest.

The goal of this study is to investigate the interaction of the S protein with platelets and understand its effects upon binding followed by ultrastructural changes in the platelet morphology. For this purpose, their interplay was explored using *in cellulo* live-imaging and structural *in situ* studies using cryo-electron tomography.

2.2 Results

2.2.1 Platelets undergo morphological deformation in the presence of SARS-CoV-2 S protein

Platelets were isolated from healthy, de-identified blood donors in order to investigate their behaviour in the presence the SARS-CoV-2 spike protein. After incubation with the S protein their subsequent exposure to different types of extracellular matrix (collagen I, poly-L-lysine and fibronectin) was observed by differential interference contrast (DIC) microscopy in order to track the morphological changes in the platelet appearance.

After the platelets settled on the coated surface, discoid-shaped platelets in their resting state were predominately observed in both, the control as well as the SARS-CoV-2 pre-incubation. Over the time course of the experiment, platelet activation in form of spiky protrusions and eventually further spreading on the ECM-coated surfaces was observed (Figure 2.6 A-C).

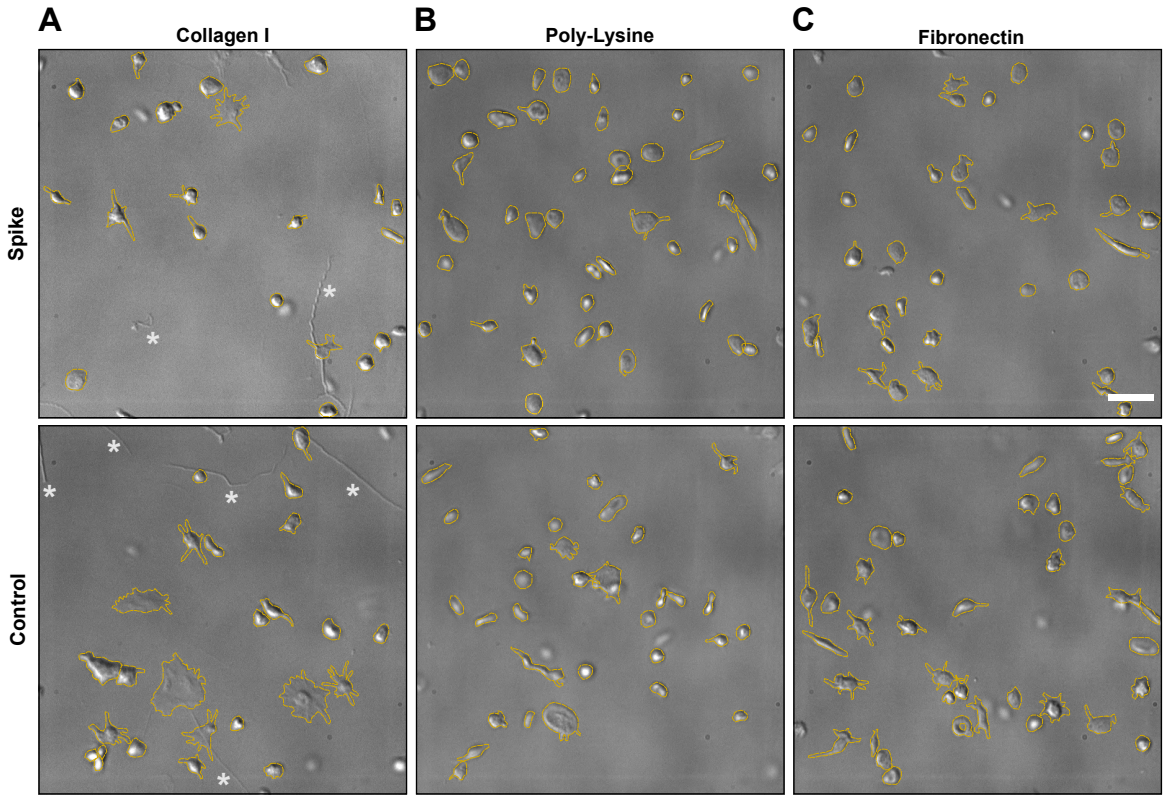

Figure 2.6. Platelet morphology of platelets on different coatings with and without SARS-CoV-2 S protein. (A) DIC images of platelets without (Control) and pre-incubated with 20 µg/ml S protein (Spike) on a collagen I support. * indicates collagen I fibers. (B) DIC images of platelets without and pre-incubated with S on a poly-L-lysine support. (C) DIC images of platelets without and pre-incubated with S protein on a fibronectin support. Scale bar: 5 µm (A-C).

In addition, a small cohort of elongated platelets, which resemble a barbell-like shape, were present under all conditions (Figure 2.7). The elongated platelets indicate the presence of proplatelets in the circulatory system. Usually, the proplatelet transition from a discoid to a barbell shape is a reversible process, controlled by cytoskeletal remodelling. Normally, the barbell-shaped proplatelets can abscise smaller platelets from the tips of their elongated structure, thereby generating fresh platelets (Schwertz *et al.*, 2010; Thon *et al.*, 2010). Though, apart from their classic barbell shape, samples pre-incubated with S protein showed stretched proplatelets with extra bulges along their body. An extension up to 32 µm in the long axis and 1.4 µm in the short axis with multiple swellings was measured in FIJI, though the platelet boundaries weren't determined exactly due to the limitations of the light microscopic resolution. Also, occasionally hollow, ring-like morphologies were observed when platelet had been pre-incubated with spike protein prior ECM exposure (Figure 2.7, white arrow head). Both, the proplatelets with multiple swellings as well as ring-like structures may indicate an effect on the cytoskeletal dynamics necessary for proplatelet maturation. Based on this observation, SARS-CoV-2 S protein could influence the cytoskeletal rearrangements of proplatelets, thereby affecting their capabilities of successful platelet abscission and ultimately the generation of platelets.

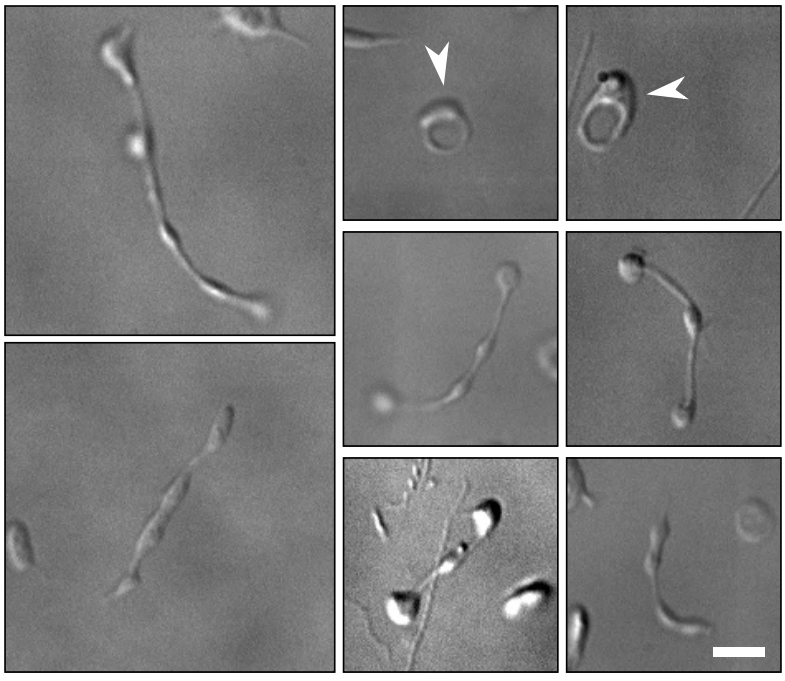

Figure 2.7. Platelets incubated with SARS-CoV-2 S protein reveal proplatelet-like morphologies.
A subset of platelets showed a tubular appearance with multiple globular bodies along their elongated shape after the incubation with S protein. Some platelets had a ring-shaped appearance in the presence of the S protein. Scale bar: 5 µm.

2.2.2 Platelets elongate and increase their protrusions formation in presence of the S protein

In order to analyse their morphological changes, the platelet shapes were manually traced in FIJI. Therefore, all platelets were tracked under different conditions over the time course of 1 h. Next, the circularity and axial ratio of each platelet was calculated. The circularity values range from 0 to 1, where values closer to 1 equal a more circular shape, while values towards 0 represent platelets with a spiky appearance. For the aspect ratio (AR), the minimum value of 1 corresponds to a round shape. An increase in the AR value of the traced platelet correlates with a more elongated shape instead. After their calculation, the time point combining the highest AR and lowest circularity value were selected for each platelet. These values were used to quantify and further compare the impact of the SARS-CoV-2 spike protein on the platelet morphology.

Firstly, the axial ratio of the traced platelets increased significantly after pre-incubation with the S protein for the three tested matrix types. Here, the median values of 1.687, 1.491 and 1.756 for collagen I, poly-L-lysine and fibronectin coating rose to 1.960, 1.565 and 1.786 when platelets were pre-incubated with the S protein (Figure 2.8A). The rather small, though significant increase for all tested surface coatings, may be due to the small share of proplatelets in the circulatory system. Overall, the increase in the median AR values describes correlation between the SARS-CoV-2 spike protein and the platelet deformation from discoid to an elongated appearance.

Secondly, a decrease in circularity was measured in the presence of the SARS-CoV-2 spike protein on all three matrix types. The circularity medians dropped from 0.686, 0.668 and 0.650 on collagen I, poly-L-lysine and fibronectin under control conditions to 0.559, 0.649 and 0.613 in presence of S protein respectively (Figure 2.8B). The quantification results confirm the initial observation of more adhering platelets and their subsequent protrusion formation under SARS-CoV-2 S protein conditions (Figure 2.6).

Furthermore, in the presence of the S protein, more platelets changed discoid appearance in the resting state to the spread shape in the activated state. The amount spiky and spread platelets was quantified in respective to the discoid shaped platelets in each sample. As a result, a proportional increase of activated platelets from 4.92% for collagen I, 0% for poly-L-lysine and 5.26% for fibronectin in the control, to 9.21%, 4.00%, 8.57% for collagen I, poly-L-lysine and fibronectin for S protein treated platelets was observed (Figure 2.8C, Figure 2.9D).

It is worth to mention, that the effect of platelet activation was less dominant when coated with poly-L-lysine. This observation can be due to the reason, that poly-L-lysine solely promotes platelet attachment to the surface by generation of positive charged environment, while collagen I and fibronectin are ECMs with platelet-specific receptors.

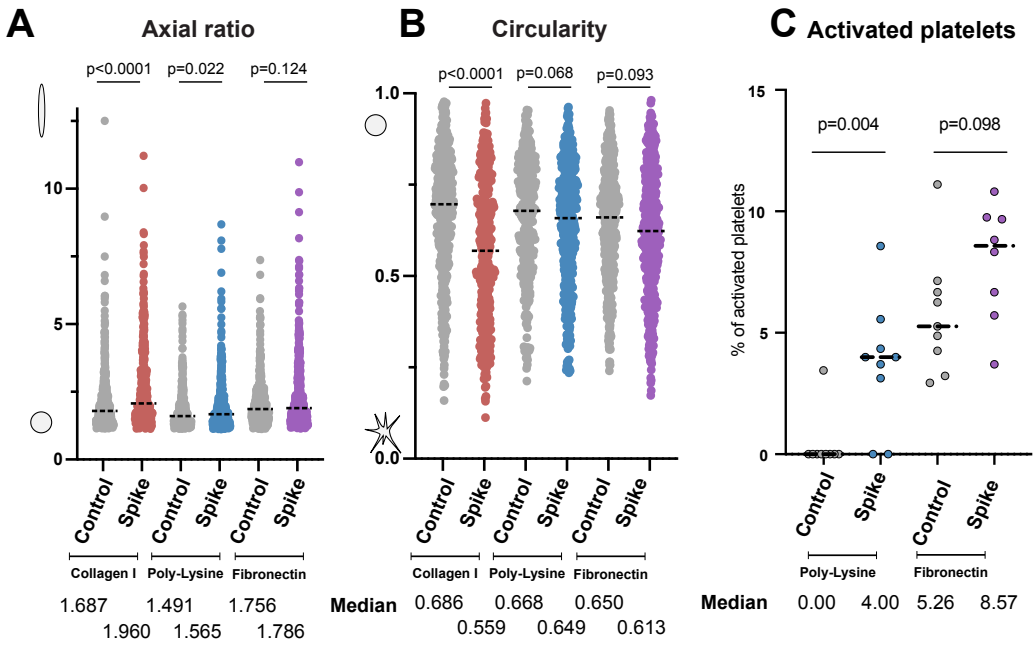

Figure 2.8. Quantification of platelet characteristics with and without SARS-CoV-2 S protein.

(A) Quantification of the axial ratio of platelets (major axis/minor axis) on different coated surfaces, without and in the presence of S protein. The median axial ratio is shown below the corresponding violin plot. The significance was determined by two-tailed Mann-Whitney U test. Number of platelets (collagen control: 442, collagen spike: 391, Poly-L-lysine control: 343, Poly-L-lysine spike: 430, Fibronectin control: 505, Fibronectin spike: 446) examined over n=3 independent experiments, from n=3 biologically independent doners. Each dot represents the value from a single platelet. (B) Quantification of the circularity of platelets on different coated surfaces, without and in the presence of S protein. The median circularity is shown below the corresponding violin plot. The significance was determined by two-tailed Mann-Whitney U test. Number of platelets (collagen control: 442, collagen spike: 391, Poly-L-lysine control: 343, Poly-L-lysine spike: 430, Fibronectin control: 505, Fibronectin spike: 446) examined over n=3 independent experiments, from n=3 biologically independent donors. Each dot represents the value from a single platelet. (C) Comparison of platelet activation, incubated with and without S protein, on Poly-L-Lysine (left), and on Fibronectin (right) Platelets with amoeba-like morphologies were defined as activated platelets. The median percentage of the activation is shown below the corresponding dot plot. The significance was determined by two-tailed Mann-Whitney U test. Number of platelets (collagen control: 442, collagen spike: 391, Poly-L-lysine control: 343, Poly-L-lysine spike: 430, Fibronectin control: 505, Fibronectin spike: 446) examined over n=3 independent experiments, from n=3 biologically independent donors. Each dot represents the value from a series of experiment.

2.2.3 Elongation and activation are dependent on the S protein concentration

The impact of the S protein concentration on platelets was investigated by the pre-incubation of platelets with 0.2 µg/ml (0.47 nM), 2 µg/ml (4.7 nM), and 20 µg/ml (47 nM) spike protein. The protein concentration range was selected similar to previous studies and the availability of SARS-CoV-2 spike protein for this study (Zhang *et al.*, 2020c). After the incubation, the platelets were exposed to collagen I coated surfaces, the matrix on which the most pronounced

morphological changes were observed previously. The elongation and activation were evaluated as described above. Already at 0.2 µg/ml SARS-CoV-2 S protein the deformation of platelets could be observed (Figure 2.9A). Though, the deformation and activation of platelets increased along with the S protein concentration, and showed the most pronounced effect on the highest tested spike protein concentration of 20 µg/ml (Figure 2.9B-C). For this reason, higher S protein concentrations were chosen for the following experiments.

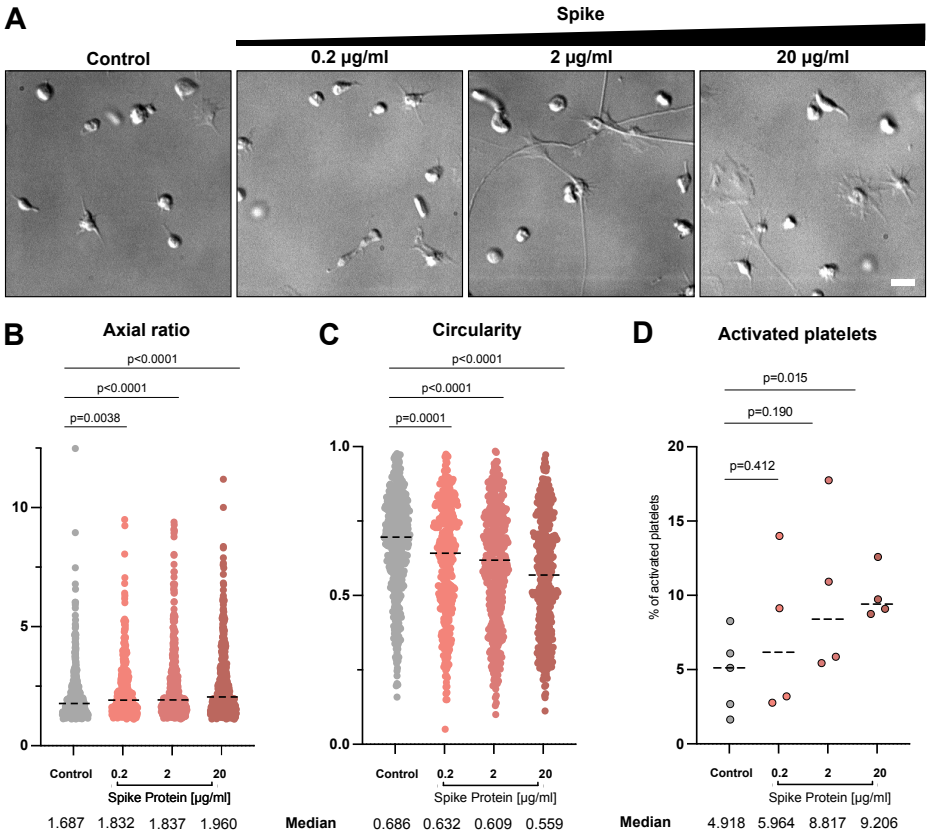

Figure 2.9. Platelet morphology depending on SARS-CoV-2 S protein concentration.

(A) DIC images of platelets in the presence of different amounts of S protein plated onto collagen I-coated surfaces. Scale bar: 5 µm. (B) Quantification of the axial ratio of platelets on collagen I-coated surfaces, without and in the presence of different S protein concentrations. The median axial ratio is shown below the corresponding violin plot. The significance was determined by two-tailed Mann-Whitney U test. n= 442 (control), n= 359 (0.2 µg/ml S protein), n= 443 (2 µg/ml S protein), n=391 (20 µg/ml S protein) platelets examined over n=3 independent experiments, from three biologically independent donors. Each dot represents the value from a single platelet. (C) Quantification of the circularity of platelets on collagen I-coated surfaces, without and in the presence of different S protein concentrations. The median circularity is shown below the corresponding violin plot. The significance was determined by two-tailed Mann-Whitney U test. n= 442 (control), n= 359 (0.2µg/ml S protein), n= 443 (2 µg/ml S protein), n=391 (20 µg/ml S protein) platelets examined over three independent experiments, from n=3 biologically independent donors. Each dot represents the value from a single platelet. The plots for control and in the presence of 20 µg/ml spike protein in (B) and (C) are same as those in Figure 2.8A and 2.8B, respectively. (D) Quantification of platelet activation on Collagen I depending on S protein concentration. The median percentage of the activation is shown below the

corresponding dot plot. The significance was determined by two-tailed Mann-Whitney U test. n= 442 (control), n= 359 (0.2 μg/ml S protein), n= 443 (2 μg/ml S protein), n=391 (20 μg/ml S protein) platelets examined over three independent experiments, from n=3 biologically independent donors. Each dot represents the value from a single platelet. Each dot represents the value from a series of experiment.

2.2.4 Increased PF4 release and pFAK levels in S protein exposed platelets

To observe the cellular platelet response to the S protein, the supernatants and the adherend platelets were collected after exposure to collagen I. Platelets which remained in the supernatant, were pelleted by a gentle centrifugation step and treated as individual sample.

The platelet-free supernatant was used to quantify the platelet activation in dependence of the platelet factor 4 (PF4) concentration. PF4 is cargo of alpha-granules, which are released upon platelet activation and can trigger the platelet activation cascade (Smith, 2022). To determine PF4 concentration in the supernatant, a solid-phase sandwich ELISA assay was performed. Here, the samples pre-incubated with SARS-CoV-2 spike protein showed a higher PF4 concentration in comparison to the supernatant from control-treated counterparts (Figure 2.10A).

After their lysis, the activation of adherent platelets as well as the platelets pelleted from the supernatant were estimated by the phosphorylation levels of the focal adhesion kinase (pFAK). The pFAK responds to the signalling cascade of focal adhesion pathway during platelet spreading (Guidetti et al., 2019). The individual samples were normalized against the housekeeping enzyme GAPDH (glyceraldehyde-3-phospahtedehydrogenase). For the adhered platelets pre-incubated with SARS-CoV-2 S protein, the signal for pFAK detected by Western blot is 1.45 ± 0.51 times higher than for the control sample (Figure 2.10B-C). Interestingly, no detectable pFAK level was measured for the non-adherent platelets separated from the supernatant (Figure 2.10D). Hence the focal adhesion pathway wasn't activated in those platelets, neither for the control nor the S protein treated.

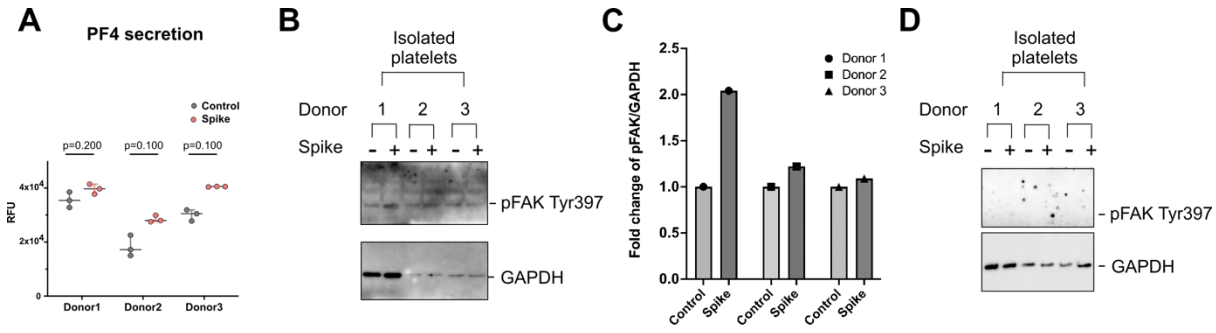

Figure 2.10. Quantification of platelet activation markers.

(A) Sandwich ELISA assay detecting PF4 release in the absence and presence of S protein. The mean ± SD is shown below the corresponding dot plot. The significance was determined by two-tailed Mann-Whitney U test. n= 3 independent experiments from n=3 biologically independent donors. (B) The adherent platelets were collected in RIPA lysis buffer and the total concentration was quantified with Bradford assay. 30 µg of total protein was loaded on the gel and probed against pFAK or GAPDH. (C) Quantification of pFAK in adherent platelets normalized against GAPDH concentrations, showing the values of 2.04 (donor 1), 1.22 (donor 2) and 1.09 (donor 3). (D) The floating platelets were handled as specified in (B) and probed against pFAK, or GAPDH.

2.2.5 Cryo-ET studies reveal the formation of fine protrusions in presence of the spike protein

To gain information about the morphological changes of platelets in the presence of the SARS-CoV-2 S protein, cryo-ET experiments were performed. Platelets in presence and absence of the spike protein were exposed to collagen I on silicone oxide coated gold grids.

Platelets incubated without the SARS-CoV-2 S protein showed a compact, discoid in shape and more electron dense appearance under cryo-EM condition. The overall shape was already observed in the DIC microscopy experiments and resembles the appearance of resting platelets (Figure 2.11A-C). In close proximity to collagen I fibrils, platelets in the control setup showed the formation pseudopodia-like formations (Figure 2.11C). In contrast, the platelets pre-incubated with the S protein formed long and thin protrusions independent of the collagen I fibril interaction (Figure 2.11D-F). At high magnification (33,000x), the pseudopodal protrusion revealed a dense F-actin network. The assembly of actin bundles in a filopodia-like manner could facilitate the formation of thin platelet extension which formed narrow extension with diameter as small as 43 nm (Figure 2.12A).

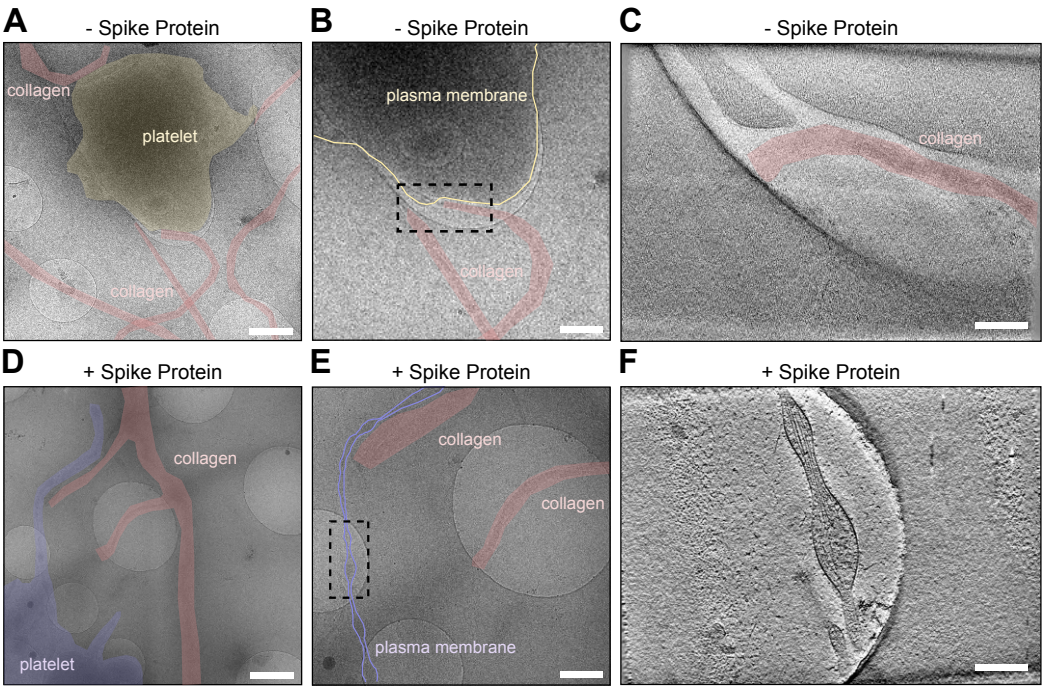

Figure 2.11. Platelets under cryo-EM with and without SARS-CoV-2 S protein.

(A) and (B) Low magnification views of a platelet on collagen I. The dashed box in B represents the area of tomographic data collection in C. (C) Representative slice of the reconstructed tomogram of platelet plasma membrane. (D) and (E) Low magnification views of a platelet in the presence of S protein on collagen I. The dashed box in E represents the area of tomographic data collection in F. (F) Tomographic slice of the platelet protrusion in the presence of S protein. Scale bars: (A),(D) = 1 μm; (B),(E) = 0.5 μm; (C),(F) = 200 nm.

Segmentation of the actin filaments revealed the presence of long filaments along the protrusion axis, which could reach a length a more than 100 nm. On the other hand, short actin filaments appear to bridge the space between long filaments and the platelet plasma membrane (Figure 2.12B-C). In addition to the length, angles were assigned for each 10 nm actin repeat in respective to the longest site of the tomogram, which corresponds the horizontal axis in Figure 2.12A. The angular distribution of actin sections results in two peaks, the first at 10° and the second one at 80° (Figure 2.12D). While the first peak at 10 degree represent the sections of long actin filaments along the protrusion axis, the peak at 80 degree corresponds to the short filaments bridging between the longer ones and the platelet membrane. The difference between the two peaks of the angular distribution is 70°. Interestingly, actin branching mediated by the Arp2/3 complex forms 70 degree connections between actin filaments, which could explain the spacing between the two distinct peaks of angular actin orientations observed in the tomogram (Mullins et al., 1998).

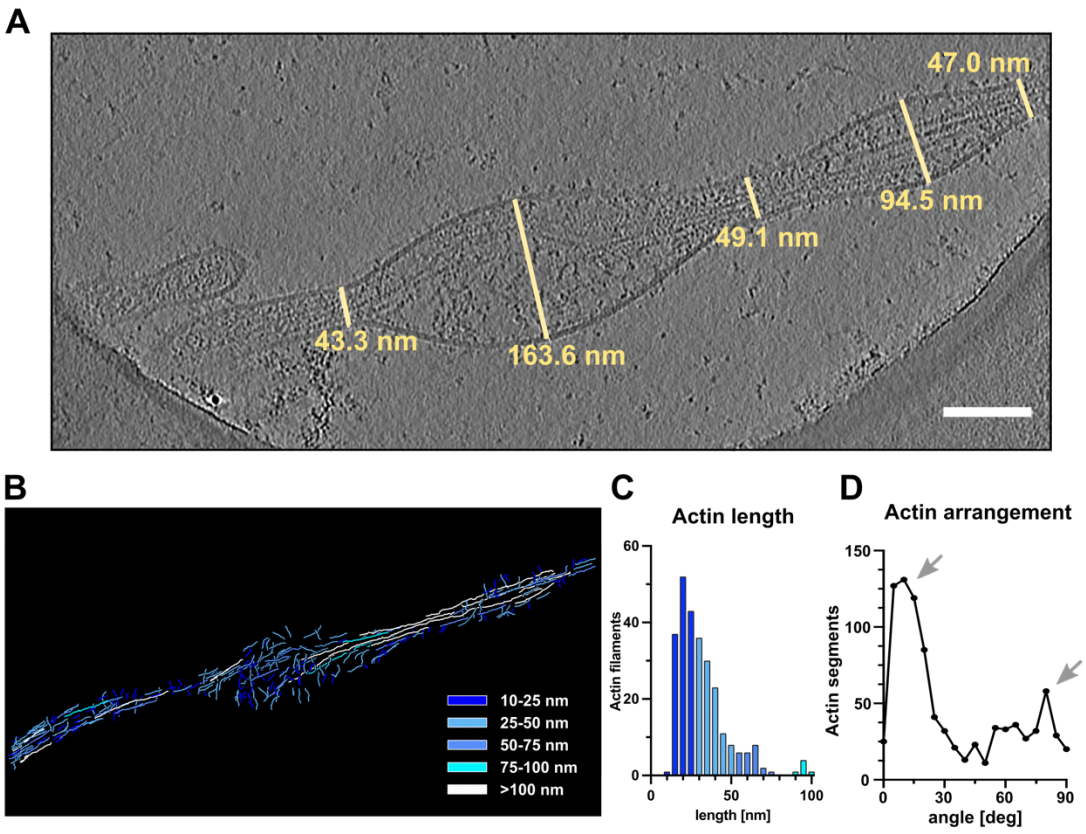

Figure 2.12. Actin filaments in filopodial protrusion after incubation with SARS-CoV-2 spike protein.
(A) Filopodia width of the platelet incubated with S protein. (B) Length of the traced actin filaments of the tomographic reconstruction in G. (C) Length distribution of traced actin filaments depicted in I. Actin filaments ≥100 nm (12 in total) are not represented in the graph. (D) Angular arrangement of actin filaments along the platelet protrusion. Scale Bars: (A) = 100 nm.

2.2.6 Protein densities decorate the plasma membrane after S protein pre-incubation under cryo-EM

Under control conditions the platelet membrane surface exposed only smaller faint bands at high magnification. Interestingly, the membrane extensions of SARS-CoV-2 spike protein incubated platelets showed a decoration of densities on their surface (see Figure 2.13). To analyse the molecular appearance of the identified density, subtomogram averaging was applied. In an initial step, the locations of 4167 protein densities were manual picked and 3D volumes extracted at the selected coordinates from eight tomograms.

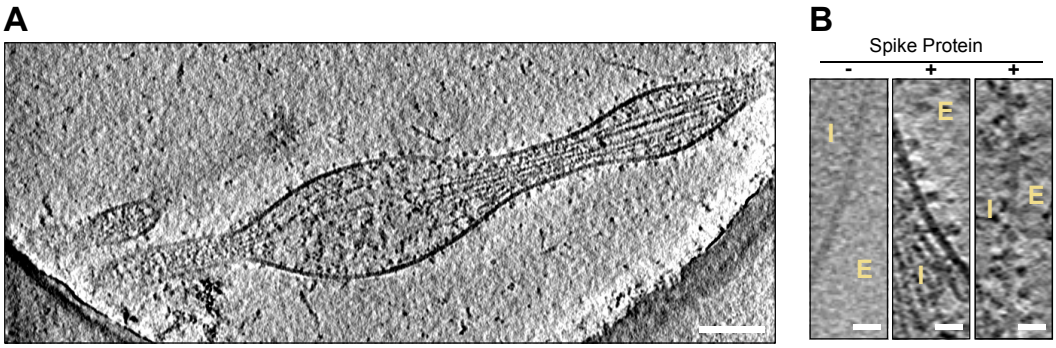

Figure 2.13. Proteins densities on platelets incubated with the SARS-CoV-2 S protein.

(A) Central slice of example tomogram used for particle picking. (B) Magnified views on the platelet plasma membrane without and in the presence of S protein (E - extracellular, I –intracellular). Scale Bars: (A) = 100 nm. (B) = 20nm.

Subsequently, the extracted protein densities were aligned. To circumvent the dominant influence of the membrane during alignment, PySeg was used to subtract the membrane signal. The subtomogram averaging with an applied C3 symmetry results in a coulomb map that reproduces the iconic pedal shaped form of the spike protein (Figure 2.14A). The resolution of the S protein corresponds to 13.8 A according to FSC0.143, although this appears to be a slightly overestimated (Figure 2.14B). Nevertheless, the structure of the previous publication by Wrapp et al. was fitted into the STA density and gives size and shape accordingly. In addition, a SPA dataset of the obtained S protein was collected to determine the quality and appearance of the used spike protein sample. The size and shape of the SPA and STA EM maps show similar characteristics, supporting the hypotheses that the densities are the S protein (Figure 2.14C).

Furthermore, the cryo-EM map was reconstructed without applied C3 symmetry. This map resembles the appearance as if an RBD is in the up position, which is oriented towards the membrane. Thus, the S protein could interact with receptors on the platelet surface through its displayed RBD (Figure 2.14D). Interestingly, at some chosen spike coordinates, additional protein density between the membrane and the spike protein could be detected (Figure 2.14E). This density could originate from the receptor on the platelet surface.

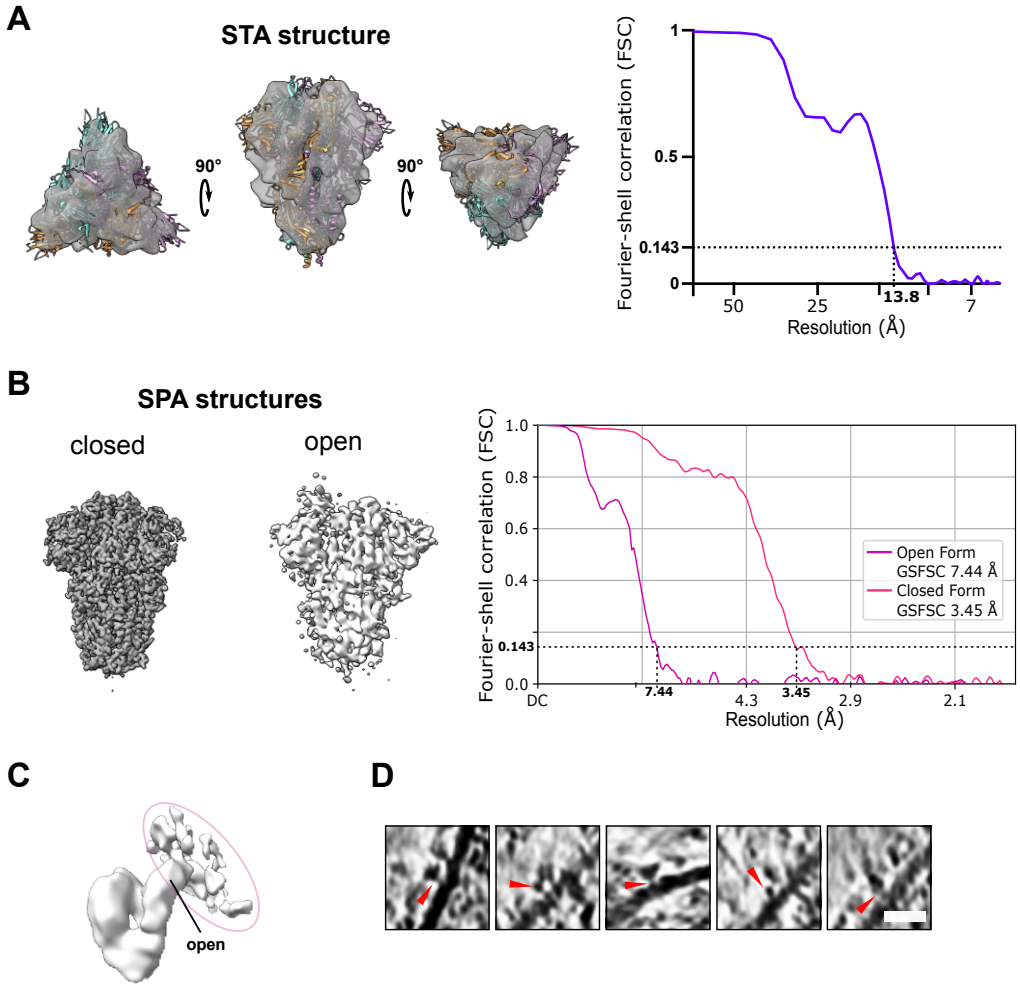

Figure 2.14. SARS-CoV-2 S protein reconstruction and membrane decoration analysis.

(A) Structure of S protein with closed conformation fitted in the sub-tomogram reconstruction. FSC curve of the sub-tomogram averaged S protein reconstruction in the closed conformation with an estimated resolution of 13.8 Å at FSC=0.143. (B) Cryo-EM map of S protein in the open conformation at a resolution of 7.44 Å. Cryo-EM map of S protein in the closed conformation at a resolution of 3.56 Å at FSC=0.143. Gold standard FSC curves of the reconstructed S protein in the open and closed conformation. (C) Structure of S protein calculated without C3 symmetry, revealing the uplifted RBD domain connected to additional densities from the host platelets. The additional densities connected to the open RBD domain is circled in magenta. (I) Additional densities (red allow-heads) between picked S protein and platelet plasma membrane. Scale bar: (I): 20nm.

2.2.7 SARS-CoV-2 S protein binds to the platelet membrane surface flexibly

To assess how the S protein recognizes the platelet surface, the spike STA map was back-projected into a volume of the reconstructed tomogram including the segmented membrane (Figure 2.15A). Therefore, the alignment parameters of the individual spike densities obtained by subtomogram averaging were taken into account. The determined median inter-distance between two S was 27.3 nm with a peak around the 15 nm bin center (Figure 2.15B). However, no periodic

arrangement of the S protein was detected. The median distance between two S corresponds to a circular area of 585 nm^2 on which a single S protein is located. Although there are regions where some spike proteins are further apart from each other. Based on the determined spike size of 17 nm, most are in the relative proximity of each other.

Furthermore, the median distance between the center of the S protein and the platelet membrane was estimated to be 16 nm, where the majority of S covers an approximate distance between 10 nm to 25 nm (Figure 2.15C). However, not all S proteins behave the same and a relatively scattered angular distribution of spike protein orientations to the platelet membrane was determined. This suggests that a wide range of angles can be adopted to interact with the platelet surface and angles between 45°-135° are most frequently observed (Figure 2.15D).

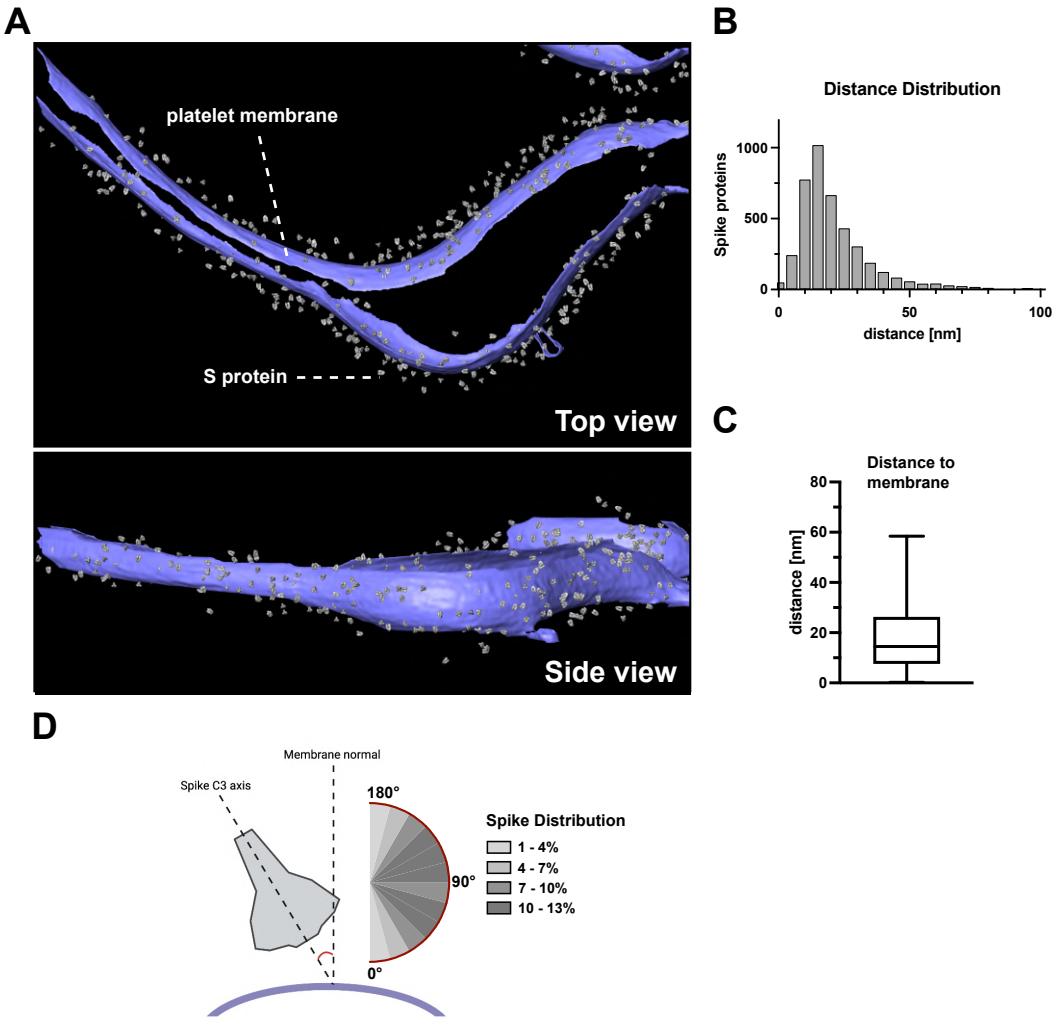

Figure 2.15. Characteristic of S proteins in cryo-electron tomogram.

(A) Densities of the reconstructed S protein back-plotted to the segmented platelet plasma membrane. The tomogram lacks top and bottom due to the missing wedge effect of tomographic data collection. (B) Nearest neighbor distance distribution of S protein densities on the platelet surface membrane. The distances are calculated using the originally manually picked coordinates. The median distance between two S protein is 27.3 nm. (C) Distance of S protein from the membrane. The median distance from the center of S protein to the membrane is 16 nm. The box plot represents 25 and 75 percentiles (8.6 and 27 nm, whiskers). (D) Orientation of S protein on the membrane surface. The scheme depicts the angle determination of S protein C3 axis and the normal of the platelet plasma membrane. The range from 45-120° was observed to be favorable for S protein interaction with the platelet surface.

Next, the local membrane curvature in the presence of the S protein was studied. For this purpose, the membrane curvature of the manually segmented platelet surface was calculated using PySeg (Martinez-Sanchez et al., 2020). Subsequently, the curvature was compared at positions with and without S protein interaction. This revealed that the S protein is potentially bound to slightly more

curved membrane surfaces (see Figure 2.16). The underlying cause of this result may be the increased formation of filopodial protrusions observed in the presence of S protein. However, whether the S protein stabilizes filopodial structures or induces their formation cannot be anticipated.

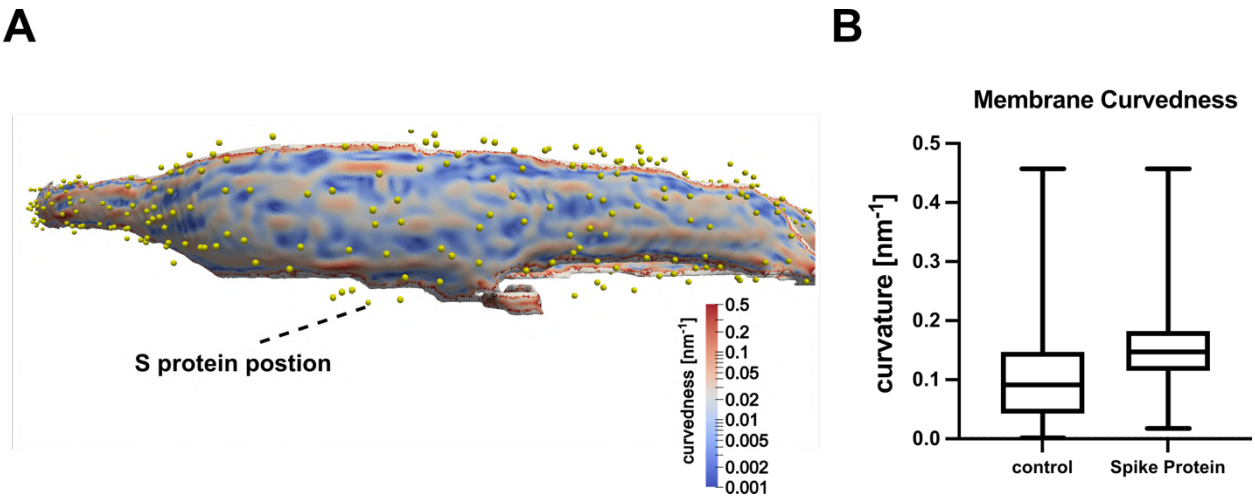

Figure 2.16. Membrane curvature on platelet in presence of SARS-CoV-2 spike protein.
(A) Visualization of the platelet plasma membrane curvedness and the position of S protein on the platelet surface. The top and bottom edge of the segmented membrane was excluded from the estimation. (B) Membrane Curvature comparison of S protein bound and surface protein free areas on the platelet plasma membrane. The box plots represent 25, median and 75 percentiles. Control: 25% 0.043, median 0.091 and 75% 0.15. + S protein: 25% 0.11, median 0.14 and 75% 0.17.

2.2.8 Integrin $\alpha_v\beta_3$ shows affinity to the SARS-CoV-2 S protein

The presence of the SARS-CoV-2 spike protein major receptor ACE2 on the platelet surface is inconclusive, for this reason its involvement in platelet activation is uncertain. However, it has been shown that other cellular receptors can also interact with the S protein. Especially the RGD motif, a short stretch in the RBD of the S protein, plays an interesting role, as it can be recognized by integrins. The abundance of integrins on platelets and the observed decoration of protein densities on the platelet membrane in the previous tomography experiment gave the idea to test the interaction between the spike protein and different platelet integrins. For this purpose, the three RGD-motif-recognizing integrins $\alpha_{IIb}\beta_3$, $\alpha_v\beta_3$, and $\alpha_5\beta_1$ were selected. While $\alpha_{IIb}\beta_3$ is expressed exclusively at high levels on platelets, $\alpha_v\beta_3$ and $\alpha_5\beta_1$ are also present in other tissue cells.

The interaction between the respective integrins and the S protein was determined by an ELISA-like solid-phase equilibrium binding assay (Figure 2.17A). The measured signals for an interaction between integrin and the S protein were compared with a non-coated control and the corresponding endogenous binding partners of the integrins (vitronectin for $\alpha_v\beta_3$, fibrinogen for $\alpha_{IIb}\beta_3$ and fibronectin for $\alpha_5\beta_1$). A significant interaction could be measured for $\alpha_v\beta_3$, whereas $\alpha_5\beta_1$

shows only a very weak binding to the S protein. $\alpha_{IIb}\beta_3$, on the other hand, shows no interaction with the spike protein (Figure 2.17B). However, the interactions with $\alpha_v\beta_3$ and $\alpha_5\beta_1$, respectively, and the S protein are close to ten times lower than to their physiological binding partners. This weak binding could be related to the moderate morphologic changes observed in the previous experiments.

Based on this result, platelet activation was tested in the presence of the cyclic RGD-peptide cilengitide. Platelets were first incubated with cilengitide to load the RGD binding sites of the integrins. Subsequently, their activation behavior was investigated in the presence and absence of the spike protein. The addition of the RGD-peptide reduces the activation in the presence of the S protein, suggesting that integrin is involved in this process (Figure 2.17C).

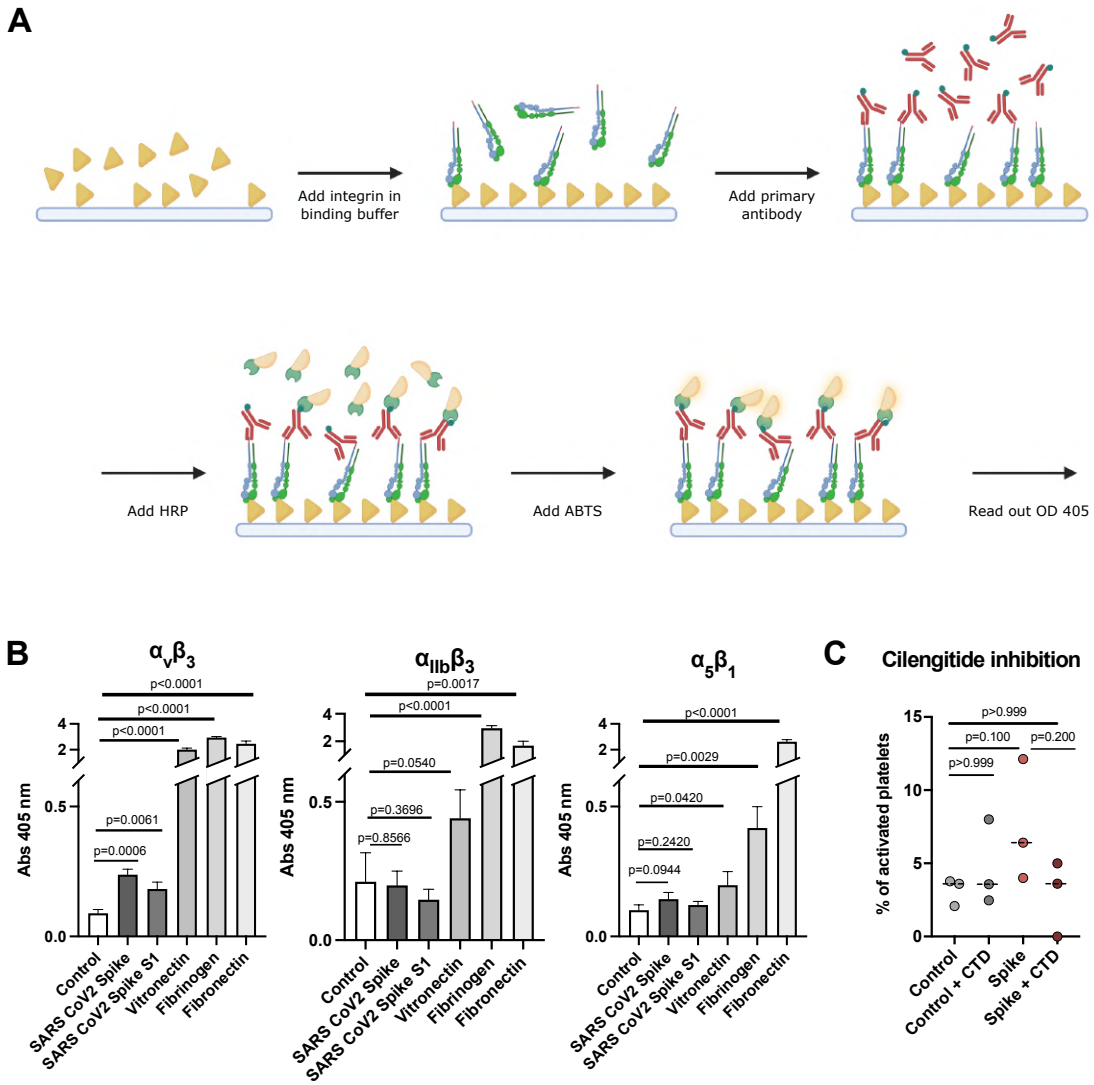

Figure 2.17. Interaction of integrin receptors with SARS-CoV-2 S protein and various ECM proteins.

(A) Scheme of the experimental setup. Immunoplates were coated with either S protein or ECM proteins. The ligands were incubated with various integrin-velcro constructs. Biotinylated anti-velcro polyclonal antibody, subsequently coupled to Streptavidin-HRP, was used to label ligand-bound integrins. Detection of the binding was measured at 405 nm, 10 min after addition of ABTS. The scheme was created with Biorender.com. (B) Binding of integrins $\alpha_v\beta_3$, $\alpha_{IIb}\beta_3$, and $\alpha_5\beta_1$ to S protein and their physiological ECM ligands: $\alpha_v\beta_3$ - vitronectin, $\alpha_{IIb}\beta_3$ - fibrinogen, $\alpha_5\beta_1$ - fibronectin. Data are from a representative experiment out of three independent ones, and shown as mean ± SD. The significance was determined by a two-tailed unpaired t test. (C) Quantification of platelet activation on Collagen I depending on S protein concentration and integrin inhibitor cilengitide. The significance was determined by a two-tailed Mann-Whitney U test. n= 363 (control), n= 278 (control + CTD), n= 339 (+Spike), n= 358 (+Spike, +CTD) platelets examined over n=3 independent experiments, from n=3 biologically independent donors.

2.2.9 Platelet deformation in the presence of pseudotyped viral particles

The previous experiments indicate that the platelet deformation is more pronounced in the presence of higher SARS-CoV-2 spike protein amounts. In line with previous observations, viruses also inhabit an environment with locally elevated concentrations of S protein. In their case, the proteins are anchored to their viral surface, thereby creating locally a high supply of spikes. With this in mind, the effect of SARS-CoV-2 pseudo virus-like-particles (VLPs) on platelet deformation was investigated.

For this purpose, SARS-CoV-2 pseudotyped VLPs were generated based on previous published protocols(Crawford et al., 2020). The titer of the pseudotyped VLPs was determined by their infectivity on HEK-293T-hACE2 cells, a modified HEK-293T cell line that consistently expresses human ACE2. The infection level, as determined by flow cytometry, was approximately 10^4-10^6 viruses/ml, confirming the insertion of the SARS-CoV-2 S protein into the viral membrane (Figure 2.18A-B). This titer is consistent with previous reports of SARS-CoV-2 pseudotyped VLPs production (Crawford *et al.*, 2020). Subsequently, the shape of the particles was checked by negative stain electron microscopy (Figure 2.18C) The observed round membrane structures correspond to the pseudotyped VLPs, but no S protein could be detected on their surface at this magnification.

However, when platelets are incubated with SARS-CoV-2 S pseudotyped VLPs, vesicles can be observed in the close proximity of filopodia-like protrusions in cryo-EM conditions (Figure 2.19A). In contrast, extracellular vesicles with similar properties but cellular origin, such as exosomes, appear to arise by budding from a concave platelet plasma membrane (Figure 2.19B). Furthermore, various tomographic slices through the VLP at the filopodial protrusion indicate densities protruding from the membrane surface (Figure 2.19C). To determine the distance between VLP and platelet filopodia, their membranes were segmented in the tomogram. Subsequent measurement of the gap resulted in a distance of approximately 20 nm, which is similar to the distance of 16 nm determined between the S protein center and the platelet membrane in the STA experiment. This distance of 20 nm can be bridged by a platelet receptor and/or the SARS-CoV-2 spike, thus an interaction between particle and platelet filopodia can be assumed.

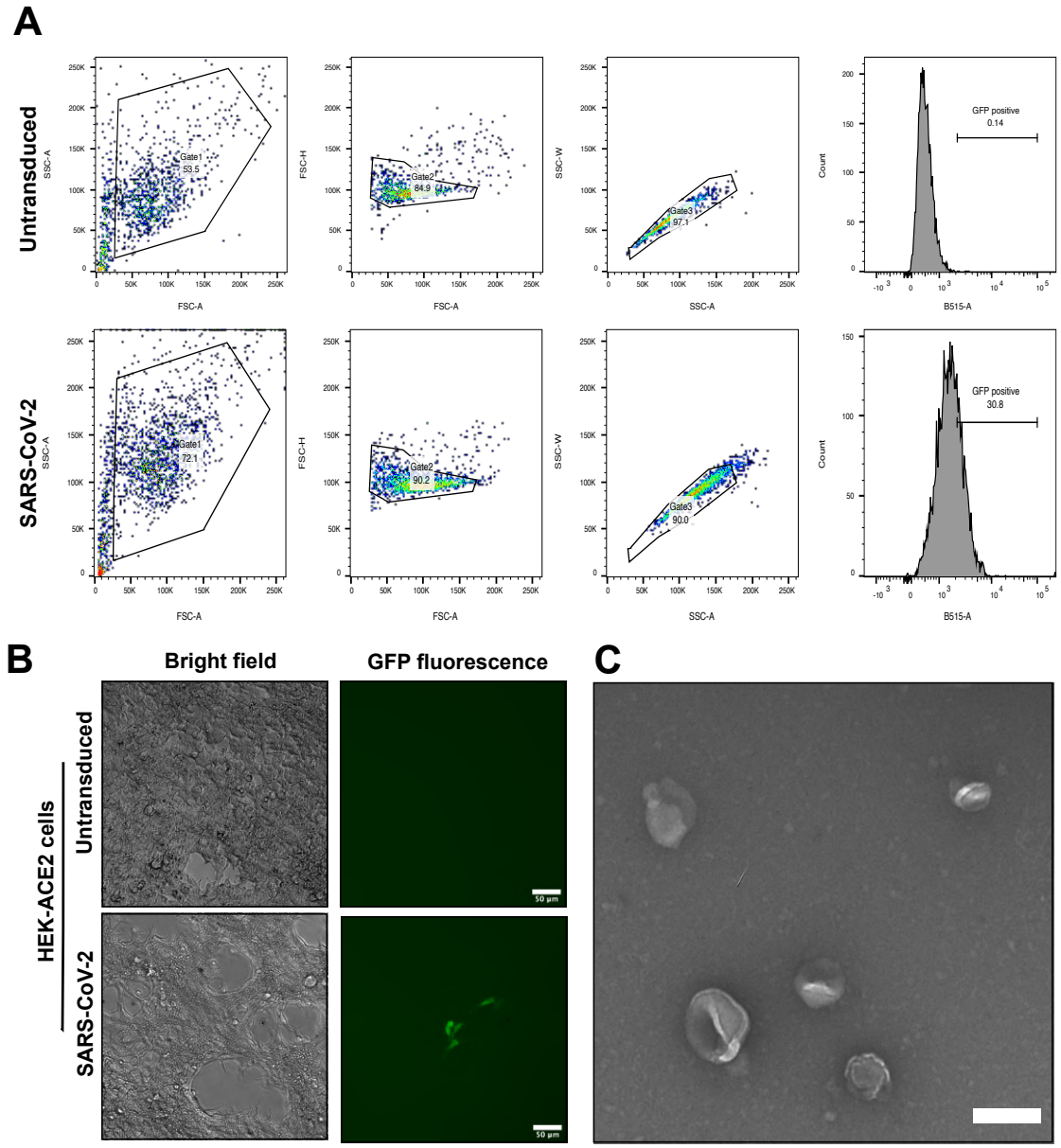

Figure 2.18. Characterization of SARS-CoV-2 S-pseudotyped lentiviral particles.

(A) Flowcytometry analysis of HEK-hACE2 cells transduced with pseudotyped lentivirus encoding ZsGreen backbone plasmid. The plot shows percentage of green-fluorescent cells with or without the incubation of S-pseudotyped lentivirus with HEK-hACE2 cells. (B) Light microscopic images of HEK-hACE2 cells with or without treatment with pseudotyped lentivirus encoding ZsGreen. (C) Negative-staining EM with 2% uranyl acetate of SARS-CoV-2 S-pseudotyped lentiviral particles. Scale bars: (B) = 50 µm; (C) = 100 nm.

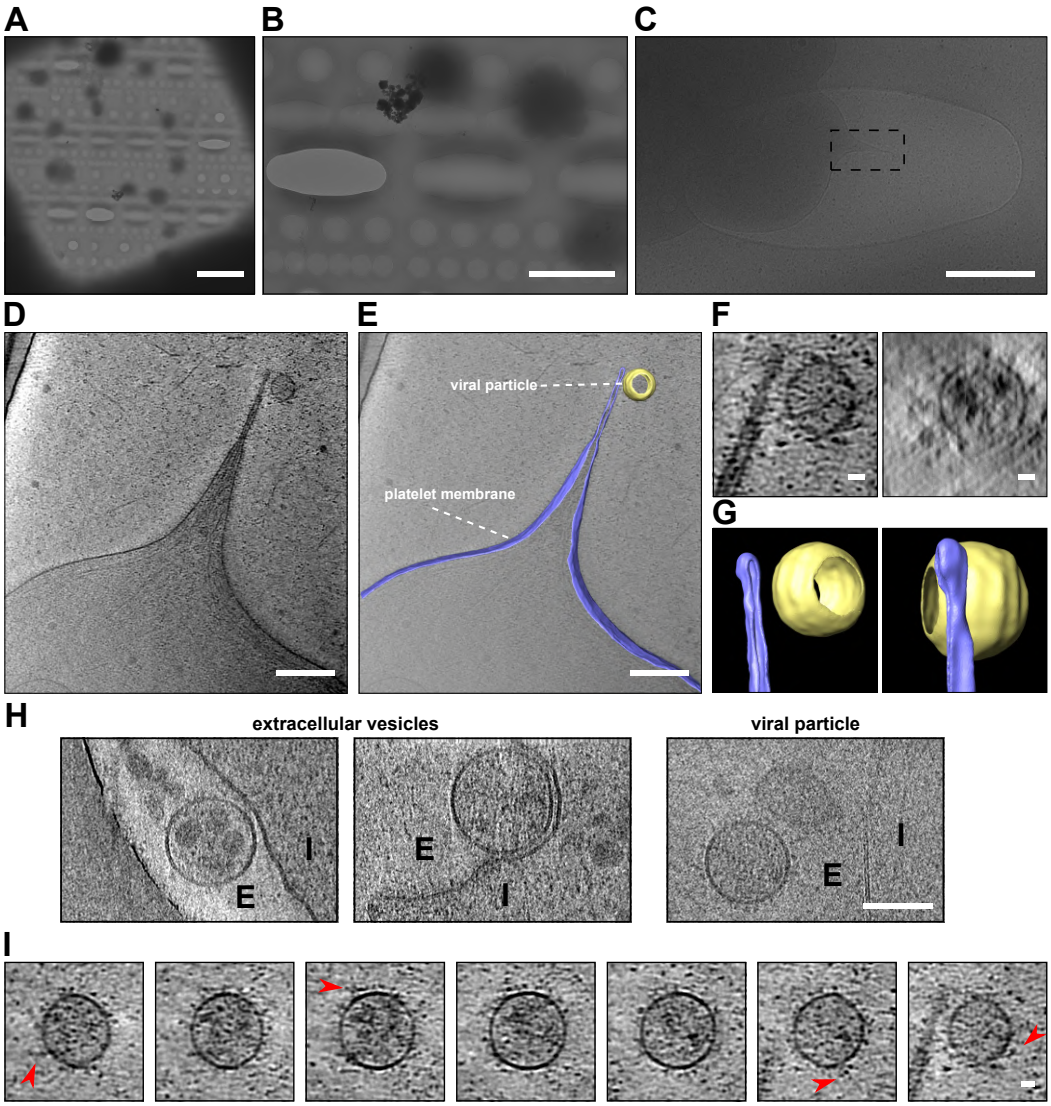

Figure 2.19. SARS-CoV-2 S-pseudotyped viral particles on platelet plasma membrane by cryo-ET.

(A) Overview of grid square of platelets incubated with pseudotyped viral particles. (B) Low magnification of platelets observed in the presence of pseudotyped viral particles. (C) Platelet with pseudotyped viral particle exhibits the formation of a filopodial protrusion. The dashed box indicates the area of tomogram data collection. (D) Slice of the reconstructed tomogram showing a virus-like particle on the platelet plasma membrane. (E) Segmentation of the tomogram with virus-like particle at the platelet plasma membrane (purple – platelet plasma membrane, yellow – virus-like particle membrane). The tomogram lacks top and bottom due to the "missing wedge" effect of tomographic data collection. (F) Zoom-in views on the contact site of platelet and virus-like particle. (G) Zoom-in view on the segmented platelet membrane and virus-like particle membrane (purple – platelet plasma membrane, yellow – virus-like particle membrane). (H) Extracellular vesicles and S protein pseudotyped virus under cryo-EM condition. (E: extracellular, I: intracellular). (I) Slices thorough the virus-like particle at the filopodia tip. Red arrows point at the protein densities on the membrane surface. Scale bars: (A)=10 μm; (B)= 5 μm; (C)=1 μm; (D)&(E)=200 nm; (F)&(I)=20 nm; (H)=100 nm.

2.3 Discussion

2.3.1 Summary

COVID-19, caused by the novel coronavirus SARS-CoV-2, shows a wide range of pathological symptoms. Especially in severe cases, a common COVID-19 symptom is the abnormal behavior of platelets, which can lead to various coagulopathic occurrences. The COVID-19 caused coagulopathy includes various disease patterns such as thrombocytopenia, microvascular thrombosis and clot formation (Al-Samkari *et al.*, 2020; Lippi *et al.*, 2020; Tang *et al.*, 2020a).

To understand the origin of this cause, the influence of the SARS-CoV-2 spike protein on isolated platelets was investigated in this project (see Results COVID19 project). In light microscopy experiments, it was observed that platelets formed more protrusions in the presence of the S protein. In addition, an increased amount of dumbbell-shaped proplatelets, a platelet precursor, could be observed. Elongated proplatelets with multiple swellings were only seen in the presence of the spike protein. Furthermore, the formation of filopodia-like protrusions in the presence of the S protein were also observed under cryo-ET conditions. Protein densities detected along the pseudopodia resembled a low resolution structure of the S protein using STA. Finally, a slight interaction between RGD-motif recognizing integrins $\alpha_v\beta_3$ and the SARS-CoV-2 S protein, exposing this motif in its RBD, was observed by an ELISA.

2.3.2 SARS-CoV-2 potentially exploits RGD-recognizing integrins for cell entry

Previous studies have addressed the direct impact of the spike protein on platelets. For example, Zhang et al. observed increased platelet spreading when in presence of the SARS-CoV-2 S protein. In their study, the interaction of the S protein with ACE2 on the platelet surface was suggested (Zhang *et al.*, 2020c). Even though they detected the presence of ACE2 and its mRNA in platelets using proteomic and transcriptomic assays, other studies were not able to confirm their presence, neither on expressional nor transcriptional level. However, two independent studies have detected SARS-CoV-2 RNA in platelets isolated from COVID-19 patients, implying a interaction and subsequent internalization of the virus (Manne *et al.*, 2020; Zaid *et al.*, 2020). Indeed, sections from platelets exposed to SARS-CoV-2 showed internalized viral particles under TEM (Koupenova *et al.*, 2021; Zhang *et al.*, 2020c).

Interestingly, RGD-motif recognizing integrins, abundantly expressed on the platelet membrane were shown to mediate viral cell entry (Wickham et al., 1993). The results presented previously (see Figure 2.17) exhibit a decreased activation probability when platelets were incubated with the RGD-mimicking integrin inhibitor cilengitide prior S protein exposure. This suggests an interaction between the spike protein and integrins. Furthermore, an ELISA shows the interaction

between $\alpha_v\beta_3$ and the SARS-CoV-2 spike protein, while $\alpha_{IIb}\beta_3$ and $\alpha_5\beta_1$ didn't show a significant binding. However, this interaction appears to be less prominent compared to its physiological binding partner vitronectin. The weak affinity of the spike protein to the platelet integrin receptors may be the reason why coagulopathic events during COVID-19 are dominantly observed in severe cases of disease. Nevertheless, also other non-integrin receptors on the platelet surface can take part in the interaction with the SARS-CoV-2 protein, such as TLR4 and CD147 (Wang *et al.*, 2020a; Zhao *et al.*, 2021). Therefore, it is likely that combinatory effects are responsible for the interaction between SARS-CoV-2 and platelets followed by their morphological rearrangements.

Furthermore, different biochemical and cellular studies show an interplay between RGD-recognizing integrins and the spike protein. While the interaction with $\alpha_5\beta_1$ seems to mediate the internalization of the virus, and the $\alpha_v\beta_3$-binding shows the dysregulation of cellular processes (Liu *et al.*, 2022; Nader *et al.*, 2021).

2.3.3 Spike protein interaction leads to stabilization of the cytoskeleton

In the DIC microscopy experiments shown in this project (see Figure 2.6), uncommon barbell-shaped platelets with multiple bulges were observed (see Figure 2.7). These elongated platelets resemble the shape of proplatelets, an intermediate in the platelet maturation process. It is hypothesized that a platelet-precursor in the circulatory system, called preplatelet, can alter between a circular and elongated proplatelet-shape. Their morphological transformation is dependent on a cytoskeletal-based remodeling (Schwertz *et al.*, 2010; Thon *et al.*, 2010). The stabilization of the actin-network due to the interaction of the S protein with platelet integrins could interfere with the ultimate step in the preplatelet life-cycle, the abscission of small platelets in the circulatory system. Therefore, the interaction of the S protein with $\alpha_v\beta_3$ on the platelet surface could prevent the production of platelets in the blood stream and thereby contribute to thrombocytopenia observed in COVID-19 patients. Interestingly, no detectable levels of phosphorylated FAK, a cytoskeletal platelet activation marker, were detected in floating platelets (Figure 2.10D). This suggests a reversible process between elongated and discoid-shaped platelets. However, after attachment to a collagen I coated surface, an interconnected actin network can be observed in a filopodia-like protrusion. The platelet membrane in this area is decorated with spike protein densities (see Figure 2.13). Analysis of the angle resulted in a difference of 70° the two peaks (see Figure 2.12). This result presumes the involvement of the Arp2/3 complex, connecting the branching actin filaments (Mullins *et al.*, 1998). Furthermore, the increased pFAK signal observed for adherent platelets after S protein exposure implies formation of a stable cytoskeletal

network subsequent to ECM attachment (Figure 2.10B). Accordingly, once the platelet attaches to the surface, the formation of pseudopodia is stabilized.

2.3.4 Spike protein flexibly attaches to platelet surface

The detected protein densities attached to the platelet surface resemble in size the iconic petal-shaped SARS-CoV-2 spike protein after STA. Their distance to the membrane spans a range mainly between 8.6 nm to 27.0 nm from the center of the S protein, with a median of 16 nm. Distances in this range can be bridged by integrins in their extended active state. The rather wide distribution of distances from the center of the S protein to the membrane indicates binding of various platelet receptors. However, the distance distribution can also be partly explained by the different orientations of the spike protein to the platelet surface. Since the distance was measured from the center of the S protein, the determined distance does not necessarily correspond to the distance of the spike RBD to the membrane (Figure 2.20). For S proteins with an orientation from 0°-90° towards the membrane, the actual distance is shorter than the calculated distance because the RBD is positioned between the membrane and the S protein center. Accordingly, in case of a horizontal orientation (90°) to the membrane, the determined median distance corresponds to the RBD's. On the other hand, when the angle is higher than 90°, the actual distance between RBD and platelet surface become larger. Nevertheless, it is likely that both, the multiple orientations to and different interactions with the platelet membrane, are responsible for the binding distance range.

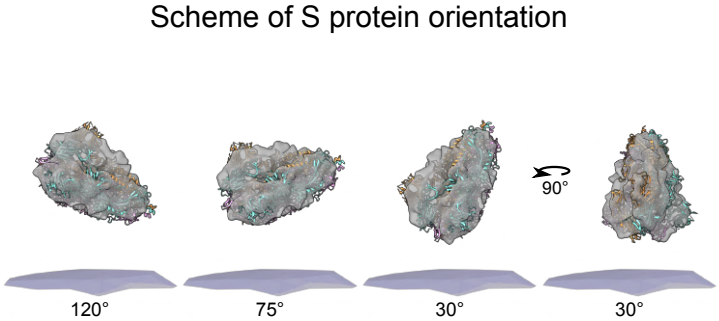

Figure 2.20. Schematic depiction of S protein orientation in different angles towards platelet plasma membrane.

Furthermore, due to the different binding angles, it can be concluded that the S protein can align according to the receptors on the platelet surface. In previous studies with SARS-CoV-2 viral particles, multiple kinking points were detected in the stalk of the S protein. The flexible motion can allow the individual S protein on the viral surface to adapt to curved host cell surfaces (Ke *et*

al., 2020; Turonova *et al.*, 2020b). Hence, the flexible adjustment from the stalk to the RBD of the S protein can promote an efficient action of SARS-CoV-2 on host cell receptors.

Based on the observations presented in this chapter, following hypothesis can be introduced (Figure 2.21). The interaction between platelet integrins and the SARS-CoV-2 S protein is mediated by the RGD-motif located in their RBD. After binding, the development and stabilization of platelet pseudopodia is promoted by a distinct actin network in the filopodia-like protrusions. Ultimately, the integrin-induced filopodia formation leads to the activation and subsequent spreading of platelets.

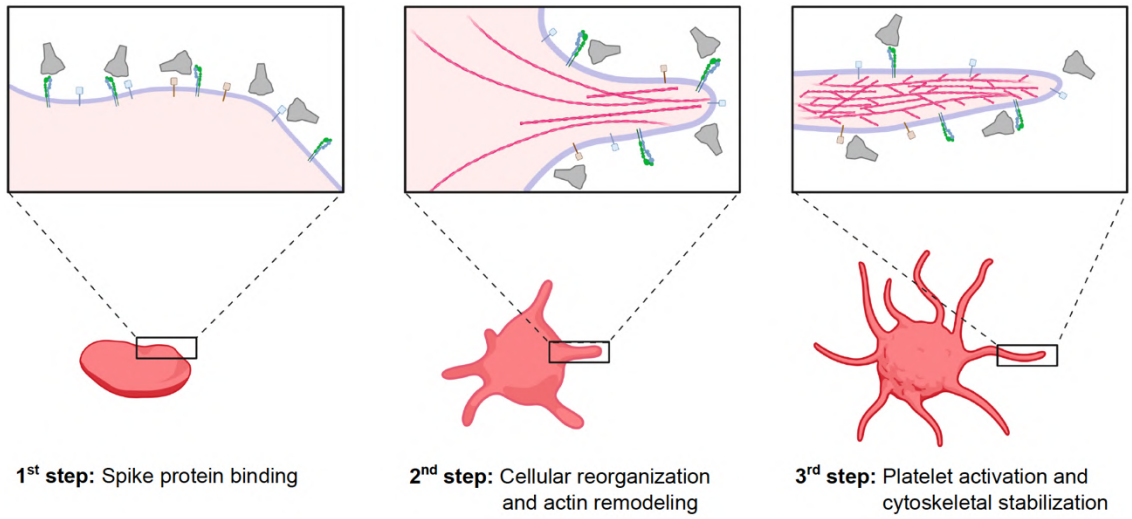

Figure 2.21. Schematic representation of potential SARS-CoV-2 S platelet interaction.

First, the S protein binds to receptors on the platelet surface, inducing the deformation and priming the activation. Protrusions are forming as a consequence of actin remodeling. This leads to the activation of platelets by the formation of filopodia and the stabilization of the cytoskeleton network. The scheme was created with Biorender.com.

2.3.5 Outlook

Overall, the binding of S protein to platelets in combination with further coagulation factors may induce an irreversible activation of platelets and the dysregulation of hemostasis in COVID-19. However, further studies are needed to fully understand the platelet activation by direct binding of S protein. For instance, in addition to RGD-recognizing integrins, other receptors shown to engage with the S protein are present on the platelet surface (Wang *et al.*, 2020a; Zhao *et al.*, 2021). Further exploring the role of the individual receptors as well as their interplay would help to understand platelet hyperactivity caused by the interaction with spike protein. In this context, biochemical and structural investigation on the S protein interaction with integrin could shed light on the mechanism attachment and internalization of the SARS-CoV-2 by platelets.

Moreover, isolated human platelets provide a close context to physiological conditions, but they also contribute a high variability factor. Minor changes can be sufficient to influence the sensitive behavior of platelets. Therefore, reproducing the study with platelets derived from cultured megakaryocytes would provide the opportunity to address the open questions in a controlled system.

Distinct factors, such as the influence of different platelet receptors, can thus be studied in detail. An initial study by Shen et al. were able to detect the infection of the megakaryocyte cell line MEG-01. However, the underlying mechanism and the responsible receptor weren't identified (Shen et al., 2021). Also, samples from COVID-19 patients revealed the presence of SARS-CoV-2 in megakaryocytes as well as their platelets, which also have an altered transcriptome post-infection (Barrett et al., 2021; Zhu et al., 2022). In this regard, cultured megakaryocytes can further be used to study the influence of the SARS-CoV-2 spike protein on the platelet development. In particular, if cultured megakaryocytes display a reduced platelet production due to stabilized proplatelets or weather if this phenomenon is limited to pre-/proplatelets population in the circularity system.

2.4 Methods

2.4.1 Platelet Isolation

Human platelets were isolated from whole blood samples of de-identified healthy donors. The whole blood was collected by the NIH Blood Bank in 50 mM acid-citrate dextrose to prevent coagulation. For isolation of platelets, 50 ml whole blood was centrifuged for 20 min at 200 g at RT. The top 10 ml of the plasma were carefully transferred to a fresh tube, to separate from the red and white blood cells. Next, 10 ml HEP buffer (14 mM NaCl, 2.7 mM KCl, 3.8 mM HEPES, 5 mM EGTA, 1 µM Prostaglandin E1, pH 7.4.) were added and gently mixed. This was followed by a 20 min centrifugation step at 100 g and RT to pellet remaining blood cells other than platelets. 15 ml of the platelet solution was transferred to the fresh tube, the remaining 5 ml including the pellet were discarded. In a final centrifugation step at 800 g for 20 min at RT, the platelets were pelleted. The supernatant was discarded, the pellet washed twice with 1 ml Platelet Wash buffer (10 mM sodium citrate, 150 mM NaCl, 1 mM EDTA, 1% (w/v) dextrose, pH 7.4) and afterwards gently resuspended in 10 ml Tyrode's buffer (134 mM NaCl, 12 mM $NaHCO_3$, 2.9 mM KCl, 0.34 mM Na_2HPO_4, 1 mM $MgCl_2$, 10 mM HEPES, 5 mM Glucose, 3 mg/ml BSA, pH 7.4). The isolated platelets were rested for 1 h prior determination of the platelet concentration using a hemacytometer.

2.4.2 Coating of LM dishes

To ensure the attachment of platelets to light-microscopy wells, coating solutions were applied before addition of platelets. To each well of the imaging chamber (µ-Slide 8 well glass bottom, ibidi #80827-90), 200 µl coating solution were applied and incubated at 37°C (for further information see table 2.1). After the coating procedure, the imaging chambers were three times washed with PBS and afterwards blocked with 1% BSA in PBS for at least 90 min.

Table 2.1. Coating properties for light microscopy chambers.

Solution	dilution	time	Vendor
Poly-L-Lysine	0.01%	overnight	Sigma #P2636
Fibronectin	10 µg/ml	overnight	R&D systems #3420-001-01
Collagen-I	25 µg/ml	30 min	Chrono-Log #385

2.4.3 Sample preparation for LM experiments

S-protein. Isolated platelets were mixed with SARS-CoV-2 S protein (Cube Biotech #28703) at a final concentration of 0.2 µg/ml, 2 µg/ml and 20 µg/ml at a concentration of $1.5x10^7$ platelets/ml (in Tyrode's buffer) and incubated for 4 h at 37 °C.

Control. For the control without S protein, samples were prepared by adding Cube Biotech's S protein buffer (20 mM HEPES pH 7.5, 150 mM NaCl, 0.01% LMNG, 1 mM Rho1D4-peptide) instead of S protein. Furthermore, the concentration of the rho1d4-elution peptide was adjusted to 1 mM, the highest concretion suggested for the manufacturer.

Integrin-inhibitor cilengitide. Isolated platelets at $1.67x10^7$ platelets/ml were pre-incubated with cilengitide (Millipore-Sigma #ML1594) at a concentration of 111 µg/ml. After for 20 min at 37°C, S protein or vehicle control was added to the cilengitide-exposed platelets. The final concentration of cilengitide was thereby adjusted to 100 µg/ml with a final concentration of $1.5x10^7$ platelets/ml.

2.4.4 Differential Inference Contrast Microscopy imaging

In an initial step, the live-cell imaging chamber was set to 37°C using the integrated water bath chamber. The coated imaging chambers were fixed inside the live-cell imaging chamber for temperature adjustment prior addition of platelets. The incubated platelet samples were added to the coated imaging chambers using wide orifice tips and further diluted to $0.75x10^7$ platelets/ml. After 15 min of settling time, the platelet samples were imaged for 1 h, a frame time of 2 min and 5 images in z-direction (steps of 0.5 µm). One experimental series was recorded for 58 min.

2.4.5 Differential Inference Contrast Microscopy analysis

For the analysis of DIC movies, FIJI was used (Schindelin et al., 2012). The platelet shape was manually tracked using the 'freehand selection' tool every 6 min over the entire imaging period. Therefore, the z-image with clearest platelet outline was utilised. The circularities (4π[area/perimeter^2]) and aspect ratios (major axis and minor axis of the fitted ellipse) of the segmented platelets were calculated using the FIJI measurement plugin. The data was quantified and analysed using GraphPad PRISM. For each condition, at least three movies from three different donors were used.

2.4.6 Enzyme-linked Immunosorbent assays (ELISAs)

Platelet factor 4 release. To estimate the activation-dependent release of PF4 filled alpha-granules, isolated platelets from 3 different donors were incubated with 20 µg/ml S protein or control as described before. Subsequently the platelets were exposed to Collagen-I coated imaging chambers for 1 h prior collection of the supernatant. For determination of the PF4 concentration, the Human PF4 CatchPoint® SimpleStep ELISA® Kit (Abcam #ab278096) was used. 50 µl samples or standards were pipetted in the according wells and 50 µl antibody cocktail

were added. After 1 h of gently shaking at RT, the solution was aspirated and each well was washed with 350 µl 1x wash buffer PT. 100 µl CatchPoint HRP Development Solution was applied to the wells. While gently shaking, the samples were incubated for 10 min in the dark. Subsequently, a BioTek Synergy H1 plate reader was used to measure the fluorescence at excitation/emission 530/590 nm.

Integrin Binding. To test S protein interaction with RGD-recognizing integrins on the platelet surface, the interaction with $\alpha_v\beta_3$, $\alpha_{IIb}\beta_3$, and $\alpha_5\beta_1$ was tested. Therefore, dilutions of human plasma vitronectin (5 µg/ml), human fibrinogen (20 µg/ml), bovine plasma fibronectin (10 µg/ml), S protein (residues 1-1212 with stabilizing mutations R684G, R685S, R678G, K998P, and V999P with a C-terminal foldon motif and a hexaHis-tag, 20 µg/ml) and SARS-CoV-2 S1(residues 1-696 with a C-terminal foldon motif and a hexaHis-tag, 20 µg/ml) in TBS were incubated for 6 h at RT to coat 96-well polyvinylchloride microtiter plates (Nunc Maxisorp #44-2404-21). For determination of background values from unspecific binding, uncoated wells were used. All wells, including the non-coated well, were blocked (Blocking One, Nacalai #03953-95), at 4°C overnight. Velcro-tagged versions of the three RGD-binding integrins $\alpha_v\beta_3$, $\alpha_{IIb}\beta_3$, and $\alpha_5\beta_1$ diluted at 10 µg/ml (20 mM HEPES pH 7.2, 150 mM NaCl, 1 mM $MnCl_2$) were incubated for 2 h at RT to allow binding to the immobilized ligands. Integrin binding was quantified by an ELISA-like solid-phase assay using biotinylated rabbit anti-velcro antibody, against the ACID/BASE coiled-coil and HRP-conjugated streptavidin (VECTOR Laboratories #SA-5004). ABTS was added and subsequently the signal was read out at 405 nm.

2.4.7 Western Blot

Sample preparation. Platelets, incubated with S protein and vehicle control as previously described, were seeded on 8-well chamber cover glass slides coated with 25 µg/ml Collagen I. After exposure for 1 h, the floating (supernatant) and adherent platelets were separately prepared in NP-40 lysis buffer (50 mM Tris-HCl pH 7.4, 150 mM NaCl, 1 mM NaF, 1 mM Na_3VO_4, 1% IGEPAL® CA-630, 1 mM EDTA, protease inhibitors). The Pierce™ Rapid Gold BCA Protein Assay Kit (Thermo Fisher #53226) was used total protein determination.

Immunoblot. 30 µg of each sample was mixed with Laemmli buffer (180 mM DTT, 4% SDS, 160 mM Tris-HCl pH 6.8, 20% glycerol, bromophenol blue), boiled at 95°C for 5 min and spun down. Then, the samples were loaded on a Bolt™ 4-12% Bis-tris gel (Invitrogen #NW04120BOX), and SDS-PAGE was run for 40 min at 180-V in 1x MES buffer. Next, the gel was prepared for the Trans-Blot® Turbo system (Bio-Rad) for transferring the proteins from the gel to a PVDF membrane according to the manufacturer's instructions. Subsequently, the

membrane was blocked for 3 h at 4°C in 1x TBST buffer (20 mM Tris-HCl, 150 mM NaCl, 0.1% Tween® 20) with 4% blocking agent (Cytiva #RPN2125). In case of later incubation with phospho-antibodies, 4% BLOCK ACE (Bio-Rad # BUF029) in 1xTBST was used instead. Afterwards, primary antibodies were used for incubation at 4°C overnight. After primary antibody exposure, the membranes were washed three times in 1x TBST for 5 min at RT and subsequently incubated with secondary horseradish peroxidase-coupled goat anti-rabbit or anti-mouse antibodies for 60 min at 4°C.

Table 2.2. Primary and Secondary antibodies for Immunoblot.

Type	Target	Dilution	Vendor
Primary	Phospho-FAK (Tyr397) Polyclonal	1:1000	Thermo Fisher, 44-624G
Primary	Anti-GAPDH Mouse monoclonal	1:1000	Sigma #8795; 1:1000
Secondary	Goat anti-rabbit	10,000	Bethyl #A120-201P
Secondary	Goat anti-mouse	10,000	Bethyl #A90-516P

After secondary antibody incubation, the membranes were three times washed in 1x TBST. ECL substrate (Bio-Rad) was applied for 2 min to reveal chemiluminescence signal and immediately imaged using Amersham™ Imager 600.

Analysis. For quantification of the signals, FIJI was used. GAPDH was used for normalization of the signals. As actin and tubulin can remodel upon platelet activation, they were avoided as normalization target.

2.4.8 Pseudotyped SARS-CoV-2 S lentiviral particle

Preparation. In a first step X-Lenti 293T cells (Takara #632180) plated in 6-well plates were co-transfected as follows:

Table 2.3. Transfection scheme for lentivirus production pseudotyped with S-Protein. Only one type of viral entry protein was used per batch of pseudotyped viruses, either SARS-CoV-2 spike protein or VSVG as control. The described amounts were used to transfect one well of a 6-well plate.

Type	Name	Amount	Vendor
lentiviral backbone	ZsGreen	1 µg	BEI #NR-52516
helper plasmids	HDM-Hgpm2	0.22 µg	BEI #NR-52517
helper plasmids	HDM453 tat1b	0.22 µg	BEI #NR-52518
helper plasmids	pRC-CMV-Rev1b	0.22 µg	BEI #NR-52519
viral entry protein	SARS-CoV-2 Spike	0.34 µg	BEI #NR-454 53742
viral entry protein	pCMV-VSVG	0.34 µg	Addgene plasmid #8454
transfection reagent	TransIT-293	8 µl	Mirus Bio #MIR 2705

The day after the transfection, the media was exchanged. The virus-containing supernatants were collected 60 h post transfection, passed through a 0.45 µm filter and stored at -80°C.

Titer-estimation. The transduction level of the viral particles was tested by adding different volumes of the filtered virus-containing supernatants to HEK-293T cells constitutively expressing ACE2 (HEK-293T hACE2; BEI #NR-52511). The cells were incubated for 60 h and analysed by a BD LSRFortessa Cell Analyzer scanning for GFP-positive cells.

2.4.9 Negative Staining of SARS-CoV-2 S pseudotyped virus

To observe the shape of SARS-CoV-2 S lentiviral particles, larger quantities were produced and concentrated by ultracentrifugation on a 20% sucrose cushion. 10 µl of concentrated sample were incubated on carbon coated grids (EMS #CF200-CU), which were glow discharged using a Pelco easiGlow™ for 45 s at negative discharge, 15 mA plasma current and 0.38 mbar residual air pressure. After 30 min, excess solution was removed by back-blotting. Next, the grids were washed three times in a drop of each, 1xPBS and water. The specimens were stained by applying 5 µl of 2% (w/v) uranyl acetate solution for 60 s.

A Tecnai T12 transmission electron microscope (FEI) operated at 120 kV was used to observe the pseudovirus grids.

2.4.10 Preparation of platelet cryo-ET samples

To prepare platelet samples for cryo-EM, carbon-coated MultiA Au200 and SiO_2-coated R1/4 Au200 grids (Quantifoil) were glow discharged in ambient air, 15 mA plasma current and 0.38 mbar residual air pressure for 45 s using a Pelco easiGlow™. Next, the grids were placed in a

cell culture dish (greiner #627170), and coated with 25 µg/ml collagen-I solution for 30 min or 10 µg/ml fibronetin solution overnight at 37°C. After coating, the grids were washed three times in 1xPBS, blocked with 1% BSA in PBS overnight and then covered in Tyrode's buffer. Then, isolated platelets were incubated with 9.75 µg/ml SARS-CoV-2 spike protein or control buffer (20 mM HEPES, 150 mM NaCl, 0.01% LMNG, pH 7.5) for 4 h before pipetted with a wide orifice to the coated grids and incubated for 1 h at RT. Prior plunge vitrification, 3 µl Tyrode's buffer was added to grids. Adhered platelets were vitrified in liquid ethane using a Vitrobot MarkVI (Thermo Fisher Scientific) conditioned at 37°C and 100% humidity with an applied blotting force of 4 for 12 s.

2.4.11 Cryo-ET collection of platelet samples

Raw tilt series were recorded using a Titan Krios (Thermo Fischer Scientific) operated at an acceleration voltage of 300 keV, equipped with a Gatan Quantum 967 LS and K3 Summit direct detector. The tilt series were acquired with a defocus range between -3 µm to -5 µm from -60° to 60° with angular increment of 2°. A nominal magnification of 33000x, corresponding to 2.76 Å/px, was used for the data collection. The accumulated electron dose per tilt series was 123 $e^-/Å^2$, each tilt was acquired as six-frame move in super-resolution mode. In total, 8 tilt series were assessed.

2.4.12 Tomogram reconstruction

The movies of all tilt series were corrected for stage- and beam-induced drift as well as weighted for their cumulative dose using MotionCor2 (Zheng *et al.*, 2017). Subsequently, IMOD ETOMO was used to align the tilt-series. Both, 4x bin and unbinned tomograms were reconstructed using the weighted back projection in IMOD (Mastronarde and Held, 2017). To improve the contrast for better visualization, deconvolution filter in Matlab were applied. For CTF estimation, GCTF was used and for the phase correction, the IMOD ctfphaseflip was applied (Mastronarde and Held, 2017; Zhang, 2016).

2.4.13 Subtomogram averaging of the S protein

On eight 4-binned tomograms, a total of 4167 S protein densities were manually picked using 3dmod in IMOD. Subsequently, the particle coordinates were scaled for unbinned tomograms and imported to RELION3 (Zivanov *et al.*, 2018). For particle extraction, a box size of 120 px (331.2 Å) was applied. To avoid the dominant impact of the platelet plasma membrane during the averaging process, the membrane densities were suppressed using Pyseg. Due to their higher

density, the individual subtomograms were first aligned with respect to the membrane in RELION3 and then the membranes were identified with a mask. Next, the membranes in each sub-volume were replaced by randomly assigned noise from the background. The initial model for alignment of the membrane-suppressed particles is a 60 Å low-pass filtered SPA structure, which only presents the overall shape of the SARS-CoV-2 S protein. The 3D refinement and classification were used to align the particles and divide them into four classes. Classes exhibiting leftover membrane signal were discarded for further reconstruction. The class with most features was selected, resulting in 976 subtomograms. For the final reconstruction step, a C3 symmetry and mask based on the previous run, were applied. To estimate the final resolution, the particles from the final reconstruction were separated in an odd and even half-set. Two independent reconstructions were computed and the Fourier shell correlation determined at the 0.143 FSC criterion, resulting in a resolution of 13.8 Å.

For the refinement without applied C3 symmetry, the final resolution at the 0.143 FSC criterion was estimated to be 20 Å.

2.4.14 Membrane Curvature analysis

The manually segmented membrane from AMIRA (Thermo Fischer Sceintific) was used as an input to determine the membrane curvature in the Python-based PyCurv software, following the standard workflow. In an initial step, PyCurv converts the segmented membrane into a surface-mesh of triangles. Then, the triangular surface-mesh was translated into a surface graph and for each triangle the normal vectors and local curvature was computed. The membrane curvature of S protein areas was then compared to the ones without.

2.4.15 Analysis of reconstructed S protein in reconstructed tomograms

Nearest neighbour distance analysis. The coordinates from the individual Spike proteins, defined by manual picking, were used to calculate their nearest neighbour distances via the Python3 libraries NumPy and SciPy. The results are depicted as distance distribution histogram in GraphPad PRISM by plotting the closest neighbouring distance for each S protein.

Orientation towards the platelet membrane. The orientation of the Spike protein with respect to the membrane was calculated by measuring the angle between the vector pointing towards the longest axis of S protein and the normal vector of the closest triangle, using the Python3 libraries NumPy and SciPy.

Distance from the platelet membrane. The closest distance between the S protein and platelet plasma membrane was measured by considering the shortest Euclidean distance between the

refined coordinates of the S protein particle to all the triangles on the membrane surface. For the calculation, the Python3 libraries NumPy and SciPy were used.

2.4.16 Actin analysis

282 actin filaments were manually segmented using IMOD. The model files were converted to coordinate files using model2point function in IMOD. Then, each filament was subdivided into 3 nm and 10 nm spaced segments for further analysis. The final data is shown as histogram plots using GraphPad PRISM.

Length distribution. The length of each manually segmented actin filament was estimated by the sum of the individual 3 nm sub-segments per filament, using the Python NumPy and SciPy libraries.

Angular arrangement. The angle of the individual 10 nm actin sub-segments against the longitudinal axis of the platelet protrusion were calculated by determining a reference vector pointing towards the longitudinal platelet axis and subsequently measuring the angle between this vector and each 10 nm actin sub-segment using the Python3 NumPy library.

2.4.17 Tomogram Visualization

Membranes. The membranes of platelets were manually segmented and generated in AMIRA (Thermo Fisher Scientific).

S proteins. A 3D scene was created by the 'Place Object' plug-in in Chimera based on the S protein structure obtained by STA and the coordinates of the assessed particle positions during the extraction. Furthermore, the orientation was applied based on the alignment. The created scene was imported into AMIRA and a surface was generated to visualize the Spike proteins on the membrane of the platelet protrusion.

Actin filaments. The actin filaments were segmented and coloured according to their estimated filament length. The model was then depicted in IMOD.

2.4.18 Single particle analysis of SARS-Cov-2 S protein, data collection and image analysis

Sample Preparation. Carbon-coated Cu200 R1.2/1.3 grids (Quantifoil) were glow-discharged at 20 mA plasma current for 20 s. 3 µl of SARS-CoV-2 S protein (Cube Biotech) at 0.3 mg/ml were applied, blotted for 3.5 s and vitrified in liquid ethane using a Vitrobot MarkVI (Thermo Fisher Scientific) operated at 4°C and 100% humidity.

Data acquisition. The micrographs were acquired on a Glacios (Thermo Fisher Scientific) operated at 200 keV, equipped with a Falcon 4 direct electron detector. The EPU software (Thermo Fisher Scientific) was used for data collection. 3060 movies, divided in 40 frames and a total dose of 49 $e^-/Å^2$, were collected at a pixel size of 0.93 Å and defocus range from -0.8 to -2.4 μm.

Image analysis. For all data processing steps, cryoSPARC v.3.3.172 was used (Punjani *et al.*, 2017). Both pre-processing steps, Motion correction and CTF estimation, were performed in patch mode. An initial set of particles, picked by the blob picking algorithm and subsequently sorted by 2D classification, was used to train a Topaz picking model. The model was optimized over several rounds and resulted in final set of 11,549 particles. Two ab-initio 3D models were generated for the separation of the one-up open and closed Spike protein states by heterogenous refinement. For the closed S protein conformation, 7,618 particles were obtained and further refined with C3 symmetry. The final map of 3.56 Å resolution at the FSC 0.143 criterion was reconstructed by non-uniform refinement with per particle CTF estimation and aberration correction. The 3,931 particles for the one-up Spike protein state were analysed in the same manner, resulting in a final reconstruction at 7.44 Å resolution with the FSC 0.143 criterion.

Visualization. The final maps were sharpened by DeepEMhancer and visualized in ChimeraX (Pettersen et al., 2021; Sanchez-Garcia et al., 2021).

Chapter 3 - Structures of GEN1 in complex with Holliday Junction & 5' flap reveal the basic principle of its coordinated DNA substrate processing

Preface

The following chapter focuses on the importance of the DNA joint molecule resolution for genome maintenance, particularly on the canonical Holliday junction resolvase GEN1. In this study, the structure of dimeric *Ct*GEN1 in complex with its Holliday junction substrate is displayed using cryo-EM SPA. Interestingly, the GEN1-HJ complex exhibits an asymmetric dimer configuration, which is supported with a bridging loop originating from one of the two monomers. Furthermore, the structure of monomeric *Ct*GEN1 bound to a 5' flap substrate is shown. The substrate recognition of different DNA structures and the mechanisms of cleavage will be discussed.

The cryo-EM study on *Ct*GEN1 in complex with the Holliday junction and 5' flap substrate and the subsequent structural characterization were performed under supervision of Christian Biertümpfel and Naoko Mizuno in the laboratory of Structural Cell Biology at the NHLBI, NIH in Bethesda. The protocol for protein purification and initial characterization were established in the master thesis "Functional and Structural Characterisation of Eukaryotic Holliday Junction Resolution and Analysis of Knowledge Transfer Mechanics in Research Institutions" in 2018 at the MPI of Biochemistry and shown for completeness of the project.

Introduction

3.1.1 Homologous recombination in response to DNA double-strand breaks

Organisms from the three branches of life store their genetic information as deoxyribonucleic acids (DNAs), which are based on the sequential pairing of the nucleobases adenine-thymine and guanine-cytosine (Watson and Crick, 1953). These double-stranded nucleotide sequences encode numerous genes, providing the information for biomacromolecules and vital processes. To ensure the correct functioning of fundamental pathways, it is crucial to avoid damages on the DNA. One of the most serious DNA damages are double-strand breaks (DSBs) that can occur from metabolic reactive oxygen species, ionizing radiation, but also during the processing of inter-strand crosslinks and broken replication forks. When the DNA is damaged, it is important to restore nucleotide sequence correctly, as failure of DNA repair lead to major consequences such as genetic diseases or cancer (Scully et al., 2019; Srinivas et al., 2019). DNA double-strand breaks on chromosomes initiate a coordinated DNA damage response to activate cellular pathways responsible for DNA repair and the maintenance of genomic stability. DSBs can be fixed by various pathways including nonhomologous end-joining (NHEJ), single-strand annealing, microhomology mediated end-joining (MMEJ) as well as homologous recombination (HR) (Figure 3-1)(Li and Heyer, 2008; Pannunzio et al., 2018; Sallmyr and Tomkinson, 2018).

HR restores the genetic information after DSBs in an error-free manner in mitotic cells (Kowalczykowski, 2015; San Filippo et al., 2008). Cells preferentially use a sister chromatid as the template to prevent the loss of heterozygosity (LOH) through somatic crossover during HR (Moynahan and Jasin, 2010). Therefore, homologous recombination is solely triggered in the late S phase and G2 phase, where the newly replicated chromosomes are available(Heyer, 2015). Apart from restoring DNA in mitosis, HR also plays an important role in meiosis. Here, it has a critical role during chromosome segregation and introduction of gene diversity by DNA cross-over (Petronczki et al., 2003).

Overall, homologous recombination holds an important role in the preservation of the genomic diversity. While the biochemical background is widely studied, structural information on the process is scarce. Hence, it is of particular interest to gain insight in structural processes underlying HR to further understand the molecular mechanism of DNA restoration.

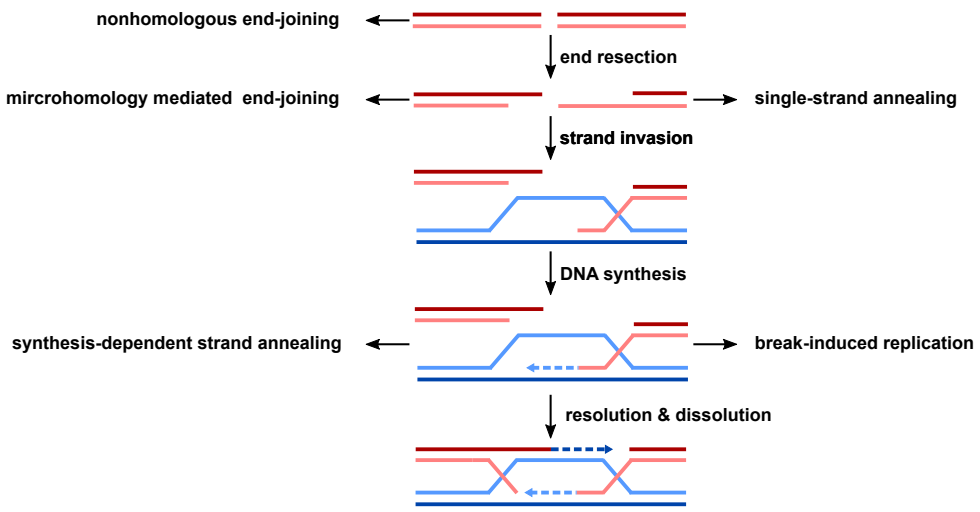

Figure 3.1. Repair pathways after DSBs.

After a DNA double-strand break occurs, different repair pathways can be triggered. Prior resection, NHEJ can connect the blunt ends. Once the DNA is resected in 3'-end direction, single-strand annealing or microhomology mediated end-joining can fix the DSB by pairing flanking homologous repeats. Furthermore, a strand invasion can follow the end resection forming a D-loop structure. Subsequent to DNA synthesis, different repair pathways can be taken, including synthesis-dependent strand annealing and break-induced replication. To restore the DNA by the resolution or dissolution pathway, a second-end capture after D-loop formation is necessary.

3.1.1.1 Mechanism of homologous recombination

During the first step of homologous recombination the DSB ends are nucleolytically resected and 3'-OH single-stranded DNA (ssDNA) overhangs are created (see Figure 3-1). Repair Pathways after DSBs] (Symington, 2014). In humans, this process is initialized by the endonuclease activity of MRE11-RAD50-NBS1 complex (MRN complex, Mre11-Rad50-Xrs2 in budding yeast) and its cofactor CtIP (Sae2 in budding yeast), introducing an incision proximal to the protected DNA ends close to the break site (Anand et al., 2016; Cannavo and Cejka, 2014; Her and Bunting, 2018; Peterson et al., 2011; Symington and Gautier, 2011). The MRN complex creates a short 3' overhang using its 3'-5' exonuclease activity. Next, EXO1 (exonuclease 1) and BLM-DNA2 (Bloom's syndrome helicase; DNA replication ATP-dependent helicase/nuclease 2; in budding yeast Dna2-Sgs1, slow growth suppressor 1) continue the resection in 5'-3' end direction (Mimitou and Symington, 2008; Nimonkar et al., 2011; Wright et al., 2018).

The exposed ssDNA is rapidly coated by the heterotrimeric replication protein A (RPA) (Wold, 1997). The engagement of RPA with single-stranded DNA blocks interactions between ssDNA intermediates and contributes to the unwinding of DNA secondary structures. (Scully *et al.*, 2019). In the next step, the RPA filament has to be replaced by recombinase Rad51 (RAD51 in human)

in order to initiate strand invasion and D-loop formation. Study on yeast homologs showed that due to a higher affinity to ssDNA, RPA hinders the loading of Rad51 and this can be overcome by recombination meditators, such as Rad52 in budding yeast, to enable the loading of Rad51 on the ssDNA (Sung, 1997; Sung et al., 2003). In vertebrates and some fungal species, BRCA2 (breast cancer type 2 susceptibility protein) primarily mediates the RAD51-ssDNA engagement. Apart from binding to ssDNA, BRCA2 exposes several binding sites for RAD51, serving as a nucleation point for Rad51 loading (Davies and Pellegrini, 2007; Pellegrini et al., 2002; Thorslund et al., 2010; Yang et al., 2005). The formation of the RAD51-ssDNA nucleoprotein filament, so called presynaptic filament, requires ATP (adenosine triphosphate) binding to RAD51 (Chi et al., 2006). Upon binding, RAD51 forms a dynamic helical structure on the ssDNA, locking the DNA in an extended state (Ogawa et al., 1993; Yu et al., 2001).

Based on studies on the prokaryotic RAD51-homolog RecA, the nucleoprotein filament is essential for the subsequent homology search, facilitating the invasion of duplex DNA and pairing with the homologous sequences (Bianchi et al., 1983; Wright *et al.*, 2018). Here, the binding to the homologue donor dsDNA leads to the formation of a paranemic joint, in which the three strands in the RAD51-ssDNA-dsDNA complex align side-by-side (Xu et al., 2017). Next, the non-base-paired strand of the invaded duplex DNA in RAD51-ssDNA-dsDNA, also referred as synaptic complex, is displaced and leads to the formation of a displacement loop (D-loop). This process is driven by RAD51-mediated hydrolysis of ATP, thereby reducing its affinity towards the DNA and resulting in the disassembly of the RAD51 filament (Scully *et al.*, 2019; Solinger et al., 2002; Wright *et al.*, 2018). After dissociation of RAD51, DNA polymerases can engage at the 3' end of the invading strand and extend along the D-loop by using the invaded donor strand as template (Li et al., 2009; McVey et al., 2016).

Three major pathways can follow after D-loop formation to restore the genetic information, namely the break-induced replication (BIR), the synthesis-dependent strand annealing (SDSA) and the double Holliday junction (dHJ) (Figure 3-1). During BIR, the invading DNA strand is extended until to the end of the template chromosome. As the non-invading strand of the nascent DNA is never engaged, and therefore possibly results in LOH, it is suggested that BIR is suppressed when DSBs have two ends (Llorente et al., 2008).

Regarding SDSA, the invading strand disengages after synthesis along the template chromosome and reanneals with the second end of the DSB. The D-loop dissolves and the missing genetic information is restored, exclusively leading to non-crossover (NCO) products (Maher et al., 2011).

3.1.1.2 Double Holliday junction mechanism

By contrast, in the third pathway the D-loop engages with the non-invasive DNA strand of the duplex to be repaired. This leads to the formation of a four-way branched DNA structure, named after Robin Holliday who proposed the branchpoint for strand exchange among homologues sequences (Holliday, 1964). After DNA synthesis of the invading DNA strand along its homologous template sequence, it recaptures the original strand and forms another four-way branchpoint, the so called double Holliday junction is created (Mehta and Haber, 2014). The model of the dHJ, based on four-way branched DNA structures initially proposed by Robin Holliday, is a widely accepted mechanism for the DSB repair (Szostak et al., 1983).

In a final step, the joint nucleoprotein complex has to be resolved faithfully to maintain genome integrity. Depending on the orientation of resolution, the cleavage of dHJ can result in non-crossover (NCO) or crossover (CO) outcomes (Bzymek et al., 2010; Sarbajna and West, 2014).

3.1.2 Joint molecule processing in eukaryotes

Holliday junctions and other joint molecules which can arise during HR physically link chromosomes and therefore pose a threat to cells if not dissected accurately prior cell division (Liu and West, 2004). In eukaryotes, the pathways of Holliday junction (HJ) dissolution as well as HJ resolution have been identified to remove the inter-chromosomal linkages subsequent to homologous recombination. To ensure the cellular genomic integrity, both systems are highly regulated and deployed in timely and spatial manner (Bizard and Hickson, 2014; Matos and West, 2014).

3.1.2.1 The Holliday Junction Dissolution pathway

The disentanglement of double Holliday junctions by dissolution is unique to eukaryotic cells (Figure 3.2, left panel). Interestingly, this pathway provides a mechanism to separate the linked dsDNA strands by solely generating NCO products, therefore offering a particularly robust approach to avoid LOH or chromosomal rearrangements during HR (Chaganti et al., 1974). Dissolution is active throughout the cell-cycle and the so called dissolvasome, or BTR complex is the central player in the HJ processing (Bizard and Hickson, 2014). In humans, this complex is composed of the helicase BLM (Bloom syndrome helicase), the topoisomerase IIIα (topo IIIα), a type IA topoisomerase and RMI1/2 (RecQ-mediated instability protein 1 and 2)(Wu et al., 2000; Wu and Hickson, 2003). While the topoisomerase IIIα catalyzes the relaxation and decatenation of the dHJ, the BLM helicase stimulates this process by remodeling the substrate and providing

ssDNA segments (Wu and Hickson, 2002; Yang et al., 2010). Furthermore, the BLM guides the convergent branch migration, possibly by its unwinding and annealing RecQ helicase properties (Karow et al., 2000). In turn, topo IIIα acquires a supportive role during the branch migration process, presumably relaxing the nascent supercoil structures and therefore reducing the topological stress on the DNA (Plank et al., 2006).

For efficient dissolution, RMI1 and RMI2 (RecQ-mediated instability protein 1 and 2) is necessary (Bythell-Douglas and Deans, 2021). The association of RMI1 with BLM and topo IIIα mainly stimulates the affinity of topoisomerase IIIα to the Holliday junction substrate, thus promoting the decatenation step (Bocquet et al., 2014; Yang *et al.*, 2010). In addition, RMI1 contains a C-terminal domain for RMI2 recruitment which completes the BTR (BLM helicase-Topoisomerase IIIα-RMI1-RMI2) complex formation(Bythell-Douglas and Deans, 2021; Wang et al., 2010). Failed interaction between RMI1 and RMI2 can lead to disruption of BLM and topo IIIα and increase sister chromatid exchange (Hoadley et al., 2010). Hence, only the stable assembly of the BTR complex during the HJ dissolution can ensure generation of non-crossover products in HR (Hodson et al., 2022).

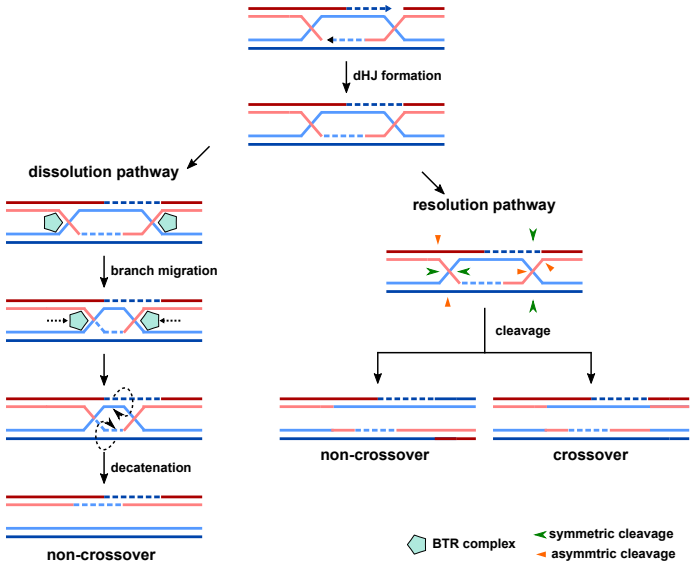

Figure 3.2. The resolution and dissolution pathway to disentangle dHJs.

After formation of the double Holliday Junction, the branched DNA structure has to be resolved thoughtfully. During the dissolution pathway (lower left panel), BTR complexes bind to the four-way junctions and are essential for coordinated branch migration. This step is followed by the decatenation, untangling the dsDNA strands and solely leads to NCO products. Along the resolution pathway (lower right panel), resolvases recognize the two HJs and separate them by a nucleolytic cleavage. While this can occur in an asymmetric (MUS81-EME1; SLX1-SLX4; SLX-MUS) or symmetric manner (GEN1), both cleavage pattern result in NCO and CO products.

3.1.2.2 The Holliday Junction Resolution pathway – A conserved mechanism

By contrast, the Holliday junction resolution is conserved among different branches of life. The enzymatic active nucleases in this pathway are classified as resolvases. Especially the prokaryotic members of this enzyme class including *E. coli* RuvC as well as phage enzymes T4 endonuclease VII, T7 endonuclease I have been studied in detail and a set of common characteristics has been observed (Bennett et al., 1993; Biertumpfel et al., 2007; Hadden et al., 2007). *In vitro*, all representative prokaryotic resolvases show a high affinity to DNA substrates, assemble as stable homodimer and disjoint HJs by introducing symmetric incisions across the junction point (Wyatt and West, 2014). The cleavage reaction yields two nicked duplexes which can be resealed by DNA ligases. In contrast to dHJ dissolution, resolution can create both crossover (CO) and non-crossover (NCO) products depending on the cleavage orientation (Figure 3.2, right panel) (Heyer, 2004).

The Holliday Junction resolution pathway in eukaryotes evolved a more sophisticated regulation mechanism in comparison to its prokaryotic counterpart (Lilley, 2017). In eukaryotes, different sets of enzymes can work on HJs to faithfully resolve the branched DNA structure. Holliday Junction resolution in eukaryotes can be accomplished by the non-canonical resolvases MUS81-EME1 (MMS and UV sensitive protein 81 - essential meiotic endonuclease 1) and SLX1-SLX4 (synthetic lethal of unknown function protein 1 & 4) as well as the canonical resolvase GEN1 (flap endonuclease GEN homolog 1) (Wyatt and West, 2014).

On contrary to solely symmetric and ready to ligate HJ resolution products in prokaryotes, asymmetric cleavage at the branchpoint of four-way junctions can be observed in eukaryotes. The so called non-canonical HJ resolvases including MUS81-EME1 complex and SLX1-SLX4 complex. (Ciccia et al., 2003; Svendsen et al., 2009; Wyatt et al., 2017). Processing by these endonucleases leads to two differing cleavage products, one carrying a flap and the other one bearing a gap. Thus, further processing steps are necessary for the generation of ligatable products and full restoration of the genomic DNA after non-canonical HJ resolution (Wyatt and West, 2014).

MUS81- EME1 is a heterodimeric nuclease, both subunits belong to the ERCC4/XPF family of structure-selective endonucleases. However, only MUS81 contains the conserved GDX_nERKX_3D nucleolytic motif, while EME1 is catalytically inactive (Chang et al., 2008; Ciccia et al., 2008; Ogrunc and Sancar, 2003). Compared to other DNA substrates such as 3'flaps, replication forks and nicked HJs, MUS81-EME1 shows a low efficiency on processing intact Holliday Junctions

(Chen et al., 2001; Dehe and Gaillard, 2017). Even though MUS81-EME1 can introduce asymmetric dual incisions on Holliday junction substrate(Taylor and McGowan, 2008), it has been shown that MUS81-EME1 exists as a heterodimeric complex in solution and further *in vitro* data suggests that it predominately binds on DNA substrate as a single heterodimer(Chang *et al.*, 2008; Schwartz et al., 2012).

Like MUS81-EME1, SLX1-SLX4 forms a stable heterodimer. Apart from Holliday Junctions, SLX1-SLX4 can process several other branched DNA structures such as 5'flaps, 3'flaps and replication forks. Interestingly, HJs are resolved in an uncoordinated fashion by SLX1-SLX4, leading to a pool of symmetrically as well as asymmetrically cleaved products. Therefore, part of the dsDNA products is directly ligatable, while the gapped and flapped products need further processing (Svendsen *et al.*, 2009). In the SLX1-SLX4 heterodimer, the catalytic activity is contributed by the GIY-YIG superfamily of endonuclease member SLX1, whereas SLX4 mediates the substrate specificity and DNA binding via its conserved C-terminal SAP-domain (Dunin-Horkawicz et al., 2006; Munoz et al., 2009). In addition, SLX4 can serve as scaffold for further protein interactions including MUS81-EME1 association (Fekairi et al., 2009).

Interestingly, SLX1-SLX4 and MUS81-EME1 can form a tetrameric SLX-MUS super-complex, which leads to a unique Holliday Junction resolvase with a higher efficiency than either MUS81-EME1 or SLX1-SLX4 (Wyatt et al., 2013). SLX-MUS follows a nick and counter-nick mechanism, in which SLX1 creates the first rate-limiting incision and MUS81 subsequently cleaves the nascent nicked-HJ intermediate. However, the cleavage along the four-way branchpoint leads to a gapped and a flapped product as observed for the heterodimeric subunits (Wyatt *et al.*, 2013).

3.1.3 GEN1 - a eukaryotic canonical Holliday Junction resolvase

3.1.3.1 Structure selectivity is part of the family

The endonuclease GEN1 is a member of the Rad2/XPG nuclease superfamily of structure-selective nucleases (Figure 3.3A). Its members share similar characteristics such as the conserved nuclease core, the Mg^{2+}-dependent catalytic activity and the execution of a unified enzymatic mechanism in several DNA repair pathways (Lee et al., 2015; Nishino et al., 2006; Tomlinson et al., 2010). Each enzyme of the Rad2/XPG nuclease family recognizes specific branched DNA structures, while having little to no specificity to the nucleotide sequence (Grasby et al., 2012). Therefore, each member plays a distinct role in genome maintenance. FEN1 (Flap endonuclease 1) recognizes 5' flaps and double flaps, XPG processes bubble structures and EXO1 has a 5'-3' exonuclease activity (Liu et al., 2004; O'Donovan et al., 1994; Orans et al., 2011). Finally, the double Holliday Junction structures occurring in homologous recombination are resolved by

the fourth member of the Rad2/XPG nuclease family, the Holliday Junction resolvase GEN1 (Ip et al., 2008).

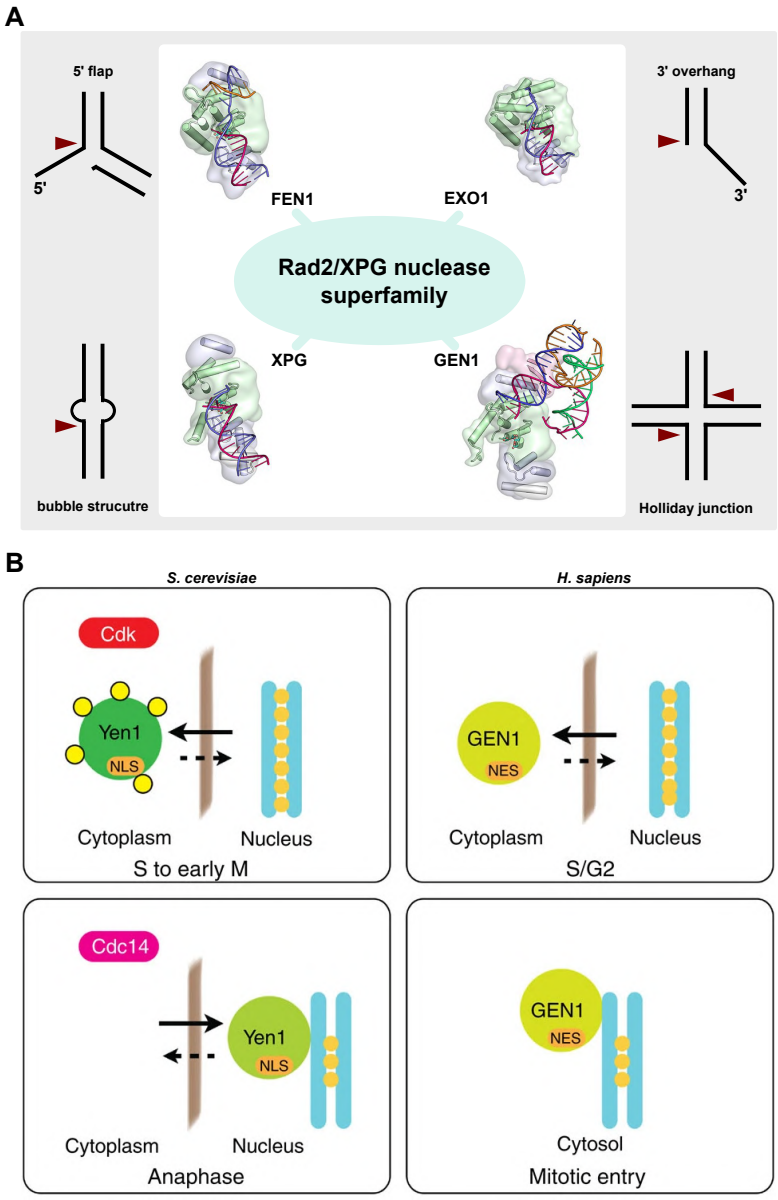

Figure 3.3. GEN1/Yen1 member of the Rad2/XPG family and its regulatory mechanism.

(A) As part of the Rad2/XPG superfamily of structure-selective nucleases, GEN1 recognizes the four-way branched HJ DNA, whereas other members preferably bind to 5' overhang (EXO1), 3' overhang (FEN1) and bubble structures (XPG). Adapted from (Lee *et al.*, 2015). (B) While Yen1 in *S. cerevisiae* enters the nucleus in a phosphorylation-dependent manner, controlled by Cdk & Cdc14 (left panel), HsGEN1 can interact with genomic DNA after break-down of the nuclear envelope during mitotic entry (right panel). Adapted from (Chan and West, 2014).

3.1.3.2 Biological role of the eukaryotic canonical resolvase

As non-crossover products prevent sister chromatid exchange and LOH, somatic cells predominately use the dissolution pathway throughout the cell cycle. Nevertheless, not all branched-DNA intermediates are successfully processed and remain unresolved to later stages of the cell-cycle. Along with the non-canonical HJ resolvase, GEN1 can capture the escaped four-way junctions prior cell division (Dehe and Gaillard, 2017; Wild and Matos, 2016). The studies of GEN1 orthologs among higher eukaryotes, including the rice *Oryza sativa* (*Os*SEND-1), the fungus *Chaetomium thermophilum* (*Ct*GEN1), *Caenorhabditis elegans* (GEN-1), *Drosophila melanogaster* (DmGEN), *Homo sapiens* (*Hs*GEN1) and the brewer's yeast *Saccharomyces cerevisiae* (Yen1), demonstrate the importance of Holliday junction resolvases in genome maintenance (Bailly et al., 2010; Freeman et al., 2014; Furukawa et al., 2003; Ip *et al.*, 2008; Ishikawa et al., 2004). It was observed that both GEN1 in human cells as well as Yen1 in *S. cerevisiae*, are upregulated in the later stage of mitosis, suggesting a role in possible last stage resolution of Holliday junction prior chromosome segregation. Interestingly, the human and yeast homologs use different mechanisms to ensure their timely engagement to the joint DNA molecules. Yen1 is a nuclear protein which is regulated by cell cycle phosphorylation events. On the other hand, GEN1 exhibits a nuclear export signal, that solely makes its access to DNA possible after the nuclear envelope breakdown in prophase (Figure 3.3B) (Blanco et al., 2014; Chan and West, 2014; Garcia-Luis et al., 2014).

3.1.3.3 Holliday Junction resolution and more

Compared to other eukaryotic HJ resolvases, only GEN1 resolves Holliday junctions in a symmetric fashion (Rass et al., 2010). For processing of HJ, a cooperative effort by two GEN1 units is required. While prokaryotic resolvases exist as stable homodimers in solution, GEN1 is predominately monomeric (Chan and West, 2015; Wyatt and West, 2014). Upon recognition of the four-way junction, with a minor sequence preference to double G residues near to a T-rich region, GEN1 assembles as a functional dimer on Holliday junctions (Rass *et al.*, 2010; Shah Punatar et al., 2017). The binding of the first GEN1 subunit occurs in a faster and tighter fashion in relation to the second (Bellendir et al., 2017). Following the dimerization on the Holliday junction, the joint DNA intermediate is sequentially processed in a harmonized nick and counter-nick mechanism (Figure 3.4). After one subunit incises the first cut, at the diametric opposed position a second incision is performed by the other subunit, leading to a symmetric resolution of the HJ (Chan and West, 2015). Both incisions occur within the lifetime of the GEN1-HJ complex, thereafter the two emerging nicked duplexes are enzymatically ligated (Ip *et al.*, 2008; Rass *et al.*, 2010). GEN1 high affinity to nicked HJ substrate suggests that the complex

remains assembled until HJ is fully processed (Sobhy et al., 2019). However, the fundamental mechanism of the two-step Holliday junction cleavage by homodimerically engaged GEN1 remains elusive.

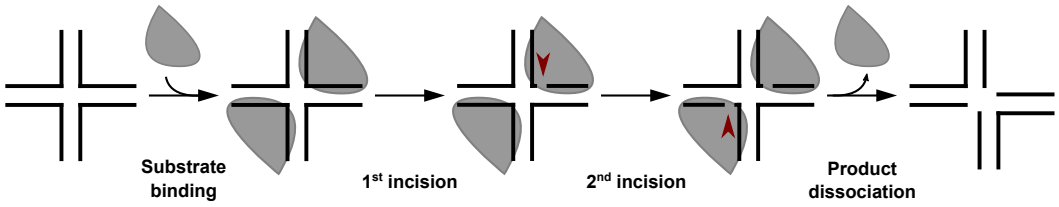

Figure 3.4. Schematic cleavage mechanism of GEN1.

GEN1, in solution a monomer, recognizes and forms a stable homodimer on its HJ substrate. In a sequential nick and counter-nick mechanism, GEN1 catalyzes a 1st and a 2nd incision, to fully resolve the Holliday Junction. Only after the two dsDNA strands are disentangled, GEN1 dissociates from its products.

Besides the cleavage of HJs, the human, *D. melanogaster* and *S. cerevisiae* GEN1 orthologs show 5' flap endonuclease activity, where a single incision is sufficient to cleave the DNA substrate. The broad specificity for different branched DNA structures implies a role in the remodeling of replication fork (Ip *et al.*, 2008; Kanai et al., 2007; Olmezer et al., 2016).

3.1.3.4 Structural insight of monomeric GEN1

The enzymatic characteristics of GEN1 originate from the conserved N-terminal Rad2/XPG nuclease core, organized in three defined domains (Figure 3.5A). The nuclease core is composed of a XPG N-terminal domain, followed by the XPG internal domain and 5'-3' exonuclease C-terminal domain including a DNA-binding helix-hairpin-helix motif. The nuclease core is followed by a chromodomain, shown to be critical for accurate recognition and cleavage of DNA substrates. The carboxy-terminal region of GEN1 is predicted to be disordered and diverse among different species (Ip *et al.*, 2008; Lee *et al.*, 2015). Crystal structures of the human GEN1 non-specifically bound to HJ and the ortholog from thermophilic yeast *C. thermophilum* in complex with a cleavage product unveiled the structural arrangement of conserved nucleolytic core, revealing the similar architecture to other Rad2/XPG nucleases (Figure 3.5B-C). The positively charged electrostatic surface highlights two DNA-binding interfaces on the nuclease core, which are separated by a hydrophobic wedge. Such arrangement facilitates the engagement with two DNA arms from the branched junction substrate (Lee *et al.*, 2015; Liu et al., 2015). In addition, a helical arch is located next to the hydrophobic wedge. Biochemical results suggest that the arch

plays an important role in substrate discrimination (Lee *et al.*, 2015). Moreover, the crystal structure of *Hs*GEN1 reveals the chromodomain, which is unique among the Rad2/XPG family and is essential for efficient Holliday junction binding and cleavage. In the human structure, the chromodomain has direct contact with DNA. However, its mechanism and the arrangement with substrates is still ambiguous, as the crystallized complex is not functionally active. Interestingly, the crystal packing of the *Ct*GEN1 in complex with the nicked dsDNA product exhibits a coaxial alignment along the arms of the uncleaved DNA helices suggesting a symmetric dimer conformation. However, the missing electron density at the DNA junction point in the crystal structure leaves open questions about the functional GEN1-HJ complex arrangement (Figure 3.5D) (Liu *et al.*, 2015).

In conclusion, the information gained by crystallographic analysis of monomeric GEN1-DNA complexes revealed the overall structural features of GEN1. However, the molecular mechanism of GEN1 dimerization remains enigmatic and the underlying molecular regulation of the two-phased HJ cleavage, resulting in symmetric resolution, is still unclear.

3.1.4 Thermophilic GEN1 is a promising target to study eukaryotic Holliday junction resolution

In the past decades, cellular and biochemical studies on GEN1/Yen1 revealed their resolution activity on four-way branched recombination intermediate. Unlike other eukaryotic resolvases, GEN1 processes Holliday junctions in a symmetric manner, similarly to its prokaryotic analogs. Structural studies on *Hs*GEN1 and *Ct*GEN1 further show the similarity of domain arrangement among these orthologs. In contrast to *Hs*GEN1, *Ct*GEN1 exhibits higher stability in *in vitro* studies. Even though *Ct*GEN1 misses a 5' endonuclease activity on flaps, a property shared with eukaryotic orthologs, the HJ resolvase from the thermophilic fungus *Chaetomium thermophilum* is a promising candidate for structural studies on eukaryotic Holliday Junction resolution.

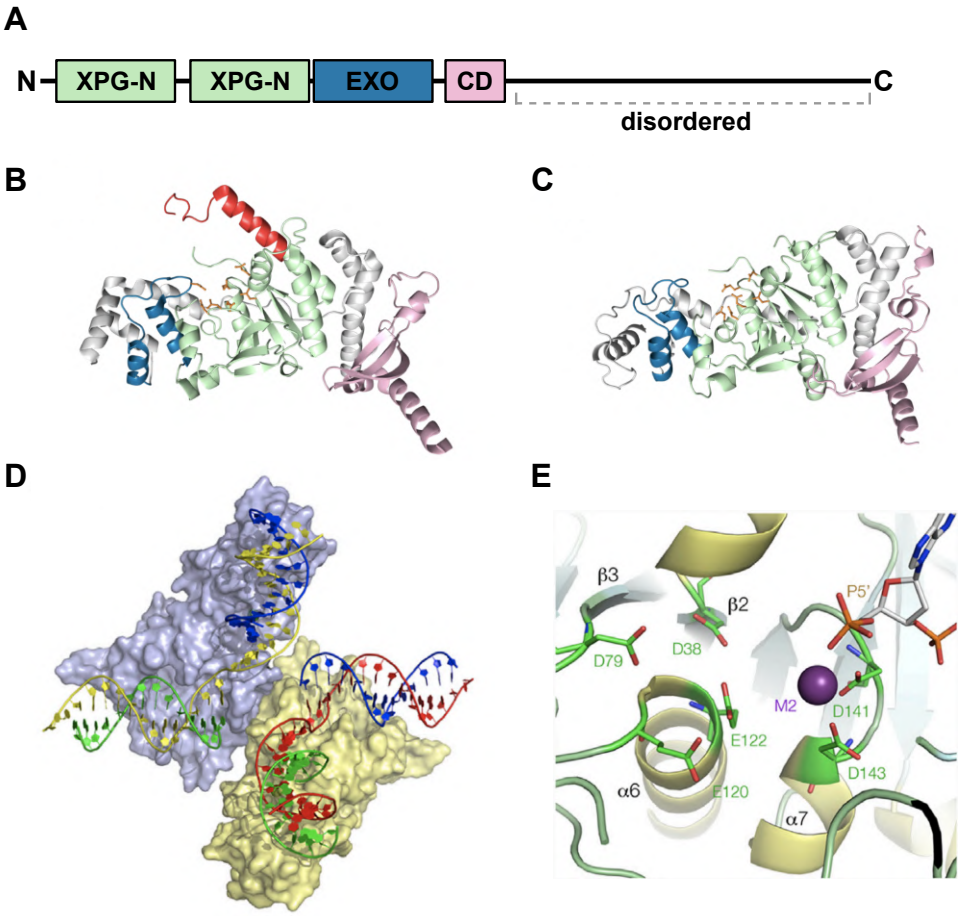

Figure 3.5. Structural information of GEN1.

(A) Domain architecture of the canonical resolvase GEN1. The N-terminal conserved Rad2/XPG nuclease core of GEN1 comprises an XPG N-terminal (XPG-N), XPG internal (XPG-I) and an 5'-3' exonuclease (EXO) domain followed by the chromodomain (CD). C-terminally, GEN1 is diverse among species and predicted to be disordered. (B) Crystal structures of *Hs*GEN1 [PDB: 5T9J] & (C) *Ct*GEN1 [PDB: 5CO8]. The domains are colored according to (A): green: XPG-N and XPG-I; blue: EXO; pink: CD. The additional arch in the *Hs*GEN1 structure, highlighted in red, is part of the XPG domain and important for proper recognition of DNA substrates (Lee *et al.*, 2015; Liu *et al.*, 2015). (D) *Ct*GEN1 monomers, bound to their DNA-product, showed a symmetric dimer appearance based on the packaging of the crystal structure. Adapted from (Liu *et al.*, 2015). (E) Coordination of Mg^{2+} at the active site in *Ct*GEN1. Adapted from (Liu *et al.*, 2015).

3.1.5 Aim of the project

The second study presented in this thesis focuses on the eukaryotic Holliday junction resolvase GEN1, which cleaves branched four-way junctions, thereby ensuring genome integrity. GEN1 follows a sequential process of dimerization on the Holliday junction substrate and subsequent cleavage by a nick counter-nick mechanism of the branched DNA substrate. Despite the available biochemical information, GEN1 dimeric assembly on the Holliday junction is still unknown. Furthermore, elucidating how the protein arrangement enables the sequential catalytic process is crucial, but remains an open question due to lack of structural information of the full complex.

The aim of this project focuses on substrates recognition of GEN1, and explored the structural properties underlying sequential processing of Holliday junction. Biochemical and structural studies on the GEN1-substrates complexes were conducted. Previous studies have shown that human GEN1 is a challenging target for structural analysis. Therefore, the homolog from the thermophilic yeast *Chaetomium thermophilum* (*Ct*GEN1) was used in this study. Apart from its high protein stability, *Ct*GEN1 has high sequence analogy to the human homolog, and the two proteins share similar structural features. The structural insight from *Ct*GEN1 and its substrates will provide valuable information on joint molecules processing in eukaryotes.

Results

3.2.1 Purification of *C. thermophilum* GEN1$^{1-515}$

For functional and structural studies on the catalytic core of *C. thermophilum* GEN1 (*Ct*GEN1$^{1-515}$), different variants were overexpressed in *E. coli* BL21(DE3) gold cells. The protein solubility was enhanced by a C-terminally attached self-cleaving cysteine protease domain (CPD) from *Vibrio cholerae* MARTX, followed by an octa-histidine tag for affinity purification (Shen et al., 2009). The different variants were expressed and purified using the analogous procedures, which is described below using the wild type as an example. The expression of recombinant protein was monitored by SDS-PAGE of the bacterial lysate. After over expression, a pronounced band around 80 kDa was detected (Figure 3.6A 'Lysate') which corresponds to the 81.2 kDa *Ct*GEN1$^{1-515}$-CPD-His$_8$ fusion protein.

The *Ct*GEN1$^{1-515}$ construct was purified to homogeneity with three chromatographic steps. First, the purity was largely improved by a Ni-affinity purification, which removes most of the endogenous *E. coli* proteins (Figure 3.6A 'Elution'). After Ni-affinity purification, the self-cleaving CPD activity was induced by addition of its ligand inositol hexaphosphate (IP_6) in order to remove the solubility tag. After self-processing of CPD, two dominant bands appeared on the SDS-PAGE at around 60 kDa and 24 kDa, which corresponding to the *Ct*GEN1$^{1-515}$ (57.2 kDa) and the cleaved CPD-His$_8$ tag (24 kDa), respectively (Figure 3.6A 'Load'). In the second step, ion exchange was used to separate *Ct*GEN1$^{1-515}$ from the cleaved CPD tag and the uncleaved GEN1. The sample was diluted to salt concentration of 150 mM and loaded on a sulfopropyl-sepharose (SP) cation exchange column. Due to its low isoelectric point (pI= 6.30), the CPD-His$_8$ tag does not absorb to the column and GEN1 can be eluted from the column by a KCl gradient. The UV_{280nm} absorption peak is at the conductivity range from 17 to 35 mS/cm, and the corresponding fractions were examined by SDS-PAGE (Figure 3.6B). The fractions with good purity of *Ct*GEN1$^{1-515}$ and no residual CPD-His$_8$ tag were pooled and subsequently concentrated for further purification.

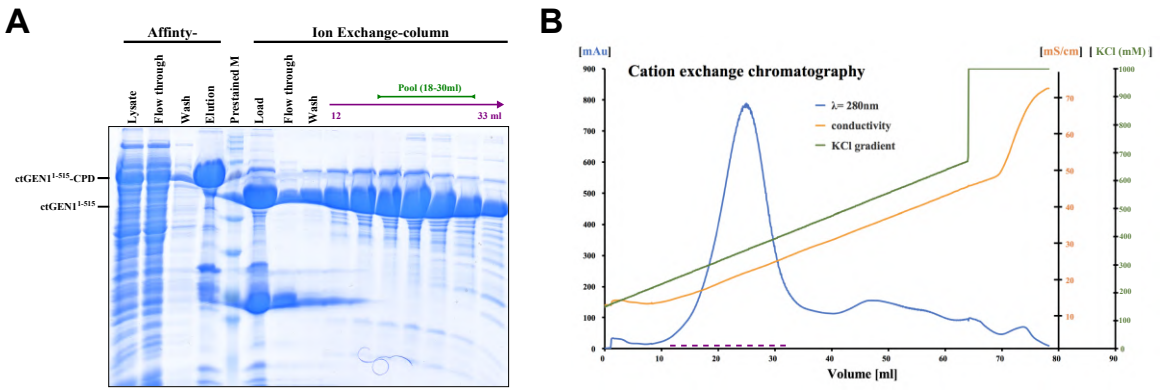

Figure 3.6. Purification of *Ct*GEN1$^{1\text{-}515}$ by Ni-affinity and ion exchange chromatography.

(A) The SDS gel displays sample purity after the Ni-affinity and ion exchange chromatography purification steps. The CPD-His$_8$-*Ct*GEN1$^{1\text{-}515}$ construct has a molecular weight of 81.2 kDa and after removing the CPD-His$_8$ tag by self-cleavage of CPD, the protein size reduced to 57.2 kDa. The cleaved CPD-His$_8$ tag has a size of 24 kDa. (B) SP column chromatogram of *Ct*GEN1$^{1\text{-}515}$ purification. An UV$_{280nm}$ absorption peak was detected at the conductivity range from 17 to 35 mS/cm. Fractions of this peak, indicated in dash purple line, were examined by SDS-PAGE and Coomassie staining in (A).

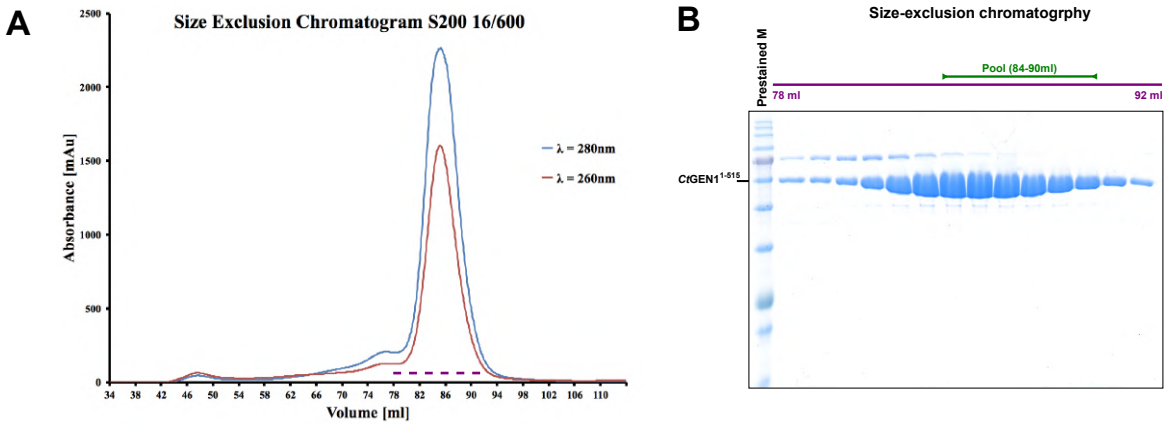

Figure 3.7. Size-exclusion chromatography of *Ct*GEN1$^{1\text{-}515}$.

(A) Chromatogram from a S200 16/600 column. The uniform UV$_{260nm/280nm}$ absorbance peak from 80 ml to 92 ml indicates the elution of *Ct*GEN1$^{1\text{-}515}$. The dashed line in purple indicates the retention volume of the fractions analysed by SDS-PAGE. (B) SDS-PAGE gel displaying the peak fractions of the S200 16/600 column run, indicated in dash purple line. Peak fractions from 84 to 90 ml were pooled for further analysis.

The last step of purification is size exclusion chromatography (SEC). The concentrated SP-column pool was loaded on a Superdex 200 16/600 column to separate the untagged *Ct*GEN1$^{1\text{-}515}$ from other impurities. The elution fractions for the UV absorption peak at 280 nm and 260 nm were inspected by SDS-PAGE (Figure 3.7A). The fractions with pure *Ct*GEN1$^{1\text{-}515}$ were collected and

concentrated for storage (Figure 3.7B). The recombinant protein purity was further checked by electrospray ionization time of flight (ESI-TOF) mass spectrometry. The main peak at a total mass of 57,116.81 Da corresponds to *Ct*GEN1$^{2\text{-}515}$ (theoretical mass of 57,116.19 Da, where the N-terminal methionine was processed by the bacterial methionyl aminopeptidase) with an additional leucine which from the C-terminal CPD-cleavage site (Figure 3.8). The minor peak at a mass of 57,229.97 Da might describe a protein species with three bound K^+ ions.

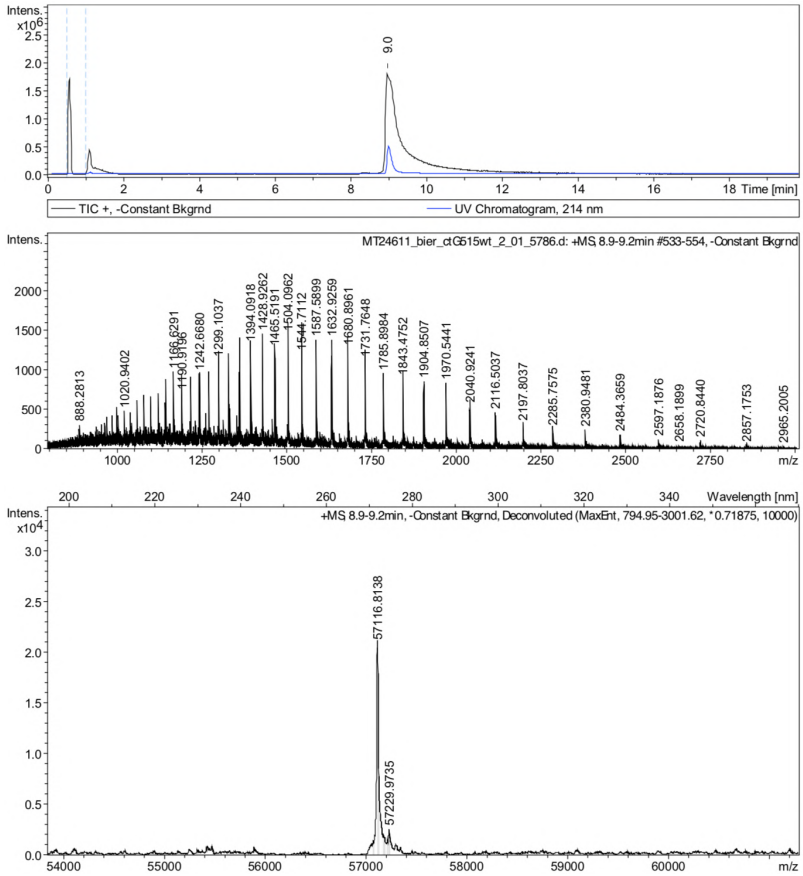

Figure 3.8. ESI-TOF mass spectrum of purified ctGEN1$^{1\text{-}515}$.

The peak at 57,116.81 Da corresponds to *Ct*GEN1$^{2\text{-}515}$ (theoretical Mw = 57,116.19 Da) with an additional C-terminal leucine from the CPD-cleavage site.

3.2.3 *Ct*GEN1$^{1\text{-}515}$ recognizes Holliday junction and 5' flap structures

For testing the properties of the *Ct*GEN1$^{1\text{-}515}$ Holliday junction binding, a wide range of protein concentrations were incubated with 80 nM fluorescently labelled HJ and investigated by electrophoretic mobility shift assays (EMSA). To avoid the nucleolytic cleavage of the HJ by GEN1, Mg^{2+} ions were omitted and possible residual traces were chelated with EDTA.

At 64 nM wild type *Ct*GEN1$^{1\text{-}515}$ concentration, two faint bands appear above the substrate band (Figure 3.9A, upper panel). While the lower band indicates monomerically bound *Ct*GEN1$^{1\text{-}515}$, the upper band describes the fully formed complex. With increasing concentrations, the HJ-dimer

band increases in intensity, while the intensity for the sole substrate band decreases. At 512 nM, additional bands appear above the dimer. Most likely these result from higher order complexes caused by non-specific interactions with the DNA substrate. Interestingly, the inactive variant *Ct*GEN1$^{1\text{-}515\ D143K}$ shows an increased affinity towards the Holliday junction. Already at 16 nM protein concentration band shifts are observed and at 256 nM protein concentration the only the dimer-HJ band is visible on the gel (Figure 3.9B, upper panel).

Besides Holliday junction binding, the 5' flap structure interaction was also investigated by EMSAs. In contrary to the Holliday junction binding, both constructs, the wild type and the D143K mutant, show a similar affinity to the 5' flap substrate (Figure 3.9A-B, lower panels). A single band shift of the substrate starts from 32 nM protein concentration. At 128 nM, a dominant single band is observed, indicating *Ct*GEN1's monomeric processing of 5' flap DNA. Also here, higher order complexes are present at high protein concentration.

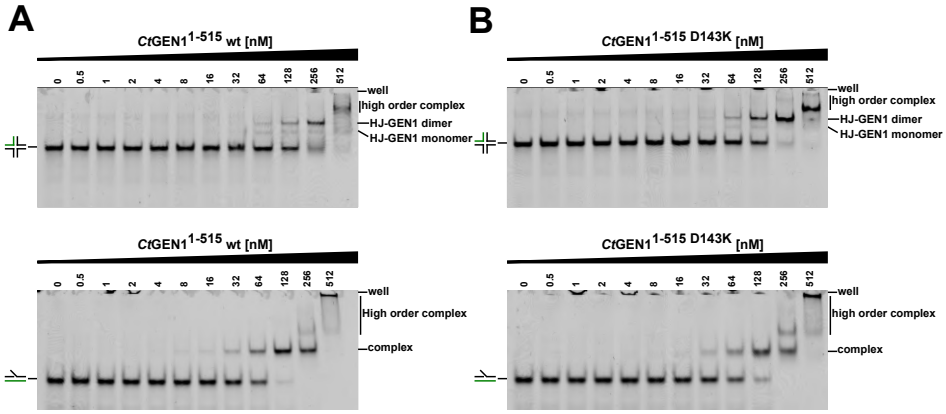

Figure 3.9. EMSA of the *Ct*GEN1 constructs on 5' flap and Holliday junction.

Recombinant *Ct*GEN1 constructs, from a protein concentration of 0.5 nM to 512 nM, were titrated to 80 nM 6FAM-labelled substrate DNA (highlighted in green in the scheme). (A) The Binding profile of *Ct*GEN1$^{1\text{-}515}$ wild type/D143K mutant to Holliday junction. The two bands describe the monomeric and dimeric bound species. Higher order band shifts observed at high protein concentration, suggesting non-specific multiple bindings can occur. (B) The Binding profile of *Ct*GEN1$^{1\text{-}515}$ wild type/D143K mutant to 5' flap substrate. A single defined band shift appears for the *Ct*GEN1-5' flap complex. Non-specific multiple bindings at high concentrations correspond to the higher order band shifts.

3.2.2 *Ct*GEN1$^{1\text{-}515}$ processes Holliday junctions and exhibits a weak 5' flap endonuclease activity

To confirm the resolvase activity of *Ct*GEN1$^{1\text{-}515}$ on its Holliday junction substrate, different concentrations of the purified protein were incubated with fluorescently labelled HJ. The processed DNA products were separated and analysed by a native acrylamide gel. *Ct*GEN1$^{1\text{-}515}$

exposes a robust HJ resolution activity from 32 nM concentration (Figure 3.10A, upper panel). The complete resolution of Holliday junction is accomplished at a concentration of 128 nM *Ct*GEN1$^{1-515}$. The resolvase activity is similar to the *Ct*GEN1$^{1-487}$ construct in a previous study (Freeman *et al.*, 2014).

The 5' flap cleavage activity of *Ct*GEN1$^{1-487}$ was not observed in the previous studies. However, this activity has been detected in GEN1 homologs from in human, fruit fly and budding yeast (AlMalki et al., 2016; Ip *et al.*, 2008; Kanai *et al.*, 2007). Based on these observations from other organisms, recombinant *Ct*GEN1$^{1-515}$ was further tested for enzymatic activity on the 5' flap DNA structure. In contrast to previous studies, the recombinant *Ct*GEN1$^{1-515}$ showed a nucleolytic activity on the 5'flap substrate (Figure 3.10A, lower panel). Though, comparing to the HJ substrate, the processing of 5'flap DNA is relatively low and only fully cleaved at 512 nM resolvase concentration. In comparison to metazoan *Dm*GEN and *Hs*GEN1, *Ct*GEN1 exhibits an significantly lower substrate processing (Bellendir *et al.*, 2017; Lee *et al.*, 2015).

In summary, *Ct*GEN1$^{1-515}$ shows complete resolution of the Holliday junction from 128 nM, in an enzyme-substrate ratio of 3.2. For the 5' flap substrate, a protein concentration of 512 nM is needed, corresponding to a ratio of 12.8, for fully processing. Moreover, the HJ substrate requires two GEN1 monomers for successful processing, while the 5' flap substrate can be cleaved by a single GEN1 subunit. Therefore, these results indicate the high enzymatic specificity of *Ct*GEN1 toward Holliday junctions, while 5' flap structures are only cleaved at high enzyme-substrate ratios. By sequence alignment with nucleases from the same protein family, the active site of *Ct*GEN1 was predicted (Freeman *et al.*, 2014). Based on the results, the variant with the D143K mutation was generated. Here, the lysine residue occupies the coordination site of the Mg^{2+} ion, thereby abolishing the two-metal ion mechanism (AlMalki *et al.*, 2016). For both tested substrates, HJ and 5' flap, no nuclease activity was detected when *Ct*GEN1$^{1-515\ D143K}$ was used, therefore implying the critical role of the aspartic acid residue at position 143 (Figure 3.10B). Importantly, the D143K mutant shows higher affinity to HJ substrate. Therefore, this construct is used for further structural study.

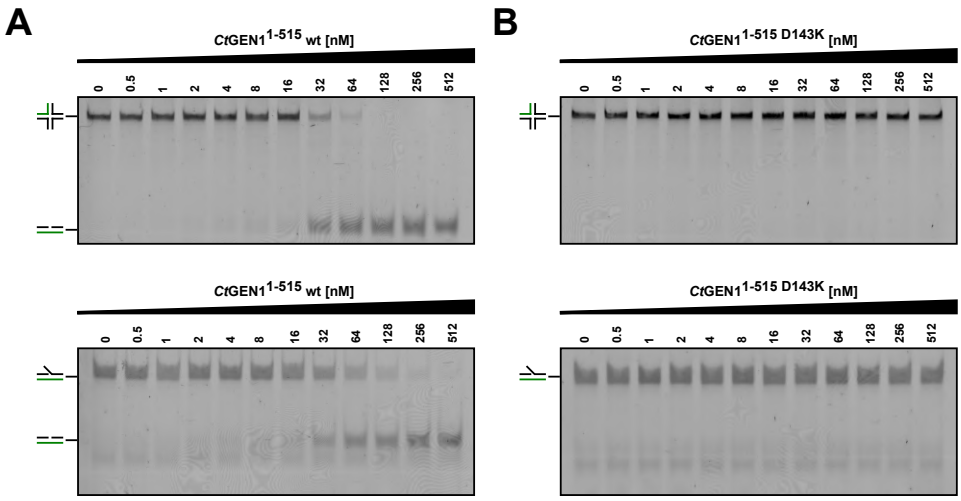

Figure 3.10. Nuclease Activity of *Ct*GEN1$^{1\text{-}515}$ wild type and the D143K mutation for different substrates.
To test the activity of GEN1, 40 nM DNA substrates were treated with active or inactive *Ct*GEN1 in a range of 0.5 to 512 nM. The reactions were separated on a native gel. For the visualization, one DNA strand was labelled with 6FAM (highlighted in green in the scheme) and was detected by $UV_{Ex/Em}$ at l473 nm/l520 nm. (A) Wild type *Ct*GEN1$^{1\text{-}515}$ shows nucleolytic activity for Holliday junction and 5'flap substrate. GEN1 shows better activity toward Holliday junction..(B) The catalytic inactive *Ct*GEN1$^{1\text{-}515\ D143K}$ mutant shows no enzymatic activity to both substrates.

3.2.4 Reconstitution of *Ct*GEN1$^{1\text{-}515\ D143K}$-HJ complex in size exclusion chromatography

The complex formation of the inactive *Ct*GEN1$^{1\text{-}515\ D143K}$ variant with its Holliday junction substrate was initially tested by SEC. The chromatograms of protein alone and the protein-DNA complex were compared. At 60 mM KCl salt concentration, purified *Ct*GEN1$^{1\text{-}515\ D143K}$ mainly elutes at a retention volume of 14.1 ml on a Superdex S200 10/300 column (Figure 3.11A). The complex was reconstituted by mixing GEN1 and Holliday junction at a molar ratio of 2:1. After size exclusion, the chromatogram of the *Ct*GEN1$^{1\text{-}515\ D143K}$-HJ complex shows a retention volume of 12.1 ml (Figure 3.11B). This shift towards a smaller retention volume indicates the formation of the larger *Ct*GEN1-HJ complex.

It is notable that in the *Ct*GEN1$^{1\text{-}515\ D143K}$ alone sample a minor peak was observed at a smaller retention volume. This might be a mixture of solely GEN1 dimer and GEN1 dimerically bound to endogenous DNA, also indicated by the $UV_{280nm/260nm}$ absorption ratio.

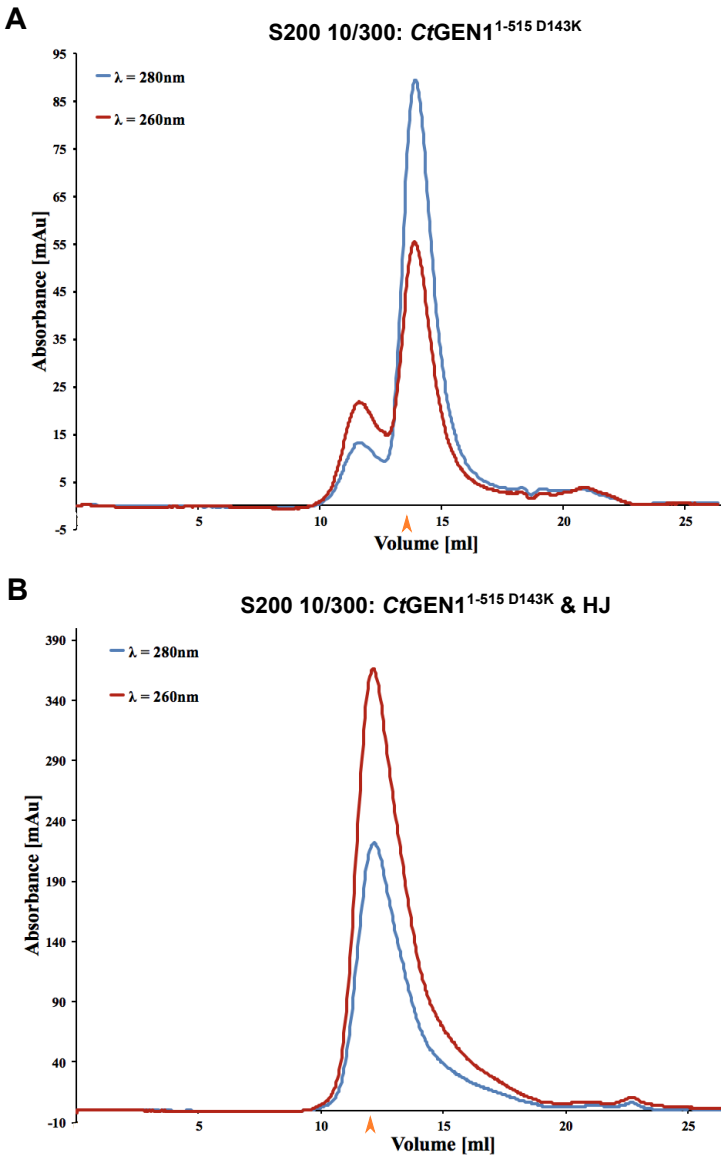

Figure 3.11. *Ct*GEN1-HJ complex reconstitution.

*Ct*GEN1$^{1\text{-}515\ D143K}$ and Holliday junction were mixed at molar ratio 2:1 and loaded onto a pre-equilibrated S200 10/300 size exclusion column. The protein sample without DNA is elutes at 14.1 ml, while the *Ct*GEN1-HJ complex has a retention volume of 12.1 ml, indicating the protein and DNA form a larger complex in solution. The orange arrow heads marl the main peaks.

3.2.5 Initial cryo-EM analysis reveals monomeric and dimeric *Ct*GEN1$^{1\text{-}515\ D143K}$ bound on Holliday junction

To better understand the substrate recognition of GEN1, single-particle cryo-EM was used to analyse the protein-DNA interaction. To reconstitute the complex, *Ct*GEN1$^{1\text{-}515\ D143K}$ was mixed with synthetic Holliday junction DNA and purified by size exclusion chromatography (SEC). The SEC profile displays a main peak, overlapping with a smaller peak at slightly slower retention

volume. The highlighted fraction, at a retention volume of 11.5 ml, was used for cryo-EM sample preparation. Mainly GEN1-HJ species from the large peak of faster retention volume is expected in this fraction. (Figure 3.12A).

Particles on the micrographs were picked using *Gautomatch* (Figure 3.12B-C) (developed by Dr Kai Zhang, MRC Laboratory of Molecular Biology, Cambridge, UK, http://www.mrc-lmb.cam.ac.uk/kzhang/Gautomatch/). The initial 2D average of particles reveal high quality of images. Interestingly, two types of arrangement can be identified. The first and predominant type of classes show a 'butterfly-shaped' protein-DNA complex, represent the dimeric GEN1 binding on a Holliday junction. In the second type of classes, a 'helicopter-shaped' arrangement showing a monomeric GEN1 binding on the Holliday junction. (Figure 3.12D).

To further characterize the structures, particles were selected according to their type of arrangement. The particles exhibiting the 'helicopter-shape' were selected and 2D classification was applied to remove particles of different appearance (see Figure 3.13A). The subsequent 3D classification revealed a shape resembling single bound *Ct*GEN1$^{1\text{-}515\ D143K}$ to Holliday junction, with the two arms captured by a single GEN1 molecule. The two unbound arms are rather flexible, their conformations are variable. Refinement of the complex lead to a map with an estimated resolution of 11 Å. The segmentation of the obtained map visualizes the four-way DNA substrate bound by a single unit of *Ct*GEN1$^{1\text{-}515\ D143K}$ (Figure 3.13B).

In a separate approach, the 'butterfly-shaped' 2D averages were pooled and further classified (see Figure 3.14A). 3D classification and subsequent refinement of the optimized set of particles resulted in the dimeric *Ct*GEN1$^{1\text{-}515\ D143K}$-HJ complex. The final resolution of the reconstruction was estimated at 7.52 Å for the FSC at 0.143. The segmentation of the final Coulomb map shows that the four arms of the HJ are bound by two GEN1 subunits (Figure 3.14B). At this resolution it is possible to follow the secondary structure elements by rigid body fitting, though essential information about the dimer interface were not visible.

A major challenge for obtaining high-resolution structures from this dataset is that the particles are suffering from serious preferred orientations (Figure 3.14C). The lack of information from the missing views hampers the 3D reconstruction.

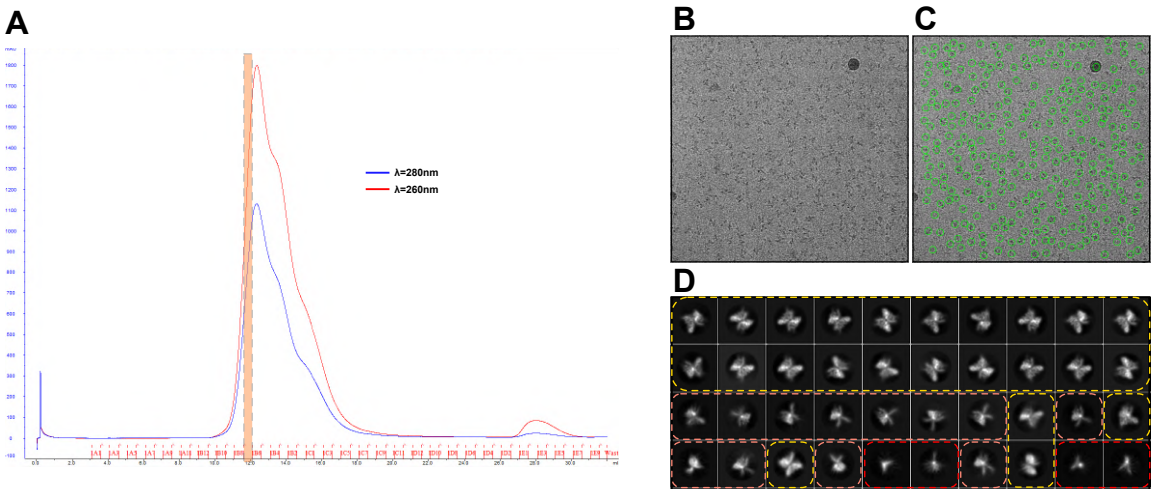

Figure 3.12. Cryo-EM sample preparation and initial processing.

(A) SEC chromatogram of *Ct*GEN1$^{1\text{-}515\ D143K}$-HJ complex on S200 10/300 column. The orange box indicates the retention volume of the peak fraction used for sample preparation. (B) Example micrograph of cryo-EM. (C) Particles detected by *Gautomatch* are circled in green. (D) Example of 2D classificaiton after preliminary processing. Classes surrounded by the yellow-dashed line indicate the "butterfly-shaped" dimer, and in orange the "helicoper-shaped" monomer and in red indicates HJ without protein bound.

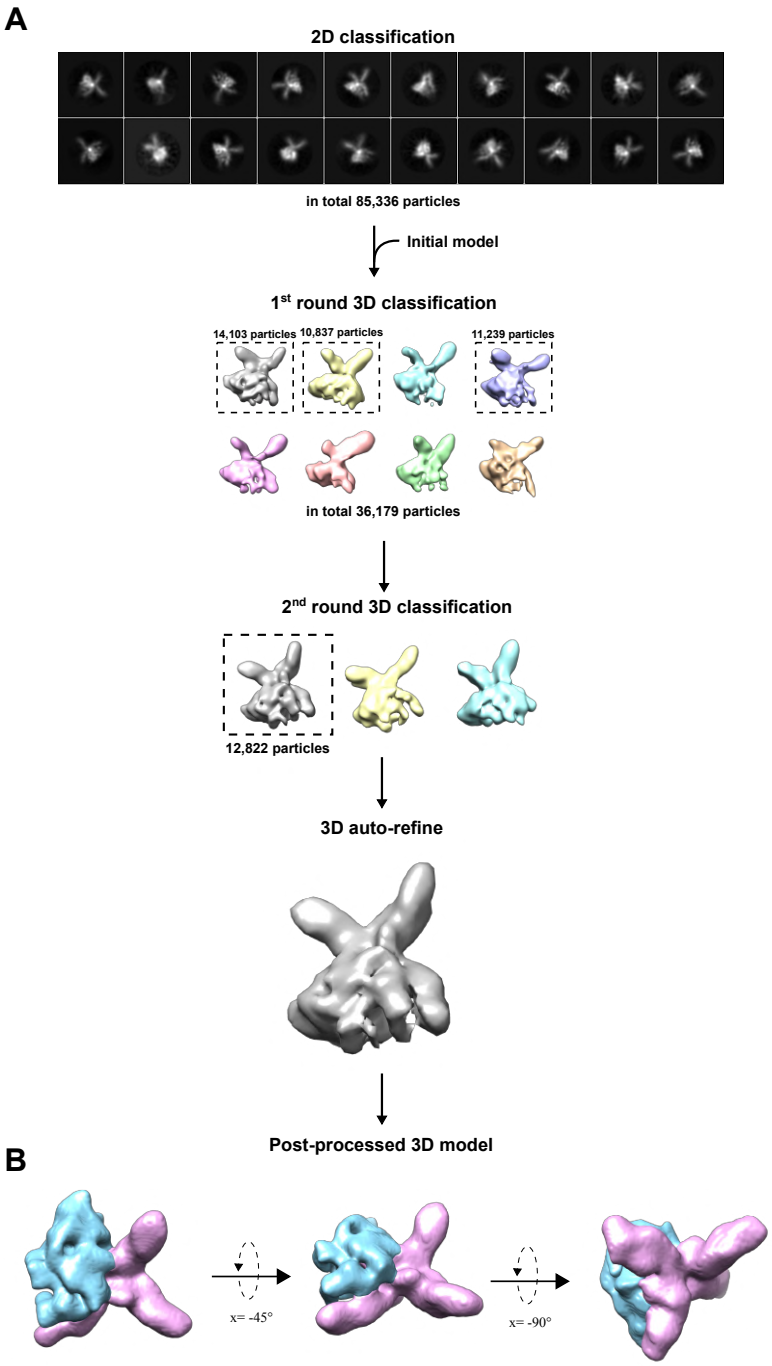

Figure 3.13. Cryo-EM data processing-pipeline for the monomeric *Ct*GEN1$^{1\text{-}515\ D143K}$-HJ complex.

(A) Represent 2D classes of monomeric *Ct*GEN1 bound to HJ. After an initial round of 3D classification, three classes highlighted with the dashed line were further classified. One class was selected for 3D refinement and further post-processed. (B) Segmented post-processed reconstruction of monomeric *Ct*GEN1$^{1\text{-}515\ D143K}$-HJ complex. The HJ is in pink and *Ct*GEN1 is coloured in blue.

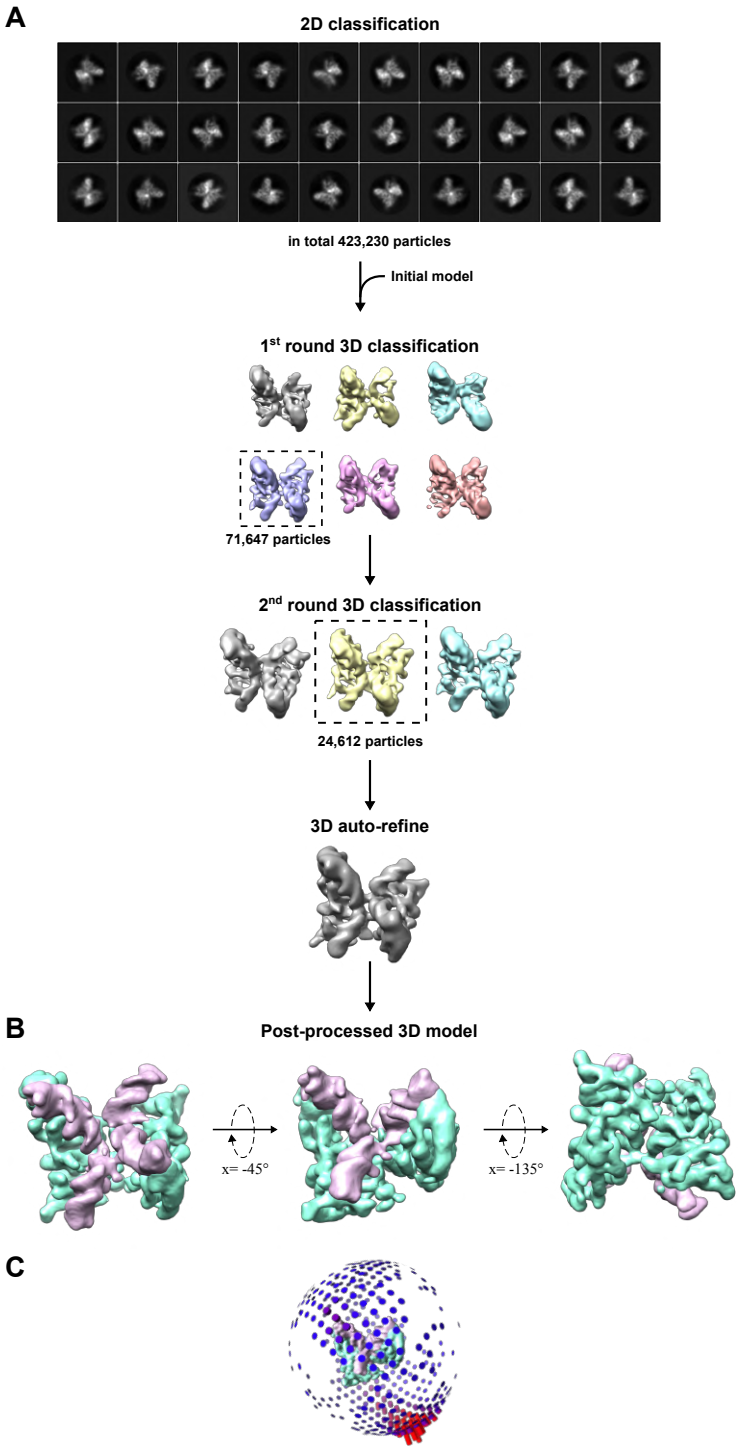

Figure 3.14. *Ct*GEN1$^{1\text{-}515\ D143K}$-HJ dimer processing pipeline from the initial dataset.

(A) The 2D averages represent the projections observed during classification of dimer particles. After two rounds of 3D classification a final set of particles was obtained which subsequently was refined and post-processed. (B) Reconstruction of *Ct*GEN1$^{1\text{-}515\ D143K}$-HJ dimer obtained from the initial dataset. The HJ is coloured in pink, and the GEN1 subunits in turquoise. (C) Angular distribution of the particles used for final reconstruction shown in (B). The red indicates a preferred orientation comprising views from the protein site of the complex. The side views, which are neither from the protein direction nor the HJ direction, are limited for the reconstruction of the final map.

3.2.6 Improved specimen revealed detailed map of dimeric *Ct*GEN1$^{1\text{-}515\ D143K}$ on HJ

To obtain the structure with better resolution, sample quality was improved and new datasets were collected. The sample preparation was using the homogeneous protein-DNA complex reconstituted as a single peak from size exclusion column (Figure 3.15).

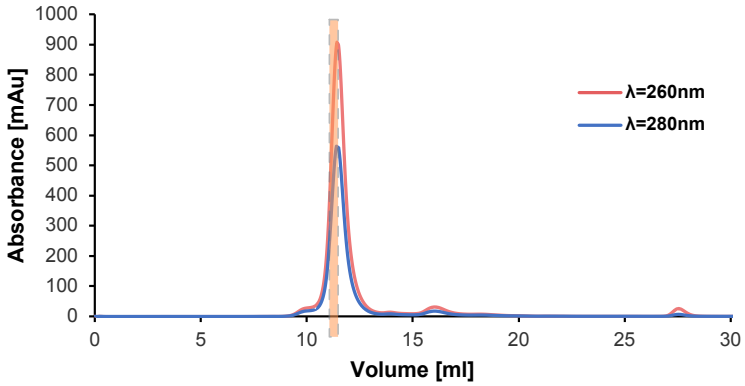

Figure 3.15. *Ct*GEN1$^{1\text{-}515\ D143K}$-HJ complex reconstitution for cryo-EM on the optimized dataset.
The re-estimation of the protein concentration, the *Ct*GEN1 and HJ were mixed in a molar ratio of 2:1. The sample was run on a S200 10/300 increase column and eluted as a single peak. The orange box indicates the elution fraction used for cryo-EM sample preparation.

Under cryo-EM conditions, the micrograph revealed a dense distribution of particles homogenously in shape and size. In addition to the standard data acquisition, another dataset was acquired at a 30° tilting angle to overcome the previously observed preferred orientations of the dimer (see Figure 3.16). During initial steps of the computational analysis, the micrographs collected with and without tilting were processed independently. Manual picked particles were classified and the best particles were used in an iterative process to train a TOPAZ picking model (Bepler *et al.*, 2019). The robust TOPAZ models were used to pick particles from the entire datasets. The 2D classifications show the well-defined 'butterfly-shape' of the dimer. In addition to 2D views not observed from the initial dataset, a more uniform distribution of particles into different classes is obtained. Subsequently, the tilted and untilted datasets were combined and a homogeneously aligned set of particles was obtained by two rounds of heterogeneous refinement. The final set of particles was CTF and non-uniformly refined and reached an estimated resolution of 3.52 Å at a FSC of 0.143.

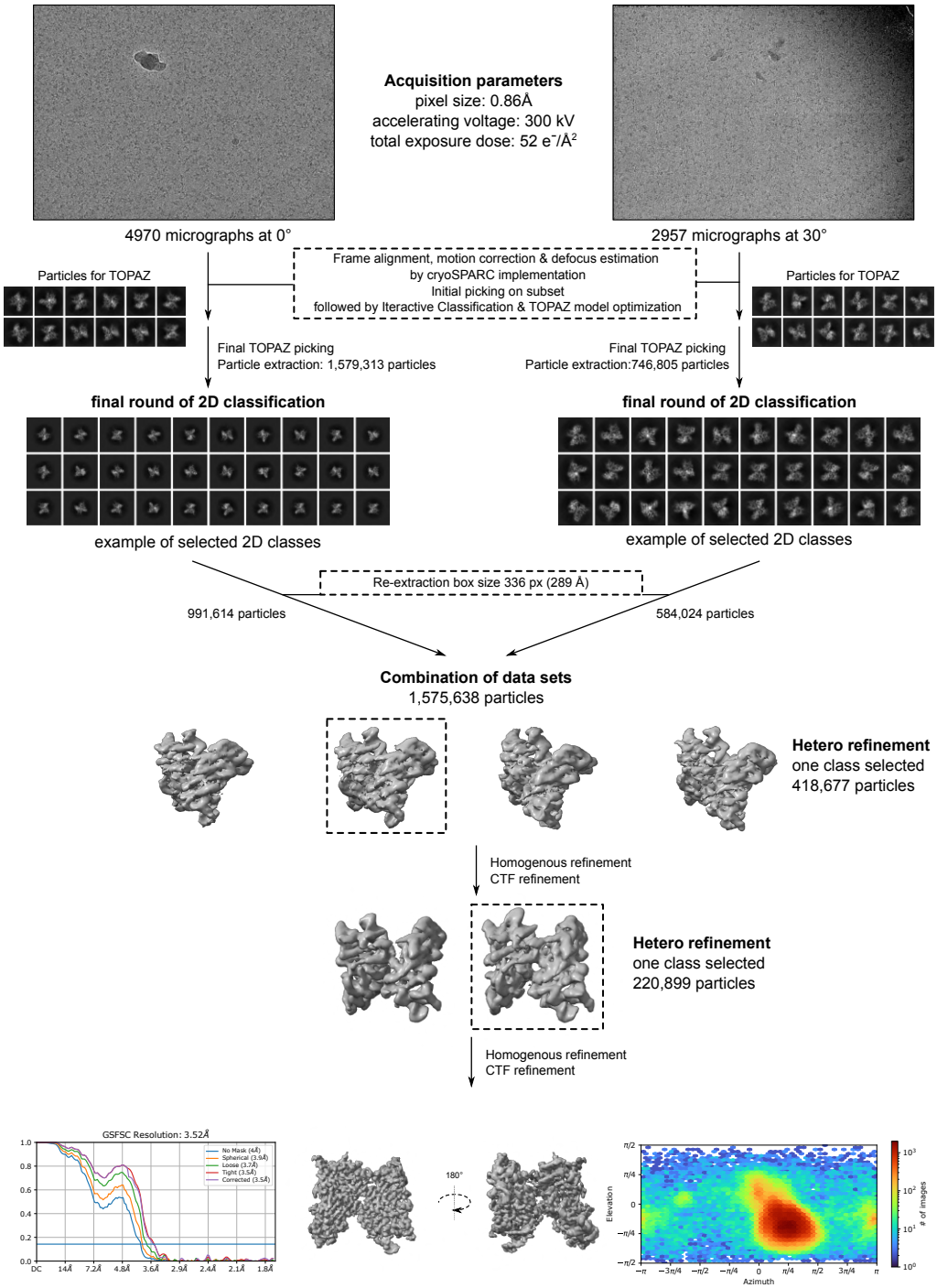

Figure 3.16. Processing scheme of *Ct*GEN1$^{1\text{-}515\ D143K}$-HJ complex.

The untilted and 30° tilt images were initially treated as separate datasets. For each dataset, an individual TOPAZ model was trained to optimize the particle picking on the images (Bepler *et al.*, 2019). Subsequent to classification in 2D, the sorted particles were combined and further processed as a single dataset. After the first round of heterogeneous refinement, the class exposing a connecting density between the two *Ct*GEN1 subunits was selected for another round of heterogeneous refinement. The class showing the connecting density was selected and homogeneous refined. The estimated resolution at an FSC of 0.143 is 3.52 Å. To the right, the angular distribution of the final reconstruction is depicted.

3.2.7 One-sided bridging loop stabilizes the asymmetric GEN1 dimer on the HJ

The map, reconstructed from the combined tilted and untilted datasets, resembles the shape of two *Ct*GEN1 subunits attached to the HJ substrate (Figure 3.17A). An atomic model of the *Ct*GEN1$^{1\text{-}515\ D143K}$-HJ complex was generated using Coot and PHENIX in an iterative manner using the monomeric *Ct*GEN1$^{1\text{-}487}$ crystal structure as template (Figure 3.17B-C) (Emsley et al., 2010; Liebschner et al., 2019; Liu *et al.*, 2015).

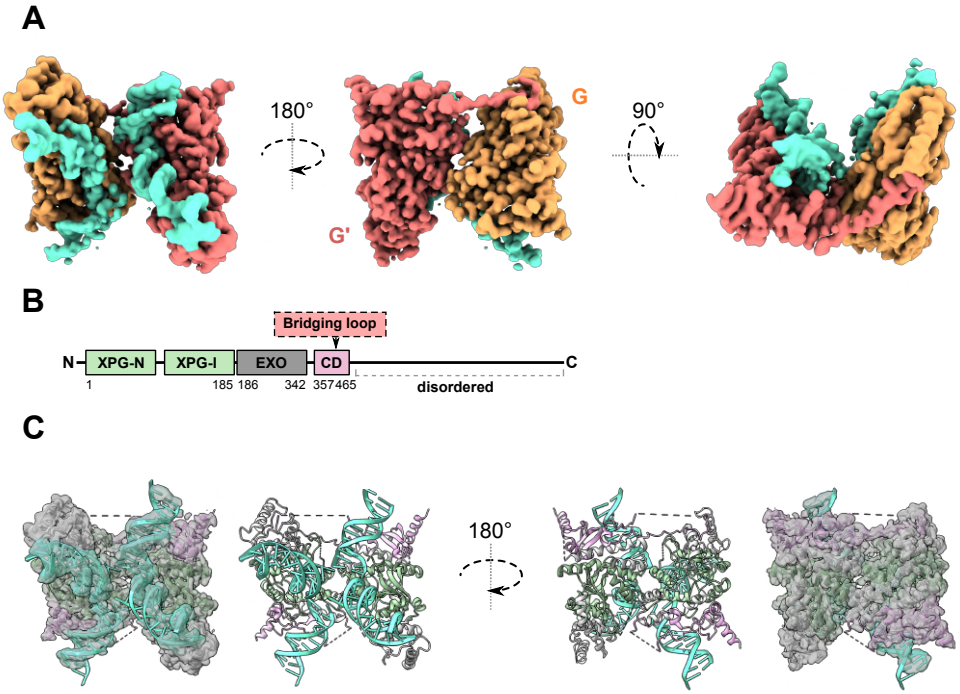

Figure 3.17. Cryo-EM structure of the *Ct*GEN1-HJ complex.

(A) Cryo-EM map of *Ct*GEN1$^{1\text{-}515\ D143K}$-HJ complex. The HJ DNA is coloured in cyan, the two CtGEN1 subunits in red and orange. (B) Schematic depiction of the *Ct*GEN1 domain architecture. The N-terminal XPG-N and XPG-I domain are followed by EXO nuclease domain and a chromo domain. The disordered C-terminal region, from residue 515, was removed for this study. (C) Cryo-EM map of *Ct*GEN1-HJ and its model coloured according to the domain architecture in (B). The Holliday junction is displayed in cyan.

Overall, GEN1 dimerizes on Holliday junction in an inverse back-to-back fashion. At the interface the electrostatic surface of the proteins shows how this arrangement allows oppositely charged regions in *Ct*GEN1 interact (Figure 3.18B). The Glu 312 buries into a positively charged pocket of the other subunit, and vice versa (Figure 3.18C). As noted in previous studies, GEN1 has a large positive charged cavity in the DNA-binding region, which allows efficient targeting of substrate DNAs (Figure 3.18B) (Lee *et al.*, 2015; Liu *et al.*, 2015).

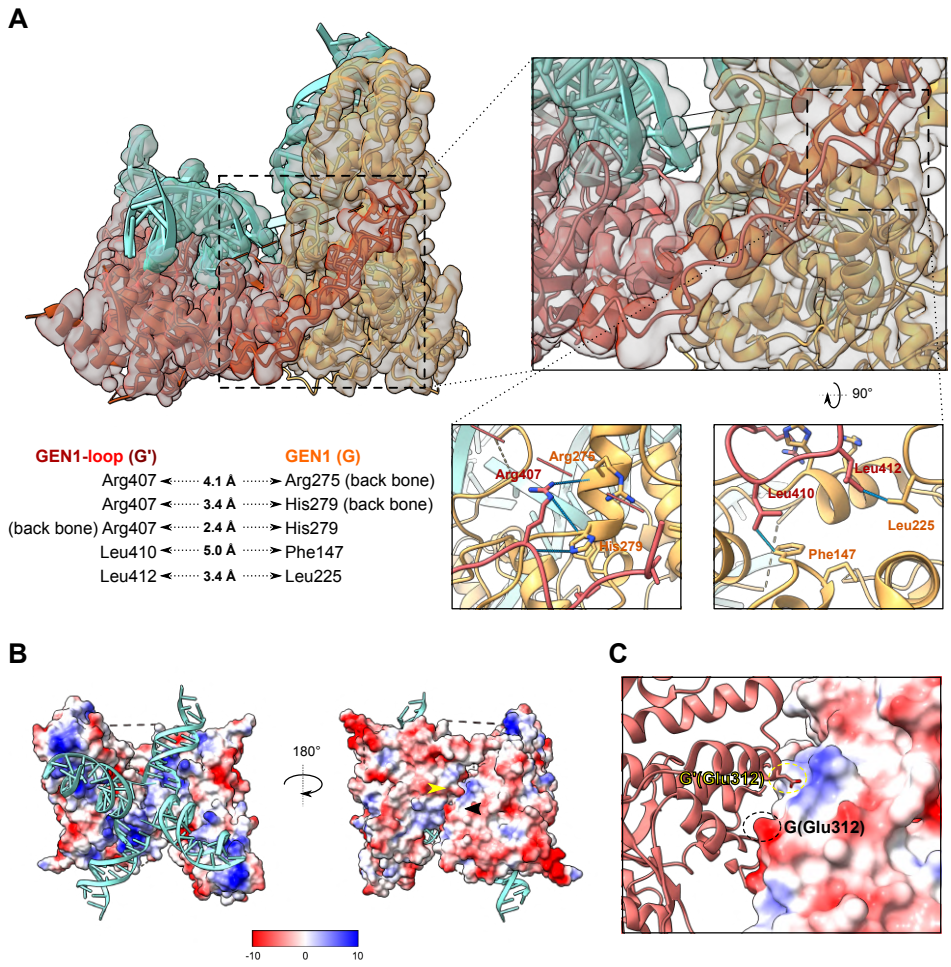

Figure 3.18. The bridging loop contributes to the inter-subunit interactions.

(A) The two *Ct*GEN1 subunits are connected by a loop highlighted in dark red. The subunits are referred to G' for the GEN1 unit exposing the bridging loop and G for the subunit binding the loop, resulting in the G'-G dimer. The dashed area indicates the zoom-in view in the right panel. Lower panel: On the right, a zoom perspective of the G'-G interaction region is displayed. The residues potentially contribute to the interaction of G'-G dimer are shown as stick model and their inter-protein distances are noted on the left (B) The electrostatic potential of the *Ct*GEN1 complex. The arrow heads point on a Glu 312, which is interacts from the top (yellow) with one subunit and is buried (black) in the other one. (C) The dimer interface presenting the electrostatic potential of one unit and ribbon diagram of the other. The mutated residues are highlighted in red. Glu 312 positions are indicated according to panel (B).

Interestingly, the cryo-EM map reveals an bridging loop (residue 400-413) which is not resolved in the available crystal structure of monomeric *Ct*GEN1 (Figure 3.18A). The bridging loop is only visible on one GEN1 subunit and creates multiple interactions to the other subunit. On the same area of the other subunit, the loop is invisible due to high flexibility, resulting in two differing dimer subunits. To simplify, the subunits are referred to G' for the GEN1 subunit forming the bridging loop, and G for the subunit binding the bridging loop (resulting in the G'/G *Ct*GEN1 dimer). The stable bridging loop seems to engage with the G subunit forming a hydrophobic

interaction between G'(Leu 412) and G(Leu 225), while the 5 Å distance between G'(Leu 410) and G(Phe 147) appears to be too far to contribute to the stabilization (see Figure 3.18A, lower panel). In addition, G'(Arg 407) in the bridging loop potentially forms hydrogen bonds with the backbone of Arg 275 and His 279 on G the subunit, G(His 279) appears to be in proximity to from an H-bond with the Arg 407 backbone.

3.2.8 The arrangement of the asymmetric dimer and its implication to the sequential dual incision mechanism

Initially, the dimer model was superimposed to a symmetric *Ct*GEN1 model, which was observed in the crystal packing of the monomeric structure (Liu *et al.*, 2015). While a single GEN1 subunit of the solved dimer structure can be aligned on the symmetric *Ct*GEN1 model, the second GEN1 subunit is misaligned (Figure 3.19A). Furthermore, three HJ arms of the obtained cryo-EM model can be superimposed on the symmetric model, the fourth arm exhibits a misalignment of 13° degree (Figure 3.19B). Consequently, the overall shape of the GEN1-dimer appears to be asymmetric, even though two identical GEN1 subunits engage on the symmetrical four-way junction.

In order to evaluate geometrical properties that facilitate the one-sided bridging loop formation, the distance between G'(Val 395) and G(Val 281), which close to where the density of the bridging loop ends, was determined and compared to the distance of G(Val 395) and G'(Val 281) on the loop-less site. While on the loop site the distance between G'(Val 395) and G(Val 281) is 31.6 Å, the distance between G(Val 395) and G'(Val 281) is 3 Å longer (34.6 Å) (Figure 3.19C). This distance is sufficient to prevent interactions between the bridging loop and its interacting region.

An alignment of the two halves of the GEN1 dimer shows that the secondary structure elements are in the same arrangement, except the bridging loop. However, the HJ arms bound to the G subunit exhibits a slight shift towards the catalytic centre of the nuclease (Figure 3.19D, indicated with the blue arrow head). The aspartate (Asp38, Asp79 & Asp143) and glutamate (Glu120 & Glu122) residues coordinating the Mg^{2+} ions at the catalytic site are similarly arranged in both subunits, only Asp141 residing loop shifts in G and therefore is positioned closer to the incision site (Figure 3.19D, right zoom-in panel). Overall, the asymmetricity of the dimer positions the DNA on the G subunit closer to the active site. These observations imply that the G subunit performs the initial nick, and the G' subunit subsequently catalyses the counter-nick to resolve the four-way junction.

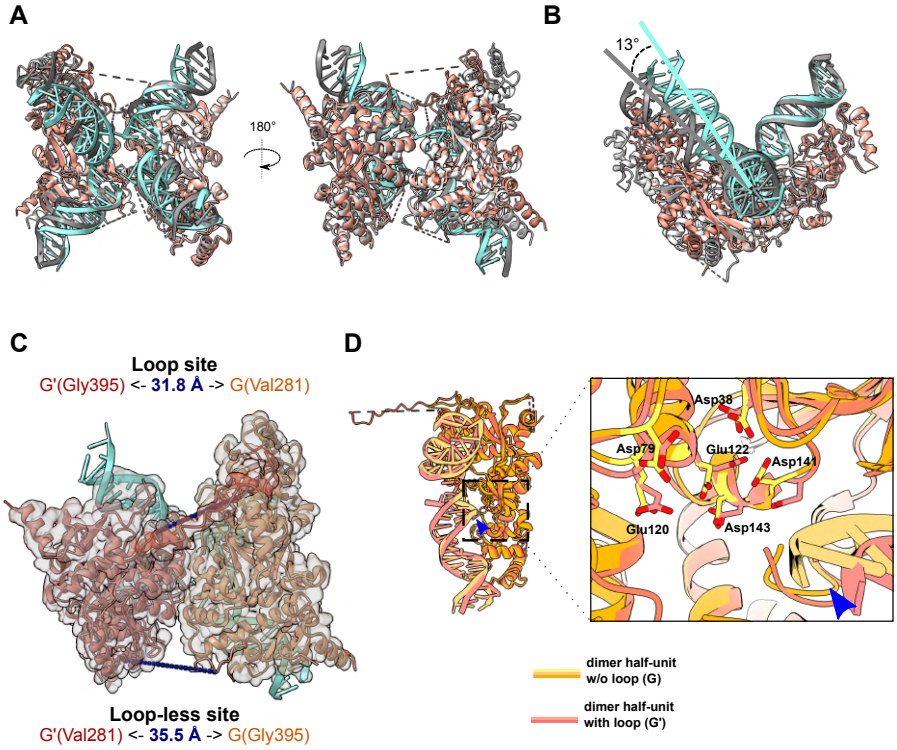

Figure 3.19. Asymmetric dimeric GEN1 complex on Holliday junction.

(A) Structural alignment of the *Ct*GEN1-HJ complex and the two-fold symmetry model. The *Ct*GEN1-HJ complex in this study is highlighted in orange/cyan, and the two-fold symmetry model is coloured in light grey. One GEN1 unit can be superimposed, while the other GEN1 subunit and the HJ are clear re-positioned. The result indicates that the two *Ct*GEN1 subunits are asymmetrically binding on the Holliday junction substrate. (B) Side view of the superimposed dimer models. The HJ arms into the plane and the right arm overlay after alignment. The fourth HJ arm of the symmetric and obtained cryo-EM model is misaligned by 13°. (C) The distance from the bridging loop origin Val 400 to the Val 281 on the opposing GEN1 subunit is shorter for the loop site and the gap site. (D) The two dimer half-units G' and G were superimposed. In comparison to G', the lower HJ-DNA arm bound to G shows a shift towards the catalytic core of the *Ct*GEN1 (indicated with the blue arrow head).

3.2.9 The bridging loop for dimerization is unique in *C. thermophilum*

To understand if the mechanism of the bridging loop is conserved among eukaryotes, the predicted AlphaFold structures and sequences of GEN1 homologs from different eukaryotes were compared (Jumper et al., 2021). In order to improve the alignment quality, the disordered C-terminal regions were removed in ChimeraX and subsequently the N-terminal regions were aligned with respective to *Ct*GEN1 (Figure 3.20A) (Pettersen *et al.*, 2021). Overall the secondary structure elements show a similar structural arrangement. However, the bridging loop region connecting the two GEN1 subunit in *C. thermophilum* is unique (Figure 3.20, purple box). Even though *Os*GEN1 and *Sc*Yen1 have a predicted loop in this region, the sequence alignment reveals rather diverse residue composition (Figure 3.20B).

Besides the bridging loop, several structure features are also diverse in GEN1 homologs. The GEN1 homologs from *H. sapiens, M. musculus, X. tropicalis and D. melanogaster* exhibit an additional domain on the observed GEN1-GEN1 interface, which was previously described as a helical arch region (Figure 3.20A, orange box) (Lee *et al.*, 2015). It was hypothesized that the helical arch can booster the 5' flap processing. This could potentially explain why *Ct*GEN1 has a relatively low 5' flap cleavage activity as this structure is missing in *Ct*GEN1. Furthermore, a Zn coordinated cluster insertion is predicted in the metazoan GEN1 homologs (Figure 3.20A, green box). However, since this domain is located next to the DNA binding interface of the nuclease core, it might play a role in substrate recognition . For both these regions, *Ct*GEN1 has no similar sequence properties (Figure 3.20B).

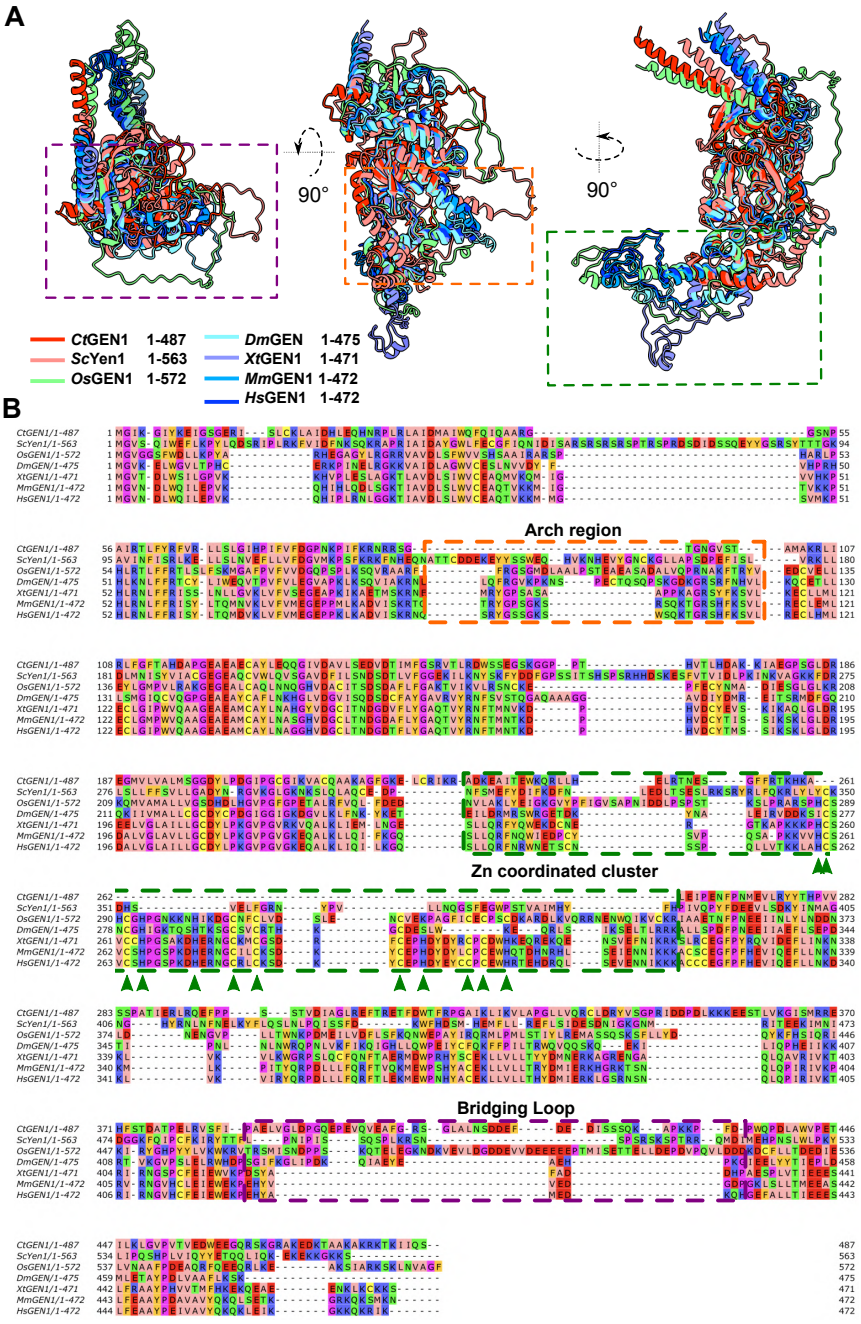

Figure 3.20. Comparison of GEN1 homologs from different species.

(A) Structure alignment of GEN1 homologs predicted by AlphaFold (Jumper *et al.*, 2021). The bridging loop region, the arch region and the predicted Zn-coordinated cluster are highlighted in purple, orange, and green dashed boxes, respectively. (B) Sequence alignment of the N-terminal part of the GEN1 homologs. The residues are colored by their physicochemical properties and the regions displayed in (A) are highlighted in the respective colors. Cysteine and histidine residues potentially coordinating.

3.2.10 Cryo-EM structure of *Ct*GEN1$^{1\text{-}515\ D143K}$ in complex with a 5' flap substrate

To understand how GEN1 recognizes different DNA structures, the GEN1-5' flap complex was reconstituted and analysed by cryo-EM. The complex was first purified by size exclusion chromatography. The chromogram reveals a shoulder eluted earlier than the main peak (see Figure 3.21). Only a small shift is expected for the *Ct*GEN1$^{1\text{-}515\ D143K}$ -5' flap complex in SEC, as the 5' flap DNA increases the molecular weight of the sample by 25 kDa. The peaks eluting after 15 ml are too small to contain to *Ct*GEN1$^{1\text{-}515\ D143K}$. For cryo-EM sample preparation, the highlighted fraction was used containing parts of the main peak and the smaller shoulder peak.

The cryo-EM micrographs of *Ct*GEN1$^{1\text{-}515\ D143K}$-5' flap exhibited a homogenous distribution of slightly smaller particles compared to the *Ct*GEN1-HJ sample. A data set was acquired and similarly analysed as the dimer complex (see Figure 3.21). First, particles were manually picked on a small subset of images. Then, a TOPAZ picking model was trained and optimized in an iterative process (Bepler *et al.*, 2019). On 6968 micrographs, 2,170,122 particles were picked with the final TOAPZ model. After three rounds of 2D classification several classes show a 'crescent' shape. These classes were expected to be *Ct*GEN1$^{1\text{-}515\ D143K}$ bound to the 5' flap substrate and hence selected for further processing in 3D. Furthermore, several classes exhibit 2D projections depicting two GEN1 units. Therefore, four ab-initio models were generated and used for an initial round of heterogeneous refinement to further separate different particle appearances. Interestingly, neither of the initial models nor the heterogeneous-refined volumes showed features for more than one GEN1 molecule. The rather different appearance of 2D averages expected to contain two GEN1 might hint an unphysiological dimer formation. Charge interactions and base-pairing of the 5' flap ssDNA arm may induce dimerization due to the locally high concentration of particles.

For the reconstruction of the *Ct*GEN1$^{1\text{-}515\ D143K}$ -5' flap complex, the 3D class depicting DNA in complex with GEN1 was subject to a homogeneous refinement and further cleaned up with two rounds of 2D classification. The final set of averages exhibits 2D classes of similar appearance and were subsequently subject to a heterogeneous refinement. Here the class showing distinct protein and DNA features was selected, comprising 153,560 particles, and refined homogenously. A final resolution of approximately 3.55 Å was estimated at a FSC of 0.143. However, the resolution might be overestimated as most of the regions only show secondary structures but lack of clear side chain densities.

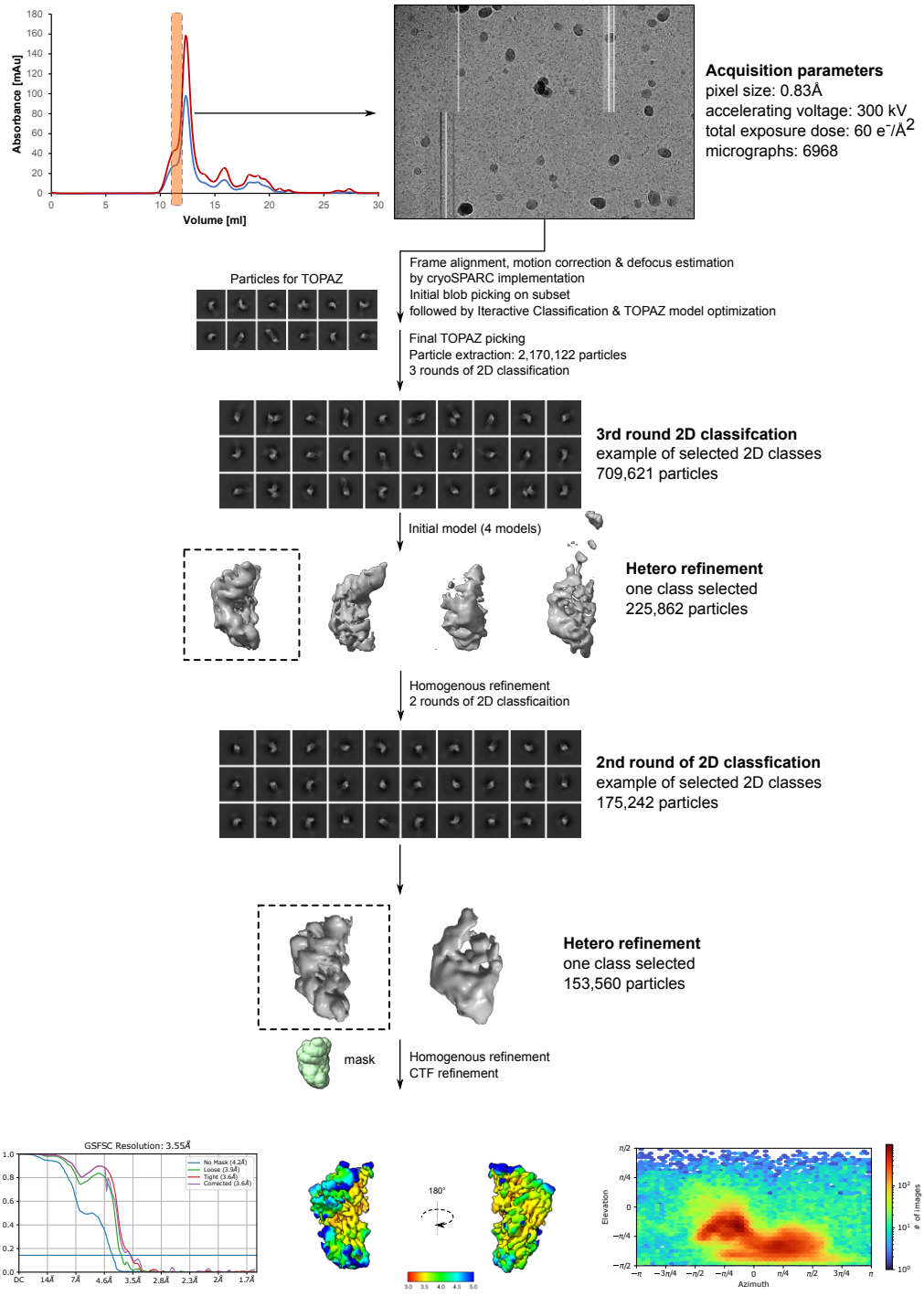

Figure 3.21. Processing scheme of *Ct*GEN1$^{1\text{-}515\ D143K}$ in complex with a 5' flap substrate.

The fraction highlighted in orange was used to prepare cryo-EM sample. The lines on the micrograph are due to damage on the K3 detector. For the data processing, a TOPAZ model was trained to optimize the picking on the images (Bepler *et al.*, 2019). Particles originated from defined 2D averages were used to for heterogeneous refinement. Subsequent 2D classification of the selected 3D volume resulted in a homogenous set of averages. An additional heterogeneous refinement was applied and a final set of particles obtained. A masked refinement resulted in a *Ct*GEN1$^{1\text{-}515\ D143K}$ in complex with a 5' flap complex with an estimated resolution of 3.55 Å at an FSC of 0.143. The angular distribution is shown to the right of the final reconstruction.

The obtained cryo-EM map exhibits a single *Ct*GEN1 unit bound to the dsDNA arms of the 5' flap substrate (see Figure 3.22A). A modified AlphaFold model of *Ct*GEN1 and Coot generated B-form dsDNA was used as template for rigid body fitting (Jumper *et al.*, 2021). After an iterative PHENIX real-space refinement and structural adjustments in Coot, the secondary structure elements were successfully built in the cryo-EM map (see Figure 3.22B) (Afonine et al., 2018; Emsley *et al.*, 2010). The overall arrangement of *Ct*GEN1 on the 5' flap is similar to that on HJ, suggesting GEN1 uses the same interface to recognize 5' flap DNA. However, the map quality is not high enough to objectively investigate the molecular interactions between *Ct*GEN1 and the 5' flap substrate.

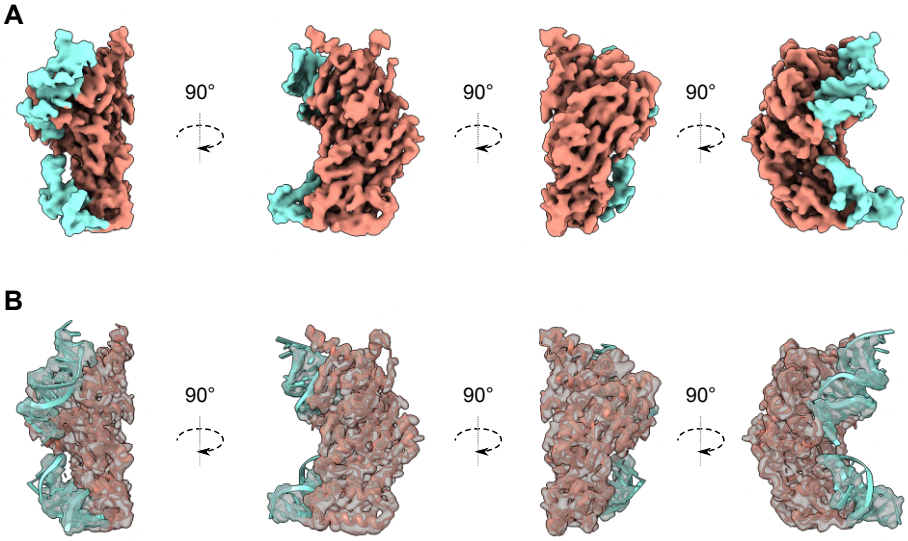

Figure 3.22. Cryo-EM map of *Ct*GEN1 in complex with a 5' flap substrate.
(A) Coulomb density of the reconstructed *Ct*GEN1$^{1\text{-}515\ D143K}$-5' flap complex. The DNA substrate is coloured in cyan, *Ct*GEN1 in orange. (B) Transparent map of *Ct*GEN1$^{1\text{-}515\ D143K}$-5' flap complex the atomic model.

3.2.11 Comparison of *Ct*GEN1 structures interacting with different DNA structures.

The binding of *Ct*GEN1 to DNA was compared using the two structures obtained from this study, *Ct*GEN1$^{1\text{-}515\ D143K}$ in complex with Holliday junction and in complex with 5' flap substrate as well as the available structure of *Ct*GEN1 bound to the cleavage product nicked DNA (Liu *et al.*, 2015). When GEN1 binds on HJ and the nicked product, the structures of the nuclease core are highly similar, the secondary structures are well aligned with RMSD of 1.424 for G and 1.149 for G'. However, when GEN1 binds on 5' flap, the nuclease core shows minor rearrangement, resulting in an RMSD of 3.124 (see Figure 3.23). The helices αI-αIII show a slight shift towards the core of the protein.. In addition to the shifted helices, the lower arm of the dsDNA shows a slight rotation in comparison to the other structures. The rotation of the DNA and minorly different oriented

5’ flap might shift the helices αI-αIII. To obtain detailed information about the conformational changes of GEN1 depending on the bound DNA, a higher resolved *Ct*GEN1$^{1\text{-}515\ D143K}$-5’ flap complex is necessary.

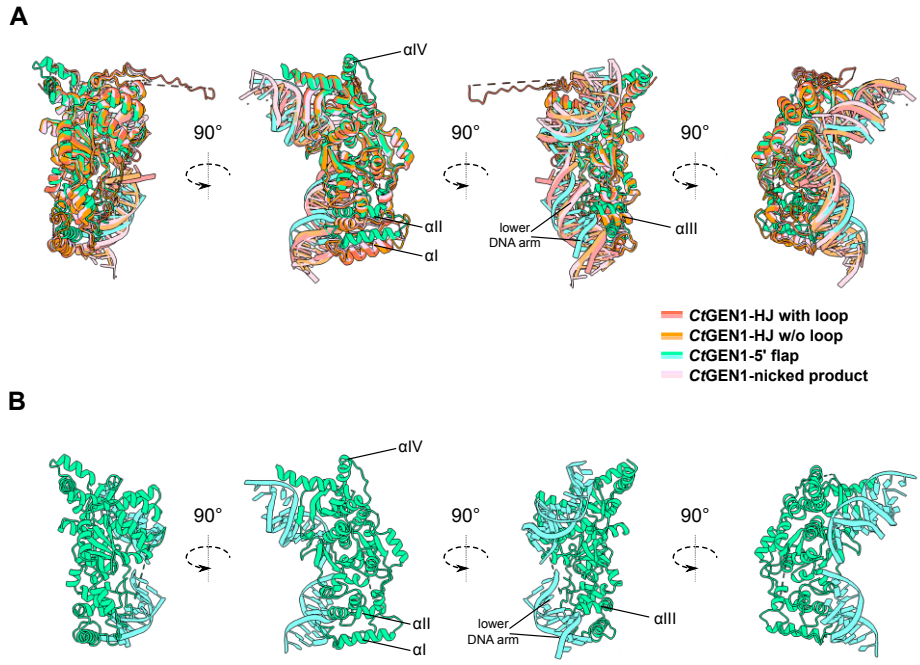

Figure 3.23. Structural comparison of *Ct*GEN1 binding on different DNA structures.

*Ct*GEN1-DNA complexes were aligned on the nuclease core. The structures in complex with HJ and 5’ flap were generated from this study. The structures of *Ct*GEN1 interacting with nicked dsDNA was published previously (PDB: 5C08; (Liu *et al.*, 2015). The helices III and IV are based on the AlphaFold model. While these helices weren’t assigned in the initial crystal structure model, later structural models of *Ct*GEN1 with the resolution product did (Liu et al., 2018). Also for *Ct*GEN1$^{1\text{-}515\ D143K}$-HJ and *Ct*GEN1$^{1\text{-}487}$ in complex with the nicked product these regions are resolved, though no helix features are assigned.

Discussion

3.3.1 Summary

The disentanglement of Holliday junctions is crucial during HR to prevent the rise of toxic recombination intermediates. The canonical resolvase GEN1 recognizes and cleaves these four-way DNA structures (Ip *et al.*, 2008). Previous studies on GEN1 revealed its structural core in complex with non-substrate DNA in its monomeric form. *H. sapiens* and *C. thermophilum* GEN1 exhibit an overall similar structure and share the same domain architecture (Lee *et al.*, 2015; Liu *et al.*, 2015). Still, to understand the engagement of GEN1 on its DNA substrates, further structural studies are necessary.

In this study, the substrate specificity of *Ct*GEN1 is functionally and structurally characterized. An active and inactive (D143K) variant comprising the N-terminal nuclease core (residues 1-515) were successfully expressed and purified. While the active *Ct*GEN1 construct was capable of processing HJ substrate, the inactive mutant did not show any nucleolytic activity. Interestingly, besides binding to HJ, both variants were also able to bind 5' flap DNA. In addition, the nucleolytic cleavage of the 5' flap was detected in the presence of the active GEN1 variant. The 5' flap processing activity has been observed in GEN1 homologs from many organisms except *Ct*GEN1, which is reported inactive toward 5' flap structure. (AlMalki *et al.*, 2016; Freeman *et al.*, 2014; Ip *et al.*, 2008; Kanai *et al.*, 2007). Here the results demonstrated that CtGEN1 does process 5' flap, even though higher protein concentration is required.

Further cryo-EM studies revealed the structure of the dimeric *Ct*GEN1$^{1\text{-}515\ D143K}$ binding on Holliday junction at 3.5 Å resolution. A key finding of this structure is that on one GEN1 subunit a predicted disordered loop spans to the other subunit. This unique interaction presumably contributes to the asymmetric arrangement of the dimer and plays a role in the sequential dual incision of HJ. In addition to the GEN1-HJ complexes, a cryo-EM was obtained for the *Ct*GEN1$^{1\text{-}515\ D143K}$ bound 5' flap substrate, affirming the interaction observed in the biochemical assays.

3.3.2 Optimization of cryo-EM sample lead to high resolution structure

The reconstruction of GEN1 dimer, from the initial dataset using Quantifoil grid, yield a map in medium resolution which shows the helical features of the DNA substrate and the secondary structure of GEN1. However, the lack of high-resolution information hinders the detection of the interactions between the GEN1 subunits. Therefore, a subsequent dataset was optimized by using an Ultrafoil grid. In addition, a tilted dataset was also collected in order to overcome the preferred orientation problem. The data processing revealed a structure at 3.5 Å resolution. Several factors

potentially contribute to the improved resolution of the map. First of all, the final reconstruction of the initial dataset contains a relatively small amount of particles, while the final map obtained from the optimized dataset has around tenfold more particles. Second, the increased amount of good particles benefits from the homogeneous sample observed after preparation of the Ultrafoil grids. The Ultrafoil grids, which are coated with a holey gold film that is thicker than the carbon film on Qunatifoil grids, could influence the particle behavior during vitrification (Russo and Passmore, 2016b). Generally, Ultrafoil grids are used to reduce the beam-induced motion caused by electron beam illumination. The reduction of the beam-induced motion further contributes to the extraction of high-resolution information during data processing (Russo and Passmore, 2014). Finally, the optimized dataset contains particles acquired at a tilted angle. The additional acquisition at a 30° tilt angle widens the distribution of dominant views, therefore a wider angular distribution was observed. Overall, the combined impact of these factors lead to the improvement of the final resolution of the GEN1-HJ structure.

3.3.3 Structural evidence of sequential GEN1 loading on Holliday junctions

Processing of an initial cryo-EM data set of *Ct*GEN1$^{1\text{-}515\ D143K}$ and Holliday junction complex revealed, apart from the HJ bound by dimeric GEN1, also HJ bound by a single *Ct*GEN1 molecule. This observation is consistent with the previous study by Chan et al. In the absence of the HJ substrate, GEN1 is in monomeric form in solution. Upon recognition of the Holliday junction, the GEN1 dimer forms in a two-step process on the substrate. Solely symmetrical cleaved DNA products are observed after nucleolytic cleavage by GEN1 dimer, whereas monomeric GEN1 on HJ is not catalytically active and therefore suggested to be an intermediate during formation of the active complex (Chan and West, 2015). The reconstructed cryo-EM volume of the monomeric *Ct*GEN1-HJ complex represents the initial step of GEN1 mediated Holliday junction resolution, the binding of the first GEN1 subunit to the substrate. However, due to conformation heterogeneity of the complex and low amount of particles, the data processing is limited to low resolution.

3.3.4 Structural elucidation of asymmetric arrangement of *Ct*GEN1 on Holliday junction substrate

The structure of GEN1-HJ complex reveals the back-to-back engagement of *Ct*GEN1$^{1\text{-}515\ D143K}$ on the Holliday junction substrate. The dimer is arranged in an asymmetric manner. A bridging loop from residue 400-413 is connecting the two GEN1 subunits. Interestingly, the map only shows

the loop on one side of the dimer while this loop is invisible on the corresponding position on the opposite subunit.

Between the loop and its interacting GEN1 subunit G, the density map hints several residues important for the interaction between the two subunits. The G' Leu 410 in the bridging loop is in proximity to the Phe 147 on G. The hydrophobic interaction could play a role in locking the asymmetric dimer. Furthermore, the arginine from G' at position 407 is in close proximity of the protein back bone at the resides Arg 275 and His 279 on G. Here, H-bonds could further contribute to the transient asymmetric dimer state. From the other site, G(His 279) can interact with loop backbone at G' Ser 408. Potentially these interactions stabilize the asymmetric conformation of the dimer to induce the first cleavage.

Overall, the dimer interface exposes patches of slightly charged areas on its surface. Due to the inverse back-to-back interaction surface, the Glu 312 can interact with a positively charged area on the opposing subunits. While G(Glu 312) is buried in the positive charged area on G', G'(Glu 312) interacts from the top with the same positively charged patch on G. Nevertheless, these interactions do not seem to be sufficient for the formation of stable protein dimer. Without the HJ substrate, GEN1 behaves as a monomer in solution, which as also observed in previous studies (Chan and West, 2015). An additional feature of the electrostatic surface of GEN1 is the strong positive charge at the DNA-binding cavity. The high affinity towards the HJ substrate and the imposed close proximity after loading of the GEN1 subunits might also serve as a scaffold where the Holliday junction supports the dimerization of GEN1. Subsequent to the cleavage event, the *Ct*GEN1$^{1\text{-}515\ D143K}$-HJ dimer falls apart and is expected to release the nicked dsDNA products(Liu *et al.*, 2015).

3.3.5 Structural insight in the GEN1's Holliday junction resolution process

The observed cryo-EM map can help to explain the two step nick counter-nick mechanism used by GEN1 for HJ resolution (Chan and West, 2015). Under physiological conditions Holliday junctions are predominately in the 'stacked-X configuration' (Ortiz-Lombardia et al., 1999). After binding of first GEN1 subunit, the HJ takes an open-bent conformation (see Figure 3.24). The bent conformation eventually promotes the binding of the second GEN1 subunit. Also the dimer cryo-EM map reveals an arched appearance of the HJ and potentially introduces tension to the four-way branched DNA. Due to the observed asymmetry, the initial nick on the HJ is favored for the G subunit (Figure 3.24, orange colored subunit), in which the active is in closer proximity to the substrate DNA region due to the bridging loop stabilization. After the first incision, tension is released from the HJ substrate and might induce a conformational change. This leads to the

detachment of the bridging loop connecting the two GEN1 subunits and probably favors the loop engagement on the other side of the dimer to prime for the second incision (see Figure 3.24, upper panel). Ultimately, the cleavage leads to two symmetrical product-GEN1 complexes with an nick in the dsDNA which has to be sealed later by endogenous ligases (Bennett *et al.*, 1993; Liu *et al.*, 2015). Altogether, the following catalytic sequence of GEN1 Holliday junction resolution can be derived from the structural data (see Figure 3.24, lower panel).

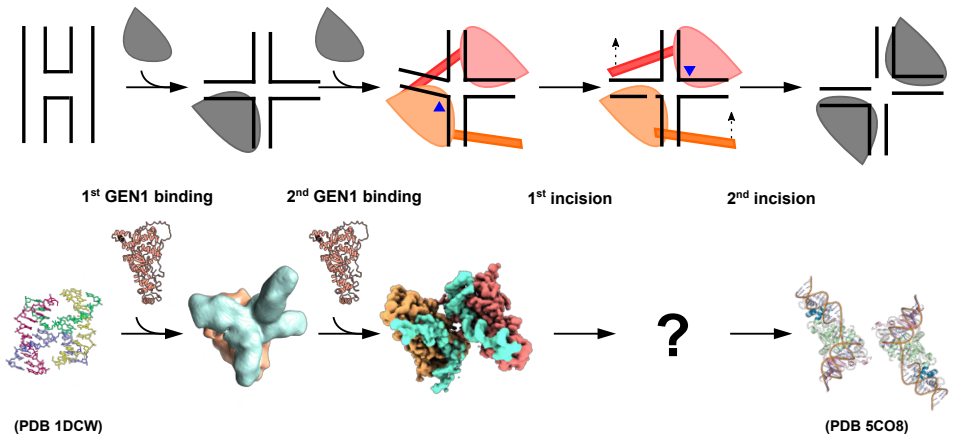

Figure 3.24. Structural insights on the GEN1 Holliday junction resolution.
During homologous recombination, Holliday junction intermediates arise. The initial binding of a single GEN1 unit leads to a conformation change of the HJ from the physiological preferred 'stacked-X configuration' to a bend conformation (Ortiz-Lombardia *et al.*, 1999). The binding of a second GEN1 subunit results in the formation of the asymmetric GEN1-HJ complex. After the first incision, the GEN1 stays dimerically attached to the nicked-HJ. Only the second incision at the diametric opposed position leads to the resolution of the HJ and dissociation of the GEN1 dimer (Liu *et al.*, 2015). Upper panel: scheme of the mechanism. During the nick-counter nick resolution mechanism, the two GEN1 units take sequentially different tasks, depicted in orange and red. Lower panel: Available structures on the GEN1 Holliday Junction resolution. Structural information on the nicked-HJ GEN1 complex is not available.

3.3.6 *Ct*GEN1 recognizes and processes 5' flap substrate

In this study, the wild type *Ct*GEN1 shows binding as well as nucleolytic processing of 5' flap structures. This activity was previously observed for homologs from other species except *C. thermophilum*. The lower 5' flap nucleolytic activity of *Ct*GEN1 compared to *Dm*GEN and *Hs*GEN1 potentially because it lacks the helical arch structure adjacent to the active site, which was reported having an important function in 5' flap cleavage. In addition, the insertion of a Zn coordinated cluster which is only predicted in metazoan GEN1 homologs, may also plays a role (Bellendir *et al.*, 2017; Lee *et al.*, 2015).

Previous studies on *C. thermophilum* GEN1$^{1-487}$ suggested that this enzyme has no cleavage activity toward 5' flap structure. (AlMalki *et al.*, 2016; Freeman *et al.*, 2014; Ip *et al.*, 2008; Kanai *et al.*, 2007). However, the cryo-EM map of *Ct*GEN1$^{1-515\ D143K}$ bound to 5' flap DNA did not reveal Coulomb density beyond residue 469. Therefore, the impact of the residues 487-515 on the 5' flap processing is not expected. Nevertheless, investigation of this stretch is of interest to exclude its potential role in the 5' flap processing of *Ct*GEN1. The final reconstruction of *Ct*GEN1$^{1-515\ D143K}$ in complex with 5' flap substrate yields a map in resolution of 3.6 Å. However, the resolution is overestimated as most part of the map did not show information of bulky side chains. It is expected that the nominal resolution should be in the range of 4-5 Å. Nonetheless, the obtained map reveals the overall secondary structure arrangement of the *Ct*GEN1 nuclease core bound to the 5' flap DNA. Overall, the *Ct*GEN1 interaction with 5' flap or HJ as well as the previously reported interaction with nicked product show similar arrangement of the secondary structures (Liu *et al.*, 2015). Only the helices αI to αIII in proximity of the DNA substrate show a slight shift while binding to different DNA structures. Apart from the DNA-protein interface, some secondary structure elements are slightly moved in respective to the HJ and nicked product structure. This observation suggested that the GEN1 nuclease core can slightly breath in order to adopt various DNA structures.

3.3.7 Role of GEN1 in processing different DNA intermediates

In comparison to the human homolog, *Ct*GEN1 exhibits a lower activity on 5' flap structures. A structural alignment of the AlphaFold predictions shows that metazoan GEN1 has an additional zinc coordinated cluster next to the nuclease core. Such cluster structure is often involved in DNA interaction (Jumper *et al.*, 2021). Potentially, this can contribute to the robust 5' flap processing activity observed in human homolog.

While GEN1's role in Holliday junction resolution during homologous recombination is widely studied, its 5' flap cleavage activity *in vivo* is largely unknown. A recent observation implies that its role may related to the processing of replication intermediates (see Figure 3.25A). It was shown that GEN1 cleaves at common fragile site in response to replication stress. In absence of GEN1, a decrease in mitotic DNA replication as well as the rise of anaphase bridges was observed, eventually resulting in DNA damage in the following cell cycle. Therefore, it is suggested that GEN1 is needed for 5' flap and fork endonuclease activity (see Figure 3.25B) (Benitez et al., 2023). The 5' flap-*Ct*GEN1 complex may represent the DNA processing intermediate occurring during replication, while the dimer structure displays the classical HJ resolution complex during homologous recombination

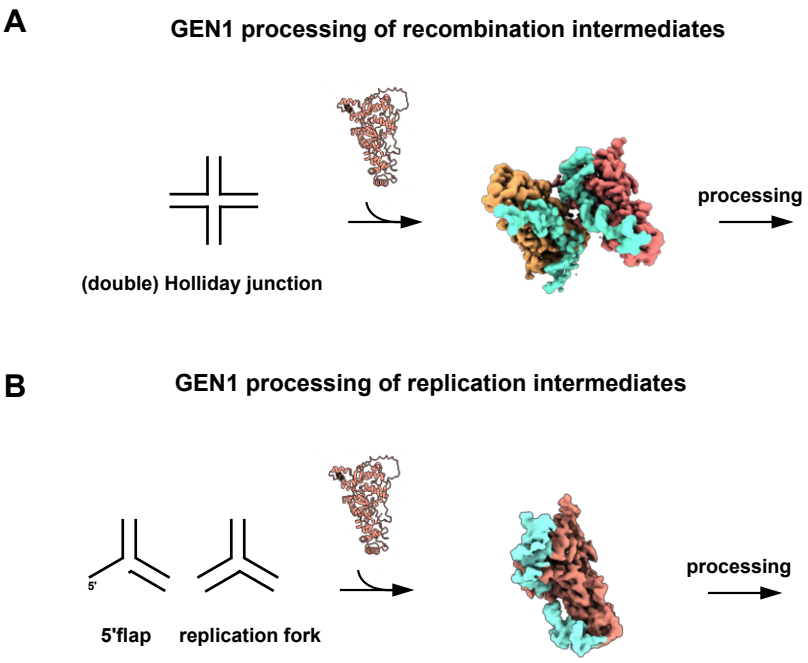

Figure 3.25. Versatile roles of the structure-selective resolvase GEN1.

(A) GEN1 recognizes Holliday junctions, a four-way branched DNA structure, during HR. It dimerizes on the recombination intermediate and faithfully resolves the HJ in a symmetric manner. (B) Furthermore, GEN1 can cleave other DNA structures such as 5' flap structures and replication forks. These intermediates can arise during replicational stress and their processing is essential.

3.3.8 Outlook

The presented structures reveal important information about the recognition and alignment of GEN1 to its substrate DNA. Still, further questions need to be addressed to fully explain the underlying catalytic cycles of GEN1. In comparison to the high-resolution dimeric structure, the cryo-EM volume of Holliday junction bound by a single monomer is only resolved at low resolution. The binding of the first GEN1 monomer is considered as the rate limiting step. The high affinity of the initial monomer binding favors the loading of the second subunit rather than the dissociation of protein-DNA complex (Sobhy *et al.*, 2019). High-resolution information on the monomeric GEN1-HJ complex may reveal molecular interactions that stabilize the first GEN1 unit on the HJ substrate.

Even though structures of the substrate and product complexes of the GEN1-mediated resolution are available, no structural information about the intermediate processing step is on hand (see Figure 3.24, 'question mark'). Subsequent to the first cleavage, a molecular rearrangement of the GEN1-HJ dimer is expected to facilitate the second incision. The realignment of the GEN1 dimer on the nicked-HJ is unclear, therefore a snapshot on the intermediate processing complex can help understand the molecular details of the sequential nick counter-nick mechanism.

While most of GEN1 is structurally conserved, the bridging loop in *C. thermophilum*, stabilizing the dimeric GEN1-HJ complex in a primed conformation, appears to be unique. Still, *Hs*GEN1 as well as *Ct*GEN1 utilize the same nick counter-nick mechanism to process branched four-way junctions. It is likely that in humans a similar asymmetric dimer forms on the HJ. Although, the first incision must be promoted by a different feature, for instance the arch region which is conserved among metazoans. Interestingly, previous studies have elucidated that even though GEN1 homologs perform the same biological role, distinct approaches can be observed among different organisms. Here, the yeast homolog Yen1 and human GEN1 engage in the same phase of the cell cycle, but their localization underlies different regulative measures (Chan and West, 2014; Dehe and Gaillard, 2017). Hence, it is an exciting puzzle to solve if *Hs*GEN1 evolved a different way to prime the nucleolytic cleavage of branched four-way DNA.

Apart from Holliday junctions, GEN1 can bind other DNA structures. The cryo-EM map of *Ct*GEN1 in complex with 5' flap DNA confirms the specific binding of this substrate, like previously observed from for other homologs. Though, a higher resolution map is needed to show the protein-DNA interactions necessary for the nucleolytic cleavage. Also further DNA intermediates like replication forks were shown to be processed by GEN1 homologs. The availability of structural data on different substrates might help to understand how GEN1 can process a wide range of DNA substrates.

Methods

3.4.1 Cloning of the expression vector

The coding GEN1 gene from the thermophilic fungus *Chaetomium thermophilum*, was cloned into a bacterial expression vector harbouring an ampicillin resistant gene as the selection marker. To enhance protein solubility and purification, the recombinant protein is fused to a C-terminal CPD- and an octa-histidine-tag. The T7 promoter-driven gene expression is regulated by the lac operon.

3.4.2 Protein production

Expression. A 40 s heat shock at 42°C was conducted for transformation of the expression vector into the *E. coli* strain BL21(DE3)gold. Colonies were grown on ampicillin selective agar plates overnight, resuspended in 8 ml Lysogeny Broth (LB) media and transferred to baffled beakers containing 1 l of Terrific Broth (TB) media with 100 µg/ml ampicillin. The bacteria were grown in exponential phase at 37°C and once the OD_{600} reached ~1.0, the temperature was reduced to 16°C. Overnight protein expression was induced by setting the final concentration of IPTG (Isopropyl β-D-1-thiogalactopyranoside) to 0.2 mM. Afterwards, the bacteria were harvested by centrifugation at 6,000 rpm for 10 min. Pellets were snap-frozen in liquid nitrogen and stored at -80°C.

Purification. Bacterial pellets were resuspended in lysis buffer (1×PBS with additional 500 mM NaCl, 10% Glycerol, 1 mM Leupeptin, 1 mM AEBSF, 0.2 mM Pepstatin A, 0.3 µM Aproptinin), the cell membranes were broken down by sonication with VS70T probe in 0.5 s on/off cycle for 15 min with amplitude of 40% on ice. The lysed cells were centrifuged at 75,600 ×*g* for 45 min to remove the cell debris. Subsequently, the residual debris was cleared by vacuum filtration through a 0.22 µm membrane filter. For the nickel affinity purification, a cOmplete (Roche #6781535001) nickel column was equilibrated with buffer (20 mM Tris-HCl pH 7.5, 500 mM NaCl, 10% glycerol, 2 mM DTT). The lysate was loaded, washed with 20 column volumes (CV) of wash buffer (20 mM Tris-HCl pH 7.5, 500 mM NaCl, 10% glycerol, 2 mM DTT, 7.5 mM imidazole) and then eluted with elution buffer (20 mM Tris-HCl pH 7.5, 500 mM NaCl, 10% glycerol, 2 mM DTT, 300 mM imidazole). The C-terminal CPD-His_8-tag was removed by addition of 1 mM inositol hexaphosphate (IP_6) to the collected elution, inducing the self-cleavage of CPD. The cleavage reaction was incubated on ice overnight in presence of 1 mM TCEP to prevent the formation of disulfide bridges. Next, the CPD-cleaved elution was diluted with buffer (20 mM Tris-HCl pH 7.5, 1 mM EDTA, 10% glycerol) to a final NaCl concentration of 150 mM and filtered with a 0.22 µm membrane to remove potential aggregations. Then, the protein solution was loaded onto a SP

column (cytiva #17115201) pre-equilibrated with SP-A buffer (20 mM Tris-HCl pH 7.5, 150 mM KCl, 1 mM EDTA, 10% glycerol) and washed with 5 CV of the same buffer. The column was connected to a ÄKTA Prime system and fractionated with a 150-450 mM KCl gradient over 16 CV. The purity of the recombinant *Ct*GEN1 constructs was examined by SDS-PAGE stained with Coomassie blue. Peak fractions were pooled, concentrated to ~2 ml and loaded on a HiLoad™ 16/600 Superdex 200 pg column (Cytiva #28-9893-35) pre-equilibrated with SEC buffer (20 mM Tris-HCl pH 7.5, 60 mM KCl, 5% glycerol, 2 mM TCEP). After size exclusion on the ÄKTA Purifier system, fractions containing the recombinant protein were identified by the $UV_{260/280nm}$ absorption and subsequently their purity was confirmed by SDS-PAGE. Pure elution fractions were pooled, concentrated, snap-frozen in liquid nitrogen and stored at -80 °C.

Protein concentration determination. The UV_{280nm} absorption, caused by the intrinsic tryptophan and tyrosine residues, was measured using the Nanodrop photometer. The concentration of *Ct*GEN1 constructs was calculated by the Beer–Lambert law with extinction coefficients of $e_{absolute}$ = 0.881 l/(g x cm) and e_{molar}= 50420 l/(mol x cm) calculated by ExPASy PROTPARAM.

3.4.3 DNA substrate preparation

DNA substrates were prepared by heating complementary oligonucleotides (Eurofins Genomics, Ebersberg, Germany) in equimolar ratios mixed in annealing buffer (10 mM HEPES-KOH pH 8.5, 50 mM KCl, 0.1 mM EDTA) to 85°C for 5 min and subsequent slow-cooling to room temperature. Until further usage, the DNA substrates were stored at -20°C.

3.4.4 Electrophoretic mobility shift assay(EMSA)

Protein samples were mixed with 80 nM 6FAM-labeled DNA substrates (Eurofins Genomics, Ebersberg, Germany) in 20 mM Tris-HCl pH 8.0, 50 ng/µl BSA, 0.5 mM TCEP, 5 mM $CaCl_2$ and 5% (v/v) glycerol. To allow the binding of protein to the DNA-substrates, the individual reactions were incubated on ice for 5 min. Subsequently, the samples were loaded on a 6% 0.5× TB gel and ran at 2 W for 1 h on ice. The fluorescent signal was detected with a Typhoon FLA 7000 phosphoimager at $\lambda_{[FAM]}$= 473 nm with a PMT value of 800.

3.4.5 Nuclease Activity Assay

40 nM 6FAM-labeled substrates (Eurofins Genomics, Ebersberg, Germany) were mixed with indicated amounts of CtGEN1 in 20 mM Tris-HCl pH 8.0, 50 ng/µl bovine serum

albumin (BSA), 0.5 mM TCEP. To determine the substrate preference and the cleavage activity of *Ct*GEN1 constructs, the samples were initiated by addition of 5 mM $MgCl_2$. and incubated for 15 min at 37°C. The reactions were terminated with 15 mM EDTA and 0.3% SDS, followed by a de-proteinization with 1 mg/ml proteinase K at 37°C for 15 min. Loading buffer was added and the samples were run on an 8% 1×TB native polyacrylamide gel at 100 V for 40 min. The fluorescent signal was detected with a Typhoon FLA 7000 phosphoimager at $\lambda_{[FAM]}$= 473 nm with a PMT value of 800.

3.4.6 Complex formation assay

The formation of the *Ct*GEN1-HJ complex was investigated by size exclusion chromatography. The inactive variant *Ct*GEN1$^{1\text{-}515\ D143K}$ in presence or absence of Holliday junction substrate was loaded on a Superdex 200 10/300 column (Cytiva #17517501). Synthetic HJ and the *Ct*GEN1 construct were mixed in a molar ratio of 1:2. Prior injecting the specimen, the final salt concentration was adjusted to 60 mM KCl and 2 mM $CaCl_2$. Then, the sample was loaded on the column, pre-equilibrated with 20 mM Tris-HCl pH 7.5, 60 mM KCl, 2 mM $CaCl_2$, 2 mM TCEP and 5% (v/v) glycerol, and the UV absorption at 260 nm and 280 nm were monitored.

3.4.7 Single particle cryo-EM sample preparation

Initial GEN1-HJ complex. *Ct*GEN1$^{1\text{-}515\ D143K}$ was added to its HJ substrate in a molar ratio of 2:1, based on the *Ct*GEN1$^{1\text{-}515\ D143K}$ concentration before snap-freezing in liquid nitrogen for long-term storage. The buffer was adjusted to 60 mM KCl and 2 mM $CaCl_2$ and loaded on HiLoad Superdex S200 increase 10/300 column (Cytiva #28990944) pre-equilibrated with 20 mM Tris-HCl pH 7.5, 60 mM KCl, 2 mM $CaCl_2$, 2 mM TCEP and 5% (v/v) glycerol. After the run, the peak fraction was collected and diluted four times. Next, 3 µl were applied on a Quantifoil R1.2/1.3 Cu200 grid. The specimens were blotted 3.5 s with blotting force of 4, and plunged froze into a liquid ethane/propane mixture using a Vitrobot Mark IV plunge freezer (Thermo Fisher Scientific) operating at 4°C and humidity 95%.

Optimised GEN1-HJ complex. The concentration of *Ct*GEN1$^{1\text{-}515\ D143K}$ was remeasured after thawing, and subsequently mixed with Holliday junction substrate in a molar ratio of 2:1, based on the determined protein concentration. The final salt concentration was adjusted to 60 mM KCl and 2 mM $CaCl_2$. The protein-DNA mixture was loaded onto an HiLoad Superdex S200 increase 10/300 column (Cytiva #28990944) pre-equilibrated with 20 mM Tris-HCl pH 7.5, 60 mM KCl, 2 mM $CaCl_2$, 2 mM TCEP and 5% (v/v) glycerol. The peak fraction at a retention volume of 11 ml was diluted by the factor of 3. Then, 3 µl of sample were applied on a UltaAufoil Au300 R1.2/1.3

gird (Quantifoil), glow discharged using the Pelco easiGlow™ at a plasma current of 20 mA for 45 s. After blotting for 3.5 s with the blotting force 4 at 4°C and 95% humidity, the sample was vitrified in liquid ethane using a Vitrobot Mark IV (Thermo Fisher Scientific).

GEN1-5'flap complex. *Ct*GEN1$^{1\text{-}515\ D143K}$ and 5' flap substrate were mixed in a molar ratio of 1:1. The final salt concentration was adjusted to 60 mM KCl and 2 mM $CaCl_2$. The *Ct*GEN1$^{1\text{-}515\ D143K}$-5' flap mixture was applied onto an HiLoad Superdex S200 increase 10/300 column (Cytiva #28990944) pre-equilibrated with 20 mM Tris-HCl pH 7.5, 60 mM KCl, 2 mM $CaCl_2$, 2 mM TCEP and 5% (v/v) glycerol. The peak fraction at a retention volume of 12 ml was diluted two times. 3 µl of dilution were pipetted on a Quantifoil Cu200 R1.2/1.3 gird (Quantifoil), priorly glow discharged using the Pelco easiGlow™ at a plasma current of 20 mA for 45 s. The specimen was blotted for 3.5 s with the blotting force 4 at 4°C and 100% humidity using a Vitrobot Mark IV (Thermo Fisher Scientific). Immediately after blotting, the sample was vitrified in liquid ethane.

3.4.8 Cryo-EM data acquisition

Initial GEN1-HJ complex. In total 5442 micrographs were acquired using a Titan Krios (Thermo Fisher Scientific) at 300 keV equipped with a K2 summit camera (Gatan) in the Max Planck Institute of Biochemistry. The images, subdivided into 40 frames, were collected at a calibrated pixel size of 0.822 Å in a defocus range from -1.5 to -3.5 µm with an total exposure of 88.2 $e^-/Å^2$.

Optimised GEN1-HJ complex. The data was acquired on a Krios (Thermo Fisher Scientific) operated at 300 keV, equipped with a with a Gatan Quantum 967 LS energy filter and K3 Summit direct detector in NIH. Serial EM software was used to collect images at a pixel size of 0.86 Å with a defocus range of -0.8 to -2.0 µm. A total of 4970 movies at 0° and 2954 movies at 30° tilted stage, subdivided in 22 or 23 frames, respectively, were collected with a total dose of 52 $e^-/Å^2$.

GEN1-5'flap complex. For the data acquisition, a Krios (Thermo Fisher Scientific) equipped with a with a Gatan Quantum 967 LS energy filter and K3 Summit direct detector was used at an acceleration voltage of 300 keV in NIH. Images were recorded with the Serial EM software at a defocus range of -0.8 to -2.0 µm and a pixel size of 0.83 Å. In total 6968 movies were collected, divided in 27 frames and a total dose of 60 $e^-/Å^2$.

3.4.9 Cryo-EM single particle analysis

Initial GEN1-HJ complex. The movies were corrected for beam-induced movement using *MotionCorr2* (Zheng *et al.*, 2017). Next, *Gautomatch* (developed by Dr Kai Zhang, MRC Laboratory

of Molecular Biology, Cambridge, UK, http://www.mrc-lmb.cam.ac.uk/kzhang/Gautomatch/) was used to pick particles. The reference-free picking with a diameter 120 Å resulted in a total of 1,281,406 particles. Both, the motion-corrected micrographs and the particle coordinates were imported to RELION 2.1.0 (Kimanius et al., 2016). The CTF of the micrographs was estimated by Gctf (Zhang, 2016). Next, the particles were extracted with a box size of 256 px (corresponding to 210 Å). During 2D classification, two distinct types of 2D averages, expected to be *Ct*GEN1 in monomeric and dimeric composition bound to HJ, and therefore processed individually.

Monomeric GEN1-HJ particles, exhibiting a 'helicopter-shaped' appearance during 2D classification, were pooled. Further 2D classification was conducted resulting in a final set of 85,336 particles. An initial model was created from roughly 40,000 particles. Two rounds of 3D classification were performed. The final set of 12,822 particles was used for refinement and post-processing. The gold-standard FSC 0.143 was estimated for a resolution of 11 Å.

2D averages displaying a 'butterfly-shaped' form, which resemble the dimeric GEN1 bound on HJ, were subject to further 2D classification to archive a homogeneous set of 423,230 particles. After creation of an initial model, two more rounds classified in 3D. The best class, consisting of 24,612 particles, was further refined and post-processed. The resolution of the final map was estimated at 7.52 Å at a FSC of 0.143.

Both, the monomeric and the dimeric assembly of *Ct*GEN1 on the Holliday junction substrate was visualized using Chimera (Pettersen et al., 2004).

Optimised GEN1-HJ complex. The collected micrographs were first imported to cryoSAPRC v.3.3.1(Punjani *et al.*, 2017). The motion correction implementation in patch mode was used to correct the beam-induced motion and exposure-dependent dose-weighting of the individual frames. Next the CTF was estimated using the cryoSPARC implementation in patch mode. The 0° tilt and the 30° tilt data acquisition were initially treated as two independent data sets. In the first step, several hundred particles were manually picked. Subsequently, undefined particles were removed by 2D classification. These particles were used for training a TOPAZ picking model (Bepler *et al.*, 2019). In an iterative process, the TOPAZ model was independently optimized for the 0° tilt and 30° tilt micrographs. For the 0° tilt data, the final TOPAZ model was used to pick 1,579,313 particles which were extracted with a box size of 336 px (corresponding to 279 Å). After several rounds of 2D classification, 991,614 particles were selected and subject to a 3D refinement. In parallel, the TOPAZ model, trained on the 30° tilt data, was applied on the tilted micrographs for particle identification. A total of 746,805 particles were picked. After sorting in 2D, 584,024 particles were used with the same box size as the 0° tilt (336 px, corresponding to 279 Å) for an initial round of 3D refinement. The final set of particles from the 0° tilt and 30° tilt data sets were

combined and subsequently subject to a heterogeneous refinement, using four different classes. The best looking class containing 418,677 particles was selected and further refined prior to the local and global CTF refinement. A second round of heterogenous refinement was applied, dividing the particles into two classes. The better class including 220,899 particles was selected and subject to final round of homogeneous refinement, resulting in a map of 3.47 Å at a FSC of 0.143. The final map was sharpened using DeepEMhancer (Sanchez-Garcia *et al.*, 2021). ChimeraX was used for visualization and segmentation (Pettersen *et al.*, 2021).

GEN1-5'flap complex. The collected micrographs were imported to cryoSAPRC v.3.3.1, motion corrected and their CTF was estimated using the cryoSPARC implantation in patch mode (Punjani *et al.*, 2017). First, an initial round of manual picking was conducted. Subsequently, the particles were classified in 2D and a set of defined classes was selected. Then, in iterative process of TOPAZ training and classification, the robust picking model was generated resulting in 2,170,122 particles (Bepler *et al.*, 2019). After three rounds of 2D classification, a total of 709,621 particles were obtained. Next, four *ab-initio* models were generated and used for a following round of heterogeneous refinement. The class with the appearance of a single GEN1 bound to DNA substrate, including 225,862 particles, were subject to two more rounds of 2D classification. 175,242 particle were used for another round of heterogeneous refinement using two references. The better resolved map comprising 153,560 particles was selected and refined by non-uniform refinement with per particle CTF estimation and aberration correction(Punjani et al., 2020). The final reconstruction with a mask to remove information from the flexible DNA arm resulted in a map with a resolution of 3.64 Å with the FSC of 0.143 criterion.

DeepEMhancer was used to sharpen the final map of the *Ct*GEN1$^{1\text{-}515\ D143K}$ in complex with the 5' flap substrate (Sanchez-Garcia *et al.*, 2021). For visualization and segmentation of the Coulomb map, the sharpened map was imported to ChimeraX (Pettersen *et al.*, 2021).

3.4.10 Data fitting and modelling of cryo-EM maps

Initial GEN1-HJ complex. Two *Ct*GEN1 (PDB 5CO8; recombinant *Ct*GEN1$^{1\text{-}487}$(Liu *et al.*, 2015)) were individually fitted in the dimer structure using Chimera (Pettersen *et al.*, 2004).

Optimised GEN1-HJ complex. The available X-ray crystallography structure of the *Ct*GEN1 (PDB 5CO8; recombinant *Ct*GEN1$^{1\text{-}487}$ (Liu *et al.*, 2015)) was rigid body fitted into the final map using USCF Chimera (Pettersen *et al.*, 2004). Then the model was manually adjusted in Coot, and the four HJ arms were generated according to their sequences and fitted into the map (Emsley *et al.*, 2010).

The created model was real-space refined in Phenix (Liebschner *et al.*, 2019). First, a round of rigid-body fitting was applied. Here, the two GEN1 monomers as well as the four DNA-HJ arms were defined as individual bodies. Individual residues were manually optimized to fit them according to the map in the favoured restraint-regions. Finally, for the regions were invisible in previous structures, the model was extended and built manually, for instance the bridging loop which stretches between the two GEN1 subunits.

GEN1-5'flap complex. The sharpened map was imported to Chimera and the *Ct*GEN1 AlphaFold model (UniProt G0RYN2) was rigid body fitted (Jumper *et al.*, 2021; Pettersen *et al.*, 2004). The disordered region from residue 489-922 was deleted. Subsequently, the *Ct*GEN1$^{1\text{-}489}$ model was imported into Coot, and the loop residing at position 392-437 was removed and two B-form dsDNA arms were generated for the 5' flap substrate (Emsley *et al.*, 2010). The model of *Ct*GEN1$^{1\text{-}489\ \Delta 392\text{-}437}$ was refitted into the Coulomb map using Chimera. Then, PHENIX real-space refinement was used to refine the *Ct*GEN1$^{1\text{-}489\ \Delta 392\text{-}437}$ structure and the DNA arms in the cryo-EM map by applying the rigid-body. Next, the parts of GEN1 and DNA lacking information in the Coulomb map were removed in Coot. Then the model fitting was optimized using morphing, global minimazation and local grid search (Afonine *et al.*, 2018; Liebschner *et al.*, 2019).

Table 3.1. Refinement statistics for Final GEN1-HJ and GEN1-5'flap complex.

	*Ct*GEN1$^{1\text{-}515\ D143K}$-5'flap	*Ct*GEN1$^{1\text{-}515\ D143K}$-HJ
Chains	5	12
Atoms	4091	8600
Residues	Protein: 411 Nucleotide: 46	Protein: 831 Nucleotide: 104
Bonds (RMSD)		
Length (Å)	0.004	0.005
Angle (°)	0.677	0.858
MolProbity score	2.18	2.13
Clash score	18.62	15.64
Ramachandran plot (%)		
Outliers	0.00	0.74
Allowed	6.17	5.80
Favored	93.83	93.46
Rotamer outliers (%)	0.00	0.00
Cβ ≤ outliers (%)	0.00	0.00
CaBLAM outliers (%)	1.00	5.06
ADP (B-factors)		
Iso/Aniso (#)	4091/0	8600/0
min/max/mean		
Protein	30.08/97.24/45.67	10.31/175.73/50.21
Nucleotide	20.00/20.00/20.00	20.00/20.00/20.00

3.4.11 Alignment of GEN1 homologs from different eukaryotes

Structural alignment. The AlphaFold predicted structures of GEN1 homologs from different model organisms (see Table 3.2) were imported in ChimeraX (Jumper *et al.*, 2021; Pettersen *et al.*, 2021). The C-terminal unstructured region was removed. The N-terminal structural regions were aligned in respective to the *Ct*GEN1 model using Matchmaker.

Sequence alignment. The sequences of the N-terminal structural region, defined in Table 3.2, were aligned using Clustal Omega (Sievers et al., 2011). The aligned sequences were imported to Jalview 2 (Waterhouse et al., 2009). The residues of the aligned sequences were colored according to their physicochemical properties using the Zappo scheme.

Table 3.2. GEN1 homologs used for structural and sequence alignment.

Organism	Acronym	UniProt	residues
Chaetomium thermophilum	*Ct*GEN1	G0RYN2	1-487
Homo sapiens	*Hs*GEN1	Q17RS7	1-472
Mus musculus	*Mm*GEN1	Q8BMI4	1-472
Drosophila melanogaster	*Dm*GEN	Q9VRJ0	1-475
Xenopus tropicalis	*Xt*GEN1	A0A6I8PYB0	1-471
Oryza sativa subsp. japonica	*Os*GEN1	Q64MA3	1-572
Saccharomyces cerevisiae	*Sc*Yen1	P40028	1-563

Abbreviations

2D	two-dimensional
3D	three-dimensional
ACE2	angiotensin-converting enzyme 2
AR	aspect ratio
ATP	adenosine triphosphate
AWI	air-water interface
BIR	break-induced replication
BLM	Bloom's syndrome helicase
BLM	RecQ-like DNA helicase BLM
BRCA2	breast cancer type 2 susceptibility protein
BTR	BLM helicase-Topoisomerase IIIα-RMI1-RMI2
CD	chromodomain
CD147	transmembrane protein cluster of differentiation 147
CO	crossover
COVID-19	corona virus disease 2019
CPD	ysteine protease domain from *Vibrio cholerae* MARTX
*Ct*GEN1	*Chaetomium thermophilum* GEN1
cryo-CLEM	cryo-correlative light electron microscopy
cryo-EM	cryo-electron microscopy
cryo-ET	cryo-electron tomography
cryo-FIB	cryo-focused ion beam
CTF	contrast transfer function
CV	column volume
DDD	direct detection detector
DNA	deoxyribonucleic acid
DNA2	DNA replication ATP-dependent helicase/nuclease 2
dHJ	double Holliday junction
D-loop	displacement loop
DIC	differential interference contrast
DMV	double-membrane vesicle
DSB	double-strand break
dsDNA	double-stranded DNA
ECM	extracellular matrix
EME1	essential meiotic endonuclease 1
EMSA	electrophoretic mobility shift assay
E protein	envelope protein
ER	endoplasmic reticulum
ERGIC	ER-Golgi intermediate compartment
ESI-TOF	electrospray ionization time of flight
EXO	5'-3' exonuclease
EXO1	exonuclease 1
FEG	field emission gun
FEN1	Flap endonuclease 1

FP	fusion peptide
FSC	Fourier shell correlation
GAPDH	glyceraldehyde-3-phospahtedehydrogenase
GEN1	flap endonuclease GEN homolog 1
HJ	Holliday Junction
HR	homologous recombination
HR1	heptapeptide repeat 1
HR2	heptapeptide repeat 2
*Hs*GEN1	*Homo sapiens* GEN1
IP_6	inositol hexaphosphate
IPTG	Isopropyl β-D-1-thiogalactopyranoside
LB	lysogeny broth
LOH	loss of heterozygosity
MERS-CoV	Middle East respiratory syndrome coronavirus
MMEJ	microhomology mediated end-joining
M protein	membrane protein
MRN	MRE11-RAD50-NBS1
mRNA	messenger RNA
MUS81	MMS and UV sensitive protein 81
NCO	non-crossover
N-CTD	nucleocapsid protein C-terminal domain
NETs	neutrophil extracellular traps
NHEJ	nonhomologous end-joining
N-NTD	nucleocapsid protein N-terminal domain
N protein	nucleocapsid protein
NRP-1	neuopilin-1
nsp	non-structural protein
ORF	open reading frame
PF4	platelet factor 4
pFAK	phosphorylated focal adhesion kinase
PRR	pattern recognition receptor
RBD	receptor-binding domain
RBM	receptor binding motif
RGD	Arginine-Glycine-Aspartic acid
RMI1	RecQ-mediated instability protein 1
RMI2	RecQ-mediated instability protein 2
RNP	ribonucleocapsid complex
RPA	replication protein A
RTC	replication and transcription complex
SARS-CoV	severe acute respiratory syndrome coronavirus
SARS-CoV-2	severe acute respiratory syndrome coronavirus 2
SDSA	synthesis-dependent strand annealing
SLX1	synthetic lethal of unknown function protein 1
SLX4	synthetic lethal of unknown function protein 4
SNR	signal-to-noise ratio

SP	sulfopropyl-sepharose
SPA	single particle analysis
S protein	spike protein
ssDNA	single-stranded DNA
STA	subtomogram-averaging
TB	terrific broth
TEM	transmission electron microscope
TLR	toll-like receptor
TLR4	toll-like receptor 4
TM	transmembrane
TMPRSS2	transmembrane serine protease 2
topo IIIα	topoisomerase IIIα
VWF	von Willebrand factor
XPG-I	XPG internal
XPG-N	XPG N-terminal
Yen1	*Saccharomyces cerevisiae* Holliday junction resolvase Yen1

Bibliography

<https://www.nobelprize.org/prizes/chemistry/2017/summary/>, T.N.P.i.C.N.o.N.P.O.A.S.M.

Aboudounya, M.M., and Heads, R.J. (2021). COVID-19 and Toll-Like Receptor 4 (TLR4): SARS-CoV-2 May Bind and Activate TLR4 to Increase ACE2 Expression, Facilitating Entry and Causing Hyperinflammation. Mediators Inflamm *2021*, 8874339. 10.1155/2021/8874339.

Adrian, M., Dubochet, J., Lepault, J., and McDowall, A.W. (1984). Cryo-electron microscopy of viruses. Nature *308*, 32-36. 10.1038/308032a0.

Afonine, P.V., Poon, B.K., Read, R.J., Sobolev, O.V., Terwilliger, T.C., Urzhumtsev, A., and Adams, P.D. (2018). Real-space refinement in PHENIX for cryo-EM and crystallography. Acta Crystallogr D Struct Biol *74*, 531-544. 10.1107/S2059798318006551.

Al-Samkari, H., Karp Leaf, R.S., Dzik, W.H., Carlson, J.C.T., Fogerty, A.E., Waheed, A., Goodarzi, K., Bendapudi, P.K., Bornikova, L., Gupta, S., et al. (2020). COVID-19 and coagulation: bleeding and thrombotic manifestations of SARS-CoV-2 infection. Blood *136*, 489-500. 10.1182/blood.2020006520.

AlMalki, F.A., Flemming, C.S., Zhang, J., Feng, M., Sedelnikova, S.E., Ceska, T., Rafferty, J.B., Sayers, J.R., and Artymiuk, P.J. (2016). Direct observation of DNA threading in flap endonuclease complexes. Nat Struct Mol Biol *23*, 640-646. 10.1038/nsmb.3241.

Anand, R., Ranjha, L., Cannavo, E., and Cejka, P. (2016). Phosphorylated CtIP Functions as a Co-factor of the MRE11-RAD50-NBS1 Endonuclease in DNA End Resection. Mol Cell *64*, 940-950. 10.1016/j.molcel.2016.10.017.

Andrews, R.K., Shen, Y., Gardiner, E.E., Dong, J.F., Lopez, J.A., and Berndt, M.C. (1999). The glycoprotein Ib-IX-V complex in platelet adhesion and signaling. Thromb Haemost *82*, 357-364.

Arya, R., Kumari, S., Pandey, B., Mistry, H., Bihani, S.C., Das, A., Prashar, V., Gupta, G.D., Panicker, L., and Kumar, M. (2021). Structural insights into SARS-CoV-2 proteins. J Mol Biol *433*, 166725. 10.1016/j.jmb.2020.11.024.

Astuti, I., and Ysrafil (2020). Severe Acute Respiratory Syndrome Coronavirus 2 (SARS-CoV-2): An overview of viral structure and host response. Diabetes Metab Syndr *14*, 407-412. 10.1016/j.dsx.2020.04.020.

Bai, Z., Cao, Y., Liu, W., and Li, J. (2021). The SARS-CoV-2 Nucleocapsid Protein and Its Role in Viral Structure, Biological Functions, and a Potential Target for Drug or Vaccine Mitigation. Viruses *13*. 10.3390/v13061115.

Bailly, A.P., Freeman, A., Hall, J., Declais, A.C., Alpi, A., Lilley, D.M., Ahmed, S., and Gartner, A. (2010). The Caenorhabditis elegans homolog of Gen1/Yen1 resolvases links DNA damage signaling to DNA double-strand break repair. PLoS Genet *6*, e1001025. 10.1371/journal.pgen.1001025.

Barrett, T.J., Bilaloglu, S., Cornwell, M., Burgess, H.M., Virginio, V.W., Drenkova, K., Ibrahim, H., Yuriditsky, E., Aphinyanaphongs, Y., Lifshitz, M., et al. (2021). Platelets contribute to disease severity in COVID-19. J Thromb Haemost *19*, 3139-3153. 10.1111/jth.15534.

Beck, M., and Baumeister, W. (2016). Cryo-Electron Tomography: Can it Reveal the Molecular Sociology of Cells in Atomic Detail? Trends Cell Biol *26*, 825-837. 10.1016/j.tcb.2016.08.006.

Becker, R.P., and De Bruyn, P.P. (1976). The transmural passage of blood cells into myeloid sinusoids and the entry of platelets into the sinusoidal circulation; a scanning electron microscopic investigation. Am J Anat *145*, 183-205. 10.1002/aja.1001450204.

Beddingfield, B.J., Iwanaga, N., Chapagain, P.P., Zheng, W., Roy, C.J., Hu, T.Y., Kolls, J.K., and Bix, G.J. (2021). The Integrin Binding Peptide, ATN-161, as a Novel Therapy for SARS-CoV-2 Infection. JACC Basic Transl Sci *6*, 1-8. 10.1016/j.jacbts.2020.10.003.

Behl, T., Kaur, I., Aleya, L., Sehgal, A., Singh, S., Sharma, N., Bhatia, S., Al-Harrasi, A., and Bungau, S. (2022). CD147-spike protein interaction in COVID-19: Get the ball rolling with a novel receptor and therapeutic target. Sci Total Environ *808*, 152072. 10.1016/j.scitotenv.2021.152072.

Bellendir, S.P., Rognstad, D.J., Morris, L.P., Zapotoczny, G., Walton, W.G., Redinbo, M.R., Ramsden, D.A., Sekelsky, J., and Erie, D.A. (2017). Substrate preference of Gen endonucleases highlights the importance of branched structures as DNA damage repair intermediates. Nucleic Acids Res *45*, 5333-5348. 10.1093/nar/gkx214.

Benitez, A., Sebald, M., Kanagaraj, R., Rodrigo-Brenni, M.C., Chan, Y.W., Liang, C.C., and West, S.C. (2023). GEN1 promotes common fragile site expression. Cell Rep *42*, 112062. 10.1016/j.celrep.2023.112062.

Bennett, R.J., Dunderdale, H.J., and West, S.C. (1993). Resolution of Holliday junctions by RuvC resolvase: cleavage specificity and DNA distortion. Cell *74*, 1021-1031. 10.1016/0092-8674(93)90724-5.

Bepler, T., Morin, A., Rapp, M., Brasch, J., Shapiro, L., Noble, A.J., and Berger, B. (2019). Positive-unlabeled convolutional neural networks for particle picking in cryo-electron micrographs. Nat Methods *16*, 1153-1160. 10.1038/s41592-019-0575-8.

Bharat, T.A., and Scheres, S.H. (2016). Resolving macromolecular structures from electron cryo-tomography data using subtomogram averaging in RELION. Nat Protoc *11*, 2054-2065. 10.1038/nprot.2016.124.

Bhella, D. (2019). Cryo-electron microscopy: an introduction to the technique, and considerations when working to establish a national facility. Biophys Rev *11*, 515-519. 10.1007/s12551-019-00571-w.

Bianchi, M., DasGupta, C., and Radding, C.M. (1983). Synapsis and the formation of paranemic joints by E. coli RecA protein. Cell *34*, 931-939. 10.1016/0092-8674(83)90550-0.

Biertumpfel, C., Yang, W., and Suck, D. (2007). Crystal structure of T4 endonuclease VII resolving a Holliday junction. Nature *449*, 616-620. 10.1038/nature06152.

Bizard, A.H., and Hickson, I.D. (2014). The dissolution of double Holliday junctions. Cold Spring Harb Perspect Biol *6*, a016477. 10.1101/cshperspect.a016477.

Blanco, M.G., Matos, J., and West, S.C. (2014). Dual control of Yen1 nuclease activity and cellular localization by Cdk and Cdc14 prevents genome instability. Mol Cell *54*, 94-106. 10.1016/j.molcel.2014.02.011.

Bocquet, N., Bizard, A.H., Abdulrahman, W., Larsen, N.B., Faty, M., Cavadini, S., Bunker, R.D., Kowalczykowski, S.C., Cejka, P., Hickson, I.D., and Thoma, N.H. (2014). Structural and mechanistic insight into Holliday-junction dissolution by topoisomerase IIIalpha and RMI1. Nat Struct Mol Biol *21*, 261-268. 10.1038/nsmb.2775.

Bohm, J., Frangakis, A.S., Hegerl, R., Nickell, S., Typke, D., and Baumeister, W. (2000). Toward detecting and identifying macromolecules in a cellular context: template matching applied to electron tomograms. Proc Natl Acad Sci U S A *97*, 14245-14250. 10.1073/pnas.230282097.

Bosch, B.J., van der Zee, R., de Haan, C.A., and Rottier, P.J. (2003). The coronavirus spike protein is a class I virus fusion protein: structural and functional characterization of the fusion core complex. J Virol *77*, 8801-8811. 10.1128/jvi.77.16.8801-8811.2003.

Boursnell, M.E., Brown, T.D., Foulds, I.J., Green, P.F., Tomley, F.M., and Binns, M.M. (1987). Completion of the sequence of the genome of the coronavirus avian infectious bronchitis virus. J Gen Virol *68 (Pt 1)*, 57-77. 10.1099/0022-1317-68-1-57.

Brasen, C.L., Christensen, H., Olsen, D.A., Kahns, S., Andersen, R.F., Madsen, J.B., Lassen, A., Kierkegaard, H., Jensen, A., Sydenham, T.V., et al. (2021). Daily monitoring of viral load measured as SARS-CoV-2 antigen and RNA in blood, IL-6, CRP and complement C3d predicts outcome in patients hospitalized with COVID-19. Clin Chem Lab Med *59*, 1988-1997. 10.1515/cclm-2021-0694.

Brennan, M.P., Loughman, A., Devocelle, M., Arasu, S., Chubb, A.J., Foster, T.J., and Cox, D. (2009). Elucidating the role of Staphylococcus epidermidis serine-aspartate repeat protein G in platelet activation. J Thromb Haemost *7*, 1364-1372. 10.1111/j.1538-7836.2009.03495.x.

Bythell-Douglas, R., and Deans, A.J. (2021). A Structural Guide to the Bloom Syndrome Complex. Structure *29*, 99-113. 10.1016/j.str.2020.11.020.

Bzymek, M., Thayer, N.H., Oh, S.D., Kleckner, N., and Hunter, N. (2010). Double Holliday junctions are intermediates of DNA break repair. Nature *464*, 937-941. 10.1038/nature08868.

Cai, Y., Zhang, J., Xiao, T., Peng, H., Sterling, S.M., Walsh, R.M., Jr., Rawson, S., Rits-Volloch, S., and Chen, B. (2020). Distinct conformational states of SARS-CoV-2 spike protein. Science *369*, 1586-1592. 10.1126/science.abd4251.

Cannavo, E., and Cejka, P. (2014). Sae2 promotes dsDNA endonuclease activity within Mre11-Rad50-Xrs2 to resect DNA breaks. Nature *514*, 122-125. 10.1038/nature13771.

Cantuti-Castelvetri, L., Ojha, R., Pedro, L.D., Djannatian, M., Franz, J., Kuivanen, S., van der Meer, F., Kallio, K., Kaya, T., Anastasina, M., et al. (2020). Neuropilin-1 facilitates SARS-CoV-2 cell entry and infectivity. Science *370*, 856-860. 10.1126/science.abd2985.

Castano-Diez, D., Kudryashev, M., Arheit, M., and Stahlberg, H. (2012). Dynamo: a flexible, user-friendly development tool for subtomogram averaging of cryo-EM data in high-performance computing environments. J Struct Biol *178*, 139-151. 10.1016/j.jsb.2011.12.017.

Chaganti, R.S., Schonberg, S., and German, J. (1974). A manyfold increase in sister chromatid exchanges in Bloom's syndrome lymphocytes. Proc Natl Acad Sci U S A *71*, 4508-4512. 10.1073/pnas.71.11.4508.

Chambers, P., Pringle, C.R., and Easton, A.J. (1990). Heptad repeat sequences are located adjacent to hydrophobic regions in several types of virus fusion glycoproteins. J Gen Virol *71 (Pt 12)*, 3075-3080. 10.1099/0022-1317-71-12-3075.

Chan, Y.W., and West, S. (2015). GEN1 promotes Holliday junction resolution by a coordinated nick and counter-nick mechanism. Nucleic Acids Res *43*, 10882-10892. 10.1093/nar/gkv1207.

Chan, Y.W., and West, S.C. (2014). Spatial control of the GEN1 Holliday junction resolvase ensures genome stability. Nat Commun *5*, 4844. 10.1038/ncomms5844.

Chang, C.K., Hsu, Y.L., Chang, Y.H., Chao, F.A., Wu, M.C., Huang, Y.S., Hu, C.K., and Huang, T.H. (2009). Multiple nucleic acid binding sites and intrinsic disorder of severe acute respiratory syndrome coronavirus nucleocapsid protein: implications for ribonucleocapsid protein packaging. J Virol *83*, 2255-2264. 10.1128/JVI.02001-08.

Chang, J.H., Kim, J.J., Choi, J.M., Lee, J.H., and Cho, Y. (2008). Crystal structure of the Mus81-Eme1 complex. Genes Dev *22*, 1093-1106. 10.1101/gad.1618708.

Chao, C.H., Wu, W.C., Lai, Y.C., Tsai, P.J., Perng, G.C., Lin, Y.S., and Yeh, T.M. (2019). Dengue virus nonstructural protein 1 activates platelets via Toll-like receptor 4, leading to thrombocytopenia and hemorrhage. PLoS Pathog *15*, e1007625. 10.1371/journal.ppat.1007625.

Chen, L., Wang, G., Long, X., Hou, H., Wei, J., Cao, Y., Tan, J., Liu, W., Huang, L., Meng, F., et al. (2021). Dynamics of Blood Viral Load Is Strongly Associated with Clinical Outcomes in Coronavirus Disease 2019 (COVID-19) Patients: A Prospective Cohort Study. J Mol Diagn *23*, 10-18. 10.1016/j.jmoldx.2020.10.007.

Chen, M., Bell, J.M., Shi, X., Sun, S.Y., Wang, Z., and Ludtke, S.J. (2019). A complete data processing workflow for cryo-ET and subtomogram averaging. Nat Methods *16*, 1161-1168. 10.1038/s41592-019-0591-8.

Chen, N., Zhou, M., Dong, X., Qu, J., Gong, F., Han, Y., Qiu, Y., Wang, J., Liu, Y., Wei, Y., et al. (2020). Epidemiological and clinical characteristics of 99 cases of 2019 novel coronavirus pneumonia in Wuhan, China: a descriptive study. Lancet *395*, 507-513. 10.1016/S0140-6736(20)30211-7.

Chen, X.B., Melchionna, R., Denis, C.M., Gaillard, P.H.L., Blasina, A., Van de Weyer, I., Boddy, M.N., Russell, P., Vialard, J., and McGowan, C.H. (2001). Human Mus81-associated endonuclease cleaves Holliday junctions in vitro. Mol Cell *8*, 1117-1127. 10.1016/s1097-2765(01)00375-6.

Chen, Z., Mi, L., Xu, J., Yu, J., Wang, X., Jiang, J., Xing, J., Shang, P., Qian, A., Li, Y., et al. (2005). Function of HAb18G/CD147 in invasion of host cells by severe acute respiratory syndrome coronavirus. J Infect Dis *191*, 755-760. 10.1086/427811.

Cheng, V.C., Lau, S.K., Woo, P.C., and Yuen, K.Y. (2007). Severe acute respiratory syndrome coronavirus as an agent of emerging and reemerging infection. Clin Microbiol Rev *20*, 660-694. 10.1128/CMR.00023-07.

Cheng, Y., Grigorieff, N., Penczek, P.A., and Walz, T. (2015). A primer to single-particle cryo-electron microscopy. Cell *161*, 438-449. 10.1016/j.cell.2015.03.050.

Cherry, J.D., and Krogstad, P. (2004). SARS: the first pandemic of the 21st century. Pediatr Res *56*, 1-5. 10.1203/01.PDR.0000129184.87042.FC.

Chi, P., Van Komen, S., Sehorn, M.G., Sigurdsson, S., and Sung, P. (2006). Roles of ATP binding and ATP hydrolysis in human Rad51 recombinase function. DNA Repair (Amst) *5*, 381-391. 10.1016/j.dnarep.2005.11.005.

Choi, E.S., Nichol, J.L., Hokom, M.M., Hornkohl, A.C., and Hunt, P. (1995). Platelets generated in vitro from proplatelet-displaying human megakaryocytes are functional. Blood *85*, 402-413.

Chua, E.Y.D., Mendez, J.H., Rapp, M., Ilca, S.L., Tan, Y.Z., Maruthi, K., Kuang, H., Zimanyi, C.M., Cheng, A., Eng, E.T., et al. (2022). Better, Faster, Cheaper: Recent Advances in Cryo-Electron Microscopy. Annu Rev Biochem *91*, 1-32. 10.1146/annurev-biochem-032620-110705.

Ciccia, A., Constantinou, A., and West, S.C. (2003). Identification and characterization of the human mus81-eme1 endonuclease. J Biol Chem *278*, 25172-25178. 10.1074/jbc.M302882200.

Ciccia, A., McDonald, N., and West, S.C. (2008). Structural and functional relationships of the XPF/MUS81 family of proteins. Annu Rev Biochem *77*, 259-287. 10.1146/annurev.biochem.77.070306.102408.

Clark, S.R., Ma, A.C., Tavener, S.A., McDonald, B., Goodarzi, Z., Kelly, M.M., Patel, K.D., Chakrabarti, S., McAvoy, E., Sinclair, G.D., et al. (2007). Platelet TLR4 activates neutrophil extracellular traps to ensnare bacteria in septic blood. Nat Med *13*, 463-469. 10.1038/nm1565.

Collado, J., and Fernandez-Busnadiego, R. (2017). Deciphering the molecular architecture of membrane contact sites by cryo-electron tomography. Biochim Biophys Acta Mol Cell Res *1864*, 1507-1512. 10.1016/j.bbamcr.2017.03.009.

Corman, V.M., Muth, D., Niemeyer, D., and Drosten, C. (2018). Hosts and Sources of Endemic Human Coronaviruses. Adv Virus Res *100*, 163-188. 10.1016/bs.aivir.2018.01.001.

Coronaviridae Study Group of the International Committee on Taxonomy of, V. (2020). The species Severe acute respiratory syndrome-related coronavirus: classifying 2019-nCoV and naming it SARS-CoV-2. Nat Microbiol *5*, 536-544. 10.1038/s41564-020-0695-z.

Coutard, B., Valle, C., de Lamballerie, X., Canard, B., Seidah, N.G., and Decroly, E. (2020). The spike glycoprotein of the new coronavirus 2019-nCoV contains a furin-like cleavage site absent in CoV of the same clade. Antiviral Res *176*, 104742. 10.1016/j.antiviral.2020.104742.

Crawford, K.H.D., Eguia, R., Dingens, A.S., Loes, A.N., Malone, K.D., Wolf, C.R., Chu, H.Y., Tortorici, M.A., Veesler, D., Murphy, M., et al. (2020). Protocol and Reagents for Pseudotyping Lentiviral Particles with SARS-CoV-2 Spike Protein for Neutralization Assays. Viruses *12*. 10.3390/v12050513.

D'Imprima, E., Floris, D., Joppe, M., Sanchez, R., Grininger, M., and Kuhlbrandt, W. (2019). Protein denaturation at the air-water interface and how to prevent it. Elife *8*. 10.7554/eLife.42747.

Daly, J.L., Simonetti, B., Klein, K., Chen, K.E., Williamson, M.K., Anton-Plagaro, C., Shoemark, D.K., Simon-Gracia, L., Bauer, M., Hollandi, R., et al. (2020). Neuropilin-1 is a host factor for SARS-CoV-2 infection. Science *370*, 861-865. 10.1126/science.abd3072.

Dandey, V.P., Wei, H., Zhang, Z., Tan, Y.Z., Acharya, P., Eng, E.T., Rice, W.J., Kahn, P.A., Potter, C.S., and Carragher, B. (2018). Spotiton: New features and applications. J Struct Biol *202*, 161-169. 10.1016/j.jsb.2018.01.002.

Davies, O.R., and Pellegrini, L. (2007). Interaction with the BRCA2 C terminus protects RAD51-DNA filaments from disassembly by BRC repeats. Nat Struct Mol Biol *14*, 475-483. 10.1038/nsmb1251.

de Kleijn, D., and Pasterkamp, G. (2003). Toll-like receptors in cardiovascular diseases. Cardiovasc Res *60*, 58-67. 10.1016/s0008-6363(03)00348-1.

de Mast, Q., Groot, E., Lenting, P.J., de Groot, P.G., McCall, M., Sauerwein, R.W., Fijnheer, R., and van der Ven, A. (2007). Thrombocytopenia and release of activated von Willebrand Factor during early Plasmodium falciparum malaria. J Infect Dis *196*, 622-628. 10.1086/519844.

Dedden, D., Schumacher, S., Kelley, C.F., Zacharias, M., Biertumpfel, C., Fassler, R., and Mizuno, N. (2019). The Architecture of Talin1 Reveals an Autoinhibition Mechanism. Cell *179*, 120-131 e113. 10.1016/j.cell.2019.08.034.

Dehe, P.M., and Gaillard, P.H.L. (2017). Control of structure-specific endonucleases to maintain genome stability. Nat Rev Mol Cell Biol *18*, 315-330. 10.1038/nrm.2016.177.

Deutsch, V.R., and Tomer, A. (2006). Megakaryocyte development and platelet production. Br J Haematol *134*, 453-466. 10.1111/j.1365-2141.2006.06215.x.

Dobro, M.J., Melanson, L.A., Jensen, G.J., and McDowall, A.W. (2010). Plunge freezing for electron cryomicroscopy. Methods Enzymol *481*, 63-82. 10.1016/S0076-6879(10)81003-1.

Du, L., He, Y., Zhou, Y., Liu, S., Zheng, B.J., and Jiang, S. (2009). The spike protein of SARS-CoV--a target for vaccine and therapeutic development. Nat Rev Microbiol *7*, 226-236. 10.1038/nrmicro2090.

Dubochet, J., Adrian, M., Chang, J.J., Homo, J.C., Lepault, J., McDowall, A.W., and Schultz, P. (1988). Cryo-electron microscopy of vitrified specimens. Q Rev Biophys *21*, 129-228. 10.1017/s0033583500004297.

Dubochet, J., Lepault, J., Freeman, R., Berriman, J.A., and Homo, J.-C. (1982). Electron microscopy of frozen water and aqueous solutions. Journal of Microscopy *128*, 219-237. https://doi.org/10.1111/j.1365-2818.1982.tb04625.x.

Dunin-Horkawicz, S., Feder, M., and Bujnicki, J.M. (2006). Phylogenomic analysis of the GIY-YIG nuclease superfamily. BMC Genomics *7*, 98. 10.1186/1471-2164-7-98.

Emsley, P., Lohkamp, B., Scott, W.G., and Cowtan, K. (2010). Features and development of Coot. Acta Crystallogr D Biol Crystallogr *66*, 486-501. 10.1107/S0907444910007493.

Fajgenbaum, D.C., and June, C.H. (2020). Cytokine Storm. N Engl J Med *383*, 2255-2273. 10.1056/NEJMra2026131.

Fajnzylber, J., Regan, J., Coxen, K., Corry, H., Wong, C., Rosenthal, A., Worrall, D., Giguel, F., Piechocka-Trocha, A., Atyeo, C., et al. (2020). SARS-CoV-2 viral load is associated with increased disease severity and mortality. Nat Commun *11*, 5493. 10.1038/s41467-020-19057-5.

Fang, X., Gao, J., Zheng, H., Li, B., Kong, L., Zhang, Y., Wang, W., Zeng, Y., and Ye, L. (2007). The membrane protein of SARS-CoV suppresses NF-kappaB activation. J Med Virol *79*, 1431-1439. 10.1002/jmv.20953.

Fantini, J., Di Scala, C., Chahinian, H., and Yahi, N. (2020). Structural and molecular modelling studies reveal a new mechanism of action of chloroquine and hydroxychloroquine against SARS-CoV-2 infection. Int J Antimicrob Agents *55*, 105960. 10.1016/j.ijantimicag.2020.105960.

Fekairi, S., Scaglione, S., Chahwan, C., Taylor, E.R., Tissier, A., Coulon, S., Dong, M.Q., Ruse, C., Yates, J.R., 3rd, Russell, P., et al. (2009). Human SLX4 is a Holliday junction resolvase subunit that binds multiple DNA repair/recombination endonucleases. Cell *138*, 78-89. 10.1016/j.cell.2009.06.029.

Fernandez, J.J., Li, S., Bharat, T.A.M., and Agard, D.A. (2018). Cryo-tomography tilt-series alignment with consideration of the beam-induced sample motion. J Struct Biol *202*, 200-209. 10.1016/j.jsb.2018.02.001.

Finkel, Y., Mizrahi, O., Nachshon, A., Weingarten-Gabbay, S., Morgenstern, D., Yahalom-Ronen, Y., Tamir, H., Achdout, H., Stein, D., Israeli, O., et al. (2021). The coding capacity of SARS-CoV-2. Nature *589*, 125-130. 10.1038/s41586-020-2739-1.

Flower, T.G., Buffalo, C.Z., Hooy, R.M., Allaire, M., Ren, X., and Hurley, J.H. (2021). Structure of SARS-CoV-2 ORF8, a rapidly evolving immune evasion protein. Proc Natl Acad Sci U S A *118*. 10.1073/pnas.2021785118.

Frangakis, A.S., Bohm, J., Forster, F., Nickell, S., Nicastro, D., Typke, D., Hegerl, R., and Baumeister, W. (2002). Identification of macromolecular complexes in cryoelectron tomograms of phantom cells. Proc Natl Acad Sci U S A *99*, 14153-14158. 10.1073/pnas.172520299.

Frank, J., Zhu, J., Penczek, P., Li, Y., Srivastava, S., Verschoor, A., Radermacher, M., Grassucci, R., Lata, R.K., and Agrawal, R.K. (1995). A model of protein synthesis based on cryo-electron microscopy of the E. coli ribosome. Nature *376*, 441-444. 10.1038/376441a0.

Franken, L.E., Grunewald, K., Boekema, E.J., and Stuart, M.C.A. (2020). A Technical Introduction to Transmission Electron Microscopy for Soft-Matter: Imaging, Possibilities, Choices, and Technical Developments. Small *16*, e1906198. 10.1002/smll.201906198.

Freeman, A.D.J., Liu, Y., Declais, A.C., Gartner, A., and Lilley, D.M.J. (2014). GEN1 from a thermophilic fungus is functionally closely similar to non-eukaryotic junction-resolving enzymes. J Mol Biol *426*, 3946-3959. 10.1016/j.jmb.2014.10.008.

Furukawa, T., Kimura, S., Ishibashi, T., Mori, Y., Hashimoto, J., and Sakaguchi, K. (2003). OsSEND-1: a new RAD2 nuclease family member in higher plants. Plant Mol Biol *51*, 59-70. 10.1023/a:1020789314722.

Galaz-Montoya, J.G., and Ludtke, S.J. (2017). The advent of structural biology in situ by single particle cryo-electron tomography. Biophys Rep *3*, 17-35. 10.1007/s41048-017-0040-0.

Gao, X., Zhu, K., Qin, B., Olieric, V., Wang, M., and Cui, S. (2021). Crystal structure of SARS-CoV-2 Orf9b in complex with human TOM70 suggests unusual virus-host interactions. Nat Commun *12*, 2843. 10.1038/s41467-021-23118-8.

Garcia-Luis, J., Clemente-Blanco, A., Aragon, L., and Machin, F. (2014). Cdc14 targets the Holliday junction resolvase Yen1 to the nucleus in early anaphase. Cell Cycle *13*, 1392-1399. 10.4161/cc.28370.

Garraud, O., Berthet, J., Hamzeh-Cognasse, H., and Cognasse, F. (2011). Pathogen sensing, subsequent signalling, and signalosome in human platelets. Thromb Res *127*, 283-286. 10.1016/j.thromres.2010.10.015.

Ghosh, S., Dellibovi-Ragheb, T.A., Kerviel, A., Pak, E., Qiu, Q., Fisher, M., Takvorian, P.M., Bleck, C., Hsu, V.W., Fehr, A.R., et al. (2020). beta-Coronaviruses Use Lysosomes for Egress Instead of the Biosynthetic Secretory Pathway. Cell *183*, 1520-1535 e1514. 10.1016/j.cell.2020.10.039.

Ghoshal, K., and Bhattacharyya, M. (2014). Overview of platelet physiology: its hemostatic and nonhemostatic role in disease pathogenesis. ScientificWorldJournal *2014*, 781857. 10.1155/2014/781857.

Glaeser, R.M., and Han, B.G. (2017). Opinion: hazards faced by macromolecules when confined to thin aqueous films. Biophys Rep *3*, 1-7. 10.1007/s41048-016-0026-3.

Gosert, R., Kanjanahaluethai, A., Egger, D., Bienz, K., and Baker, S.C. (2002). RNA replication of mouse hepatitis virus takes place at double-membrane vesicles. J Virol *76*, 3697-3708. 10.1128/jvi.76.8.3697-3708.2002.

Grasby, J.A., Finger, L.D., Tsutakawa, S.E., Atack, J.M., and Tainer, J.A. (2012). Unpairing and gating: sequence-independent substrate recognition by FEN superfamily nucleases. Trends Biochem Sci *37*, 74-84. 10.1016/j.tibs.2011.10.003.

Gui, M., Song, W., Zhou, H., Xu, J., Chen, S., Xiang, Y., and Wang, X. (2017). Cryo-electron microscopy structures of the SARS-CoV spike glycoprotein reveal a prerequisite conformational state for receptor binding. Cell Res *27*, 119-129. 10.1038/cr.2016.152.

Guidetti, G.F., Torti, M., and Canobbio, I. (2019). Focal Adhesion Kinases in Platelet Function and Thrombosis. Arterioscler Thromb Vasc Biol *39*, 857-868. 10.1161/ATVBAHA.118.311787.

Guo, L., and Rondina, M.T. (2019). The Era of Thromboinflammation: Platelets Are Dynamic Sensors and Effector Cells During Infectious Diseases. Front Immunol *10*, 2204. 10.3389/fimmu.2019.02204.

Guo, Y.R., Cao, Q.D., Hong, Z.S., Tan, Y.Y., Chen, S.D., Jin, H.J., Tan, K.S., Wang, D.Y., and Yan, Y. (2020). The origin, transmission and clinical therapies on coronavirus disease 2019 (COVID-19) outbreak - an update on the status. Mil Med Res *7*, 11. 10.1186/s40779-020-00240-0.

Hadden, J.M., Declais, A.C., Carr, S.B., Lilley, D.M., and Phillips, S.E. (2007). The structural basis of Holliday junction resolution by T7 endonuclease I. Nature *449*, 621-624. 10.1038/nature06158.

Hadid, T., Kafri, Z., and Al-Katib, A. (2021). Coagulation and anticoagulation in COVID-19. Blood Rev *47*, 100761. 10.1016/j.blre.2020.100761.

Hagen, W.J.H., Wan, W., and Briggs, J.A.G. (2017). Implementation of a cryo-electron tomography tilt-scheme optimized for high resolution subtomogram averaging. J Struct Biol *197*, 191-198. 10.1016/j.jsb.2016.06.007.

Hartenian, E., Nandakumar, D., Lari, A., Ly, M., Tucker, J.M., and Glaunsinger, B.A. (2020). The molecular virology of coronaviruses. J Biol Chem *295*, 12910-12934. 10.1074/jbc.REV120.013930.

Hartwig, J.H. (2006). The platelet: form and function. Semin Hematol *43*, S94-100. 10.1053/j.seminhematol.2005.11.004.

Helmy, Y.A., Fawzy, M., Elaswad, A., Sobieh, A., Kenney, S.P., and Shehata, A.A. (2020). The COVID-19 Pandemic: A Comprehensive Review of Taxonomy, Genetics, Epidemiology, Diagnosis, Treatment, and Control. J Clin Med *9*. 10.3390/jcm9041225.

Henderson, R., Baldwin, J.M., Ceska, T.A., Zemlin, F., Beckmann, E., and Downing, K.H. (1990). Model for the structure of bacteriorhodopsin based on high-resolution electron cryo-microscopy. J Mol Biol *213*, 899-929. 10.1016/S0022-2836(05)80271-2.

Her, J., and Bunting, S.F. (2018). How cells ensure correct repair of DNA double-strand breaks. J Biol Chem *293*, 10502-10511. 10.1074/jbc.TM118.000371.

Heyer, W.D. (2004). Recombination: Holliday junction resolution and crossover formation. Curr Biol *14*, R56-58. 10.1016/j.cub.2003.12.043.

Heyer, W.D. (2015). Regulation of recombination and genomic maintenance. Cold Spring Harb Perspect Biol *7*, a016501. 10.1101/cshperspect.a016501.

Hoadley, K.A., Xu, D., Xue, Y., Satyshur, K.A., Wang, W., and Keck, J.L. (2010). Structure and cellular roles of the RMI core complex from the bloom syndrome dissolvasome. Structure *18*, 1149-1158. 10.1016/j.str.2010.06.009.

Hodson, C., Low, J.K.K., van Twest, S., Jones, S.E., Swuec, P., Murphy, V., Tsukada, K., Fawkes, M., Bythell-Douglas, R., Davies, A., et al. (2022). Mechanism of Bloom syndrome complex assembly required for double Holliday junction dissolution and genome stability. Proc Natl Acad Sci U S A *119*. 10.1073/pnas.2109093119.

Hoffmann, M., Kleine-Weber, H., Schroeder, S., Kruger, N., Herrler, T., Erichsen, S., Schiergens, T.S., Herrler, G., Wu, N.H., Nitsche, A., et al. (2020). SARS-CoV-2 Cell Entry Depends on ACE2 and TMPRSS2 and Is Blocked by a Clinically Proven Protease Inhibitor. Cell *181*, 271-280 e278. 10.1016/j.cell.2020.02.052.

Holliday, R. (1964). The Induction of Mitotic Recombination by Mitomycin C in Ustilago and Saccharomyces. Genetics *50*, 323-335. 10.1093/genetics/50.3.323.

Hottz, E.D., Oliveira, M.F., Nunes, P.C., Nogueira, R.M., Valls-de-Souza, R., Da Poian, A.T., Weyrich, A.S., Zimmerman, G.A., Bozza, P.T., and Bozza, F.A. (2013). Dengue induces platelet activation, mitochondrial dysfunction and cell death through mechanisms that involve DC-SIGN and caspases. J Thromb Haemost *11*, 951-962. 10.1111/jth.12178.

Huang, C., Wang, Y., Li, X., Ren, L., Zhao, J., Hu, Y., Zhang, L., Fan, G., Xu, J., Gu, X., et al. (2020a). Clinical features of patients infected with 2019 novel coronavirus in Wuhan, China. Lancet *395*, 497-506. 10.1016/S0140-6736(20)30183-5.

Huang, J., Li, X., Shi, X., Zhu, M., Wang, J., Huang, S., Huang, X., Wang, H., Li, L., Deng, H., et al. (2019). Platelet integrin alphaIIbbeta3: signal transduction, regulation, and its therapeutic targeting. J Hematol Oncol *12*, 26. 10.1186/s13045-019-0709-6.

Huang, Y., Yang, C., Xu, X.F., Xu, W., and Liu, S.W. (2020b). Structural and functional properties of SARS-CoV-2 spike protein: potential antivirus drug development for COVID-19. Acta Pharmacol Sin *41*, 1141-1149. 10.1038/s41401-020-0485-4.

Ip, S.C., Rass, U., Blanco, M.G., Flynn, H.R., Skehel, J.M., and West, S.C. (2008). Identification of Holliday junction resolvases from humans and yeast. Nature *456*, 357-361. 10.1038/nature07470.

Ishikawa, G., Kanai, Y., Takata, K., Takeuchi, R., Shimanouchi, K., Ruike, T., Furukawa, T., Kimura, S., and Sakaguchi, K. (2004). DmGEN, a novel RAD2 family endo-exonuclease from Drosophila melanogaster. Nucleic Acids Res *32*, 6251-6259. 10.1093/nar/gkh962.

Italiano, J.E., Jr. (2013). Unraveling mechanisms that control platelet production. Semin Thromb Hemost *39*, 15-24. 10.1055/s-0032-1331157.

Italiano, J.E., Jr., Lecine, P., Shivdasani, R.A., and Hartwig, J.H. (1999). Blood platelets are assembled principally at the ends of proplatelet processes produced by differentiated megakaryocytes. J Cell Biol *147*, 1299-1312. 10.1083/jcb.147.6.1299.

Johnson, B.A., Xie, X., Bailey, A.L., Kalveram, B., Lokugamage, K.G., Muruato, A., Zou, J., Zhang, X., Juelich, T., Smith, J.K., et al. (2021). Loss of furin cleavage site attenuates SARS-CoV-2 pathogenesis. Nature *591*, 293-299. 10.1038/s41586-021-03237-4.

Johnson, R.M., Higgins, A.J., and Muench, S.P. (2019). Emerging Role of Electron Microscopy in Drug Discovery. Trends Biochem Sci *44*, 897-898. 10.1016/j.tibs.2019.07.003.

Jumper, J., Evans, R., Pritzel, A., Green, T., Figurnov, M., Ronneberger, O., Tunyasuvunakool, K., Bates, R., Zidek, A., Potapenko, A., et al. (2021). Highly accurate protein structure prediction with AlphaFold. Nature *596*, 583-589. 10.1038/s41586-021-03819-2.

Junt, T., Schulze, H., Chen, Z., Massberg, S., Goerge, T., Krueger, A., Wagner, D.D., Graf, T., Italiano, J.E., Jr., Shivdasani, R.A., and von Andrian, U.H. (2007). Dynamic visualization of thrombopoiesis within bone marrow. Science *317*, 1767-1770. 10.1126/science.1146304.

Kanai, Y., Ishikawa, G., Takeuchi, R., Ruike, T., Nakamura, R., Ihara, A., Ohashi, T., Takata, K., Kimura, S., and Sakaguchi, K. (2007). DmGEN shows a flap endonuclease activity, cleaving the blocked-flap structure and model replication fork. FEBS J *274*, 3914-3927. 10.1111/j.1742-4658.2007.05924.x.

Karow, J.K., Constantinou, A., Li, J.L., West, S.C., and Hickson, I.D. (2000). The Bloom's syndrome gene product promotes branch migration of holliday junctions. Proc Natl Acad Sci U S A *97*, 6504-6508. 10.1073/pnas.100448097.

Kato, T., Makino, F., Nakane, T., Terahara, N., Kaneko, T., Shimizu, Y., . . . Namba, K. (2019). CryoTEM with a Cold Field Emission Gun That Moves Structural Biology into a New Stage. Microscopy and Microanalysis *25* (*S2*), 998-999.

Ke, Z., Oton, J., Qu, K., Cortese, M., Zila, V., McKeane, L., Nakane, T., Zivanov, J., Neufeldt, C.J., Cerikan, B., et al. (2020). Structures and distributions of SARS-CoV-2 spike proteins on intact virions. Nature *588*, 498-502. 10.1038/s41586-020-2665-2.

Kimanius, D., Dong, L., Sharov, G., Nakane, T., and Scheres, S.H.W. (2021). New tools for automated cryo-EM single-particle analysis in RELION-4.0. Biochem J *478*, 4169-4185. 10.1042/BCJ20210708.

Kimanius, D., Forsberg, B.O., Scheres, S.H., and Lindahl, E. (2016). Accelerated cryo-EM structure determination with parallelisation using GPUs in RELION-2. Elife *5*. 10.7554/eLife.18722.

Klein, S., Cortese, M., Winter, S.L., Wachsmuth-Melm, M., Neufeldt, C.J., Cerikan, B., Stanifer, M.L., Boulant, S., Bartenschlager, R., and Chlanda, P. (2020). SARS-CoV-2 structure and replication characterized by in situ cryo-electron tomography. Nat Commun *11*, 5885. 10.1038/s41467-020-19619-7.

Knoops, K., Kikkert, M., Worm, S.H., Zevenhoven-Dobbe, J.C., van der Meer, Y., Koster, A.J., Mommaas, A.M., and Snijder, E.J. (2008). SARS-coronavirus replication is supported by a reticulovesicular network of modified endoplasmic reticulum. PLoS Biol *6*, e226. 10.1371/journal.pbio.0060226.

Koetzner, C.A., Parker, M.M., Ricard, C.S., Sturman, L.S., and Masters, P.S. (1992). Repair and mutagenesis of the genome of a deletion mutant of the coronavirus mouse hepatitis virus by targeted RNA recombination. J Virol *66*, 1841-1848. 10.1128/JVI.66.4.1841-1848.1992.

Koupenova, M., Corkrey, H.A., Vitseva, O., Tanriverdi, K., Somasundaran, M., Liu, P., Soofi, S., Bhandari, R., Godwin, M., Parsi, K.M., et al. (2021). SARS-CoV-2 Initiates Programmed Cell Death in Platelets. Circ Res *129*, 631-646. 10.1161/CIRCRESAHA.121.319117.

Kowalczykowski, S.C. (2015). An Overview of the Molecular Mechanisms of Recombinational DNA Repair. Cold Spring Harb Perspect Biol *7*. 10.1101/cshperspect.a016410.

Kuhlbrandt, W. (2014). Biochemistry. The resolution revolution. Science *343*, 1443-1444. 10.1126/science.1251652.

Kumar, B., Hawkins, G.M., Kicmal, T., Qing, E., Timm, E., and Gallagher, T. (2021). Assembly and Entry of Severe Acute Respiratory Syndrome Coronavirus 2 (SARS-CoV2): Evaluation Using Virus-Like Particles. Cells *10*. 10.3390/cells10040853.

Ladinsky, M.S. (2010). Micromanipulator-assisted vitreous cryosectioning and sample preparation by high-pressure freezing. Methods Enzymol *481*, 165-194. 10.1016/S0076-6879(10)81008-0.

Lan, J., Ge, J., Yu, J., Shan, S., Zhou, H., Fan, S., Zhang, Q., Shi, X., Wang, Q., Zhang, L., and Wang, X. (2020). Structure of the SARS-CoV-2 spike receptor-binding domain bound to the ACE2 receptor. Nature *581*, 215-220. 10.1038/s41586-020-2180-5.

Laue, M., Kauter, A., Hoffmann, T., Moller, L., Michel, J., and Nitsche, A. (2021). Morphometry of SARS-CoV and SARS-CoV-2 particles in ultrathin plastic sections of infected Vero cell cultures. Sci Rep *11*, 3515. 10.1038/s41598-021-82852-7.

Lee, S.H., Princz, L.N., Klugel, M.F., Habermann, B., Pfander, B., and Biertumpfel, C. (2015). Human Holliday junction resolvase GEN1 uses a chromodomain for efficient DNA recognition and cleavage. Elife *4*. 10.7554/eLife.12256.

Leigh, K.E., Navarro, P.P., Scaramuzza, S., Chen, W., Zhang, Y., Castano-Diez, D., and Kudryashev, M. (2019). Subtomogram averaging from cryo-electron tomograms. Methods Cell Biol *152*, 217-259. 10.1016/bs.mcb.2019.04.003.

Li, L., Tan, C., Zeng, J., Luo, C., Hu, S., Peng, Y., Li, W., Xie, Z., Ling, Y., Zhang, X., et al. (2021). Analysis of viral load in different specimen types and serum antibody levels of COVID-19 patients. J Transl Med *19*, 30. 10.1186/s12967-020-02693-2.

Li, X., and Heyer, W.D. (2008). Homologous recombination in DNA repair and DNA damage tolerance. Cell Res *18*, 99-113. 10.1038/cr.2008.1.

Li, X., Stith, C.M., Burgers, P.M., and Heyer, W.D. (2009). PCNA is required for initiation of recombination-associated DNA synthesis by DNA polymerase delta. Mol Cell *36*, 704-713. 10.1016/j.molcel.2009.09.036.

Li, Z., Delaney, M.K., O'Brien, K.A., and Du, X. (2010). Signaling during platelet adhesion and activation. Arterioscler Thromb Vasc Biol *30*, 2341-2349. 10.1161/ATVBAHA.110.207522.

Liebschner, D., Afonine, P.V., Baker, M.L., Bunkoczi, G., Chen, V.B., Croll, T.I., Hintze, B., Hung, L.W., Jain, S., McCoy, A.J., et al. (2019). Macromolecular structure determination using X-rays, neutrons and electrons: recent developments in Phenix. Acta Crystallogr D Struct Biol *75*, 861-877. 10.1107/S2059798319011471.

Lilley, D.M.J. (2017). Holliday junction-resolving enzymes-structures and mechanisms. FEBS Lett *591*, 1073-1082. 10.1002/1873-3468.12529.

Lippi, G., Plebani, M., and Henry, B.M. (2020). Thrombocytopenia is associated with severe coronavirus disease 2019 (COVID-19) infections: A meta-analysis. Clin Chim Acta *506*, 145-148. 10.1016/j.cca.2020.03.022.

Liu, J., Lu, F., Chen, Y., Plow, E., and Qin, J. (2022). Integrin mediates cell entry of the SARS-CoV-2 virus independent of cellular receptor ACE2. J Biol Chem *298*, 101710. 10.1016/j.jbc.2022.101710.

Liu, Y., Freeman, A.D., Declais, A.C., and Lilley, D.M.J. (2018). A monovalent ion in the DNA binding interface of the eukaryotic junction-resolving enzyme GEN1. Nucleic Acids Res *46*, 11089-11098. 10.1093/nar/gky863.

Liu, Y., Freeman, A.D.J., Declais, A.C., Wilson, T.J., Gartner, A., and Lilley, D.M.J. (2015). Crystal Structure of a Eukaryotic GEN1 Resolving Enzyme Bound to DNA. Cell Rep *13*, 2565-2575. 10.1016/j.celrep.2015.11.042.

Liu, Y., Kao, H.I., and Bambara, R.A. (2004). Flap endonuclease 1: a central component of DNA metabolism. Annu Rev Biochem *73*, 589-615. 10.1146/annurev.biochem.73.012803.092453.

Liu, Y., and West, S.C. (2004). Happy Hollidays: 40th anniversary of the Holliday junction. Nat Rev Mol Cell Biol *5*, 937-944. 10.1038/nrm1502.

Llorente, B., Smith, C.E., and Symington, L.S. (2008). Break-induced replication: what is it and what is it for? Cell Cycle *7*, 859-864. 10.4161/cc.7.7.5613.

Lodigiani, C., Iapichino, G., Carenzo, L., Cecconi, M., Ferrazzi, P., Sebastian, T., Kucher, N., Studt, J.D., Sacco, C., Bertuzzi, A., et al. (2020). Venous and arterial thromboembolic complications in COVID-19 patients admitted to an academic hospital in Milan, Italy. Thromb Res *191*, 9-14. 10.1016/j.thromres.2020.04.024.

Lu, G., Wang, Q., and Gao, G.F. (2015). Bat-to-human: spike features determining 'host jump' of coronaviruses SARS-CoV, MERS-CoV, and beyond. Trends Microbiol *23*, 468-478. 10.1016/j.tim.2015.06.003.

Lu, R., Zhao, X., Li, J., Niu, P., Yang, B., Wu, H., Wang, W., Song, H., Huang, B., Zhu, N., et al. (2020). Genomic characterisation and epidemiology of 2019 novel coronavirus: implications for virus origins and receptor binding. Lancet *395*, 565-574. 10.1016/S0140-6736(20)30251-8.

Lu, S., Ye, Q., Singh, D., Cao, Y., Diedrich, J.K., Yates, J.R., 3rd, Villa, E., Cleveland, D.W., and Corbett, K.D. (2021). The SARS-CoV-2 nucleocapsid phosphoprotein forms mutually exclusive condensates with RNA and the membrane-associated M protein. Nat Commun *12*, 502. 10.1038/s41467-020-20768-y.

Lucic, V., Forster, F., and Baumeister, W. (2005). Structural studies by electron tomography: from cells to molecules. Annu Rev Biochem *74*, 833-865. 10.1146/annurev.biochem.73.011303.074112.

Lucic, V., Rigort, A., and Baumeister, W. (2013). Cryo-electron tomography: the challenge of doing structural biology in situ. J Cell Biol *202*, 407-419. 10.1083/jcb.201304193.

Luo, H., Wu, D., Shen, C., Chen, K., Shen, X., and Jiang, H. (2006). Severe acute respiratory syndrome coronavirus membrane protein interacts with nucleocapsid protein mostly through their carboxyl termini by electrostatic attraction. Int J Biochem Cell Biol *38*, 589-599. 10.1016/j.biocel.2005.10.022.

Mageswaran, S.K., Yang, W.Y., Chakrabarty, Y., Oikonomou, C.M., and Jensen, G.J. (2021). A cryo-electron tomography workflow reveals protrusion-mediated shedding on injured plasma membrane. Sci Adv *7*. 10.1126/sciadv.abc6345.

Maher, R.L., Branagan, A.M., and Morrical, S.W. (2011). Coordination of DNA replication and recombination activities in the maintenance of genome stability. J Cell Biochem *112*, 2672-2682. 10.1002/jcb.23211.

Makowski, L., Olson-Sidford, W., and J, W.W. (2021). Biological and Clinical Consequences of Integrin Binding via a Rogue RGD Motif in the SARS CoV-2 Spike Protein. Viruses *13*. 10.3390/v13020146.

Malone, B., Urakova, N., Snijder, E.J., and Campbell, E.A. (2022). Structures and functions of coronavirus replication-transcription complexes and their relevance for SARS-CoV-2 drug design. Nat Rev Mol Cell Biol *23*, 21-39. 10.1038/s41580-021-00432-z.

Mandala, V.S., McKay, M.J., Shcherbakov, A.A., Dregni, A.J., Kolocouris, A., and Hong, M. (2020). Structure and drug binding of the SARS-CoV-2 envelope protein transmembrane domain in lipid bilayers. Nat Struct Mol Biol *27*, 1202-1208. 10.1038/s41594-020-00536-8.

Manne, B.K., Denorme, F., Middleton, E.A., Portier, I., Rowley, J.W., Stubben, C., Petrey, A.C., Tolley, N.D., Guo, L., Cody, M., et al. (2020). Platelet gene expression and function in patients with COVID-19. Blood *136*, 1317-1329. 10.1182/blood.2020007214.

Mariano, G., Farthing, R.J., Lale-Farjat, S.L.M., and Bergeron, J.R.C. (2020). Structural Characterization of SARS-CoV-2: Where We Are, and Where We Need to Be. Front Mol Biosci *7*, 605236. 10.3389/fmolb.2020.605236.

Marko, M., Hsieh, C., Schalek, R., Frank, J., and Mannella, C. (2007). Focused-ion-beam thinning of frozen-hydrated biological specimens for cryo-electron microscopy. Nat Methods *4*, 215-217. 10.1038/nmeth1014.

Martinez-Sanchez, A., Kochovski, Z., Laugks, U., Meyer Zum Alten Borgloh, J., Chakraborty, S., Pfeffer, S., Baumeister, W., and Lucic, V. (2020). Template-free detection and classification of membrane-bound complexes in cryo-electron tomograms. Nat Methods *17*, 209-216. 10.1038/s41592-019-0675-5.

Masri, M.F.B., Mantri, C.K., Rathore, A.P.S., and John, A.L.S. (2019). Peripheral serotonin causes dengue virus-induced thrombocytopenia through 5HT2 receptors. Blood *133*, 2325-2337. 10.1182/blood-2018-08-869156.

Masters, P.S. (2019). Coronavirus genomic RNA packaging. Virology *537*, 198-207. 10.1016/j.virol.2019.08.031.

Mastronarde, D.N., and Held, S.R. (2017). Automated tilt series alignment and tomographic reconstruction in IMOD. J Struct Biol *197*, 102-113. 10.1016/j.jsb.2016.07.011.

Matos, J., and West, S.C. (2014). Holliday junction resolution: regulation in space and time. DNA Repair (Amst) *19*, 176-181. 10.1016/j.dnarep.2014.03.013.

McVey, M., Khodaverdian, V.Y., Meyer, D., Cerqueira, P.G., and Heyer, W.D. (2016). Eukaryotic DNA Polymerases in Homologous Recombination. Annu Rev Genet *50*, 393-421. 10.1146/annurev-genet-120215-035243.

Mehrbod, M., Trisno, S., and Mofrad, M.R. (2013). On the activation of integrin alphaIIbbeta3: outside-in and inside-out pathways. Biophys J *105*, 1304-1315. 10.1016/j.bpj.2013.07.055.

Mehta, A., and Haber, J.E. (2014). Sources of DNA double-strand breaks and models of recombinational DNA repair. Cold Spring Harb Perspect Biol *6*, a016428. 10.1101/cshperspect.a016428.

Mendonca, L., Howe, A., Gilchrist, J.B., Sheng, Y., Sun, D., Knight, M.L., Zanetti-Domingues, L.C., Bateman, B., Krebs, A.S., Chen, L., et al. (2021). Correlative multi-scale cryo-imaging unveils SARS-CoV-2 assembly and egress. Nat Commun *12*, 4629. 10.1038/s41467-021-24887-y.

Miao, G., Zhao, H., Li, Y., Ji, M., Chen, Y., Shi, Y., Bi, Y., Wang, P., and Zhang, H. (2021). ORF3a of the COVID-19 virus SARS-CoV-2 blocks HOPS complex-mediated assembly of the SNARE complex required for autolysosome formation. Dev Cell *56*, 427-442 e425. 10.1016/j.devcel.2020.12.010.

Middleton, E.A., He, X.Y., Denorme, F., Campbell, R.A., Ng, D., Salvatore, S.P., Mostyka, M., Baxter-Stoltzfus, A., Borczuk, A.C., Loda, M., et al. (2020). Neutrophil extracellular traps contribute to immunothrombosis in COVID-19 acute respiratory distress syndrome. Blood *136*, 1169-1179. 10.1182/blood.2020007008.

Middleton, E.A., Weyrich, A.S., and Zimmerman, G.A. (2016). Platelets in Pulmonary Immune Responses and Inflammatory Lung Diseases. Physiol Rev *96*, 1211-1259. 10.1152/physrev.00038.2015.

Millet, J.K., and Whittaker, G.R. (2018). Physiological and molecular triggers for SARS-CoV membrane fusion and entry into host cells. Virology *517*, 3-8. 10.1016/j.virol.2017.12.015.

Mimitou, E.P., and Symington, L.S. (2008). Sae2, Exo1 and Sgs1 collaborate in DNA double-strand break processing. Nature *455*, 770-774. 10.1038/nature07312.

Moynahan, M.E., and Jasin, M. (2010). Mitotic homologous recombination maintains genomic stability and suppresses tumorigenesis. Nat Rev Mol Cell Biol *11*, 196-207. 10.1038/nrm2851.

Mullins, R.D., Heuser, J.A., and Pollard, T.D. (1998). The interaction of Arp2/3 complex with actin: nucleation, high affinity pointed end capping, and formation of branching networks of filaments. Proc Natl Acad Sci U S A *95*, 6181-6186. 10.1073/pnas.95.11.6181.

Munoz, I.M., Hain, K., Declais, A.C., Gardiner, M., Toh, G.W., Sanchez-Pulido, L., Heuckmann, J.M., Toth, R., Macartney, T., Eppink, B., et al. (2009). Coordination of structure-specific nucleases by human SLX4/BTBD12 is required for DNA repair. Mol Cell *35*, 116-127. 10.1016/j.molcel.2009.06.020.

Murata, K., and Wolf, M. (2018). Cryo-electron microscopy for structural analysis of dynamic biological macromolecules. Biochim Biophys Acta Gen Subj *1862*, 324-334. 10.1016/j.bbagen.2017.07.020.

Nader, D., Fletcher, N., Curley, G.F., and Kerrigan, S.W. (2021). SARS-CoV-2 uses major endothelial integrin alphavbeta3 to cause vascular dysregulation in-vitro during COVID-19. PLoS One *16*, e0253347. 10.1371/journal.pone.0253347.

Nakane, T., Kimanius, D., Lindahl, E., and Scheres, S.H. (2018). Characterisation of molecular motions in cryo-EM single-particle data by multi-body refinement in RELION. Elife *7*. 10.7554/eLife.36861.

Nakane, T., Kotecha, A., Sente, A., McMullan, G., Masiulis, S., Brown, P., Grigoras, I.T., Malinauskaite, L., Malinauskas, T., Miehling, J., et al. (2020). Single-particle cryo-EM at atomic resolution. Nature *587*, 152-156. 10.1038/s41586-020-2829-0.

Naydenova, K., Jia, P., and Russo, C.J. (2020). Cryo-EM with sub-1 A specimen movement. Science *370*, 223-226. 10.1126/science.abb7927.

Nedozralova, H., Basnet, N., Ibiricu, I., Bodakuntla, S., Biertumpfel, C., and Mizuno, N. (2022). In situ cryo-electron tomography reveals local cellular machineries for axon branch development. J Cell Biol *221*. 10.1083/jcb.202106086.

Neuman, B.W., Kiss, G., Kunding, A.H., Bhella, D., Baksh, M.F., Connelly, S., Droese, B., Klaus, J.P., Makino, S., Sawicki, S.G., et al. (2011). A structural analysis of M protein in coronavirus assembly and morphology. J Struct Biol *174*, 11-22. 10.1016/j.jsb.2010.11.021.

Nieswandt, B., Pleines, I., and Bender, M. (2011). Platelet adhesion and activation mechanisms in arterial thrombosis and ischaemic stroke. J Thromb Haemost *9 Suppl 1*, 92-104. 10.1111/j.1538-7836.2011.04361.x.

Nimonkar, A.V., Genschel, J., Kinoshita, E., Polaczek, P., Campbell, J.L., Wyman, C., Modrich, P., and Kowalczykowski, S.C. (2011). BLM-DNA2-RPA-MRN and EXO1-BLM-RPA-MRN constitute two DNA end resection machineries for human DNA break repair. Genes Dev *25*, 350-362. 10.1101/gad.2003811.

Nishiga, M., Wang, D.W., Han, Y., Lewis, D.B., and Wu, J.C. (2020). COVID-19 and cardiovascular disease: from basic mechanisms to clinical perspectives. Nat Rev Cardiol *17*, 543-558. 10.1038/s41569-020-0413-9.

Nishino, T., Ishino, Y., and Morikawa, K. (2006). Structure-specific DNA nucleases: structural basis for 3D-scissors. Curr Opin Struct Biol *16*, 60-67. 10.1016/j.sbi.2006.01.009.

Noble, A.J., Dandey, V.P., Wei, H., Brasch, J., Chase, J., Acharya, P., Tan, Y.Z., Zhang, Z., Kim, L.Y., Scapin, G., et al. (2018). Routine single particle CryoEM sample and grid characterization by tomography. Elife *7*. 10.7554/eLife.34257.

Nogales, E., and Scheres, S.H. (2015). Cryo-EM: A Unique Tool for the Visualization of Macromolecular Complexity. Mol Cell *58*, 677-689. 10.1016/j.molcel.2015.02.019.

O'Donovan, A., Davies, A.A., Moggs, J.G., West, S.C., and Wood, R.D. (1994). XPG endonuclease makes the 3' incision in human DNA nucleotide excision repair. Nature *371*, 432-435. 10.1038/371432a0.

O'Sullivan, J.M., Preston, R.J., O'Regan, N., and O'Donnell, J.S. (2016). Emerging roles for hemostatic dysfunction in malaria pathogenesis. Blood *127*, 2281-2288. 10.1182/blood-2015-11-636464.

Ogawa, T., Yu, X., Shinohara, A., and Egelman, E.H. (1993). Similarity of the yeast RAD51 filament to the bacterial RecA filament. Science *259*, 1896-1899. 10.1126/science.8456314.

Ogrunc, M., and Sancar, A. (2003). Identification and characterization of human MUS81-MMS4 structure-specific endonuclease. J Biol Chem *278*, 21715-21720. 10.1074/jbc.M302484200.

Olmezer, G., Levikova, M., Klein, D., Falquet, B., Fontana, G.A., Cejka, P., and Rass, U. (2016). Replication intermediates that escape Dna2 activity are processed by Holliday junction resolvase Yen1. Nat Commun *7*, 13157. 10.1038/ncomms13157.

Orans, J., McSweeney, E.A., Iyer, R.R., Hast, M.A., Hellinga, H.W., Modrich, P., and Beese, L.S. (2011). Structures of human exonuclease 1 DNA complexes suggest a unified mechanism for nuclease family. Cell *145*, 212-223. 10.1016/j.cell.2011.03.005.

Ortiz-Lombardia, M., Gonzalez, A., Eritja, R., Aymami, J., Azorin, F., and Coll, M. (1999). Crystal structure of a DNA Holliday junction. Nat Struct Biol *6*, 913-917. 10.1038/13277.

Pannunzio, N.R., Watanabe, G., and Lieber, M.R. (2018). Nonhomologous DNA end-joining for repair of DNA double-strand breaks. J Biol Chem *293*, 10512-10523. 10.1074/jbc.TM117.000374.

Park, E.J., Myint, P.K., Appiah, M.G., Darkwah, S., Caidengbate, S., Ito, A., Matsuo, E., Kawamoto, E., Gaowa, A., and Shimaoka, M. (2021). The Spike Glycoprotein of SARS-CoV-2 Binds to beta1 Integrins Expressed on the Surface of Lung Epithelial Cells. Viruses *13*. 10.3390/v13040645.

Pellegrini, L., Yu, D.S., Lo, T., Anand, S., Lee, M., Blundell, T.L., and Venkitaraman, A.R. (2002). Insights into DNA recombination from the structure of a RAD51-BRCA2 complex. Nature *420*, 287-293. 10.1038/nature01230.

Periayah, M.H., Halim, A.S., and Mat Saad, A.Z. (2017). Mechanism Action of Platelets and Crucial Blood Coagulation Pathways in Hemostasis. Int J Hematol Oncol Stem Cell Res *11*, 319-327.

Peterson, S.E., Li, Y., Chait, B.T., Gottesman, M.E., Baer, R., and Gautier, J. (2011). Cdk1 uncouples CtIP-dependent resection and Rad51 filament formation during M-phase double-strand break repair. J Cell Biol *194*, 705-720. 10.1083/jcb.201103103.

Petrich, B.G., Marchese, P., Ruggeri, Z.M., Spiess, S., Weichert, R.A., Ye, F., Tiedt, R., Skoda, R.C., Monkley, S.J., Critchley, D.R., and Ginsberg, M.H. (2007). Talin is required for integrin-mediated platelet function in hemostasis and thrombosis. J Exp Med *204*, 3103-3111. 10.1084/jem.20071800.

Petronczki, M., Siomos, M.F., and Nasmyth, K. (2003). Un menage a quatre: the molecular biology of chromosome segregation in meiosis. Cell *112*, 423-440. 10.1016/s0092-8674(03)00083-7.

Pettersen, E.F., Goddard, T.D., Huang, C.C., Couch, G.S., Greenblatt, D.M., Meng, E.C., and Ferrin, T.E. (2004). UCSF Chimera--a visualization system for exploratory research and analysis. J Comput Chem *25*, 1605-1612. 10.1002/jcc.20084.

Pettersen, E.F., Goddard, T.D., Huang, C.C., Meng, E.C., Couch, G.S., Croll, T.I., Morris, J.H., and Ferrin, T.E. (2021). UCSF ChimeraX: Structure visualization for researchers, educators, and developers. Protein Sci *30*, 70-82. 10.1002/pro.3943.

Pizzorno, A., Padey, B., Julien, T., Trouillet-Assant, S., Traversier, A., Errazuriz-Cerda, E., Fouret, J., Dubois, J., Gaymard, A., Lescure, F.X., et al. (2020). Characterization and Treatment of SARS-CoV-2 in Nasal and Bronchial Human Airway Epithelia. Cell Rep Med *1*, 100059. 10.1016/j.xcrm.2020.100059.

Plank, J.L., Wu, J., and Hsieh, T.S. (2006). Topoisomerase IIIalpha and Bloom's helicase can resolve a mobile double Holliday junction substrate through convergent branch migration. Proc Natl Acad Sci U S A *103*, 11118-11123. 10.1073/pnas.0604873103.

Plein, A., Fantin, A., and Ruhrberg, C. (2014). Neuropilin regulation of angiogenesis, arteriogenesis, and vascular permeability. Microcirculation *21*, 315-323. 10.1111/micc.12124.

Plow, E.F., and Byzova, T. (1999). The biology of glycoprotein IIb-IIIa. Coron Artery Dis *10*, 547-551. 10.1097/00019501-199912000-00002.

Portier, I., and Campbell, R.A. (2021). Role of Platelets in Detection and Regulation of Infection. Arterioscler Thromb Vasc Biol *41*, 70-78. 10.1161/ATVBAHA.120.314645.

Puhm, F., Allaeys, I., Lacasse, E., Dubuc, I., Galipeau, Y., Zaid, Y., Khalki, L., Belleannee, C., Durocher, Y., Brisson, A.R., et al. (2022). Platelet activation by SARS-CoV-2 implicates the release of active tissue factor by infected cells. Blood Adv *6*, 3593-3605. 10.1182/bloodadvances.2022007444.

Punjani, A., and Fleet, D.J. (2021). 3D variability analysis: Resolving continuous flexibility and discrete heterogeneity from single particle cryo-EM. J Struct Biol *213*, 107702. 10.1016/j.jsb.2021.107702.

Punjani, A., Rubinstein, J.L., Fleet, D.J., and Brubaker, M.A. (2017). cryoSPARC: algorithms for rapid unsupervised cryo-EM structure determination. Nat Methods *14*, 290-296. 10.1038/nmeth.4169.

Punjani, A., Zhang, H., and Fleet, D.J. (2020). Non-uniform refinement: adaptive regularization improves single-particle cryo-EM reconstruction. Nat Methods *17*, 1214-1221. 10.1038/s41592-020-00990-8.

Pytela, R., Pierschbacher, M.D., and Ruoslahti, E. (1985). A 125/115-kDa cell surface receptor specific for vitronectin interacts with the arginine-glycine-aspartic acid adhesion sequence derived from fibronectin. Proc Natl Acad Sci U S A *82*, 5766-5770. 10.1073/pnas.82.17.5766.

Qu, Y., Wang, X., Zhu, Y., Wang, W., Wang, Y., Hu, G., Liu, C., Li, J., Ren, S., Xiao, M.Z.X., et al. (2021). ORF3a-Mediated Incomplete Autophagy Facilitates Severe Acute Respiratory Syndrome Coronavirus-2 Replication. Front Cell Dev Biol *9*, 716208. 10.3389/fcell.2021.716208.

Radermacher, M. (1988). Three-dimensional reconstruction of single particles from random and nonrandom tilt series. J Electron Microsc Tech *9*, 359-394. 10.1002/jemt.1060090405.

Ragotte, R.J., Pulido, D., Donnellan, F.R., Hill, M.L., Gorini, G., Davies, H., Brun, J., McHugh, K., King, L.D.W., Skinner, K., et al. (2021). Human Basigin (CD147) Does Not Directly Interact with SARS-CoV-2 Spike Glycoprotein. mSphere *6*, e0064721. 10.1128/mSphere.00647-21.

Rass, U., Compton, S.A., Matos, J., Singleton, M.R., Ip, S.C., Blanco, M.G., Griffith, J.D., and West, S.C. (2010). Mechanism of Holliday junction resolution by the human GEN1 protein. Genes Dev *24*, 1559-1569. 10.1101/gad.585310.

Ravelli, R.B.G., Nijpels, F.J.T., Henderikx, R.J.M., Weissenberger, G., Thewessem, S., Gijsbers, A., Beulen, B., Lopez-Iglesias, C., and Peters, P.J. (2020). Cryo-EM structures from sub-nl volumes using pin-printing and jet vitrification. Nat Commun *11*, 2563. 10.1038/s41467-020-16392-5.

Razinkov, I., Dandey, V., Wei, H., Zhang, Z., Melnekoff, D., Rice, W.J., Wigge, C., Potter, C.S., and Carragher, B. (2016). A new method for vitrifying samples for cryoEM. J Struct Biol *195*, 190-198. 10.1016/j.jsb.2016.06.001.

Rigort, A., Bauerlein, F.J., Villa, E., Eibauer, M., Laugks, T., Baumeister, W., and Plitzko, J.M. (2012). Focused ion beam micromachining of eukaryotic cells for cryoelectron tomography. Proc Natl Acad Sci U S A *109*, 4449-4454. 10.1073/pnas.1201333109.

Rivera, J., Lozano, M.L., Navarro-Nunez, L., and Vicente, V. (2009). Platelet receptors and signaling in the dynamics of thrombus formation. Haematologica *94*, 700-711. 10.3324/haematol.2008.003178.

Rohou, A., and Grigorieff, N. (2015). CTFFIND4: Fast and accurate defocus estimation from electron micrographs. J Struct Biol *192*, 216-221. 10.1016/j.jsb.2015.08.008.

Romano, M., Ruggiero, A., Squeglia, F., Maga, G., and Berisio, R. (2020). A Structural View of SARS-CoV-2 RNA Replication Machinery: RNA Synthesis, Proofreading and Final Capping. Cells *9*. 10.3390/cells9051267.

Rondina, M.T., Weyrich, A.S., and Zimmerman, G.A. (2013). Platelets as cellular effectors of inflammation in vascular diseases. Circ Res *112*, 1506-1519. 10.1161/CIRCRESAHA.113.300512.

Russo, C.J., and Passmore, L.A. (2014). Electron microscopy: Ultrastable gold substrates for electron cryomicroscopy. Science *346*, 1377-1380. 10.1126/science.1259530.

Russo, C.J., and Passmore, L.A. (2016a). Progress towards an optimal specimen support for electron cryomicroscopy. Curr Opin Struct Biol *37*, 81-89. 10.1016/j.sbi.2015.12.007.

Russo, C.J., and Passmore, L.A. (2016b). Ultrastable gold substrates: Properties of a support for high-resolution electron cryomicroscopy of biological specimens. J Struct Biol *193*, 33-44. 10.1016/j.jsb.2015.11.006.

Saboor, M., Ayub, Q., Ilyas, S., and Moinuddin (2013). Platelet receptors; an instrumental of platelet physiology. Pak J Med Sci *29*, 891-896. 10.12669/pjms.293.3497.

Salfer, M., Collado, J.F., Baumeister, W., Fernandez-Busnadiego, R., and Martinez-Sanchez, A. (2020). Reliable estimation of membrane curvature for cryo-electron tomography. PLoS Comput Biol *16*, e1007962. 10.1371/journal.pcbi.1007962.

Sallmyr, A., and Tomkinson, A.E. (2018). Repair of DNA double-strand breaks by mammalian alternative end-joining pathways. J Biol Chem *293*, 10536-10546. 10.1074/jbc.TM117.000375.

San Filippo, J., Sung, P., and Klein, H. (2008). Mechanism of eukaryotic homologous recombination. Annu Rev Biochem *77*, 229-257. 10.1146/annurev.biochem.77.061306.125255.

Sanchez-Garcia, R., Gomez-Blanco, J., Cuervo, A., Carazo, J.M., Sorzano, C.O.S., and Vargas, J. (2021). DeepEMhancer: a deep learning solution for cryo-EM volume post-processing. Commun Biol *4*, 874. 10.1038/s42003-021-02399-1.

Sarbajna, S., and West, S.C. (2014). Holliday junction processing enzymes as guardians of genome stability. Trends Biochem Sci *39*, 409-419. 10.1016/j.tibs.2014.07.003.

Sartori, A., Gatz, R., Beck, F., Rigort, A., Baumeister, W., and Plitzko, J.M. (2007). Correlative microscopy: bridging the gap between fluorescence light microscopy and cryo-electron tomography. J Struct Biol *160*, 135-145. 10.1016/j.jsb.2007.07.011.

Satarker, S., and Nampoothiri, M. (2020). Structural Proteins in Severe Acute Respiratory Syndrome Coronavirus-2. Arch Med Res *51*, 482-491. 10.1016/j.arcmed.2020.05.012.

Schaffer, M., Pfeffer, S., Mahamid, J., Kleindiek, S., Laugks, T., Albert, S., Engel, B.D., Rummel, A., Smith, A.J., Baumeister, W., and Plitzko, J.M. (2019). A cryo-FIB lift-out technique enables molecular-resolution cryo-ET within native Caenorhabditis elegans tissue. Nat Methods *16*, 757-762. 10.1038/s41592-019-0497-5.

Scheres, S.H. (2012). RELION: implementation of a Bayesian approach to cryo-EM structure determination. J Struct Biol *180*, 519-530. 10.1016/j.jsb.2012.09.006.

Schindelin, J., Arganda-Carreras, I., Frise, E., Kaynig, V., Longair, M., Pietzsch, T., Preibisch, S., Rueden, C., Saalfeld, S., Schmid, B., et al. (2012). Fiji: an open-source platform for biological-image analysis. Nat Methods *9*, 676-682. 10.1038/nmeth.2019.

Schubert, K., Karousis, E.D., Jomaa, A., Scaiola, A., Echeverria, B., Gurzeler, L.A., Leibundgut, M., Thiel, V., Muhlemann, O., and Ban, N. (2020). SARS-CoV-2 Nsp1 binds the ribosomal mRNA channel to inhibit translation. Nat Struct Mol Biol *27*, 959-966. 10.1038/s41594-020-0511-8.

Schumacher, S., Dedden, D., Nunez, R.V., Matoba, K., Takagi, J., Biertumpfel, C., and Mizuno, N. (2021). Structural insights into integrin alpha5beta1 opening by fibronectin ligand. Sci Adv *7*. 10.1126/sciadv.abe9716.

Schwartz, C.L., Sarbash, V.I., Ataullakhanov, F.I., McIntosh, J.R., and Nicastro, D. (2007). Cryo-fluorescence microscopy facilitates correlations between light and cryo-electron microscopy and reduces the rate of photobleaching. J Microsc *227*, 98-109. 10.1111/j.1365-2818.2007.01794.x.

Schwartz, E.K., Wright, W.D., Ehmsen, K.T., Evans, J.E., Stahlberg, H., and Heyer, W.D. (2012). Mus81-Mms4 functions as a single heterodimer to cleave nicked intermediates in recombinational DNA repair. Mol Cell Biol *32*, 3065-3080. 10.1128/MCB.00547-12.

Schwertz, H., Koster, S., Kahr, W.H., Michetti, N., Kraemer, B.F., Weitz, D.A., Blaylock, R.C., Kraiss, L.W., Greinacher, A., Zimmerman, G.A., and Weyrich, A.S. (2010). Anucleate platelets generate progeny. Blood *115*, 3801-3809. 10.1182/blood-2009-08-239558.

Scully, R., Panday, A., Elango, R., and Willis, N.A. (2019). DNA double-strand break repair-pathway choice in somatic mammalian cells. Nat Rev Mol Cell Biol *20*, 698-714. 10.1038/s41580-019-0152-0.

Shah Punatar, R., Martin, M.J., Wyatt, H.D., Chan, Y.W., and West, S.C. (2017). Resolution of single and double Holliday junction recombination intermediates by GEN1. Proc Natl Acad Sci U S A *114*, 443-450. 10.1073/pnas.1619790114.

Shang, J., Wan, Y., Luo, C., Ye, G., Geng, Q., Auerbach, A., and Li, F. (2020). Cell entry mechanisms of SARS-CoV-2. Proc Natl Acad Sci U S A *117*, 11727-11734. 10.1073/pnas.2003138117.

Shen, A., Lupardus, P.J., Morell, M., Ponder, E.L., Sadaghiani, A.M., Garcia, K.C., and Bogyo, M. (2009). Simplified, enhanced protein purification using an inducible, autoprocessing enzyme tag. PLoS One *4*, e8119. 10.1371/journal.pone.0008119.

Shen, S., Zhang, J., Fang, Y., Lu, S., Wu, J., Zheng, X., and Deng, F. (2021). SARS-CoV-2 interacts with platelets and megakaryocytes via ACE2-independent mechanism. J Hematol Oncol *14*, 72. 10.1186/s13045-021-01082-6.

Shilts, J., Crozier, T.W.M., Greenwood, E.J.D., Lehner, P.J., and Wright, G.J. (2021). No evidence for basigin/CD147 as a direct SARS-CoV-2 spike binding receptor. Sci Rep *11*, 413. 10.1038/s41598-020-80464-1.

Shirato, K., and Kizaki, T. (2021). SARS-CoV-2 spike protein S1 subunit induces pro-inflammatory responses via toll-like receptor 4 signaling in murine and human macrophages. Heliyon *7*, e06187. 10.1016/j.heliyon.2021.e06187.

Shivdasani, R.A., Rosenblatt, M.F., Zucker-Franklin, D., Jackson, C.W., Hunt, P., Saris, C.J., and Orkin, S.H. (1995). Transcription factor NF-E2 is required for platelet formation independent of the actions of thrombopoietin/MGDF in megakaryocyte development. Cell *81*, 695-704. 10.1016/0092-8674(95)90531-6.

Sievers, F., Wilm, A., Dineen, D., Gibson, T.J., Karplus, K., Li, W., Lopez, R., McWilliam, H., Remmert, M., Soding, J., et al. (2011). Fast, scalable generation of high-quality protein multiple sequence alignments using Clustal Omega. Mol Syst Biol *7*, 539. 10.1038/msb.2011.75.

Sigrist, C.J., Bridge, A., and Le Mercier, P. (2020). A potential role for integrins in host cell entry by SARS-CoV-2. Antiviral Res *177*, 104759. 10.1016/j.antiviral.2020.104759.

Simon, A.Y., Sutherland, M.R., and Pryzdial, E.L. (2015). Dengue virus binding and replication by platelets. Blood *126*, 378-385. 10.1182/blood-2014-09-598029.

Simons, P., Rinaldi, D.A., Bondu, V., Kell, A.M., Bradfute, S., Lidke, D.S., and Buranda, T. (2021). Integrin activation is an essential component of SARS-CoV-2 infection. Sci Rep *11*, 20398. 10.1038/s41598-021-99893-7.

Siu, Y.L., Teoh, K.T., Lo, J., Chan, C.M., Kien, F., Escriou, N., Tsao, S.W., Nicholls, J.M., Altmeyer, R., Peiris, J.S., et al. (2008). The M, E, and N structural proteins of the severe acute respiratory syndrome coronavirus are required for efficient assembly, trafficking, and release of virus-like particles. J Virol *82*, 11318-11330. 10.1128/JVI.01052-08.

Smith, C.W. (2022). Release of alpha-granule contents during platelet activation. Platelets *33*, 491-502. 10.1080/09537104.2021.1913576.

Snijder, E.J., Limpens, R., de Wilde, A.H., de Jong, A.W.M., Zevenhoven-Dobbe, J.C., Maier, H.J., Faas, F., Koster, A.J., and Barcena, M. (2020). A unifying structural and functional model of the coronavirus replication organelle: Tracking down RNA synthesis. PLoS Biol *18*, e3000715. 10.1371/journal.pbio.3000715.

Sobhy, M.A., Bralic, A., Raducanu, V.S., Takahashi, M., Tehseen, M., Rashid, F., Zaher, M.S., and Hamdan, S.M. (2019). Resolution of the Holliday junction recombination intermediate by human GEN1 at the single-molecule level. Nucleic Acids Res *47*, 1935-1949. 10.1093/nar/gky1280.

Solinger, J.A., Kiianitsa, K., and Heyer, W.D. (2002). Rad54, a Swi2/Snf2-like recombinational repair protein, disassembles Rad51:dsDNA filaments. Mol Cell *10*, 1175-1188. 10.1016/s1097-2765(02)00743-8.

Srinivas, U.S., Tan, B.W.Q., Vellayappan, B.A., and Jeyasekharan, A.D. (2019). ROS and the DNA damage response in cancer. Redox Biol *25*, 101084. 10.1016/j.redox.2018.101084.

Srivastava, K., Field, D.J., Aggrey, A., Yamakuchi, M., and Morrell, C.N. (2010). Platelet factor 4 regulation of monocyte KLF4 in experimental cerebral malaria. PLoS One *5*, e10413. 10.1371/journal.pone.0010413.

Stahl, A.L., Svensson, M., Morgelin, M., Svanborg, C., Tarr, P.I., Mooney, J.C., Watkins, S.L., Johnson, R., and Karpman, D. (2006). Lipopolysaccharide from enterohemorrhagic Escherichia coli binds to platelets through TLR4 and CD62 and is detected on circulating platelets in patients with hemolytic uremic syndrome. Blood *108*, 167-176. 10.1182/blood-2005-08-3219.

Sung, P. (1997). Function of yeast Rad52 protein as a mediator between replication protein A and the Rad51 recombinase. J Biol Chem *272*, 28194-28197. 10.1074/jbc.272.45.28194.

Sung, P., Krejci, L., Van Komen, S., and Sehorn, M.G. (2003). Rad51 recombinase and recombination mediators. J Biol Chem *278*, 42729-42732. 10.1074/jbc.R300027200.

Svendsen, J.M., Smogorzewska, A., Sowa, M.E., O'Connell, B.C., Gygi, S.P., Elledge, S.J., and Harper, J.W. (2009). Mammalian BTBD12/SLX4 assembles a Holliday junction resolvase and is required for DNA repair. Cell *138*, 63-77. 10.1016/j.cell.2009.06.030.

Symington, L.S. (2014). End resection at double-strand breaks: mechanism and regulation. Cold Spring Harb Perspect Biol *6*. 10.1101/cshperspect.a016436.

Symington, L.S., and Gautier, J. (2011). Double-strand break end resection and repair pathway choice. Annu Rev Genet *45*, 247-271. 10.1146/annurev-genet-110410-132435.

Szostak, J.W., Orr-Weaver, T.L., Rothstein, R.J., and Stahl, F.W. (1983). The double-strand-break repair model for recombination. Cell *33*, 25-35. 10.1016/0092-8674(83)90331-8.

Tablin, F., Castro, M., and Leven, R.M. (1990). Blood platelet formation in vitro. The role of the cytoskeleton in megakaryocyte fragmentation. J Cell Sci *97 (Pt 1)*, 59-70. 10.1242/jcs.97.1.59.

Tadokoro, S., Shattil, S.J., Eto, K., Tai, V., Liddington, R.C., de Pereda, J.M., Ginsberg, M.H., and Calderwood, D.A. (2003). Talin binding to integrin beta tails: a final common step in integrin activation. Science *302*, 103-106. 10.1126/science.1086652.

Tang, N., Li, D., Wang, X., and Sun, Z. (2020a). Abnormal coagulation parameters are associated with poor prognosis in patients with novel coronavirus pneumonia. J Thromb Haemost *18*, 844-847. 10.1111/jth.14768.

Tang, T., Bidon, M., Jaimes, J.A., Whittaker, G.R., and Daniel, S. (2020b). Coronavirus membrane fusion mechanism offers a potential target for antiviral development. Antiviral Res *178*, 104792. 10.1016/j.antiviral.2020.104792.

Taylor, E.R., and McGowan, C.H. (2008). Cleavage mechanism of human Mus81-Eme1 acting on Holliday-junction structures. Proc Natl Acad Sci U S A *105*, 3757-3762. 10.1073/pnas.0710291105.

Teesalu, T., Sugahara, K.N., Kotamraju, V.R., and Ruoslahti, E. (2009). C-end rule peptides mediate neuropilin-1-dependent cell, vascular, and tissue penetration. Proc Natl Acad Sci U S A *106*, 16157-16162. 10.1073/pnas.0908201106.

Temmam, S., Vongphayloth, K., Baquero, E., Munier, S., Bonomi, M., Regnault, B., Douangboubpha, B., Karami, Y., Chretien, D., Sanamxay, D., et al. (2022). Bat coronaviruses related to SARS-CoV-2 and infectious for human cells. Nature *604*, 330-336. 10.1038/s41586-022-04532-4.

Theveny, L.M., Mageswaran, S.K., Chen, W.D., Martinez, M., Guerin, A., and Chang, Y.W. (2022). Parasitology meets cryo-electron tomography - exciting prospects await. Trends Parasitol *38*, 365-378. 10.1016/j.pt.2022.01.006.

Thomas, S.G. (2019). 3 - The Structure of Resting and Activated Platelets, 4 Edition (Academic Press). https://doi.org/10.1016/B978-0-12-813456-6.00003-5.

Thoms, M., Buschauer, R., Ameismeier, M., Koepke, L., Denk, T., Hirschenberger, M., Kratzat, H., Hayn, M., Mackens-Kiani, T., Cheng, J., et al. (2020). Structural basis for translational shutdown and immune evasion by the Nsp1 protein of SARS-CoV-2. Science *369*, 1249-1255. 10.1126/science.abc8665.

Thon, J.N., Macleod, H., Begonja, A.J., Zhu, J., Lee, K.C., Mogilner, A., Hartwig, J.H., and Italiano, J.E., Jr. (2012). Microtubule and cortical forces determine platelet size during vascular platelet production. Nat Commun *3*, 852. 10.1038/ncomms1838.

Thon, J.N., Montalvo, A., Patel-Hett, S., Devine, M.T., Richardson, J.L., Ehrlicher, A., Larson, M.K., Hoffmeister, K., Hartwig, J.H., and Italiano, J.E., Jr. (2010). Cytoskeletal mechanics of proplatelet maturation and platelet release. J Cell Biol *191*, 861-874. 10.1083/jcb.201006102.

Thorslund, T., McIlwraith, M.J., Compton, S.A., Lekomtsev, S., Petronczki, M., Griffith, J.D., and West, S.C. (2010). The breast cancer tumor suppressor BRCA2 promotes the specific targeting of RAD51 to single-stranded DNA. Nat Struct Mol Biol *17*, 1263-1265. 10.1038/nsmb.1905.

Tomlinson, C.G., Atack, J.M., Chapados, B., Tainer, J.A., and Grasby, J.A. (2010). Substrate recognition and catalysis by flap endonucleases and related enzymes. Biochem Soc Trans *38*, 433-437. 10.1042/BST0380433.

Toro-Nahuelpan, M., Zagoriy, I., Senger, F., Blanchoin, L., Thery, M., and Mahamid, J. (2020). Tailoring cryo-electron microscopy grids by photo-micropatterning for in-cell structural studies. Nat Methods *17*, 50-54. 10.1038/s41592-019-0630-5.

Turk, M., and Baumeister, W. (2020). The promise and the challenges of cryo-electron tomography. FEBS Lett *594*, 3243-3261. 10.1002/1873-3468.13948.

Turonova, B., Hagen, W.J.H., Obr, M., Mosalaganti, S., Beugelink, J.W., Zimmerli, C.E., Krausslich, H.G., and Beck, M. (2020a). Benchmarking tomographic acquisition schemes for high-resolution structural biology. Nat Commun *11*, 876. 10.1038/s41467-020-14535-2.

Turonova, B., Sikora, M., Schurmann, C., Hagen, W.J.H., Welsch, S., Blanc, F.E.C., von Bulow, S., Gecht, M., Bagola, K., Horner, C., et al. (2020b). In situ structural analysis of SARS-CoV-2 spike reveals flexibility mediated by three hinges. Science *370*, 203-208. 10.1126/science.abd5223.

V'Kovski, P., Kratzel, A., Steiner, S., Stalder, H., and Thiel, V. (2021). Coronavirus biology and replication: implications for SARS-CoV-2. Nat Rev Microbiol *19*, 155-170. 10.1038/s41579-020-00468-6.

van der Meijden, P.E.J., and Heemskerk, J.W.M. (2019). Platelet biology and functions: new concepts and clinical perspectives. Nat Rev Cardiol *16*, 166-179. 10.1038/s41569-018-0110-0.

van der Most, R.G., Heijnen, L., Spaan, W.J., and de Groot, R.J. (1992). Homologous RNA recombination allows efficient introduction of site-specific mutations into the genome of coronavirus MHV-A59 via synthetic co-replicating RNAs. Nucleic Acids Res *20*, 3375-3381. 10.1093/nar/20.13.3375.

Wagner, T., Merino, F., Stabrin, M., Moriya, T., Antoni, C., Apelbaum, A., Hagel, P., Sitsel, O., Raisch, T., Prumbaum, D., et al. (2019). SPHIRE-crYOLO is a fast and accurate fully automated particle picker for cryo-EM. Commun Biol *2*, 218. 10.1038/s42003-019-0437-z.

Walls, A.C., Park, Y.J., Tortorici, M.A., Wall, A., McGuire, A.T., and Veesler, D. (2020). Structure, Function, and Antigenicity of the SARS-CoV-2 Spike Glycoprotein. Cell *181*, 281-292 e286. 10.1016/j.cell.2020.02.058.

Wan, W., and Briggs, J.A. (2016). Cryo-Electron Tomography and Subtomogram Averaging. Methods Enzymol *579*, 329-367. 10.1016/bs.mie.2016.04.014.

Wan, Y., Shang, J., Graham, R., Baric, R.S., and Li, F. (2020). Receptor Recognition by the Novel Coronavirus from Wuhan: an Analysis Based on Decade-Long Structural Studies of SARS Coronavirus. J Virol *94*. 10.1128/JVI.00127-20.

Wang, F., Yang, Y., Singh, T.R., Busygina, V., Guo, R., Wan, K., Wang, W., Sung, P., Meetei, A.R., and Lei, M. (2010). Crystal structures of RMI1 and RMI2, two OB-fold regulatory subunits of the BLM complex. Structure *18*, 1159-1170. 10.1016/j.str.2010.06.008.

Wang, K., Chen, W., Zhang, Z., Deng, Y., Lian, J.Q., Du, P., Wei, D., Zhang, Y., Sun, X.X., Gong, L., et al. (2020a). CD147-spike protein is a novel route for SARS-CoV-2 infection to host cells. Signal Transduct Target Ther *5*, 283. 10.1038/s41392-020-00426-x.

Wang, Q., Zhang, Y., Wu, L., Niu, S., Song, C., Zhang, Z., Lu, G., Qiao, C., Hu, Y., Yuen, K.Y., et al. (2020b). Structural and Functional Basis of SARS-CoV-2 Entry by Using Human ACE2. Cell *181*, 894-904 e899. 10.1016/j.cell.2020.03.045.

Waterhouse, A.M., Procter, J.B., Martin, D.M., Clamp, M., and Barton, G.J. (2009). Jalview Version 2--a multiple sequence alignment editor and analysis workbench. Bioinformatics *25*, 1189-1191. 10.1093/bioinformatics/btp033.

Watson, J.D., and Crick, F.H. (1953). Molecular structure of nucleic acids; a structure for deoxyribose nucleic acid. Nature *171*, 737-738. 10.1038/171737a0.

Weissenberger, G., Henderikx, R.J.M., and Peters, P.J. (2021). Understanding the invisible hands of sample preparation for cryo-EM. Nat Methods *18*, 463-471. 10.1038/s41592-021-01130-6.

Weissenhorn, W., Dessen, A., Calder, L.J., Harrison, S.C., Skehel, J.J., and Wiley, D.C. (1999). Structural basis for membrane fusion by enveloped viruses. Mol Membr Biol *16*, 3-9. 10.1080/096876899294706.

Wickham, T.J., Mathias, P., Cheresh, D.A., and Nemerow, G.R. (1993). Integrins alpha v beta 3 and alpha v beta 5 promote adenovirus internalization but not virus attachment. Cell *73*, 309-319. 10.1016/0092-8674(93)90231-e.

Wild, P., and Matos, J. (2016). Cell cycle control of DNA joint molecule resolution. Curr Opin Cell Biol *40*, 74-80. 10.1016/j.ceb.2016.02.018.

Wold, M.S. (1997). Replication protein A: a heterotrimeric, single-stranded DNA-binding protein required for eukaryotic DNA metabolism. Annu Rev Biochem *66*, 61-92. 10.1146/annurev.biochem.66.1.61.

Wolff, G., Limpens, R., Zevenhoven-Dobbe, J.C., Laugks, U., Zheng, S., de Jong, A.W.M., Koning, R.I., Agard, D.A., Grunewald, K., Koster, A.J., et al. (2020). A molecular pore spans the double membrane of the coronavirus replication organelle. Science *369*, 1395-1398. 10.1126/science.abd3629.

Wong, N.A., and Saier, M.H., Jr. (2021). The SARS-Coronavirus Infection Cycle: A Survey of Viral Membrane Proteins, Their Functional Interactions and Pathogenesis. Int J Mol Sci *22*. 10.3390/ijms22031308.

Wrapp, D., Wang, N., Corbett, K.S., Goldsmith, J.A., Hsieh, C.L., Abiona, O., Graham, B.S., and McLellan, J.S. (2020). Cryo-EM structure of the 2019-nCoV spike in the prefusion conformation. Science *367*, 1260-1263. 10.1126/science.abb2507.

Wright, W.D., Shah, S.S., and Heyer, W.D. (2018). Homologous recombination and the repair of DNA double-strand breaks. J Biol Chem *293*, 10524-10535. 10.1074/jbc.TM118.000372.

Wu, F., Zhao, S., Yu, B., Chen, Y.M., Wang, W., Song, Z.G., Hu, Y., Tao, Z.W., Tian, J.H., Pei, Y.Y., et al. (2020). A new coronavirus associated with human respiratory disease in China. Nature *579*, 265-269. 10.1038/s41586-020-2008-3.

Wu, L., Davies, S.L., North, P.S., Goulaouic, H., Riou, J.F., Turley, H., Gatter, K.C., and Hickson, I.D. (2000). The Bloom's syndrome gene product interacts with topoisomerase III. J Biol Chem *275*, 9636-9644. 10.1074/jbc.275.13.9636.

Wu, L., and Hickson, I.D. (2002). The Bloom's syndrome helicase stimulates the activity of human topoisomerase IIIalpha. Nucleic Acids Res *30*, 4823-4829. 10.1093/nar/gkf611.

Wu, L., and Hickson, I.D. (2003). The Bloom's syndrome helicase suppresses crossing over during homologous recombination. Nature *426*, 870-874. 10.1038/nature02253.

Wu, M., and Lander, G.C. (2020). Present and Emerging Methodologies in Cryo-EM Single-Particle Analysis. Biophys J *119*, 1281-1289. 10.1016/j.bpj.2020.08.027.

Wyatt, H.D., Laister, R.C., Martin, S.R., Arrowsmith, C.H., and West, S.C. (2017). The SMX DNA Repair Tri-nuclease. Mol Cell *65*, 848-860 e811. 10.1016/j.molcel.2017.01.031.

Wyatt, H.D., Sarbajna, S., Matos, J., and West, S.C. (2013). Coordinated actions of SLX1-SLX4 and MUS81-EME1 for Holliday junction resolution in human cells. Mol Cell *52*, 234-247. 10.1016/j.molcel.2013.08.035.

Wyatt, H.D., and West, S.C. (2014). Holliday junction resolvases. Cold Spring Harb Perspect Biol *6*, a023192. 10.1101/cshperspect.a023192.

Xia, S., Liu, M., Wang, C., Xu, W., Lan, Q., Feng, S., Qi, F., Bao, L., Du, L., Liu, S., et al. (2020). Inhibition of SARS-CoV-2 (previously 2019-nCoV) infection by a highly potent pan-coronavirus fusion inhibitor targeting its spike protein that harbors a high capacity to mediate membrane fusion. Cell Res *30*, 343-355. 10.1038/s41422-020-0305-x.

Xia, X. (2021). Domains and Functions of Spike Protein in Sars-Cov-2 in the Context of Vaccine Design. Viruses *13*. 10.3390/v13010109.

Xu, J., Zhao, L., Xu, Y., Zhao, W., Sung, P., and Wang, H.W. (2017). Cryo-EM structures of human RAD51 recombinase filaments during catalysis of DNA-strand exchange. Nat Struct Mol Biol *24*, 40-46. 10.1038/nsmb.3336.

Xue, H., Zhang, M., Liu, J., Wang, J., and Ren, G. (2022). Cryo-electron tomography related radiation-damage parameters for individual-molecule 3D structure determination. Front Chem *10*, 889203. 10.3389/fchem.2022.889203.

Yan, R., Zhang, Y., Li, Y., Xia, L., Guo, Y., and Zhou, Q. (2020). Structural basis for the recognition of SARS-CoV-2 by full-length human ACE2. Science *367*, 1444-1448. 10.1126/science.abb2762.

Yang, H., Li, Q., Fan, J., Holloman, W.K., and Pavletich, N.P. (2005). The BRCA2 homologue Brh2 nucleates RAD51 filament formation at a dsDNA-ssDNA junction. Nature *433*, 653-657. 10.1038/nature03234.

Yang, H., and Rao, Z. (2021). Structural biology of SARS-CoV-2 and implications for therapeutic development. Nat Rev Microbiol *19*, 685-700. 10.1038/s41579-021-00630-8.

Yang, J., Bachrati, C.Z., Ou, J., Hickson, I.D., and Brown, G.W. (2010). Human topoisomerase IIIalpha is a single-stranded DNA decatenase that is stimulated by BLM and RMI1. J Biol Chem *285*, 21426-21436. 10.1074/jbc.M110.123216.

Ye, Q., West, A.M.V., Silletti, S., and Corbett, K.D. (2020). Architecture and self-assembly of the SARS-CoV-2 nucleocapsid protein. Protein Sci *29*, 1890-1901. 10.1002/pro.3909.

Yip, K.M., Fischer, N., Paknia, E., Chari, A., and Stark, H. (2020). Atomic-resolution protein structure determination by cryo-EM. Nature *587*, 157-161. 10.1038/s41586-020-2833-4.

Yu, X., Jacobs, S.A., West, S.C., Ogawa, T., and Egelman, E.H. (2001). Domain structure and dynamics in the helical filaments formed by RecA and Rad51 on DNA. Proc Natl Acad Sci U S A *98*, 8419-8424. 10.1073/pnas.111005398.

Yun, S.H., Sim, E.H., Goh, R.Y., Park, J.I., and Han, J.Y. (2016). Platelet Activation: The Mechanisms and Potential Biomarkers. Biomed Res Int *2016*, 9060143. 10.1155/2016/9060143.

Zaid, Y., Puhm, F., Allaeys, I., Naya, A., Oudghiri, M., Khalki, L., Limami, Y., Zaid, N., Sadki, K., Ben El Haj, R., et al. (2020). Platelets Can Associate with SARS-Cov-2 RNA and Are Hyperactivated in COVID-19. Circ Res. 10.1161/CIRCRESAHA.120.317703.

Zhang, H., Penninger, J.M., Li, Y., Zhong, N., and Slutsky, A.S. (2020a). Angiotensin-converting enzyme 2 (ACE2) as a SARS-CoV-2 receptor: molecular mechanisms and potential therapeutic target. Intensive Care Med *46*, 586-590. 10.1007/s00134-020-05985-9.

Zhang, K. (2016). Gctf: Real-time CTF determination and correction. J Struct Biol *193*, 1-12. 10.1016/j.jsb.2015.11.003.

Zhang, K., Pintilie, G.D., Li, S., Schmid, M.F., and Chiu, W. (2020b). Resolving individual atoms of protein complex by cryo-electron microscopy. Cell Res *30*, 1136-1139. 10.1038/s41422-020-00432-2.

Zhang, S., Liu, Y., Wang, X., Yang, L., Li, H., Wang, Y., Liu, M., Zhao, X., Xie, Y., Yang, Y., et al. (2020c). SARS-CoV-2 binds platelet ACE2 to enhance thrombosis in COVID-19. J Hematol Oncol *13*, 120. 10.1186/s13045-020-00954-7.

Zhao, Y., Kuang, M., Li, J., Zhu, L., Jia, Z., Guo, X., Hu, Y., Kong, J., Yin, H., Wang, X., and You, F. (2021). SARS-CoV-2 spike protein interacts with and activates TLR41. Cell Res. 10.1038/s41422-021-00495-9.

Zheng, S.Q., Palovcak, E., Armache, J.P., Verba, K.A., Cheng, Y., and Agard, D.A. (2017). MotionCor2: anisotropic correction of beam-induced motion for improved cryo-electron microscopy. Nat Methods *14*, 331-332. 10.1038/nmeth.4193.

Zhou, P., Yang, X.L., Wang, X.G., Hu, B., Zhang, L., Zhang, W., Si, H.R., Zhu, Y., Li, B., Huang, C.L., et al. (2020). A pneumonia outbreak associated with a new coronavirus of probable bat origin. Nature *579*, 270-273. 10.1038/s41586-020-2012-7.

Zhu, A., Real, F., Capron, C., Rosenberg, A.R., Silvin, A., Dunsmore, G., Zhu, J., Cottoignies-Callamarte, A., Masse, J.M., Moine, P., et al. (2022). Infection of lung megakaryocytes and platelets by SARS-CoV-2 anticipate fatal COVID-19. Cell Mol Life Sci *79*, 365. 10.1007/s00018-022-04318-x.

Zhu, C., He, G., Yin, Q., Zeng, L., Ye, X., Shi, Y., and Xu, W. (2021). Molecular biology of the SARs-CoV-2 spike protein: A review of current knowledge. J Med Virol *93*, 5729-5741. 10.1002/jmv.27132.

Zhu, N., Zhang, D., Wang, W., Li, X., Yang, B., Song, J., Zhao, X., Huang, B., Shi, W., Lu, R., et al. (2020). A Novel Coronavirus from Patients with Pneumonia in China, 2019. N Engl J Med *382*, 727-733. 10.1056/NEJMoa2001017.

Zivanov, J., Nakane, T., Forsberg, B.O., Kimanius, D., Hagen, W.J., Lindahl, E., and Scheres, S.H. (2018). New tools for automated high-resolution cryo-EM structure determination in RELION-3. Elife *7*. 10.7554/eLife.42166.

Zivanov, J., Nakane, T., and Scheres, S.H.W. (2020). Estimation of high-order aberrations and anisotropic magnification from cryo-EM data sets in RELION-3.1. IUCrJ *7*, 253-267. 10.1107/S2052252520000081.

Zuo, Y., Estes, S.K., Ali, R.A., Gandhi, A.A., Yalavarthi, S., Shi, H., Sule, G., Gockman, K., Madison, J.A., Zuo, M., et al. (2020). Prothrombotic autoantibodies in serum from patients hospitalized with COVID-19. Sci Transl Med *12*. 10.1126/scitranslmed.abd3876.

Acknowledgements

First, I sincerely want to thank my PhD supervisor Naoko Mizuno for the opportunity to explore the exciting field of cryo-electron microscopy. Throughout my graduate studies, she offered an amazing research environment at the MPI and the NIH, combined with the scientific freedom and guidance to learn and grow as a researcher.
Special thanks go to Christian Biertümpfel for great support, informative discussions, and helpful guidance during my time in the lab, especially on structure-biological and computational questions.

In particular, I would like to thank my doctoral mother Elena Conti for creating an excellent research infrastructure and truly welcoming atmosphere in her department at the Max-Planck Institute. I am especially thankful for her scientific advice and support during my PhD adventure in the US.

I also want to thank Antonio Martínez-Sánchez to introduce a different perspective as part of my TAC and furthermore providing his computational expertise as collaborator.
In this regard, I my thanks go to Junichi Takagi for his scientific input and support during our collaboration.
Extended thanks go out to Zeynep Ökten and Jim Sellers as part of my thesis advisory committee and their scientific remarks and suggestions.

In addition, I want to thank all the past and present members of the Mizuno group on both sides of the ocean: Nirakar, Satish, Young-Min, Scott, Pelayo, John, Ryan, Lorenzo, Yurika and Kenichiro for sharing a fun time at the NHLBI and the sunny terrace in the back of Building 50. Extended thanks go out to our neighbors, the Akera Lab, for creating a nice atmosphere in the lab and kitchen. Also, I want to thank the CDBC for creating a great scientific community, the NHLBI Light Microscopy department, with special thanks to Xufeng Wu for her support, and the MICEF department, especially Ulrich Baxa for his discussions, help and contagious excitement around the electron microscopes. I am really thankful to all the blood donors and the staff of the NIH Blood Bank, without whom my research would not have been possible.
Of course, I want to thank the lab and people around the MPI in Martinsried as well. First of all, I thanks to all the members of the lab on the 2nd floor: Steffi, Dirk, Hana, Sven, Charlotte, Xiang and Nirakar again as well as Giulia, Shun and Iuliia. Thanks for the amazing scientific and non-scientific moments, it has been wonderful. Many thanks go out to the whole Conti department for their welcoming nature, their scientific discussions and all the wonderful gatherings during my

times at the Max Planck Institute. Truly, there couldn't been a better lab the floor above. Furthermore, I want to thank the MPI biochemistry core facility as well as the cryo-EM facility for their amazing support, with special thanks to Daniel and Tillman for the help at any time, and their sparkling eyes while telling all about cryo-EM. Last but not least thanks to Tom & Geri for the coffee break philosophy in aquarium of the institute.

Thank you Shun, Nirakar, Giulia, Steffi, Dirk and Satish for the amazing support, above and beyond the time in the lab. I cannot imagine better lab mates and friends, it is always fun with you!
Thanks to Antonio, Andrew and Lelia for the fun times out in Bethesda and DC. It was so much to explore, and probably so much more to see – now it's your time to come (back) to Europe!
Special thanks are going out to my Green Pointers, Rodin, Dara, Maria, John, Bombi and Olive, for showing me around the fun side of New York. I am happy I always had a home in the most amazing part of Brooklyn!
Thank you Costanza for being the best mix of everything, your support and love! Now it's time to see the rest of the world!
Especially, I want to thank my friends and family for being there – always, everywhere & anytime – thank you!

Vor allem möchte ich meinen wunderbaren Eltern, meinen drei wundervollen Schwestern und meinen beiden nicht weniger tollen Brüdern danken, für deren endlose Unterstützung, zu jeder Zeit! Ohne euch wäre das nix geworden, danke!